Single-Spin Asymmetry in Electro-Production of $\pi^+\pi^-$ Pairs from a Transversely Polarized Proton Target at the HERMES Experiment

Xiao-Rui Lu

Thesis submitted to the Department of Physics in partial
fulfillment of the requirements for the degree of

Doctor of Science

at Tokyo Institute of Technology

September, 2008

Abstract

Spin structure of the nucleon is one of the fundamental topics in physics. The proton has spin 1/2, and contains quarks with spin 1/2 and gluons with spin 1. Three fundamental quark distribution functions describe the structure of the nucleon at leading twist of QCD: the unpolarized distribution $f_1(x)$, the helicity distribution $\mathrm{g}_1(x)$, and the transversity distribution $h_1(x)$. Transversity describes the distribution of transversely polarized quarks in a nucleon polarized transverse to the direction of the hard probe. Different from the other two, it is inaccessible in inclusive measurement of Deep Inelastic Scattering (DIS). Therefore it is most difficult to measure. However, it can be accessed with semi–inclusive DIS where the scattered lepton and produced hadron(s) are detected in coincidence. The single–spin asymmetry in dihadron lepto–production ($e + p^{\uparrow} \rightarrow e' + h_1 + h_2 + X$) on a transversely polarized target is related to the product of the quark transversity distribution function $h_1(x)$ and the dihadron fragmentation function. In this thesis, the measurement of an azimuthal amplitude of the asymmetry in the lepto–production of $\pi^+\pi^-$ pairs at the HERMES experiment is reported.

The HERMES experiment was designed to perform a precise measurement of the quark spin structure of the nucleon in the inclusive and semi–inclusive measurement of DIS processes. The experiment was carried out at DESY in Germany, utilizing the longitudinally polarized 27.6 GeV electron/positron beam of the HERA storage ring in combination with a longitudinally or transversely polarized gaseous target internal to the beam pipe. For the present measurement, the transversely polarized proton target was used and the beam polarization was averaged out in order to measure the asymmetry A_{UT}. A Ring Imaging Čerenkov (RICH) detector allows the precise identification of pions, kaons and protons over essentially the entire momentum range of the experiment. The atomic gas target was used in the HERMES experiment, which has an advantage of low dilution. The transversely polarized hydrogen gas target at HERMES reached a high degree of polarization, namely 75%. The transverse holding magnetic field was flipped every 60 second, so the spin states of the atomic gas was also flipped every 60 second, which significantly decreased the systematic uncertainty in the polarization measurement. All the performance of the detectors was monitored and diagnosed by Gain Monitoring System (GMS). I worked for the operation of GMS and also for combining the GMS data with other detector data from various triggers.

The asymmetry A_{UT} for $\pi^+\pi^-$ pair production was measured for the first time in the world by HERMES. It is found that the amplitude of this asymmetry is significantly non–zero with the value of $0.018 \pm 0.005(\mathrm{stat})^{+0.004}_{-0.002}(\mathrm{syst})$. It implies that both transversity and the dihadron fragmentation function are non–zero. The amplitudes are extracted as functions of different kinematic variables, which can facilitate the comparison with the theoretical models and the extraction of transversity with combination of the measurement of the dihadron fragmentation function. The positive amplitudes obtained from this work in the whole kinematic range reject the theoretical model which predicted the sign change in the vicinity of the ρ^0 mass.

Contents

4 Data Analysis 87

5 Discussion on Results 141

Chapter 1

Introduction

Scattering experiments [1] are essential tools in improving our knowledge of the structure of matter. It was applied by Rutherford for α particle scattering experiment [2], through which the internal structure of the atom was understood [3]. A similar process probing the inner structure of nucleon was performed in the experiment at the Stanford Linear Accelerator Center (SLAC) [4, 5] since the 1960s, called *deep inelastic scattering (DIS)*. In the DIS measurement, the energy E' and the scattering angle θ of the scattered lepton off the nucleon are measured. These variables can be associated with another two independent kinematic variables: Bjorken-x and Q^2. The DIS experiment has an advantage that it can measure Bjorken-x event by event. The result of this experiment suggested the quark structure of the nucleon. Later scattering experiments at CERN, SLAC, FNAL and DESY helped developing the Quantum ChromoDynamics (QCD) [6] theory of the standard model. The quark parton model [7] was proven as a good phenomenological description in explaining the point–like constituent structure of the nucleon.

The experimental data on the **unpolarized** quark density distribution with high precision nicely confirmed the quark model on the nucleon. But European Muon Collaboration (EMC) [8, 9] reported that the quark spin contribution to the proton spin is small, which is contrary to the naive quark parton model. This is called “Proton Spin Problem”. This result was confirmed by many subsequent experiments [10–19]: the spin of quarks accounts for about 30% of the nucleon spin. This unexpected phenomenon nowadays is one of the topics in particle and nuclear physics. Experiments related to this problem are being carried out and almost all the major accelerators in the world are used for this purpose.

The partonic composition of longitudinal proton spin projection (helicity) is:

$$S_z = \frac{1}{2} = \frac{1}{2}\Delta\Sigma + \Delta G + L_z^q + L_z^g \,, \tag{1.1}$$

where $\Delta\Sigma = \sum_q \mathrm{g}_1^q$ and g_1^q is the helicity distribution of the quark flavor q. $\frac{1}{2}\Delta\Sigma$ (ΔG) describes the net contribution of quark and anti–quark (gluon) helicities to the nucleon

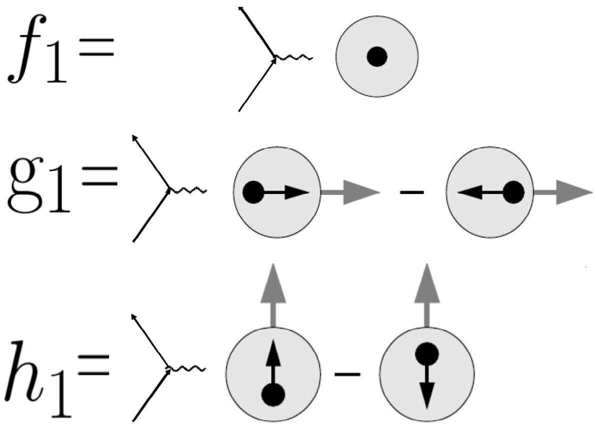

Figure 1.1: Schematic representation of three leading twist distribution functions $f_1(x)$, $g_1(x)$ and $h_1(x)$. The wavy lines illustrate the virtual–photon motion. Grey arrows indicate the nucleon spin direction, black arrows indicate the quark spin direction.

helicity and L_z^q (L_z^g) is the z component of the orbital angular momentum of all the quarks (gluons). Detailed information on $\Delta\Sigma$ and its flavor decomposition can be obtained from various experimental data [20–22]. In the naive quark parton model, all the nucleon spin is carried by quark spin. Possible solutions beyond this model include non–vanishing gluon spin ΔG or non–vanishing orbital angular momenta of partons [23, 24]. In the fit to the world experimental data, a net value of $\Delta G \sim 0.5$ [25, 26] was suggested. The studies on the values of L_z were performed in the model of Generalized Parton Distribution (GPD) [27]. It can be accessed in hard exclusive electro–production processes [28–36]. One example is Deeply Virtual Compton Scattering (DVCS) ($l+N \rightarrow l+N+\gamma$). However, at present the data do not yet constrain the value of L_z significantly[1].

In the case of transverse polarization of proton, a transverse spin sum rule was proposed [37]:

$$\frac{1}{2} = \frac{1}{2} \sum_{a=q,\bar{q}} \int \mathrm{d}\,x\; h_1^a(x) + \sum_{a=q,\bar{q},g} \langle L_T \rangle^a, \tag{1.2}$$

where the transversity distribution $h_1(x)$ is another fundamental distribution function. It can reveal information about the structure of the nucleon, L_T is the component of the orbital angular momentum L along the transverse polarization direction. Note that Eq. (1.2) does not contain the contribution of the gluon transversity, different from Eq. (1.1). Note that L_T is not yet well defined theoretically.

Hence, three fundamental parton distribution functions describe the structure of the

---

[1] Furthermore, the L_z measured with GPDs is somewhat different from the one in Eq. (1.1).

nucleon at leading twist[2]: the unpolarized distribution $f_1(x)$, the helicity distribution $\mathrm{g}_1(x)$, and the transversity distribution $h_1(x)$. As shown in Figure 1.1, the unpolarized distribution $f_1(x)$ is the quark density distribution in an unpolarized nucleon. The helicity distribution $\mathrm{g}_1(x)$ presents the distribution of longitudinally polarized quarks in a longitudinally polarized nucleon with respect to the direction of the virtual photon γ^*. The transversity describes the distribution of transversely polarized quarks in a nucleon transversely polarized with respect to the direction of the hard probe, *i.e.*, the virtual photon γ^*. It is the most difficult one to measure.

The transversity distribution was first mentioned by Ralston and Soper [39], but remains unmeasured until the recent HERMES measurement [40]. The reason is that the transversity is a chiral–odd object, which requires the combination with another chiral–odd object in helicity conserving process. Hence, unlike the other two, it is inaccessible in inclusive measurement of DIS. A class of observables sensitive to the transversity distribution is that of single–spin asymmetries in semi–inclusive measurement of DIS, which were measured by HERMES and COMPASS. The single–spin asymmetry means the asymmetry in a reaction when either the beam or the target is polarized. In the present measurement, the unpolarized beam and the polarized target were used.

The amplitudes of single-spin asymmetries A_{UT} in one–hadron production in semi–inclusive measurement of DIS ($l + p^\uparrow \to l' + h + X$) on a transversely polarized target were recently studied by HERMES [40, 41] and by COMPASS [42–44]. Here the subscript U indicates the unpolarized incident lepton beam and T the transversely polarized fixed target. Semi-inclusive measurements mean that a part of produced hadrons are measured in coincidence with the scattered lepton. For these observables, the orientation of the target transverse polarization influences the distribution of the detected hadrons around the virtual-photon direction through, *e.g.*, the so-called Collins [45] and Sivers [46] mechanisms. Particularly, the Collins asymmetry is sensitive to the transversity distribution. The hadron has a preference to move to a specific side with respect to the quark spin and the direction of its momentum. Factorization proofs [47, 48] allow the interpretation of the Collins asymmetry in terms of a convolution of the transversity distribution with a universal fragmentation function, the Collins function, which can be considered as an analyzer of the fragmenting quark's transverse polarization. This fragmentation function can be measured in other processes, *e.g.*, in e^+e^- collisions, and can then be used to extract the transversity distribution from the measured Collins asymmetry [49]. The only existing data that have been used so far to isolate transversity are from single-spin asymmetries of single hadrons in semi-inclusive DIS.

By the early 90s it had already been pointed out that single–spin asymmetries A_{UT} in semi–inclusive dihadron lepto–production ($l + p^\uparrow \to l' + h_1 + h_2 + X$) on a transversely polarized target could be sensitive to the transversity [50, 51]. The single–spin asymme-

---

[2] As proposed by Jaffe [38], we will identify the expression "leading twist" with the expression "leading order in $1/Q$"

try A_{UT} is expected to be related to the product of the little–known quark transversity distribution function and an unknown dihadron fragmentation function. In this thesis, the first measurement of the amplitude of the asymmetry A_{UT} in the lepto–production of $\pi^+\pi^-$ pairs at HERMES experiment was reported, which can provide an independent way to probe transversity.

This thesis is organized as follows: The theory of the inner structure of the nucleon is reviewed in Chapter 2 with the emphasis on the concept of factorization of the deep inelastic scattering process into quark distribution and fragmentation functions. I will show why we cannot access the transversity through inclusive process, but can access it through semi–inclusive process. There I will introduce the new T–odd chiral–odd fragmentation functions which are convoluted with the transversity distribution. In Chapter 3, the HERMES experiment is described with its main components: the polarized hydrogen gas target, the tracking and particle identification detectors of the spectrometer, the Gain Monitoring System (GMS) and the data acquisition and processing. The extraction and systematic studies on the asymmetry amplitudes related to transversity and the dihadron fragmentation function from the experimental data are presented in Chapter 4. The discussion and interpretation of the measured amplitudes can be found in Chapter 5. The summary for other possible ways to measure transversity and the dihadorn fragmentation function are also presented. Final conclusions of the whole thesis are written in Chapter 6.

Chapter 2

Deep Inelastic Scattering and Parton Distribution Functions

In this chapter the spin physics of proton, in particular the less known transversity distribution function, is introduced. It is explained how this chiral–odd function can be measured, with the focus on the lepton deep inelastic scattering processes that are accessible by the HERMES experiment [52]. Sec. 2.1 first introduces the structure functions and spin sum rules. In Sec. 2.1.5 the leading twist distribution functions will be discussed, with special focus on the chiral–odd transversity distribution function $h_1(x)$. It cannot be probed in inclusive deep inelastic scattering. In Sec. 2.3 we will see how to probe transversity h_1 in one–hadron semi–inclusive measurement of deep inelastic scattering. The Collins fragmentation function will also be introduced in this process. Sec. 2.4 will put emphasis on the two–hadron semi–inclusive deep inelastic scattering process, where transversity and the dihadron fragmentation function play important roles. This thesis reports the measurement of this process at the HERMES experiment to probe the transversity and the dihadron fragmentation function.

2.1 Deep Inelastic Scattering

Deep Inelastic Scattering (DIS) is the archetype for hard processes in QCD: a lepton — in practice an electron, muon or neutrino — with high energy scatters off a target hadron — in practice a nucleon or nucleus. But the transfer of energy and the invariant squared 4–momentum are large in these reactions [38]. Practically, charged lepton DIS experiment is relatively easier to be performed, comparing with neutrino scattering experiment. In the lowest order perturbation theory, DIS reaction proceeds via the exchange of a neutral virtual boson (γ^*, Z^0). At the HERMES center–of–mass energies the contributions from Z^0–exchange to the cross section can be safely neglected. Hence for the HERMES experiment, the dominant reaction mechanism is electromagnetism and one photon exchange

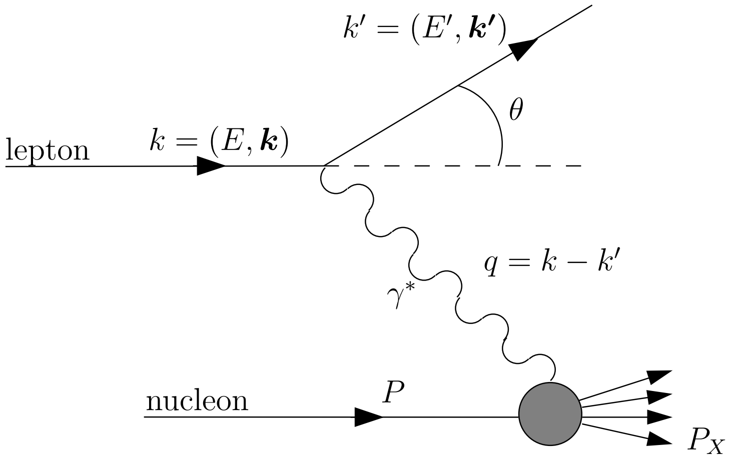

Figure 2.1: Schematic picture of deep inelastic scattering for one photon exchange. The kinematic variables are defined in Table 2.1.

is a good approximation. In DIS, one photon exchange can be used to probe the internal structure of the nucleon, where the emitted photon interacts with a quark in the nucleon through elastic scattering. The struck quark fragments into hadrons, which may be detected in a spectrometer. A lepton scattering process is called inclusive measurement if only the scattered lepton is detected. The hadronic final state might also be detected partially or completely, which is called semi–inclusive DIS or exclusive DIS respectively. We are primarily interested in experiments performed with polarized beam and/or targets in order to investigate the spin structure of the nucleon.

2.1.1 Basic Kinematic Variables

Charged lepton DIS process can be formulated as:

$$l(k) + \mathrm{N}(P) \rightarrow l'(k') + \mathrm{X}(P_X), \tag{2.1}$$

which is shown in Figure 2.1 with the related kinematics. The initial lepton (l) with 4–momentum $k = (E, \boldsymbol{k})$ exchanges a photon of 4–momentum q with a target (N) with 4–momentum P. Only the outgoing lepton (l') with 4–momentum $k' = (E', \boldsymbol{k'})$ is detected. The kinematic variables relevant for this process are listed in Table 2.1.

In the deep inelastic scattering, the Bjorken limit is where Q^2 and ν both go to infinity with the ratio, $x = \frac{Q^2}{2M\nu}$, fixed. x is known as the Bjorken (scaling) variable. Since the invariant mass of the hadronic final state is larger than or equal to the mass of the target, $(P+q)^2 \geq M^2$, one has $0 < x \leq 1$. In experiment, it is also convenient to measure the energy loss ν of the incident lepton using a dimensionless variable $y = \frac{\nu}{E}$, which has $0 \leq y \leq 1$. The behavior of cross sections at large Q^2 is much more transparent using the

m_l	Mass of incoming lepton (considered as negligible)
M	Mass of target nucleon
$k = (E, \boldsymbol{k})$, $k' = (E', \boldsymbol{k'})$	4–momenta of the initial and final state leptons
s, S	Lepton's and target's spin 4-vectors
θ, ϕ	Polar and azimuthal angle of the scattered lepton
$P \overset{\text{lab}}{=} (M, 0)$	4–momentum of the initial target nucleon
$q = (E - E', \boldsymbol{k} - \boldsymbol{k'})$	4–momentum of the virtual photon
$Q^2 = -q^2$ $\overset{\text{lab}}{\approx} 4EE' \sin^2 \frac{\theta}{2}$	Negative squared 4–momentum transfer
$\nu = \dfrac{P \cdot q}{M} \overset{\text{lab}}{=} E - E'$	Energy of the virtual photon in the target rest frame
$x = \dfrac{Q^2}{2\,P \cdot q} = \dfrac{Q^2}{2\,M\nu}$	Bjorken scaling variable
$y = \dfrac{P \cdot q}{P \cdot k} \overset{\text{lab}}{=} \dfrac{\nu}{E}$	Fractional energy of the virtual photon
$W^2 = (P + q)^2$ $= M^2 + 2M\nu - Q^2$	Squared invariant mass of the photon–nucleon system
$P_h = (E_h, \boldsymbol{P}_h)$	4–momentum of a hadron in the final state
$z = \frac{P \cdot P_h}{P \cdot q} \overset{\text{lab}}{=} \frac{E_h}{\nu}$	Fractional energy of the observed final state hadron
$x_F = \frac{P^{\parallel}_{CM}}{\lvert\boldsymbol{q}\rvert} \overset{\text{lab}}{\simeq} \frac{2\,P^{\parallel}_{CM}}{W}$	Longitudinal momentum fraction of the hadron

Table 2.1: Kinematic variables used in the description of deep inelastic scattering (DIS) in target rest frame. p, z and x_F are the variables in the case of one or more hadrons detected, *i.e.*, semi-inclusive DIS process.

set (x, y, Q^2) than using the set (E, E', θ) determined by experiments. In particular, Q^2 represents the hard scale of the process.

An additional vector $\boldsymbol{S}$, which describes the polarization direction, is needed to describe the inclusive scattering process when the target nucleon is polarized. This vector is often decomposed into the two components S_L and $\boldsymbol{S_T}$, which are the longitudinal and

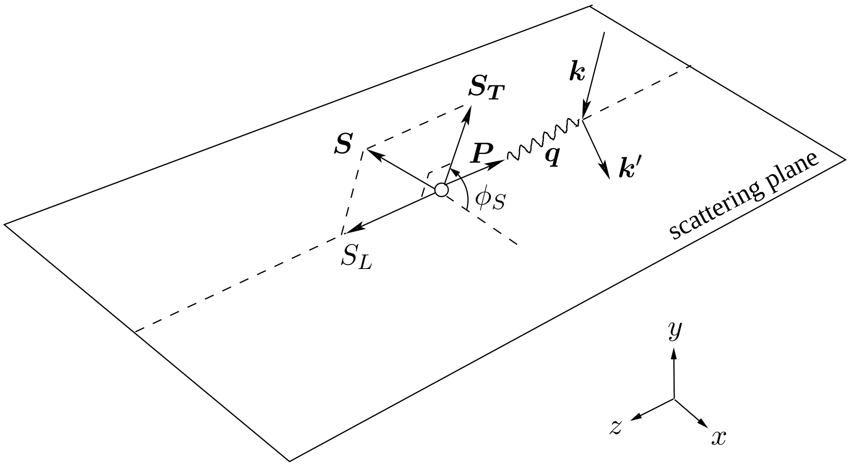

Figure 2.2: Description of the vectors involved in totally inclusive deep inelastic scattering and of the azimuthal angle ϕ_S. The vector $\boldsymbol{S}$ indicates the polarization direction of the target and S_L and $\boldsymbol{S_T}$ are the projections of $\boldsymbol{S}$ along and perpendicular to the virtual–photon direction $\boldsymbol{q}$. Here the Trento conventions are used.

transverse projections of $\boldsymbol{S}$ with respect to the virtual–photon direction $\boldsymbol{q}$, respectively. The azimuthal orientation of $\boldsymbol{S_T}$ around the virtual–photon γ^* direction is specified by the angle ϕ_S (see Figure 2.2) so that $\boldsymbol{S} = (|\boldsymbol{S_T}|\cos\phi_S, |\boldsymbol{S_T}|\sin\phi_S, S_L)$, where $|\boldsymbol{S_T}|$ has values in between 0 and 1, and S_L has values between -1 and 1. In this thesis, the Trento conventions [53] are adopted. The angle ϕ_S can be calculated as

$$\phi_S = \frac{\boldsymbol{q}\times\boldsymbol{k}\cdot\boldsymbol{S}}{|\boldsymbol{q}\times\boldsymbol{k}\cdot\boldsymbol{S}|}\cos^{-1}\frac{\boldsymbol{q}\times\boldsymbol{k}\cdot\boldsymbol{q}\times\boldsymbol{S}}{|\boldsymbol{q}\times\boldsymbol{k}||\boldsymbol{q}\times\boldsymbol{S}|}. \tag{2.2}$$

2.1.2 Cross Section and Distribution Function

The cross section for polarized lepton–nucleon scattering can be written in a general way as the contraction between a leptonic and a hadronic tensor

$$\frac{\mathrm{d}^3\sigma}{\mathrm{d}\,x\;\mathrm{d}\,y\;\mathrm{d}\,\phi_S} = \frac{\alpha^2}{2\,s\,x\,Q^2}\,L_{\mu\nu}\,2MW^{\mu\nu}, \tag{2.3}$$

where ϕ_S is azimuthal angle and $\alpha \equiv \frac{e^2}{4\pi}$ is the coupling constant of Quantum ElectroDynamics (QED). Figure 2.2 illustrates the definition of the scattering plane, the z axis of our collinear frame and the azimuthal angle ϕ_S. The leptonic tensor is given by (lepton masses are retained here):

$$\begin{aligned} L_{\mu\nu} &= \sum_{s_{k'}} \Big[\bar{u}_{k'}(k', s_{k'})\gamma_\mu u_k(k, s_k)\Big]^* \Big[\bar{u}_{k'}(k', s_{k'})\gamma_\nu u_k(k, s_k)\Big] \\ &= \mathrm{Tr}\left[(\not{k} + m_k)\,\frac{1}{2}(1 + \gamma_5 \not{s}_k)\,\gamma_\mu\,(\not{k}' + m_k)\,\gamma_\nu\right], \qquad (2.4) \end{aligned}$$

where $u(k, s_k)$ is the Dirac spinor for spin–$\frac{1}{2}$ particles with 4–momentum k and spin vector s_k. See Appendix A for the conventions and notations. The leptonic tensor contains all the information on the leptonic probe, which can be described by means of perturbative QED, while the information on the hadronic target is contained in the hadronic tensor

$$2MW^{\mu\nu}(q, P, S) = \frac{1}{2\pi} \sum_X \int \frac{\mathrm{d}^3 \boldsymbol{P}_X}{(2\pi)^3\, 2P_X^0}\,(2\pi)^4\,\delta^{(4)}\Big(q + P - P_X\Big)\,H^{\mu\nu}(P, S, P_X), \qquad (2.5)$$

$$H^{\mu\nu}(P, S, P_X) = \big\langle P,S\big|\,J^\mu(0)\,\big|X\big\rangle\big\langle X\big|\,J^\nu(0)\,\big|P,S\big\rangle. \qquad (2.6)$$

The state X symbolizes any final state, with total momentum P_X. It is integrated over since in inclusive processes the final state goes undetected. By Fourier transforming the delta function and translating one of the current operators, we can rewrite the hadronic tensor as

$$2MW^{\mu\nu}(q, P, S) = \frac{1}{2\pi}\int \mathrm{d}^4\xi\;\,\mathrm{e}^{\mathrm{i}q\cdot\xi}\,\big\langle P,S\big|\,J^\mu(\xi)\,J^\nu(0)\,\big|P,S\big\rangle. \qquad (2.7)$$

The leptonic tensor $L_{\mu\nu}$ can be decomposed into a symmetric and an antisymmetric part under $\mu - \nu$ interchange

$$L_{\mu\nu} = L^{(\mathrm{S})}_{\mu\nu}(k, k') + \mathrm{i}\,L^{(\mathrm{A})}_{\mu\nu}(k, s_k; k'), \qquad (2.8)$$

and

$$\begin{aligned} L^{(\mathrm{S})}_{\mu\nu} &= 2(k_\mu k'_\nu + k_\nu k'_\mu - g_{\mu\nu}\,k{\cdot}k'), \qquad (2.9\mathrm{a}) \\ L^{(\mathrm{A})}_{\mu\nu} &= 2m_k\,\epsilon_{\mu\nu\rho\sigma} s_k^\rho (k - k')^\sigma. \qquad (2.9\mathrm{b}) \end{aligned}$$

If the incoming lepton is longitudinally polarized, its spin vector is

$$s_k^\mu = \frac{\lambda_k}{m_k}\,k^\mu, \quad \lambda_k = \pm 1, \qquad (2.10)$$

and Eq. (2.9b) becomes

$$L^{(\mathrm{A})}_{\mu\nu} = 2\lambda_k\,\epsilon_{\mu\nu\rho\sigma} k^\rho q^\sigma. \qquad (2.11)$$

Note that the lepton mass m_l appearing in Eq. (2.9b) is cancelled by the denominator of Eq. (2.10). In contrast, if the lepton is transversely polarized, that is $s_k^\mu = s_{k\perp}^\mu$, no such cancellation occurs and the process is suppressed by a factor m_k/E. In what follows we shall consider only unpolarized or longitudinally polarized lepton beams.

The hadronic tensor $W_{\mu\nu}$ can be split as

$$W_{\mu\nu} = W_{\mu\nu}^{(\mathrm{S})}(q,P) + \mathrm{i}\, W_{\mu\nu}^{(\mathrm{A})}(q;P,S)\,, \tag{2.12}$$

where the symmetric and the antisymmetric parts are expressed in terms of two pairs of structure functions, W_1, W_2 and G_1, G_2, as

$$\begin{aligned}\frac{1}{2M}\,W_{\mu\nu}^{(\mathrm{S})} &= \left(-g_{\mu\nu} + \frac{q_\mu q_\nu}{q^2}\right) W_1(P{\cdot}q, q^2) \\ &\quad + \frac{1}{M^2}\left[\left(P_\mu - \frac{P{\cdot}q}{q^2}\,q_\mu\right)\left(P_\nu - \frac{P{\cdot}q}{q^2}\,q_\nu\right)\right] W_2(P{\cdot}q, q^2)\,, \qquad (2.13\mathrm{a}) \\ \frac{1}{2M}\,W_{\mu\nu}^{(\mathrm{A})} &= \varepsilon_{\mu\nu\rho\sigma}\,q^\rho\left\{M S^\sigma\, G_1(P{\cdot}q, q^2)\right. \\ &\quad \left. + \frac{1}{M}\left[P{\cdot}q\, S^\sigma - S{\cdot}q\, P^\sigma\right] G_2(P{\cdot}q, q^2)\right\}. \qquad (2.13\mathrm{b})\end{aligned}$$

It is customary to introduce the dimensionless structure functions

$$\begin{aligned} F_1(x,Q^2) &\equiv M\,W_1(\nu,Q^2)\,, \\ F_2(x,Q^2) &\equiv \nu\,W_2(\nu,Q^2)\,, \\ g_1(x,Q^2) &\equiv M^2\nu\,G_1(\nu,Q^2)\,, \\ g_2(x,Q^2) &\equiv M\nu^2\,G_2(\nu,Q^2)\,. \end{aligned} \tag{2.14}$$

In terms of F_1, F_2, g_1 and g_2, the hadronic tensor reads

$$\begin{aligned} W_{\mu\nu}^{(\mathrm{S})} &= 2\left(-g_{\mu\nu} + \frac{q_\mu q_\nu}{q^2}\right) F_1(x,Q^2) \\ &\quad + \frac{2}{P{\cdot}q}\left[\left(P_\mu - \frac{P{\cdot}q}{q^2}\,q_\mu\right)\left(P_\nu - \frac{P{\cdot}q}{q^2}\,q_\nu\right)\right] F_2(x,Q^2)\,, \qquad (2.15\mathrm{a}) \\ W_{\mu\nu}^{(\mathrm{A})} &= \frac{2M\,\varepsilon_{\mu\nu\rho\sigma}\,q^\rho}{P{\cdot}q}\left\{S^\sigma\, g_1(x,Q^2) + \left[S^\sigma - \frac{S{\cdot}q}{P{\cdot}q}\,P^\sigma\right] g_2(x,Q^2)\right\}. \qquad (2.15\mathrm{b}) \end{aligned}$$

In the Bjorken limit

$$\nu, Q^2 \to \infty\,, \quad x = \frac{Q^2}{2M\nu} \quad \text{fixed,} \tag{2.16}$$

F_1, F_2, g_1 and g_2 are expected to scale approximately, that is, to depend only on x. Splitting the spin vector of the nucleon into a longitudinal and transverse part (with respect to the photon axis):

$$S^\mu = S_\parallel^\mu + S_\perp^\mu\,, \tag{2.17}$$

the antisymmetric part of the hadronic tensor becomes

$$W_{\mu\nu}^{(\mathrm{A})} = \frac{2M\,\varepsilon_{\mu\nu\rho\sigma}\,q^\rho}{P{\cdot}q}\left[S_\parallel^\sigma\, g_1 + S_\perp^\sigma\,(g_1 + g_2)\right]. \tag{2.18}$$

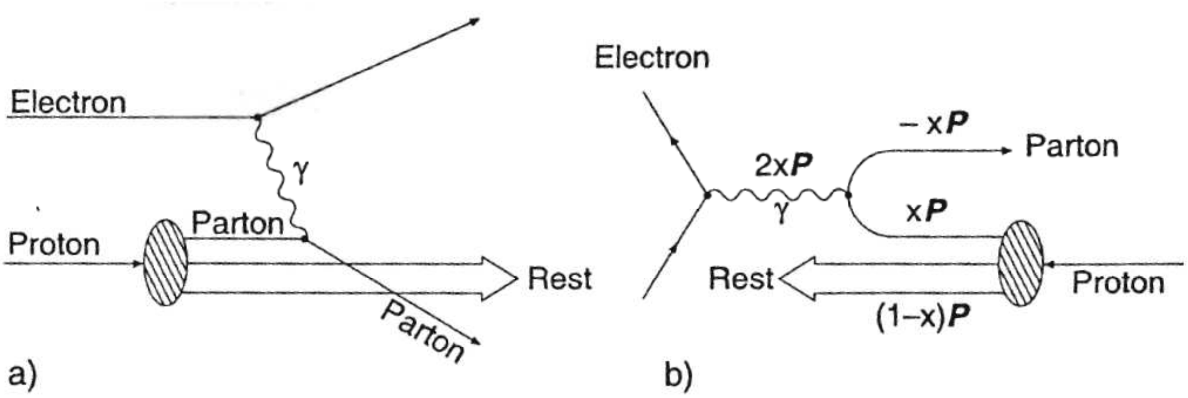

Figure 2.3: Schematic representation of deep inelastic scattering according to the parton model, in the **laboratory** system (**a**) and in an **infinite–momentum** system (**b**). This diagram shows the process in two spatial dimensions. The arrows indicate the directions of the momenta. Diagram (**b**) depicts the scattering process in the Breit frame in which the energy transferred by the virtual photon is zero. Hence the momentum of the struck parton is turned around but its magnitude is unchanged.

Thus, if the nucleon is longitudinally polarized the DIS cross–section depends only on g_1; if it is transversely polarized (with respect to the photon axis) what is measured is the sum of g_1 and g_2[1].

2.1.3 The Parton Model

In general, the structure of the hadronic tensor cannot be specified further because this would require an understanding of its inner dynamics. However, the phenomenology of DIS taught us that at sufficiently high Q^2 we can assume that the scattering of the charged lepton takes place off a quark of mass m inside the nucleon. The final state X can be split into a quark with momentum k plus a state X with momentum P_X. In the parton model as shown in Figure 2.3 (a) the virtual photon is assumed to scatter incoherently off the constituents of the nucleon (quarks and antiquarks). Currents are treated as in free field theory and any interaction between the struck quark and the target remnant is ignored.

The hadronic tensor $W^{\mu\nu}$ is then represented by the handbag diagram shown in Fig-

---

[1] Note that g_2 is suppressed by one power of Q. This makes the measurement of g_2 quite a difficult task. [54]

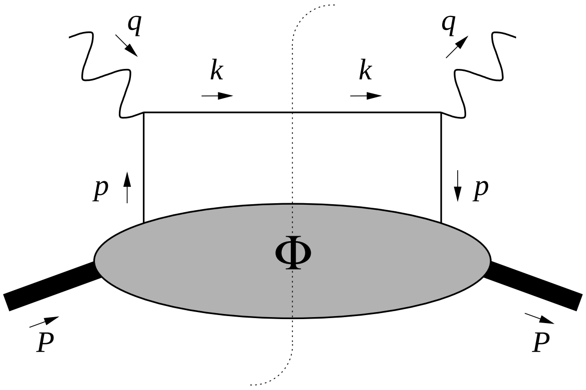

Figure 2.4: The so–called handbag diagram at tree level in inclusive deep inelastic scattering. The quantity Φ is the distribution correlator.

ure 2.4 and reads[2]

$$\begin{aligned} W^{\mu\nu} &= \frac{1}{(2\pi)} \sum_q e_q^2 \sum_X \int \frac{\mathrm{d}^3\boldsymbol{P}_X}{(2\pi)^3\, 2E_X} \int \frac{\mathrm{d}^4p}{(2\pi)^4} \int \frac{\mathrm{d}^4k}{(2\pi)^4}\, \delta(k^2) \\ &\quad \times \Big[\bar{u}(k)\gamma^\mu \phi(p;P,S)\Big]^* \Big[\bar{u}(k)\gamma^\nu \phi(p;P,S)\Big] \\ &\quad \times (2\pi)^4\, \delta^4(P-p-P_X)\; (2\pi)^4\, \delta^4(k+q-k)\,, \end{aligned} \tag{2.19}$$

where $\sum_q$ is a sum over the flavours, e_q is the quark charge in units of e, and we have introduced the matrix elements of the quark field between the nucleon and its remnant

$$\phi_i(p,P,S) = \langle X|\psi_i(0)|P,S\rangle\,. \tag{2.20}$$

We define the quark–quark correlation matrix $\Phi_{ij}(p,P,S)$ as

$$\begin{aligned} \Phi_{ij}(p,P,S) &= \sum_X \int \frac{\mathrm{d}^3\boldsymbol{P}_X}{(2\pi)^3\, 2E_X}\, (2\pi)^4\, \delta^4(P-p-P_X) \\ &\qquad \times \langle P,S|\psi_j(0)|X\rangle\langle X|\psi_i(0)|P,S\rangle\,. \end{aligned} \tag{2.21}$$

Using translational invariance and the completeness of the $|X\rangle$ states this matrix can be re–expressed in the more synthetical form

$$\Phi_{ij}(p,P,S) = \int \mathrm{d}^4\xi\; \mathrm{e}^{\mathrm{i}p\cdot\xi}\, \langle P,S|\bar{\psi}_j(0)\psi_i(\xi)|P,S\rangle\,. \tag{2.22}$$

---

[2] To simplify the presentation, we consider only quarks. The extension to anti–quarks is rather straightforward.

With the definition Eq. (2.21) the hadronic tensor becomes

$$\begin{aligned} W^{\mu\nu} &= \sum_q e_q^2 \int \frac{\mathrm{d}^4 p}{(2\pi)^4} \int \frac{\mathrm{d}^4 k}{(2\pi)^4}\, \delta(k^2)\, (2\pi)^4\, \delta^4(p+q-k)\ \mathrm{Tr}[\Phi\gamma^\mu \not{k} \gamma^\nu] \\ &= \sum_q e_q^2 \int \frac{\mathrm{d}^4 p}{(2\pi)^4}\, \delta\big((p+q)^2\big)\ \mathrm{Tr}\left[\Phi\gamma^\mu(\not{p}+\not{q})\gamma^\nu\right]. \qquad (2.23) \end{aligned}$$

By using a Sudakov parametrization [54], one can derive the structure functions F_1, F_2 and g_1 as:

$$F_2(x) = 2x\, F_1(x) = \sum_q e_q^2\, x\left[f_1^q(x) + f_1^{\bar{q}}(x)\right], \qquad (2.24a)$$

$$g_1(x) = \frac{1}{2}\sum_q e_q^2 \left[\mathrm{g}_1^q(x) + \mathrm{g}_1^{\bar{q}}(x)\right], \qquad (2.24b)$$

where f_1 and g_1 are unpolarized and spin–dependent parton distribution functions, which will be described systematically later. Hence, $F_1(x)$ and $F_2(x)$ are unpolarized structure functions, and $g_1(x)$ is spin–dependent structure function. In the kinematic region of deep inelastic scattering, the structure functions behave as functions of x alone. The Q^2 dependence is small and only shows a slow logarithmic variation $\sim \ln Q^2$. These scaling violations are shown in Figure 2.5 [55] for unpolarized structure function F_2 and Figure 2.6 for the spin–dependent structure function g_1. This behavior is associated with QCD and asymptotic freedom.

The QCD quark–gluon and gluon–gluon coupling is scale dependent and runs with the momentum transfer Q^2. In leading–order perturbation theory,

$$\alpha_s(Q^2) = \frac{4\pi}{\beta_0 \ln(Q^2/\Lambda^2)}. \qquad (2.25)$$

Here $\beta_0 = 11 - \frac{2}{3}n_f$ where n_f is the number of active quark flavors and $\Lambda \approx 200\,\mathrm{MeV}$ is the QCD scale.

2.1.4 The Moment of g_1 and Spin Sum Rules

In leading order QCD parton model and using SU(3) flavor decomposition, the first moment of g_1 is related to the scale-invariant axial charges of the target nucleon by:

$$\int_0^1 dx g_1^{p,n}(x,Q^2) = \frac{1}{2}\left(\pm\frac{1}{6}g_A^{(3)} + \frac{1}{18}g_A^{(8)} + \frac{2}{9}g_A^{(0)}\right), \qquad (2.26)$$

where

$$g_A^{(3)} = (\mathrm{g}_1^u + \mathrm{g}_1^{\bar{u}}) - (\mathrm{g}_1^d + \mathrm{g}_1^{\bar{d}}) \qquad (2.27)$$

$$g_A^{(8)} = (\mathrm{g}_1^u + \mathrm{g}_1^{\bar{u}}) + (\mathrm{g}_1^d + \mathrm{g}_1^{\bar{d}}) - 2(\mathrm{g}_1^s + \mathrm{g}_1^{\bar{s}}) \qquad (2.28)$$

$$g_A^{(0)} \equiv \Delta\Sigma = (\mathrm{g}_1^u + \mathrm{g}_1^{\bar{u}}) + (\mathrm{g}_1^d + \mathrm{g}_1^{\bar{d}}) + (\mathrm{g}_1^s + \mathrm{g}_1^{\bar{s}}) \qquad (2.29)$$

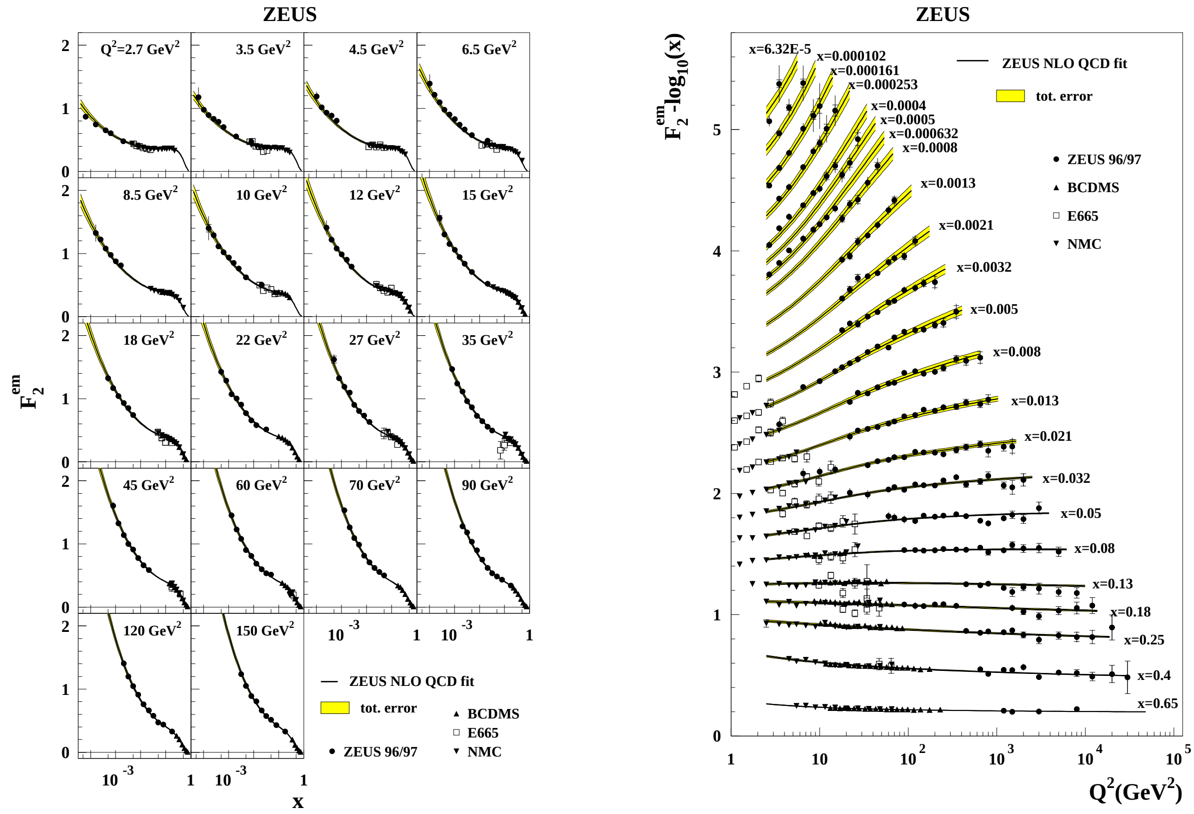

Figure 2.5: The left plot shows the world data on F_2 as a function of Q^2 for fixed values of x. The right plot shows F_2 as a function of x for fixed values of Q^2. (from Ref. [55]).

Here the +(-) sign of the $g_A^{(3)}$ holds for the proton (neutron). $g_A^{(3)}$ and $g_A^{(8)}$ are the non–singlet isovector and SU(3) octet axial charges respectively. They are independent of Q^2 to any order of $\alpha_s(Q^2)$. $g_A^{(3)} = 1.2695 \pm 0.0029$ is the measured in neutron beta decay and $g_A^{(8)} = 0.58 \pm 0.03$ is measured in hyperon beta decay [61]. $g_A^{(0)}$ is scale–invariant flavor–singlet axial charge and dependent on Q^2 in higher order. $\Delta\Sigma$, which presents in Eq. (1.1), is the fraction of the proton's spin carried by the intrinsic spin of its quarks.

At any order QCD and in leading twist, the structure function g_1 is a convolution of quark, anti–quark and gluon helicity distributions [62]. In the 'modified minimal subtraction' ($\overline{MS}$) scheme [63], no gluon polarization contributes to the first moment of g_1. Hence we have $g_A^{(0)}(Q^2) \overset{\overline{MS}}{=} \Delta\Sigma(Q^2)$. In the $\overline{\mathrm{MS}}$ scheme,

$$\int_0^1 dx g_1^{p,n}(x, Q^2) \quad = \quad \left(\pm\frac{1}{12}g_A^{(3)} + \frac{1}{36}g_A^{(8)}\right)\{1 + \sum_{l\geq 1} c_{\mathrm{NS}}\alpha_s^l(Q^2)\}$$

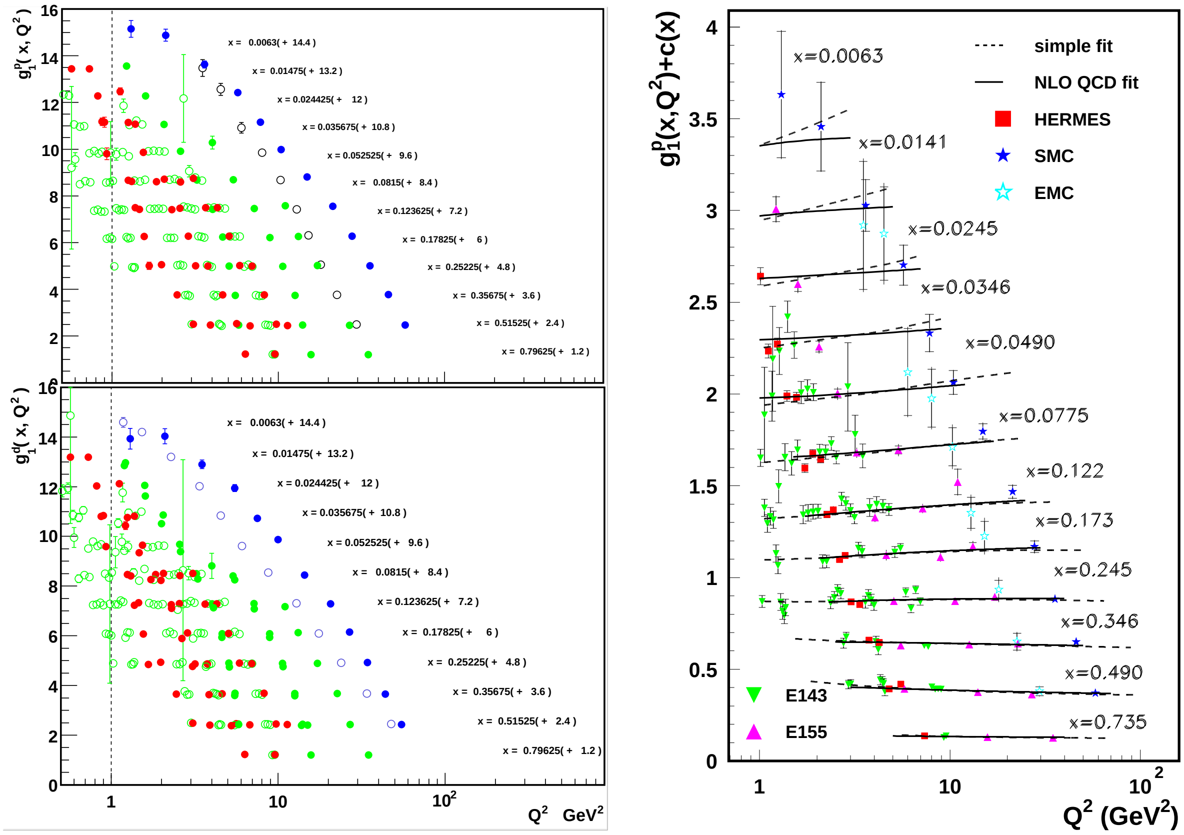

Figure 2.6: Left Plot: The compilation of all world g_1 data on proton (up panel) and deuteron (below panel) as a function of Q^2 for fixed values of x with the set shifts indicated in the brackets. Data are from experiments EMC [9], SMC [56], COMPASS [17, 57], HERMES [18, 58], E143 [15] and E155 [16, 59]. The vertical dash line is the position $Q^2 = 1\,\mathrm{GeV}^2$. Right Plot: A simple fit according to Ref. [16] and a NLO perturbative QCD fit from Ref. [60] to part of g_1^p data before 2002.

$$+\frac{1}{9}\Delta\Sigma(Q^2)\{1+\sum_{l\geq 1} c_{\mathrm{S}}\alpha_s^l(Q^2)\} + O(\frac{1}{Q^2}) - \beta_1(Q^2)\frac{Q^2}{4M^2}. \tag{2.30}$$

The flavor non–singlet c_{NS} and singlet c_{S} Wilson coefficients are calculable in l–loop perturbative QCD [64]. Provided no twist–two subtraction constant ($\beta_1(Q^2) = O(1/Q^4)$) is taken into account, the axial charge contributions saturate the first moment g_1 at leading twist. The calculation to the order of $\alpha_s^3(Q^2)$ gives that

$$\begin{aligned}\int_0^1 dx g_1^{p,n}(x, Q^2) \;&=\; \left(\pm\frac{1}{12}g_A^{(3)} + \frac{1}{36}g_A^{(8)}\right)\\ &\times\left[1 - \frac{\alpha_s(Q^2)}{\pi} - 3.5833\,\left(\frac{\alpha_s(Q^2)}{\pi}\right)^2 - 20.21527\,\left(\frac{\alpha_s(Q^2)}{\pi}\right)^3\right]\end{aligned}$$

$$+\frac{1}{9}\Delta\Sigma(Q^2)\left[1-0.33333\ \frac{\alpha_s(Q^2)}{\pi}-0.54959\ \left(\frac{\alpha_s(Q^2)}{\pi}\right)^2\right.$$
$$\left.-4.44725\ \left(\frac{\alpha_s(Q^2)}{\pi}\right)^3\right]. \tag{2.31}$$

Bjorken Sum Rule

In the isovector channel, the Bjorken sum rule [65, 66] was proposed as

$$\begin{aligned} I_{Bj} &= \int_0^1 dx[g_1^p(x,Q^2)-g_1^n(x,Q^2)] \\ &= \frac{1}{16}g_A^{(3)}\left[1-\frac{\alpha_s(Q^2)}{\pi}-3.5833\ \left(\frac{\alpha_s(Q^2)}{\pi}\right)^2-20.21527\ \left(\frac{\alpha_s(Q^2)}{\pi}\right)^3\right]. \end{aligned} \tag{2.32}$$

The above equation has been confirmed in polarized deep inelastic scattering at the level of 10%. The E155 collaboration at SLAC found $\int_0^1 dx[g_1^p(x,Q^2)-g_1^n(x,Q^2)]=0.176\pm 0.003\pm 0.007$ at $Q^2=5\,\mathrm{GeV}^2$, which is in agreement with the theoretical prediction 0.182 ± 0.005 from Eq. (2.32) [16]. The SMC experiment obtained $\int_0^1 dx[g_1^p(x,Q^2)-g_1^n(x,Q^2)] = 0.174^{+0.024}_{-0.012}$ also at $5\,\mathrm{GeV}^2$ and also in agreement with the theoretical prediction [12].

Ellis–Jaffe Sum Rule

Before EMC experiment, in order to evaluate the size of $\Delta\Sigma$, unpolarized strange quark inside spin–half nucleon $\mathrm{g}_1^s+\mathrm{g}_1^{\bar{s}}=0$ was assumed by Ellis and Jaffe [67]. With this hypothesis, we have $g_A^{(0)}=g_A^{(8)}$ and obtain the Ellis–Jaffe sum rule: $I_{p,n}=\pm\frac{1}{12}g_A^{(3)}+\frac{5}{36}g_A^{(8)}$. If we work to just first order of Eq. (2.31), we have

$$I_{p,n}^{EJ}(Q^2)=\pm\frac{1}{12}g_A^{(3)}\left(1-\frac{\alpha_s(Q^2)}{\pi}\right)+\frac{5}{36}g_A^{(8)}\left(1-\frac{7}{15}\frac{\alpha_s(Q^2)}{\pi}\right). \tag{2.33}$$

At $Q_0^2=10\,\mathrm{GeV}^2$, Eq. (2.33) leads to the expectation

$$I_{p,n}^{EJ}(Q^2)=0.167\pm 0.008. \tag{2.34}$$

But the first measurement of this quantity by European Muon Collaboration (EMC) showed only a value of $0.114\pm 0.012\pm 0.026$ in 1988 [8], which is inconsistent with the theoretical prediction. Taking this experimental as input to Eq. (2.31), we obtain that $g_A^{(0)}$ is nearly zero, which suggests a very small fraction of proton spin is contributed from quark spin. Relativistic quark models generally predict $g_A^{(0)}\sim 0.6$ with little polarized strange quark. This surprising EMC results are known as the "proton spin problem". In a fit to world g_1 data, it was found [68] that in the polarized deep inelastic scattering process for $Q_0^2 = 3\,\mathrm{GeV}^2$,

$$g_A^{(0)}|_{pDIS} = 0.30 \pm 0.01(\mathrm{stat}) \pm 0.02(\mathrm{evol}), \tag{2.35}$$

which means only 30% of proton spin is carried by intrinsic partons.

The violation of Ellis–Jaffe sum rule was first considered as a non–trivial contribution from gluon polarization ΔG, which comes from the $U(1)$ axial anomaly [69, 70]. Then the naive parton model value of $g_A^{(0)}$ should be replaced by

$$g_A^{(0)} = \Delta\Sigma - \frac{3\alpha_s(Q^2)}{2\pi}\Delta G(Q^2). \tag{2.36}$$

Only if ΔG is very large, Ellis–Jaffe could be satisfied. But this would require large orbital angular momentum in the opposite direction in order to keep the total spin $\frac{1}{2}$ of proton as shown in Eq. (1.1).

Ji Sum Rule

In view of EMC result, the orbital angular momentum structure of proton is also of interest. It is suggested that Deeply Virtual Compton Scattering (DVCS), $l + N \to l + N + \gamma$ as shown in Figure 2.7(a), can be used to investigate a new set of Generalized Parton Distributions (GPDs) which are known as Off-Forward Parton Distributions (OFPDs) and describe the quark total angular momentum J_q [27, 71]. At leading twist, four chirality conserving quark GPDs appear: the polarization-independent distributions $H_q(x,\xi,t)$ and $E_q(x,\xi,t)$, and the polarization–dependent distributions $\widetilde{H}_q(x,\xi,t)$ and $\widetilde{E}_q(x,\xi,t)$. The GPDs $H_q(x,\xi,t)$ and $\widetilde{H}_q(x,\xi,t)$ conserve nucleon helicity, while $E_q(x,\xi,t)$ and $\widetilde{E}_q(x,\xi,t)$ are associated with a helicity flip of the nucleon. Here the kinematic variables x and ξ represent respectively the average and difference of the longitudinal momentum fractions of the probed parton in the initial and final states. t is the squared four–momentum transfer $t = (p - p')^2$ to the nucleon, with p (p') the four-momentum of the nucleon in the initial (final) state. The variable ξ is typically nonzero in hard-exclusive reactions.

In the forward limit ($t \to 0$), the GPDs $H_q(x,\xi,t)$ and $\widetilde{H}_q(x,\xi,t)$ are related to the usual parton distributions as:

$$H(x,\xi,t)|_{\xi=t=0} = f_1(x), \quad \widetilde{H}(x,0,0)|_{\xi=t=0} = \mathrm{g}_1(x), \tag{2.37}$$

On the other hand, by integration over x, one obtains the nucleon form factors:

$$\begin{aligned} \int_{-1}^{1} dx H(x,\xi,t) &= F_1(t)\ , \\ \int_{-1}^{1} dx E(x,\xi,t) &= F_2(t)\ , \end{aligned}$$

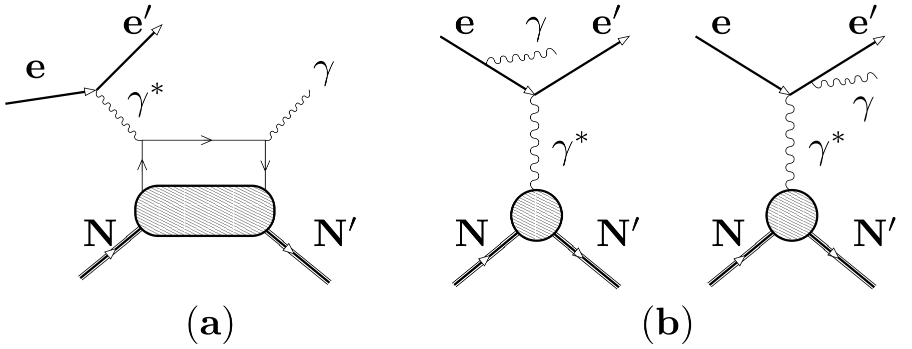

Figure 2.7: Leading-order diagrams for (a) deeply virtual Compton scattering (handbag diagram) and (b) Bethe-Heitler processes.

$$\begin{aligned} \int_{-1}^{1} dx\widetilde{H}(x,\xi,t) &= G_A(t) \ , \\ \int_{-1}^{1} dx\widetilde{E}(x,\xi,t) &= G_P(t) \ . \end{aligned} \tag{2.38}$$

Here F_1 and F_2 are the Dirac and Pauli form factors of the nucleon, and G_A and G_P are the axial and induced–pseudoscalar form–factors respectively. The dependence on ξ drops out after integration over x. Accordingly the GPDs describes not only the parton distribution function, but also the elastic form factors. Due to the violation of Ellis–Jaffe sum rule or "proton spin problem", a great interest is focused on the possibility of measuring GPDs which can access the total angular momentum (spin plus orbital angular momentum) carried by quark J_q. A sum rule was proposed by Ji [27, 72]:

$$\lim_{t\to 0}\int_0^1 \mathrm{d}\,x\ x\,(H_q(x,\xi,t)+E_q(x,\xi,t)) = J_q. \tag{2.39}$$

The total spin of the nucleon is then given by:

$$\sum_q J_q + J_g = \frac{1}{2}. \tag{2.40}$$

This finding offers for the first time a path towards solving the "nucleon spin problem" and tell how the helicities and orbital angular momenta of quarks and gluons combine to form the spin of the nucleon.

From the experimental point of view, a direct determination of GPDs seems possible at quite high energy. At lower energy one has to separate it from the Bethe–Heitler (BH) process as shown in Figure 2.7, *e.g.*, at the HERMES and Jefferson experiments. Measurements of the single–spin asymmetry in exclusive photon production have been reported in the HERMES [34–36] and CLAS [31, 32] collaborations, which have the characteristics expected from the DVCS-BH interference. DVCS has also been studied by the H1 [28, 30] and ZEUS [29] experiments at $x \sim 10^{-3}$ and close to forward limit.

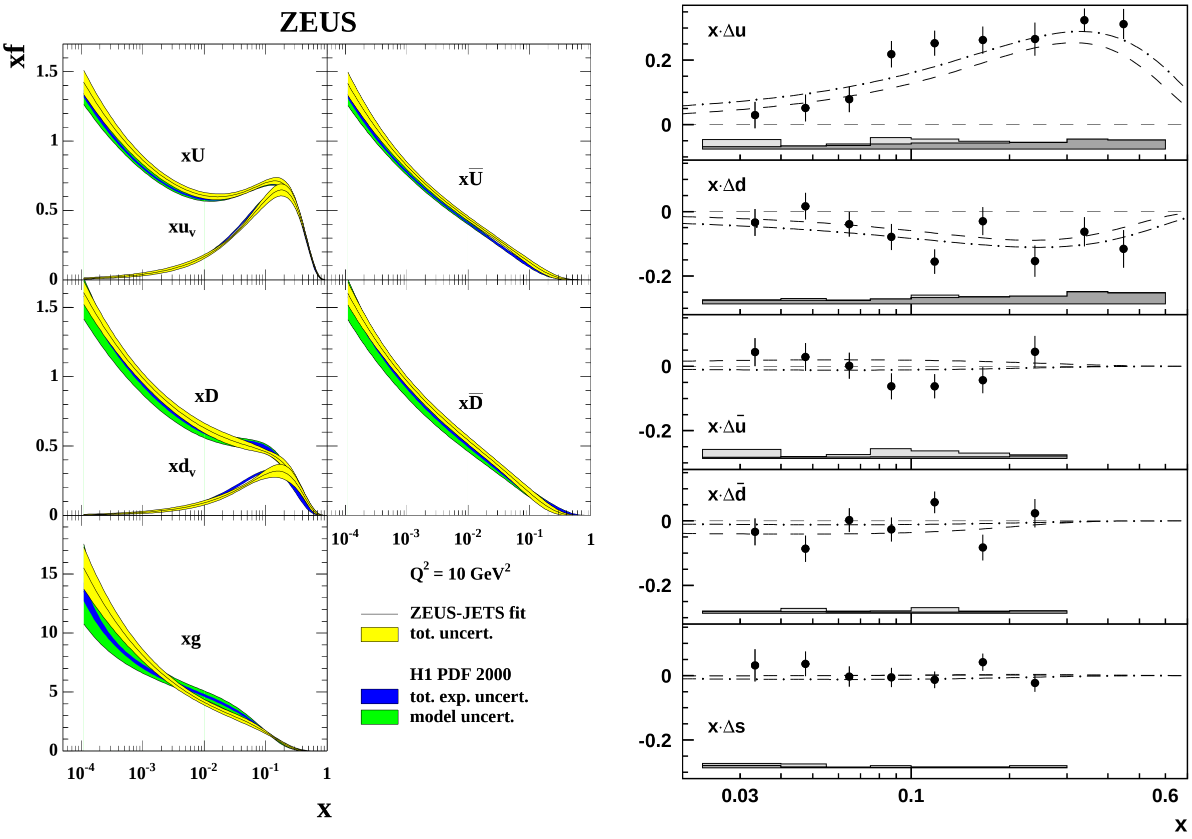

Figure 2.8: Left: The unpolarized parton distribution function $f_1(x)$ (donated as f in the figure) of the valence (up and down) quarks, sea quarks and gluon as a function of x for fixed $Q^2 = 10\,\mathrm{GeV}^2$ [73]. Right: The quark helicity distributions $x g_1^q(x, Q_0^2)$ ($x\,\Delta$q in plot) evaluated at a common value of $Q_0^2 = 2.5$ GeV^2 as a function of x [21].

2.1.5 Distribution Functions

The correlation function $\Phi_{ij}(p, P, S)$ in Eq. (2.22) can be integrated over the transverse momentum $\boldsymbol{p}_T$ of the struck quark

$$\Phi_{ji}(x, S) = \int \mathrm{d}^2\boldsymbol{p}_T \; \mathrm{d}\,p^- \; \Phi_{ji}(p, P, S)\Big|_{p^+ = xP^+} \tag{2.41}$$

It is convenient to define the projectors

$$\mathcal{P}_+ = \frac{1}{2}\,\gamma^-\gamma^+, \qquad\qquad \mathcal{P}_- = \frac{1}{2}\,\gamma^+\gamma^- . \tag{2.42}$$

Following the Hermiticity, parity and time–reversal invariance and at leading twist, we can obtain the general expression from Eq. (2.41) [74]

$$\mathcal{P}_+\,\Phi(x, S)\gamma^+ = \left(f_1(x) + S_L\,\mathrm{g}_1(x)\,\gamma_5 + h_1(x)\,\gamma_5\,\not{S}_T\right)\mathcal{P}_+ \; . \tag{2.43}$$

Eq. (2.43) is a leading twist expression [38], which refers to the order in M/Q at which the operator matrix elements contribute to the cross section. The function f_1 is usually referred to as the unpolarized parton distribution[3]. The function g_1 is the parton helicity distribution[4]. The function h_1 is known as the parton transversity distribution[5].

The meaning of the functions $f_1(x)$, $\mathrm{g}_1(x)$ and $h_1(x)$ can be understood in the **infinite–momentum frame** of the nucleon, such as the widely used Breit frame illustrated in Figure 2.3 (b). The distribution functions are probability densities for finding a quark with a certain momentum fraction x inside the nucleon. They can be distinguished by the relative polarization of the quarks and the nucleon. In this frame, the function $f_1(x)$ gives the probability for finding an unpolarized quark with momentum fraction x inside an unpolarized nucleon. Left plot in Figure 2.8 shows the recent fit to the unpolarized quark and gluon parton distributions. Note the large sea and gluon distributions at small Bjorken-x region. The valence quarks saturate the structure function almost for $x > 0.2$

The function $\mathrm{g}_1(x)$ gives the probability for finding a quark with its polarization aligned with the polarization of the nucleon minus the probability for finding a quark with its polarization anti–aligned with the polarization of the nucleon, when the nucleon is polarized along its direction of motion. Right plot in Figure 2.8 shows the recent measurement of the flavor separation from HERMES [21] which were obtained using leading–order analysis. The polarization of the up and down quarks are positive and negative respectively, while sea polarization is consistent with zero. A new measurement from HERMES [75] also shows that g_1^s is nearly zero.

The meaning of the function $h_1(x)$ is the same, except for the nucleon now being polarized perpendicular to the direction of motion. This is shown schematically in Figure 1.1, which indicates for each of three distribution functions the relative orientation of the polarization of the quark and the nucleon. In the following section, we will give a more detailed description of transversity distribution.

2.2 Transversity Distribution Function

The DIS hadronic tensor is related to forward virtual Compton scattering amplitudes [54]. Thus, leading twist quark distribution functions can be expressed in terms of quark–nucleon forward amplitudes. In the **helicity basis** these amplitudes have the form $\mathcal{A}_{\Lambda\lambda,\Lambda'\lambda'}$, where λ, λ' (Λ, Λ') are quark (nucleon) helicities. There are in general 16 amplitudes. Helicity conservation gives $\Lambda + \lambda = \Lambda' + \lambda'$. Parity invariance implies $\mathcal{A}_{\Lambda\lambda,\Lambda'\lambda'} = \mathcal{A}_{-\Lambda-\lambda,-\Lambda'-\lambda'}$. Time–reversal invariance reads $\mathcal{A}_{\Lambda\lambda,\Lambda'\lambda'} = \mathcal{A}_{\Lambda'\lambda',\Lambda\lambda}$. Hence,

---

[3] Sometimes denoted as f or q [54].

[4] Sometimes denoted as Δf or Δq [54].

[5] Sometimes denoted as δq, $\Delta_T q$ or $\Delta_T f$ [54].

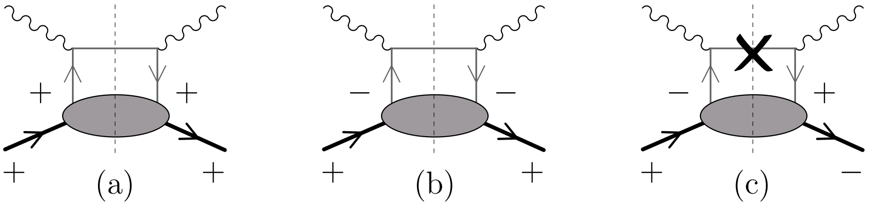

Figure 2.9: Three independent configurations of quark and nucleon helicities in the handbag diagram. The handbag diagram in panel (c) is forbidden in inclusive DIS by chirality conservation.

we are left with three independent amplitudes (see Figure 2.9)

$$\mathcal{A}_{++,++}\,,\quad \mathcal{A}_{+-,+-}\,,\quad \mathcal{A}_{+-,-+}\,. \tag{2.44}$$

Two of the amplitudes in Eq. (2.44), $\mathcal{A}_{++,++}$ and $\mathcal{A}_{+-,+-}$, are diagonal in the helicity basis (the quark does not flip its helicity: $\lambda = \lambda'$), the third, $\mathcal{A}_{+-,-+}$, is off–diagonal (helicity flip: $\lambda = -\lambda'$). Using the optical theorem we can relate these quark–nucleon helicity amplitudes to three leading twist quark distribution functions, according to the scheme

$$\begin{aligned} f_1(x) &= \;\; q_+(x) + q_-(x) \;\; \sim \mathrm{Im}(\mathcal{A}_{++,++} + \mathcal{A}_{+-,+-})\,, & \text{(2.45a)}\\ \mathrm{g}_1(x) &= \;\; q_+(x) - q_-(x) \;\; \sim \mathrm{Im}(\mathcal{A}_{++,++} - \mathcal{A}_{+-,+-})\,, & \text{(2.45b)}\\ h_1(x) &= \;\; q_\uparrow(x) - q_\downarrow(x) \;\; \sim \mathrm{Im}\,\mathcal{A}_{+-,-+}\,. & \text{(2.45c)} \end{aligned}$$

Here we see that h_1 is a chiral–odd distribution function, *i.e.*,

$$\gamma^5 h_1(x) = -h_1(x). \tag{2.46}$$

The most right plot in Figure 2.9 shows a characteristic property of h_1. It involves a simultaneous spin flip ($+- \rightarrow -+$) of parton and target. It cannot be probed in inclusive deep inelastic scattering processes due to the chirality conservation rule. In terms of parton–nucleon forward helicity amplitudes, it is easy to understand why there is no leading twist transverse polarization of gluons [76]. A hypothetical h_1^g would imply an helicity flip gluon–nucleon amplitude, which cannot exist owing to helicity conservation. In fact, gluons have helicity ±1 but the nucleon cannot undergo an helicity change ±2. As a consequence, the QCD evolution for transversity will be simpler than the other distribution functions [77], because the gluon transversity h_1^g will not mix with the quark transversity h_1^q. Target with total spin–1 may have a helicity flip gluon distribution.

In a **transversity basis** (with ↑ directed along y shown in Figure 2.2)

$$\begin{aligned} |\uparrow\rangle &= \tfrac{1}{\sqrt{2}}\Big[|+\rangle + \mathrm{i}|-\rangle\Big]\,,\\ |\downarrow\rangle &= \tfrac{1}{\sqrt{2}}\Big[|+\rangle - \mathrm{i}|-\rangle\Big]\,, \end{aligned} \tag{2.47}$$

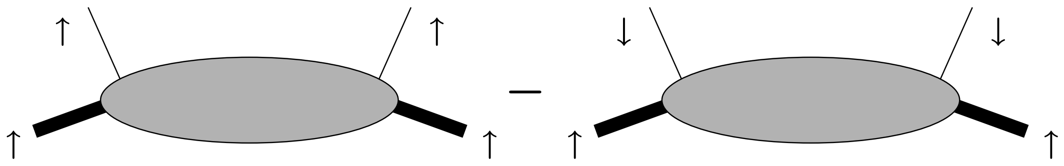

Figure 2.10: Schematic presentation of the transversity distribution function h_1 in the transversity basis.

the transverse polarization distributions h_1 is related to a diagonal amplitude

$$h_1(x) = q_\uparrow(x) - q_\downarrow(x) \sim \mathrm{Im}(\mathcal{A}_{\uparrow\uparrow,\uparrow\uparrow} - \mathcal{A}_{\uparrow\downarrow,\uparrow\downarrow}) \,, \tag{2.48}$$

which is shown in Figure 2.10.

Deriving from the correlation function in helicity formalism, the positivity conditions can be obtained as [78]:

$$f_1(x) \geq 0, \tag{2.49a}$$

$$|\mathrm{g}_1(x)| \leq f_1(x), \tag{2.49b}$$

$$|h_1(x)| \leq \tfrac{1}{2}\big(f_1(x) + \mathrm{g}_1(x)\big). \tag{2.49c}$$

The last relation is known as the Soffer bound [79].

The difference between the helicity distribution and the transversity distribution is connected to relativistic effects, because Lorentz boosts and rotation do not commute [78]. Relativistic effects influence observable quantities depending on the dynamics of the system and they can therefore give important information about this structure. The difference between helicity and transversity distributions can shed light on the structure of the nucleon and spin.

There are also predictions for transversity from theoretical models, *e.g.*, the MIT bag model [80], the colour dielectric model [81], the chiral quark soliton model [82–86], the chiral quark model [87], the light–cone model [88, 89], the spectator model [90, 91], QCD sum rules [92] and lattice evaluations [93–97]. Figure 2.11 shows the predicted Bjorken–x dependent transversity distributions from some of the models. We can see that they show nearly the same distribution. A recent review on the transversity distribution is presented in Ref. [54]. A transverse spin "sum rule", which is similar in form to the longitudinal spin sum rule, was proposed [37]

$$\frac{1}{2} = \frac{1}{2}\sum_{a=q,\bar{q}} \int \mathrm{d}\,x \; h_1^a(x) + \sum_{a=q,\bar{q},g} \langle L_T \rangle^a, \tag{2.50}$$

where L_T is the component of the orbital angular momentum L along the transverse polarization direction and the sums run over quark and antiquark flavors. Note that Eq. (2.50) does not contain the gluon transversity.

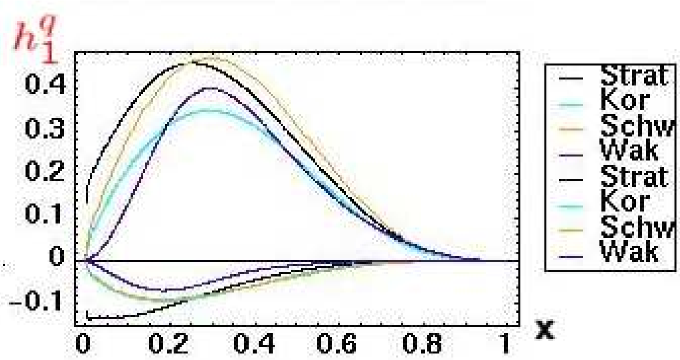

Figure 2.11: The u (above zero curve) and d (blew zero curve) quark transversity distributions (Strat [98], Kor [99], Schw [86] and Wak [100]) in proton predicted by different models, as a function of Bjorken-x.

Using Eqs. (2.3, 2.23, 2.43), we have the inclusive cross section at leading twist: [78]

$$\frac{\mathrm{d}^3\sigma}{\mathrm{d}\,x\;\mathrm{d}\,y\;\mathrm{d}\,\phi_S} \approx \frac{2\alpha^2}{sxy^2}\sum_q e_q^2\left[\left(1-y+\frac{y^2}{2}\right)f_1^q(x)+\lambda_l\,S_L\left(y-\frac{y^2}{2}\right)\mathrm{g}_1^q(x)\right], \tag{2.51}$$

where the index q denotes the quark flavor. The transversity distribution does not appear in the cross section for totally inclusive deep inelastic scattering at leading twist. The reason is that it is a chiral–odd object and in any observable it must be connected to another chiral–odd "probe". In inclusive deep inelastic scattering, what probes the structure of the correlation function is the elementary photon–quark scattering, which conserves chirality. The possible way to access transversity is to let transversity h_1 couple to another chiral–odd object. It could be another **chiral–odd distribution function**, or a **chiral–odd fragmentation function**. Compared with the unpolarized distribution function and the helicity distribution, the transversity distribution h_1 is practically unknown. Only very few experimental data exist that can be used to extract this value. So measuring transversity is important to complete the knowledge on three leading twist distribution functions.

There are two groups of processes to access the transversity distribution function: lepton–hadron collisions and hadron–hadron collisions. All these processes involve at least one transversely polarized hadron and also another one hadron. The following sections will generally focus on the lepton–nucleon semi–inclusive deep inelastic scattering, which HERMES experiment mainly measures. Transversity can be accessed with the one–hadron or two–hadron semi–inclusive DIS as described below. In the process of one–hadron semi–inclusive DIS case, the transversity h_1 is convoluted with the chiral–odd Collins fragmentation function $H_1^\perp$, which is also not known. Another direct measurement of transversity is through the process of two–hadron semi–inclusive DIS, where it appears in a direct product with another chiral–odd dihadron fragmentation function $H_1^{\sphericalangle}$. This process is more advantageous than one–hadron case, since it does not require inclusion of the transverse momentum $\boldsymbol{k_T}$ of the struck quark.

2.3 One–Hadron Fragmentation Function

The transversity distribution is not accessible in inclusive deep inelastic scattering. It is therefore desirable to turn the attention to another technique, *e.g.*, semi–inclusive measurement of deep inelastic scattering, where one or more of the fragments from the collision are detected. In those cases, we need to introduce some new non–perturbative objects; the fragmentation functions.

With a transversely polarized target, one can measure quark transverse polarization at leading twist either by looking at a possible asymmetry in the $\boldsymbol{P}_{h\perp}$[6] distribution of the produced hadron (as Collins effect [45, 51, 101, 102]), or by polarimetry of a transversely polarized final hadron (for instance, a Λ^0 hyperon) [102–105]. The only existing data that presently can be used to isolate transversity in this way are from the measurements of single–spin asymmetries of single hadrons in semi–inclusive DIS. Azimuthal single–spin asymmetries A_{UT} in single hadron production in semi–inclusive DIS ($lp \to l'hX$) on a transversely polarized target were recently measured by the HERMES collaboration for identified hadrons [40, 41, 106] and by the COMPASS collaboration for unidentified charged hadrons [42] and later for identified hadrons [43, 44]. The Collins function can be measured independently in other processes, *e.g.*, in e^+e^- collisions, and can then be used to extract the transversity distribution from the above asymmetries.

Here we consider the one–hadron semi–inclusive DIS process, in which the Collins fragmentation function will appear. For these observables the orientation of the transverse spin of the target influences the distribution of hadrons in the azimuthal angle around the virtual–photon direction through, *e.g.*, the so–called Collins [45] and Sivers [46] mechanisms. In particular, the Collins asymmetry is sensitive to the transversity distribution.

2.3.1 One–Hadron Semi–Inclusive Deep Inelastic Scattering

In one–hadron semi–inclusive deep inelastic scattering a high energy lepton collides on a target nucleon via the exchange of a photon with a high virtuality:

$$l(k) + N(P) \to l'(k') + h(P_h) + X(P_X)\,. \tag{2.52}$$

The target breaks up and several hadrons are produced. One of the produced hadrons is detected in coincidence with the scattered lepton (see Figure 2.12). As a result of the hardness of the collision, the final state should consist of two well separated “clusters” of particles, one is represented by the hadrons formed and ejected by the hard interaction

---

[6] The transverse component of $\boldsymbol{P}_h$ with respect to the virtual–photon direction.

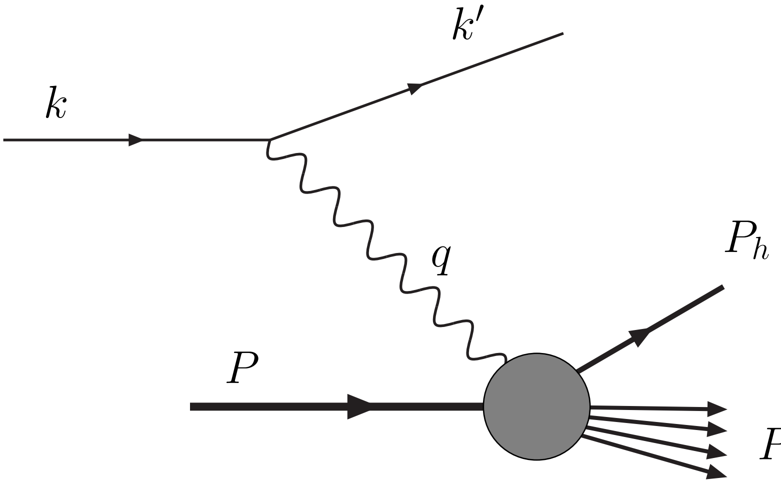

Figure 2.12: Schematic picture of one–hadron semi–inclusive deep inelastic scattering.

with the virtual photon [107], called "current fragments", and the other is represented by the debris of the target (called "target fragments"), broken by the collision. We only consider the tagged final hadron in the current fragments. For example, as shown in Figure 2.13, the detected "current fragmented" π^+ in semi–inclusive process carries information of the struck quark.

The cross section for one–hadron inclusive lepton–nucleon scattering can be written as

$$\frac{2E_h\, \mathrm{d}^6\sigma}{\mathrm{d}^3\boldsymbol{P}_h\; \mathrm{d}\,x\; \mathrm{d}\,y\; \mathrm{d}\,\phi_S} = \frac{\alpha^2}{2sxQ^2}\, L_{\mu\nu}(k,k',\lambda_e)\, 2MW^{\mu\nu}(q,P,S,P_h), \tag{2.53}$$

or equivalently as

$$\frac{\mathrm{d}^6\sigma}{\mathrm{d}\,x\; \mathrm{d}\,y\; \mathrm{d}\,z\; \mathrm{d}\,\phi_S\; \mathrm{d}^2\boldsymbol{P}_{h\perp}} = \frac{\alpha^2}{4zsxQ^2}\, L_{\mu\nu}(k,k',\lambda_e)\; 2MW^{\mu\nu}(q,P,S,P_h). \tag{2.54}$$

To obtain the previous formula, we made use of the relation $\mathrm{d}^3P_h/2E_h \approx \mathrm{d}\,z\; \mathrm{d}^2\boldsymbol{P}_{h\perp}/2z$. Other kinematic variables can be found in Table 2.1 and ϕ_S is defined in Eq. (2.2). The differential $\mathrm{d}^2\, \boldsymbol{P_{h\perp}}$ is often also written as:

$$\mathrm{d}^2\, \boldsymbol{P_{h\perp}} = |\boldsymbol{P_{h\perp}}|\; \mathrm{d}\,|\boldsymbol{P_{h\perp}}|\; \mathrm{d}\,\phi_h, \tag{2.55}$$

where the azimuthal angle ϕ_h of the hadron direction around the virtual–photon γ^* direction has been introduced:

$$\phi_h = \frac{\boldsymbol{q}\times\boldsymbol{k}\cdot\boldsymbol{P_h}}{|\boldsymbol{q}\times\boldsymbol{k}\cdot\boldsymbol{P_h}|}\cos^{-1}\frac{\boldsymbol{q}\times\boldsymbol{k}\cdot\boldsymbol{q}\times\boldsymbol{P_h}}{|\boldsymbol{q}\times\boldsymbol{k}||\boldsymbol{q}\times\boldsymbol{P_h}|}. \tag{2.56}$$

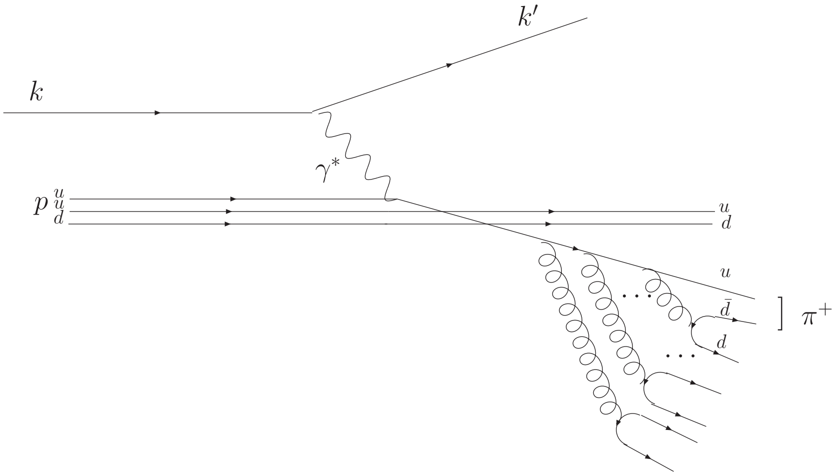

Figure 2.13: Quark line picture of semi–inclusive DIS process on the proton target, in which a π^+ is produced via the current fragmentation process and observed by the detector.

In the parton model, without explicitly including the antiquark contributions, the hadronic tensor at tree level can be written as:

$$2MW^{\mu\nu}(q,P,S,P_h) = \sum_q e_q^2 \int \mathrm{d}^4p\ \mathrm{d}^4k\ \delta^{(4)}\left(p+q-k\right)\ \mathrm{Tr}\left(\Phi(p,P,S)\,\gamma^\mu\,\Delta(k,P_h)\,\gamma^\nu\right), \tag{2.57}$$

where Φ is the correlation function and Δ is,

$$\Delta_{ij}(k,P_h) = \sum_X \int \frac{\mathrm{d}^3\boldsymbol{P_x}}{(2\pi)^3 2E_x} \langle 0|\psi_i(0)|P_h,X\rangle\langle P_h,X|\bar{\psi}_j(0)|0\rangle\delta^4(k-P_h-P_x), \tag{2.58}$$

where $|P_h,X\rangle$ represents the hadronic final state and the summation runs over all possible undetected hadronic states X. Δ is a new correlation function we need to introduce in order to describe the fragmentation process [108](see Figure 2.15).

It is convenient to take the hN collinear frame [54] (named as T frame) as reference frame, where the target N and the outgoing hadron momenta are collinear. Then the photon acquires a transverse momentum components $-\frac{\boldsymbol{P}_{h\perp}}{z}$. By neglecting terms which are $1/Q$ suppressed, we obtain the compact expression

$$2MW^{\mu\nu}(q,P,S,P_h) = 4z\,\mathcal{I}\Big[\mathrm{Tr}\left(\Phi(x,\boldsymbol{p}_T,S)\,\gamma^\mu\,\Delta(z,\boldsymbol{k}_T)\,\gamma^\nu\right)\Big], \tag{2.59}$$

where

$$\mathcal{I}\Big[\cdots\Big] = \int \mathrm{d}^2\boldsymbol{p}_T\ \mathrm{d}^2\,\boldsymbol{k}_T\,\delta^{(2)}\Big(\boldsymbol{p}_T - \frac{\boldsymbol{P}_{h\perp}}{z} - \boldsymbol{k}_T\Big)\ \Big[\cdots\Big]. \tag{2.60}$$

$\mathcal{I}$ denotes an integral over the transverse momenta, which convolutes the distribution correlator Φ and the fragmentation correlator Δ. $\boldsymbol{p_T}$ and $\boldsymbol{k_T}$ are the transverse momenta

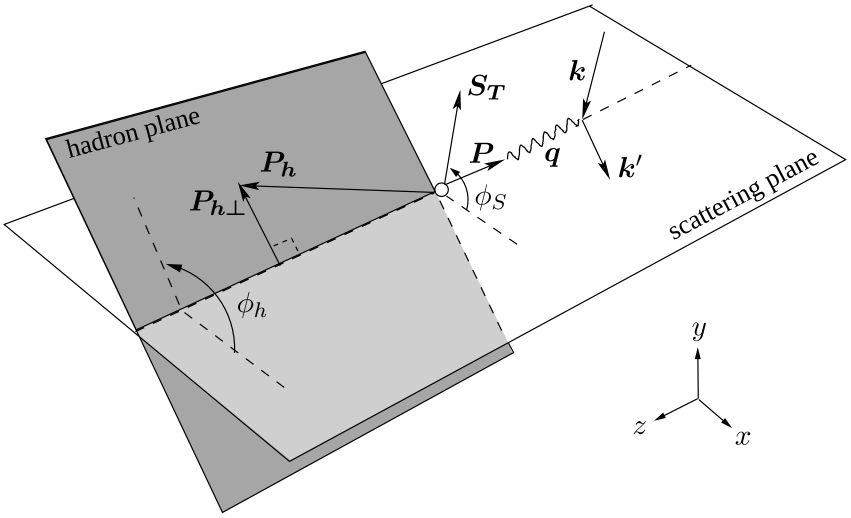

Figure 2.14: Kinematic variables describing the one–hadron semi–inclusive deep inelastic scattering process. $\boldsymbol{S_T}$ (or $\boldsymbol{S_\perp}$) is the component of target spin $\boldsymbol{S}$ perpendicular to the virtual photon direction.

of the struck quark before and after the interaction point with the virtual photon in the bag diagram Figure 2.15, respectively. If we turn back to the $\gamma^* N$ frame (named as $\perp$ frame), the transverse momentum of stuck quark $\boldsymbol{p_T}$ is from the quark intrinsic transverse momentum inside the nucleon and the transverse momentum $\boldsymbol{k_T}$ is produced from the fragmenting process. Consider the transverse–momentum dependent version of the correlation functions

$$\Phi(x, \boldsymbol{p}_T, S) \equiv \int \mathrm{d}\, p^- \Phi(p, P, S)\Big|_{p^+ = xP^+}, \tag{2.61a}$$

$$\Delta(z, \boldsymbol{k}_T) \equiv \frac{1}{4z} \int \mathrm{d}\, k^+ \Delta(k, P_h)\Big|_{k^- = P_h^-/z}. \tag{2.61b}$$

According to hermiticity and parity invariance, the general expansion of the correlator at leading twist will read as:

$$\mathcal{P}_- \, \Delta(z, \boldsymbol{k}_T)\, \gamma^- = \frac{1}{2} \left(D_1(z, z^2 \boldsymbol{k}_T^2) + i\, H_1^\perp(z, z^2 \boldsymbol{k}_T^2)\, \frac{\not{k}_T}{M_h} \right) \mathcal{P}_- \,, \tag{2.62}$$

where we introduced the fragmentation functions. D_1 is the unpolarized fragmentation function, which describes the probability for an unpolarized quark to fragment into an unpolarized hadron. The function $H_1^\perp$, called the Collins fragmentation function, is a chiral–odd function which gives the probability for a transversely polarized quark to fragment into an unpolarized hadron. This is shown schematically in Figure 2.16.

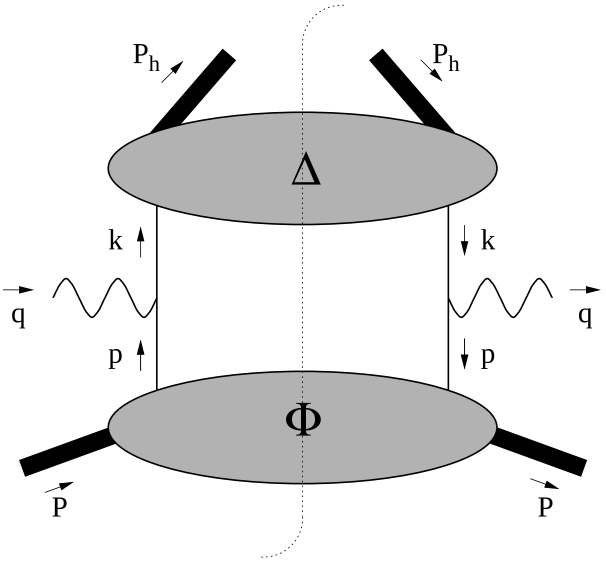

Figure 2.15: The diagram describing the hadronic tensor at tree level.

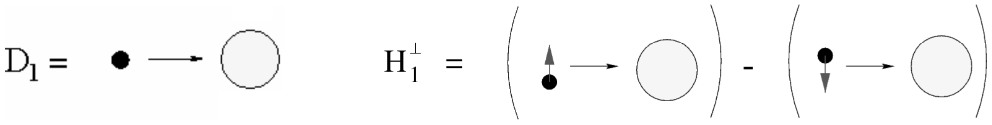

Figure 2.16: Schematic presentation for the leading twist fragmentation functions: the unpolarized fragmentation function D_1 and the Collins fragmentation function $H_1^{\perp}$ arising in the fragmentation of a current quark into an unpolarized hadron.

2.3.2 Cross Sections and Asymmetries

Then we can obtain the full cross section for one–hadron semi–inclusive deep inelastic scattering. But here only the sum and difference of transversely polarized cross sections are presented, by which the transversity distribution h_1 can be evaluated by the convolution with the Collins fragmentation function $H_1^{\perp}$. For convention, we use the symbols → or ← to indicate polarization along the virtual–photon γ^* direction or opposite to it. We also use ↑↓ to indicate transverse polarization. The subscript U will denote unpolarization, while L and T will denote longitudinally and transversely polarization. The first subscript describes always the beam polarization and the second subscript the target polarization. We define the following cross sections[7]

$$\mathrm{d}^6\sigma_{\mathrm{UU}} \equiv \frac{1}{2}\left(\mathrm{d}^6\sigma_{U\uparrow} + \mathrm{d}^6\sigma_{U\downarrow}\right), \qquad \mathrm{d}^6\sigma_{\mathrm{UT}} \equiv \frac{1}{2}\left(\mathrm{d}^6\sigma_{U\uparrow} - \mathrm{d}^6\sigma_{U\downarrow}\right). \tag{2.63}$$

---

[7] Here, $\mathrm{d}^6\,\sigma$ is short for $\mathrm{d}^6\,\sigma/(\mathrm{d}\,x\;\mathrm{d}\,y\;\mathrm{d}\,\phi_S\;\mathrm{d}\,\boldsymbol{P_h})$.

for which we obtain the following expressions in terms of distribution and fragmentation functions: [109]

$$\frac{\mathrm{d}^6\sigma_{\mathrm{UU}}}{\mathrm{d}\,x\ \mathrm{d}\,y\ \mathrm{d}\,z_h\ \mathrm{d}\,\phi_S\ \mathrm{d}^2\boldsymbol{P}_{h\perp}} = \sum_q \frac{2\alpha^2 e_q^2}{sxy^2}\left\{A(y)\mathcal{I}\left[f_1^q(x,\boldsymbol{p}_T^2)D_1^q(z_h,z_h^2\boldsymbol{k}_T^2)\right] - B(y)\cos 2\phi_h\right.$$
$$\left.\times\,\mathcal{I}\left[\frac{2(\boldsymbol{p}_T\cdot\hat{\boldsymbol{P}}_{h\perp})(\boldsymbol{k}_T\cdot\hat{\boldsymbol{P}}_{h\perp}) - \boldsymbol{p}_T\cdot\boldsymbol{k}_T}{MM_h}\,h_1^{\perp q}(x,\boldsymbol{p}_T^2)H_1^{\perp q}(z_h,z_h^2\boldsymbol{k}_T^2)\right]\right\}, \tag{2.64}$$

$$\frac{\mathrm{d}^6\sigma_{\mathrm{UT}}}{\mathrm{d}\,x\ \mathrm{d}\,y\ \mathrm{d}\,z_h\ \mathrm{d}\,\phi_S\ \mathrm{d}^2\boldsymbol{P}_{h\perp}} = -\sum_q \frac{2\alpha^2 e_q^2}{sxy^2}\,|\boldsymbol{S}_T|\left\{B(y)\sin\left(\phi_h+\phi_S\right)\mathcal{I}\left[\frac{\boldsymbol{k}_T\cdot\hat{\boldsymbol{P}}_{h\perp}}{M_h}\,h_1^q H_1^{\perp q}\right]\right.$$
$$+\,A(y)\sin\left(\phi_h-\phi_S\right)\mathcal{I}\left[\frac{\boldsymbol{p}_T\cdot\hat{\boldsymbol{P}}_{h\perp}}{M}\,f_{1T}^{\perp q}D_1^q\right] + B(y)\sin\left(3\phi_h-\phi_S\right)\times$$
$$\left.\mathcal{I}\left[\frac{4(\boldsymbol{p}_T\cdot\hat{\boldsymbol{P}}_{h\perp})^2(\boldsymbol{k}_T\cdot\hat{\boldsymbol{P}}_{h\perp}) - 2(\boldsymbol{p}_T\cdot\hat{\boldsymbol{P}}_{h\perp})(\boldsymbol{p}_T\cdot\boldsymbol{k}_T) - \boldsymbol{p}_T^2(\boldsymbol{k}_T\cdot\hat{\boldsymbol{P}}_{h\perp})}{2M^2M_h}\,h_{1T}^{\perp q}H_1^{\perp q}\right]\right\}, \tag{2.65}$$

where

$$A(y) = 1 - y + \frac{y^2}{2}, \qquad\qquad B(y) = 1 - y. \tag{2.66}$$

Azimuthal angles ϕ_h and ϕ_S are described in Figure 2.14 and the summation is over the quark flavors. From the above equations, we can see that through the cross section from the transversely polarized target, the transversity distribution function h_1 can be accessed by the characteristic $\sin(\phi_h + \phi_S)$ modulation. There is a convolution of the transversity distribution function h_1 and the Collins fragmentation function $H_1^{\perp}$ in transverse momentum through the integral $\mathcal{I}$. Therefore, it is difficult to decompose the two functions in the experimental measurement.

In transversely polarized target experiments we can only measure the following single–spin asymmetry:

$$A_{\mathrm{UT}} = \frac{1}{|\boldsymbol{S_T}|}\frac{\mathrm{d}\,\sigma(\phi_h,\phi_S) - \mathrm{d}\,\sigma(\phi_h,\phi_S+\pi)}{\mathrm{d}\,\sigma(\phi_h,\phi_S) + \mathrm{d}\,\sigma(\phi,\phi_S+\pi)} = \frac{1}{|\boldsymbol{S_T}|}\frac{\mathrm{d}\,\sigma_{\mathrm{UT}}}{\mathrm{d}\,\sigma_{\mathrm{UU}}}. \tag{2.67}$$

Many terms in Eq. (2.65) have unique form of Fourier components with dependence on the azimuthal angles, *i.e.*, ϕ_h and ϕ_S. To single out the specific term of the cross section with a distinct angular dependence, which relates to the transversity h_1, one can use the azimuthal moment, the Collins moment, of the asymmetry:

$$\begin{aligned}\langle\sin(\phi_h+\phi_S)\rangle_{\mathrm{UT}} &\equiv \frac{\int \mathrm{d}\,\phi_h\ \mathrm{d}\,\phi_S \sin(\phi_h+\phi_S)[\,\mathrm{d}\,\sigma(\phi_h,\phi_S) - \mathrm{d}\,\sigma(\phi_h,\phi_S+\pi)]}{\int \mathrm{d}\,\phi_h\ \mathrm{d}\,\phi_S[\,\mathrm{d}\,\sigma(\phi_h,\phi_S) + \mathrm{d}\,\sigma(\phi_h,\phi_S+\pi)]}\\ &= -|\boldsymbol{S_T}|\frac{B(y)\sum_q e_q^2\int \mathrm{d}^2\,\boldsymbol{P_{h\perp}}\mathcal{I}\left[\frac{\boldsymbol{k_T}\cdot\hat{\boldsymbol{P}}_{\boldsymbol{h\perp}}}{M_h}h_1^q(x,\boldsymbol{p_T^2})H_1^{\perp q}(z,z^2\boldsymbol{k_T^2})\right]}{A(y)\sum_q e_q^2 f_1^q(x)D_1^q(z)}.\end{aligned} \tag{2.68}$$

The recent preliminary measurement of Collins moments at the HERMES experiment will be discussed in Sec. 5.3.1. This moment is sensitive to the transversity distribution function $h_1(x)$ and the Collins fragmentation function $H_1^{\perp}$. In order to extract transversity purely, we need a separate measurement of Collins fragmentation function. The experimental progress will be discussed in Sec. 5.3.1. The model calculations of the Collins fragmentation function $H_1^{\perp}$ is discussed in Ref. [110].

2.4 Two-Hadron Fragmentation Function

In this section we will extend the previous topic to the two–hadron lepto–production case, through which the measurement of the transversity distribution in this thesis is proceeded. By the early 90s it had already been pointed out that single–spin asymmetries in semi–inclusive measurement of two–hadron production ($ep \rightarrow e'h_1h_2X$) on a transversely polarized target could also be sensitive to transversity [50, 51]. It provides an independent experimental constraint. The underlying mechanism differs from the Collins mechanism in that the transverse spin of the fragmenting quark is transferred to the relative **orbital angular momentum** of the hadron pair. Consequently this mechanism does not require transverse momentum of the hadron pair. Two–hadron semi–inclusive DIS has been proposed and studied by various theorists [111–114] as a process that can probe the transverse polarization distributions of the nucleon, which is coupled to dihadron[8] fragmentation functions. Model calculations have been performed in Refs. [111, 112, 114–117]. Two–pion fragmentation functions have been studied also in the context of e^+e^- annihilation with a somewhat different formalism [118, 119] and the pp collision process [120]. This section will not involve these processes.

2.4.1 Two–Hadron Semi–Inclusive Deep Inelastic Scattering

Two–hadron lepto–production (see Figure 2.17) can be written as:

$$l(k) \,+\, N^{\uparrow}(P) \rightarrow l'(k') \,+\, h_1(P_1) \,+\, h_2(P_2) \,+\, X(P_X)\,. \tag{2.69}$$

with the target transversely polarized. In this reaction two hadrons (for instance, two pions) are detected in the final state. The transverse spin of the target can be correlated via a transversely polarized quark to the relative transverse momentum between the hadronic pair instead of the transverse momentum of the outgoing hadron. This provides a way in which the transversity can be probed without including partonic transverse momenta, thus avoiding several complications and subtleties [78].

The cross–section for the reaction

$$\frac{2E_1\, 2E_2\, \mathrm{d}^9\sigma}{\mathrm{d}^3\boldsymbol{P}_1\, \mathrm{d}^3\boldsymbol{P}_2\, \mathrm{d}\,x\, \mathrm{d}\,y\, \mathrm{d}\,\phi_S} = \frac{\alpha^2}{2sxQ^2}\, L_{\mu\nu}(k,k',\lambda_e)\, 2MW^{\mu\nu}(q,P,S,P_1,P_2), \tag{2.70}$$

---

[8] Dihadron means the two hadrons, *i.e.*, h_1 and h_2, are different hadrons.

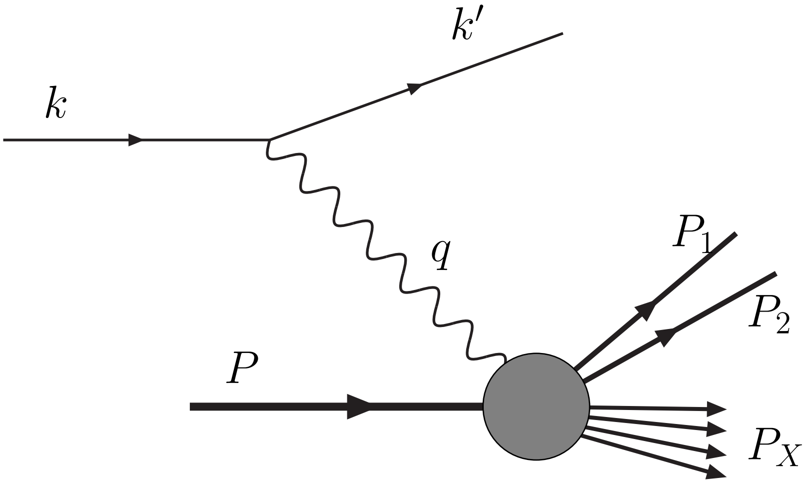

Figure 2.17: Schematic picture of two–hadron lepto–production in semi–inclusive deep inelastic scattering.

Following Ref. [113], we introduce the combinations

$$P_h \equiv P_1 + P_2, \quad R \equiv \frac{1}{2}(P_1 - P_2), \tag{2.71}$$

and the invariants

$$z_1 = \frac{P{\cdot}P_1}{P{\cdot}q}, \qquad z = z_1 + z_2 = \frac{P{\cdot}P_h}{P{\cdot}q}, \tag{2.72a}$$

$$z_2 = \frac{P{\cdot}P_2}{P{\cdot}q}, \qquad \zeta = 2\frac{R^-}{P_h^-} = \frac{z_1 - z_2}{z}, \tag{2.72b}$$

where R^- and P_h^- are light–cone components of R and P_h, respectively. In the present work, the specific process is considered and h_1 and h_2 are two oppositely charged pions. P_1 is defined as the momentum of the positive pion, consistent with the literature on the subject (as first defined in Ref. [116]).

As shown in Figure 2.18, as in the one–hadron case, P_h can be written in terms of its component $\boldsymbol{P_{h\perp}}$ perpendicular to the virtual–photon direction, which also introduces the two–hadron analogue of ϕ_h (cf. Eqs. (2.55) and (2.56)). But here P_h is the sum vector of P_1 and P_2. Also for the azimuthal angle ϕ_S, we can have same definition as Eq. (2.2). The angles ϕ_R and $\phi_{R\perp}$ shown in Figure 2.19 can be calculated from the involved vectors

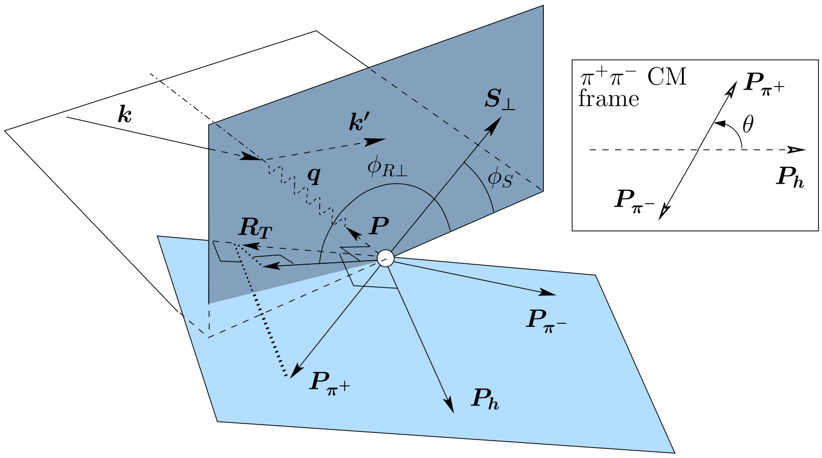

Figure 2.18: Depiction of the azimuthal angles $\phi_{R\perp}$ of dihadron and ϕ_S of the target polarization direction $\boldsymbol{S}_\perp$ in the virtual–photon–nucleon center–of–mass frame. The smaller plot at right side shows the polar angle θ in the frame of center–of–mass of two–hadron pair.

as

$$\phi_{R\perp} = \frac{\boldsymbol{q}\times\boldsymbol{k}\cdot\boldsymbol{R_T}}{|\boldsymbol{q}\times\boldsymbol{k}\cdot\boldsymbol{R_T}|}\cos^{-1}\frac{\boldsymbol{q}\times\boldsymbol{k}\cdot\boldsymbol{q}\times\boldsymbol{R_T}}{|\boldsymbol{q}\times\boldsymbol{k}||\boldsymbol{q}\times\boldsymbol{R_T}|}, \tag{2.73a}$$

$$\phi_R = \frac{\hat{\boldsymbol{n}}\cdot\boldsymbol{R_T}}{|\boldsymbol{R_T}|}\cos^{-1}\frac{\hat{\boldsymbol{n}}\cdot(\boldsymbol{P_h}\times\boldsymbol{R_T})}{|\boldsymbol{P_h}\times\boldsymbol{R_T}|}, \tag{2.73b}$$

where $\boldsymbol{R_T}$ is the component of $\boldsymbol{R}$ perpendicular to $\boldsymbol{P_h}$, *i.e.*, $\boldsymbol{R_T} = \boldsymbol{R} - (\boldsymbol{R}\cdot\hat{\boldsymbol{P}}_{\boldsymbol{h}})\hat{\boldsymbol{P}}_{\boldsymbol{h}}$, and $\hat{\boldsymbol{n}}$ is a unit vector defined by the line of intersection of the T–plane with the plane defined by $(\boldsymbol{k}\times\boldsymbol{q})$ and $\boldsymbol{P_h}$ [121]. The difference between these two angles can be ignored at leading twist analysis [122]. In this work, we will adopt $\phi_{R\perp}$ in data analysis.

Eq. (2.70) can be rewritten in terms of the different variables as

$$\frac{\mathrm{d}^9\sigma}{\mathrm{d}\zeta\ \mathrm{d}M_h^2\ \mathrm{d}\phi_{R\perp}\ \mathrm{d}z\ \mathrm{d}^2\boldsymbol{P}_{h\perp}\ \mathrm{d}x\ \mathrm{d}y\ \mathrm{d}\phi_S} = \frac{\alpha^2}{32\,zsxQ^2}\,L_{\mu\nu}(k,k',\lambda_e)\,2MW^{\mu\nu}(q,P,S,P_1,P_2). \tag{2.74}$$

The angle $\phi_{R\perp}$ is the azimuthal angle of the vector $\boldsymbol{R}_T$ with respect to the lepton plane, measured in a plane perpendicular to the direction of the outgoing hadron.

In analogy to what we presented in Sec. 2.3.1, the hadronic tensor has a form similar to that of the single–particle case in the parton model at leading order in $1/Q$ (see Figure 2.20). The hadronic tensor can be expressed in terms of correlation functions as

$$2MW^{\mu\nu}(q,P,S,P_1,P_2) = 32z\,\mathcal{I}\Big[\mathrm{Tr}\left(\Phi(x,\boldsymbol{p}_T,S)\,\gamma^\mu\,\Delta(z,\boldsymbol{k}_T,\zeta,M_h^2,\phi_{R\perp})\,\gamma^\nu\right)\Big], \tag{2.75}$$

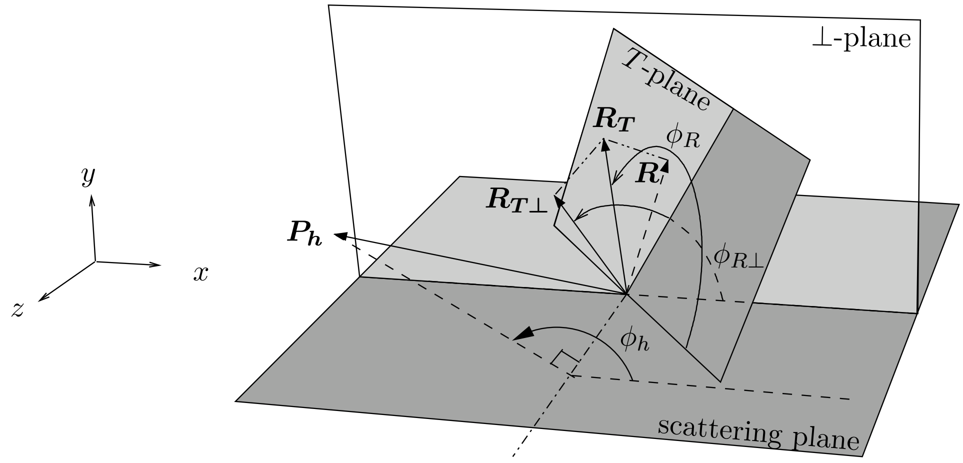

Figure 2.19: Description of the angles ϕ_R, $\phi_{R\perp}$ and ϕ_h in the virtual–photon–nucleon center–of–mass frame.

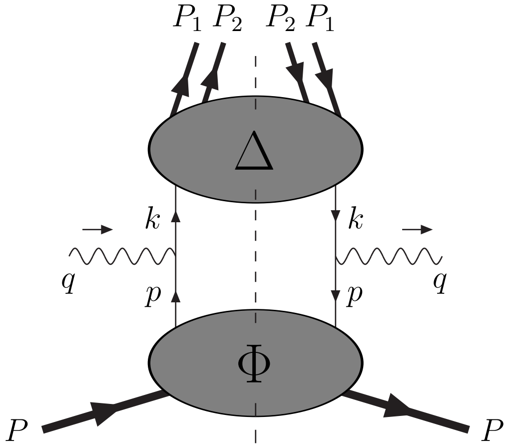

Figure 2.20: Diagram contributing to two–hadron lepto–production at tree level.

where the distribution Φ is the same function as that of one–hadron DIS. But dihadron fragmentation correlation function Δ has the dependence with the relative momentum $\boldsymbol{R}$ between two hadrons, as it is generalized to include the dependence on the vector $\boldsymbol{R}$

$$\Delta(z, \zeta, M_h^2, \phi_{R\perp}, \boldsymbol{k}_T) \equiv \frac{1}{32z} \int \mathrm{d}\, k^+ \Delta(k, P_h, R)\Big|_{k^- = P_h^-/z}. \tag{2.76}$$

The hadronic tensor and the correlation function can be integrated over the transverse

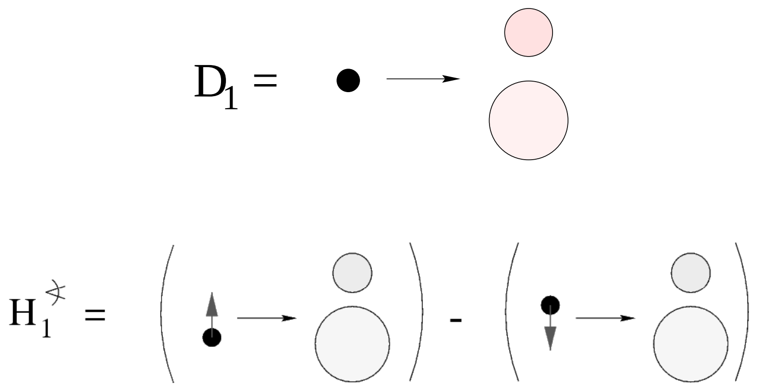

Figure 2.21: Schematic presentation for the leading order fragmentation function arising in the decay of a current quark into a pair of unpolarized hadrons. The different size of each hadron in the produced hadron pair is to illustrate that they are different hadrons.

momentum $\boldsymbol{P}_{h\perp}$[9]

$$2MW^{\mu\nu}(q,P,S,P_1,P_2) = 32z\ \mathrm{Tr}\left[\Phi(x,S)\,\gamma^{\mu}\,\Delta(z,\zeta,M_h^2,\phi_{R\perp})\,\gamma^{\nu}\right], \tag{2.77a}$$

$$\Delta(z,\zeta,M_h^2,\phi_{R\perp}) \equiv \frac{z}{32}\int \mathrm{d}\,k^+\ \mathrm{d}^2\boldsymbol{k}_T\,\Delta(k,P_h,R)\Big|_{k^-=P_h^-/z}. \tag{2.77b}$$

Respecting Hermiticity and parity invariance, we can extract the leading twist projection:

$$\mathcal{P}_-\,\Delta(z,\zeta,M_h^2,\phi_{R\perp})\,\gamma^- = \frac{1}{8\pi}\left(D_1(z,\zeta,M_h^2) + i\,H_1^{\sphericalangle}(z,\zeta,M_h^2)\,\frac{\not{R}_T}{M_h}\right)\mathcal{P}_-\,, \tag{2.78}$$

The introduced two–hadron fragmentation functions $H_1^{\sphericalangle}(z,\zeta,M_h^2)$[10] does not require the partonic transverse momentum. The conceptual descriptions about the two–hadron fragmentation functions are illustrated in Figure 2.21. For the case that the correlation functions Φ and Δ with dependence on transverse momentum, the equations are depicted in Appendix B.

2.4.2 Cross Sections and Asymmetries

By inserting the distribution function Eq. (2.43) and the two–hadron fragmentation function Eq. (2.78) into the hadronic tensor Eq. (2.75), the cross section of the two–hadron

---

[9] For the case with the transverse momentum $\boldsymbol{P}_{h\perp}$ dependence, the decompositions of the correlation functions are introduced in Appendix B.

[10] The superscript $\sphericalangle$ indicates that the two hadron momenta must not be parallel, but rather separated by a certain angle.

semi–inclusive DIS can be expressed at leading twist as [78]:

$$\frac{\mathrm{d}^7\sigma}{\mathrm{d}\,\zeta\;\mathrm{d}\,M_h^2\;\mathrm{d}\,\phi_{R\perp}\;\mathrm{d}\,z_h\;\mathrm{d}\,x\;\mathrm{d}\,y\;\mathrm{d}\,\phi_S} = \frac{2\alpha^2}{4\pi s x y^2}\sum_q e_q^2\Bigg[A(y)\,f_1^q(x)D_1^q(z,\zeta,M_h^2)$$
$$+\,\lambda_e\,S_L\,C(y)\,\mathrm{g}_1^q(x)D_1^q(z,\zeta,M_h^2) - B(y)\,|\boldsymbol{S}_\perp|\,\frac{|\boldsymbol{R}_T|}{M_h}\,\sin(\phi_{R\perp}+\phi_S)\,h_1^q(x)H_1^{\sphericalangle q}(z,\zeta,M_h^2)\Bigg]. \tag{2.79}$$

where $A(y)$ and $B(y)$ are defined in Eq. (2.66) and

$$C(y) = y(1-\frac{y}{2}) \tag{2.80}$$

are purely kinematic functions. The sub–leading twist expression can be found in Ref. [122].

The hadronization of a transversely polarized quark into the hadron pair can depend on the mixed product $\boldsymbol{S}_q\cdot(\boldsymbol{p}_q\times\boldsymbol{R})$, where $\boldsymbol{p}_q$ is the momentum of the struck quark, and $\boldsymbol{S}_q$ is its spin. This would imply a preference of h_1 to go to a specific side with respect to the spin and the momentum direction of the quark, while h_2 would go to the opposite side. This preference is revealed in the cross section (2.79) through a dependence on the angle $\phi_{R\perp}$ even after the integration over the transverse momentum component $\boldsymbol{P_{h\perp}}$. The benefits of integrating over $\boldsymbol{P_{h\perp}}$ are the following:

- issues related to factorization are simpler [123],
- the evolution equations for the fragmentation functions involved are known [124, 125] (as shown in Figure 2.27 and Figure 2.28),
- distribution and fragmentation functions appear in a simple product instead of a convolution integral over transverse momentum.

In analogy to the one–hadron asymmetry definition in Eq. (2.67), the single target spin asymmetry [116] in the two–hadron DIS process can be defined as[11]:

$$A_{\mathrm{UT}} = \frac{1}{|\boldsymbol{S_T}|}\frac{\sigma_{\mathrm{UT}}}{\sigma_{\mathrm{UU}}}. \tag{2.81}$$

The amplitude $A_{\mathrm{UT}}^{\sin(\phi_{R\perp}+\phi_S)}$ and the azimuthal moment $\langle\sin(\phi_{R\perp}+\phi_S)\rangle_{\mathrm{UT}}$ is defined as

$$\begin{aligned} A_{\mathrm{UT}}^{\sin(\phi_{R\perp}+\phi_S)} \equiv 2\,\langle\sin(\phi_{R\perp}+\phi_S)\rangle_{\mathrm{UT}} &\equiv \frac{2}{|\boldsymbol{S}_T|}\frac{\int \mathrm{d}\phi_S\;\mathrm{d}\phi_{R\perp}\;\sin(\phi_{R\perp}+\phi_S)\;\mathrm{d}^7\sigma_{\mathrm{UT}}}{\int \mathrm{d}\phi_S\;\mathrm{d}\phi_{R\perp}\;\mathrm{d}^7\sigma_{\mathrm{UU}}} \\ &= \frac{-\,B(y)\,\sum_q e_q^2\,h_1^q(x)\,\dfrac{|\boldsymbol{R}_T|}{2M_h}\,H_1^{\sphericalangle q}(z,\zeta,M_h^2)}{A(y)\,\sum_q e_q^2\,f_1^q(x)\,D_1^q(z,\zeta,M_h^2)}\;. \end{aligned} \tag{2.82}$$

---

[11] From an experimental point of view, the “longitudinal” and “transverse” are in reference to the lepton beam axis. From a theoretical point of view, it is simpler to refer to the direction of motion of the virtual photon. For the two–hadron semi–inclusive DIS at HERMES, the angle between the photon axis and the lepton beam are so small [121] that their difference can be neglected in this work.

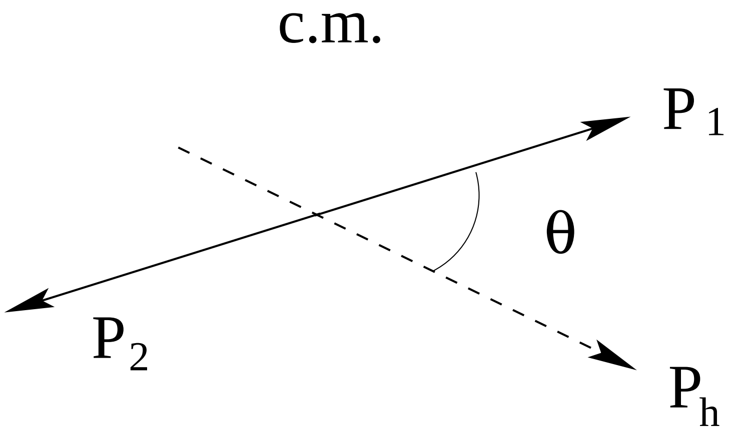

Figure 2.22: Description of the polar angle θ in the frame of center–of–mass of two–hadron pair. The polar angle θ is defined as the angle between the positive hadron P_1 and the direction of P_h, which is defined in Figure 2.19.

The cross section Eq. (2.79) is the products of the three hadron distribution functions (*i.e.*, f_1, g_1 and h_1) and the corresponding dihadron fragmentation functions. We can probe the transversity by measuring the $\sin(\phi_{R\perp} + \phi_S)$ dependence amplitude.

2.4.3 Partial Wave Expansion

It is helpful to study the inner structure of the dihadron fragmentation. For the hadron pair, it is useful to expand them in partial waves. Because the hadron pairs are almost in the system of low invariant masses, the dominant distribution come only from the lowest harmonics, *i.e.*, s and p waves. We have to do the expansion in terms of the polar angle θ in the center–of–mass (c.m.) frame of the hadron pair (see Figure 2.22). So the dihadron fragmentation function can be expanded in terms of Legendre polynomials in θ [126].

In the c.m. frame of two–hadron system, the variable ζ is linearly dependent on the center–of–mass variable $\cos\theta$ in the following way:

$$\zeta \equiv \frac{2R^-}{P_h^-} \overset{\mathrm{cm}}{=} \frac{1}{M_h}\left(\sqrt{M_1^2 + |\boldsymbol{R}|^2} - \sqrt{M_2^2 + |\boldsymbol{R}|^2} - 2|\boldsymbol{R}|\cos\theta\right). \tag{2.83}$$

where

$$|\boldsymbol{R}| = \frac{1}{2}\sqrt{M_h^2 - 2\left(M_1^2 + M_2^2\right) + \left(M_1^2 - M_2^2\right)^2 \Big/ M_h^2}. \tag{2.84}$$

If $M_1 = M_2$, notice that R is purely space–like and

$$|\boldsymbol{R}| = -|R| = \frac{1}{2}\sqrt{M_h^2 - 4M_1^2}, \qquad \zeta = -\frac{1}{M_h}\sqrt{M_h^2 - 4M_1^2}\,\cos\theta. \tag{2.85}$$

In the two–hadron systems with a low invariant mass (generally below $M_h \approx 1$ GeV), the pair can be assumed to be produced mainly in the relative s–wave channel, with a typical smooth distribution, or in the p–wave channel with a Breit–Wigner profile [127]. Therefore, it is safe to truncate the expansion and include only s–wave and p–wave contributions to the correlation function. The connection between the correlation function Δ in terms of the variable ζ and in terms of the variable $\cos\theta$ is

$$\Delta(z, \cos\theta, M_h^2, \phi_{R\perp}) = \frac{2|\boldsymbol{R}|}{M_h}\, \Delta(z, \zeta, M_h^2, \phi_{R\perp}), \tag{2.86}$$

to take into account the fact that $\mathrm{d}\,\zeta = 2|\boldsymbol{R}|/M_h\ \mathrm{d}\cos\theta$. Therefore [126],

$$\begin{aligned} &\mathcal{P}_-\Delta(z, \cos\theta, M_h^2, \phi_{R\perp})\gamma^- \\ =\ & \frac{2|\boldsymbol{R}|}{8\pi M_h}\left(D_1\big(z, \zeta(\cos\theta), M_h^2\big) + iH_1^{\sphericalangle}\big(z, \zeta(\cos\theta), M_h^2\big)\frac{|\boldsymbol{R}|}{M_h}\sin\theta \not{n}_{\phi_R}\right)\mathcal{P}_-\ , \end{aligned} \tag{2.87}$$

where $\not{n}_{\phi_R} = (0, 0, \cos\phi_R, \sin\phi_R)$.

We can write the partial wave expanded dihadron fragmentation functions as

$$\begin{aligned} \frac{2|\boldsymbol{R}|}{M_h} D_1(z, \zeta(\cos\theta), M_h^2) &= D_{1,UU}(z, M_h^2) + D_{1,UL}^{sp}(z, M_h^2)\cos\theta \\ &\quad + D_{1,LL}^{pp}(z, M_h^2)\frac{1}{4}(3\cos^2\theta - 1), \end{aligned} \tag{2.88}$$

$$\frac{2|\boldsymbol{R}|}{M_h} H_1^{\sphericalangle}(z, \zeta(\cos\theta), M_h^2) = H_{1,UT}^{\sphericalangle,sp}(z, M_h^2) + H_{1,LT}^{\sphericalangle,pp}(z, M_h^2)\cos\theta. \tag{2.89}$$

The subscripts U, L and T refer, respectively, to the hadron pair being unpolarized, longitudinally polarized and transversely polarized. This polarization refers directly to the θ–dependent factors, which appear in Eqs. (2.88) and (2.89). The function $H_{1,UT}^{\sphericalangle,sp}$ describes the interference between a pion pair produced in a relative s–wave and a pion pair in a relative p–wave. The function $H_{1,LT}^{\sphericalangle,pp}$ relates to the interference between two pion pairs which are both in relative p–waves, but which are polarized differently. The fragmentation functions in Eqs. (2.88) or (2.89) is often called dihadron fragmentation function (DiFF) or interference fragmentation function (IFF), and written without the superscript or the subscript, as they are directly related.

Aubert et al. [127] also derive out the positivity bounds of the dihadron fragmentation functions:

$$D_{1,UU}^{ss}(z, M_h^2) \geq 0, \tag{2.90a}$$

$$D_{1,UU}^{pp}(z, M_h^2) \geq 0, \tag{2.90b}$$

$$-\frac{3}{2}\, D_{1,UU}^{pp}(z, M_h^2) \leq D_{1,LL}^{pp}(z, M_h^2) \leq 3\, D_{1,UU}^{pp}(z, M_h^2), \tag{2.90c}$$

while from the positivity of the two–dimensional minors we obtain

$$\left|D_{1,UL}^{sp}\right| \leq \sqrt{\frac{3}{4}\,D_{1,UU}^{ss}\left(D_{1,UU}^{pp}+\frac{2}{3}\,D_{1,LL}^{pp}\right)} \leq \frac{3}{2}\,D_{1,UU}, \tag{2.91a}$$

$$\frac{|\boldsymbol{R}|}{M_h}\left|H_{1,UT}^{\sphericalangle\, sp}\right| \leq \sqrt{\frac{3}{8}\,D_{1,UU}^{ss}\left(D_{1,UU}^{pp}-\frac{1}{3}\,D_{1,LL}^{pp}\right)} \leq \frac{3}{2}\,D_{1,UU}, \tag{2.91b}$$

$$\frac{|\boldsymbol{R}|}{M_h}\left|H_{1,LT}^{\sphericalangle pp}\right| \leq \frac{3}{2\sqrt{2}}\sqrt{\left(D_{1,UU}^{pp}+\frac{2}{3}\,D_{1,LL}^{pp}\right)\left(D_{1,UU}^{pp}-\frac{1}{3}\,D_{1,LL}^{pp}\right)} \leq \frac{9}{8}\,D_{1,UU}. \tag{2.91c}$$

Using the partial wave expansion, the unpolarized and polarized cross section (as defined in Eq. (2.63) can be written as[12]

$$\begin{aligned}\frac{\mathrm{d}^7\sigma_{\mathrm{UU}}}{\mathrm{d}\cos\theta\ \mathrm{d}\,M_h^2\ \mathrm{d}\,\phi_{R\perp}\ \mathrm{d}\,z\ \mathrm{d}\,x\ \mathrm{d}\,y\ \mathrm{d}\,\phi_S} &= \sum_q \frac{\alpha^2 e_q^2}{2\pi s x y^2}\,A(y)\,f_1(x) \\ &\times\left(D_{1,UU}\big(z,M_h^2\big)+\cos\theta\,D_{1,UL}^{sp}\big(z,M_h^2\big)+\frac{1}{4}\big(3\cos^2\theta-1\big)\,D_{1,LL}^{pp}\big(z,M_h^2\big)\right)\end{aligned} \tag{2.92a}$$

$$\begin{aligned}\frac{\mathrm{d}^7\sigma_{\mathrm{UT}}}{\mathrm{d}\cos\theta\ \mathrm{d}\,M_h^2\ \mathrm{d}\,\phi_{R\perp}\ \mathrm{d}\,z\ \mathrm{d}\,x\ \mathrm{d}\,y\ \mathrm{d}\,\phi_S} &= \sum_q \frac{\alpha^2 e_q^2}{2\pi s x y^2}\,B(y)\,|\boldsymbol{S}_\perp|\,\frac{|\boldsymbol{R}|}{M_h} \\ &\times\sin(\phi_{R\perp}+\phi_S)\,\sin\theta\,h_1(x)\left(H_{1,UT}^{\sphericalangle\, sp}\big(z,M_h^2\big)+\cos\theta\,H_{1,LT}^{\sphericalangle pp}\big(z,M_h^2\big)\right).\end{aligned} \tag{2.92b}$$

From the partial wave analysis we see that the transversity distribution can be matched with two different chiral–odd, T–odd fragmentation functions [78], one pertaining to the interference between the s– and p–wave channels of two–hadron production, the second being a purely p–wave effect. To select the contributions from the two parts, one can use the orthogonality of Legendre polynomials to define the following two amplitudes:

$$\begin{aligned}A_{\mathrm{UT}}^{\sin(\phi_{R\perp}+\phi_S)\sin\theta} &\equiv \frac{2}{|\boldsymbol{S_T}|}\frac{\int \mathrm{d}\cos\theta\ \mathrm{d}\,\phi_{R\perp}\ \mathrm{d}\,\phi_S \sin(\phi_{R\perp}+\phi_S)(\,\mathrm{d}^7\,\sigma_{\mathrm{UT}}/\sin\theta)}{\int \mathrm{d}\cos\theta\ \mathrm{d}\,\phi_{R\perp}\ \mathrm{d}\,\phi_S\ \mathrm{d}^7\,\sigma_{\mathrm{UU}}} \\ &= -\frac{B(y)}{A(y)}\frac{|\boldsymbol{R}|}{M_h}\frac{\sum_q e_q^2 h_1(x) H_1^{\sphericalangle,sp}(z,M_h^2)}{\sum_q e_q^2 f_1(x) D_1(z,M_h^2)},\end{aligned} \tag{2.93}$$

and

$$\begin{aligned}A_{\mathrm{UT}}^{\sin(\phi_{R\perp}+\phi_S)\sin 2\theta} &\equiv \frac{3}{|\boldsymbol{S_T}|}\frac{\int \mathrm{d}\cos\theta\ \mathrm{d}\,\phi_{R\perp}\ \mathrm{d}\,\phi_S \sin(\phi_{R\perp}+\phi_S)\cos\theta(\,\mathrm{d}^7\,\sigma_{\mathrm{UT}}/\sin\theta)}{\int \mathrm{d}\cos\theta\ \mathrm{d}\,\phi_{R\perp}\ \mathrm{d}\,\phi_S\ \mathrm{d}^7\,\sigma_{\mathrm{UU}}} \\ &= -\frac{B(y)}{A(y)}\frac{|\boldsymbol{R}|}{M_h}\frac{\sum_q e_q^2 h_1(x) H_1^{\sphericalangle,pp}(z,M_h^2)}{\sum_q e_q^2 f_1(x) D_1(z,M_h^2)},\end{aligned} \tag{2.94}$$

---

[12] In some places in this thesis, the flavor notations q in the distribution function and the fragmentation function are omitted when summing over different quark flavors.

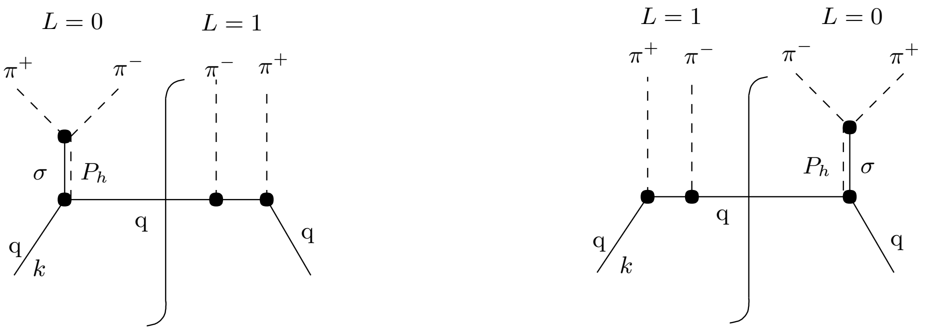

Figure 2.23: The diagrams of the interference occurs between a σ resonance (s–wave) and a p–wave background, as evaluated in the model of Ref. [115].

where the factors 2 and 3 are implemented such that the amplitudes have values in between -1 and 1 [121], in agreement with the Trento Conventions [53]. Here the subscripts in the dihadron fragmentation function symbols were skipped. These amplitudes are directly proportional to $h_1(x)$. It thus shows the potential to determine transversity through two–hadron semi–inclusive DIS measurements. Different from the amplitudes in Eq. (2.93), the amplitude in Eq. (2.82) is calculated by separately integrating the numerator and the denominator of Eq. (2.81) over $\cos\theta$. The involved dihadron fragmentation functions are also different. Eq. (2.82) is proportional to $H_1^{\sphericalangle}$ and Eq. (2.93) is proportional to $H_1^{\sphericalangle,sp}$. The relation will hold as

$$A_{\mathrm{UT}}^{\sin(\phi_{R\perp}+\phi_S)}(x,y,z,M_h^2) = \frac{\pi}{4} A_{\mathrm{UT}}^{\sin(\phi_{R\perp}+\phi_S)\sin\theta}(x,y,z,M_h^2). \tag{2.95}$$

In the work presented in this thesis, the amplitude $A_{\mathrm{UT}}^{\sin(\phi_{R\perp}+\phi_S)\sin\theta}$ can be extracted from HERMES experimental data. The theoretical consideration about its behavior will be outlined in next section.

2.4.4 Theoretical Model Prediction

From the theoretical point of view, it is important to understand the mechanism of the fragmentation of two–hadron production. First considerations on the dihadron fragmentation function are for the unpolarized cases, which focused on the probability of producing two hadrons with energy fractions z_1 and z_2 by integrating over the invariant mass of the produced pair [123, 128–132]. The experimental results about invariant mass spectra of hadron pairs produced in e^+e^- annihilation, semi–inclusive DIS and proton–proton collisions, were used to verify the unpolarized dihadron fragmentation function.

The polarized dihadron fragmentation function were also studied, mainly focused on the dihadron fragmentation function $H_1^{\sphericalangle sp}$. It arises from the interference between a pion pair produced in a relative s–wave and a pion pair produced in a relative p–wave. The earliest model calculation [115] used the Linear Sigma model to describe the polarized quark–pion interactions. In this model the interfering channels are a narrow s–wave σ resonance and a p–wave background as shown in Figure 2.23. The results has demonstrated the existence of a non–vanishing asymmetry of Eq. (2.81). But the model should only be considered to give crude qualitative information because this model only includes the simplest fragmentation of a quark to two pions which might magnify the predicted asymmetries. Anyway this work showed the large asymmetries and the spin correlation can be completely unsuppressed.

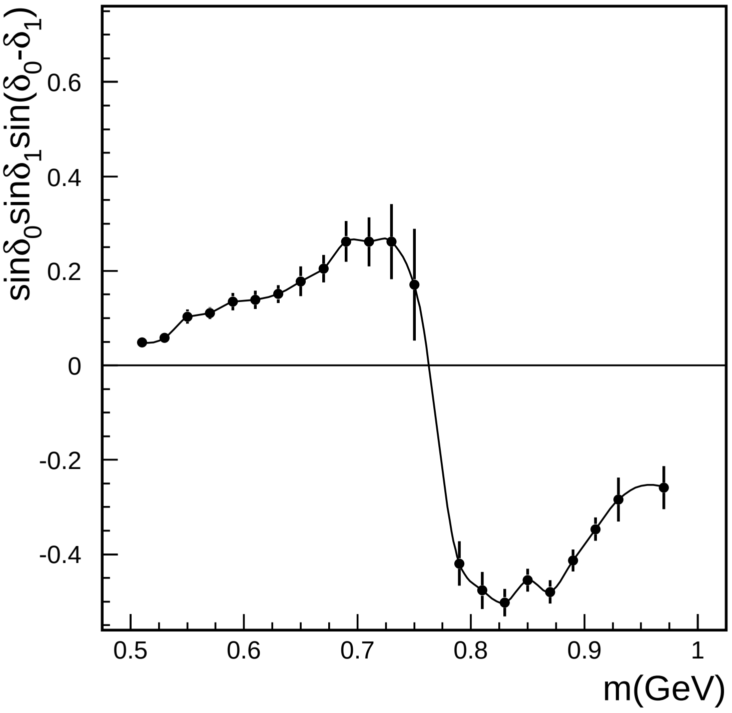

Figure 2.24: The phase factor $\sin\delta_0 \sin\delta_1 \sin(\delta_0 - \delta_1)$ with the invariant mass dependence.

The model [111, 112] considers the interference between the ρ^0 and the σ resonance, which can be measured in $\pi^+\pi^-$ scattering. The relative phases between the relative s–wave $|h\rangle$ and p–wave $|h'\rangle$ in the final state $|h_1 h_2\rangle$ was used, *i.e.*,

$$|h_1 h_2, X\rangle = e^{i\delta_0}|h, X\rangle + e^{i\delta_1}|h', X\rangle, \tag{2.96}$$

where δ_0 and δ_1 are relative phases. Thus the fragmentation function $H_1^{\sphericalangle,sp}$ can be written as

$$H_1^{\sphericalangle,sp}(z, M_h^2) = \sin\delta_0 \sin\delta_1 \sin(\delta_0 - \delta_1) H_1^{\sphericalangle,sp'}(z, M_h^2), \tag{2.97}$$

where the phases δ_0 and δ_1 depend on the invariant mass M_h. The single transverse target spin asymmetry as defined in Eq. (2.81) is directly proportional to the phase shifts $\sin\delta_0 \sin\delta_1 \sin(\delta_0 - \delta_1)$. It has a dependence on the hadron pair invariant mass M_h. These

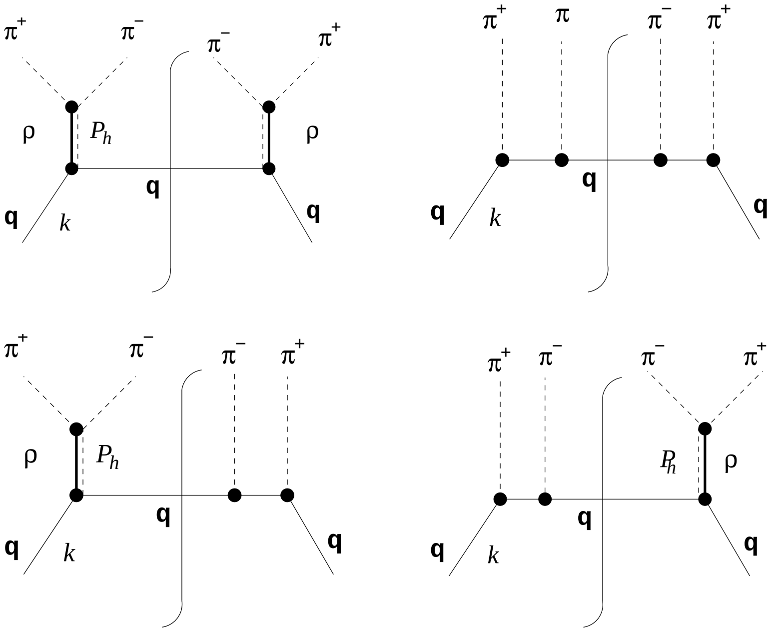

Figure 2.25: The diagrams considered for the quark fragmentation into $\pi^+\pi^-$ at leading twist and leading order in α_s in the context of the spectator model.

phases were measured [133] in a pion–nucleon scattering experiment ($\pi N \rightarrow \pi\pi N$). The phase factor $\sin\delta_0 \sin\delta_1 \sin(\delta_0 - \delta_1)$ as obtained from the experiment is shown in Figure 2.24, It predicts that the asymmetry relating to the two–pion dihadron fragmentation function $H_1^{\sphericalangle sp}$ will have a strong invariant mass dependence around the $\rho^0(770)$ resonance: a sign change around the $\rho^0(770)$ spectrum peak. But this model does not predict the exact size or sign of the asymmetry.

Radici, Jakob and Bianconi [116] proposed to calculate the interference fragmentation in the spectator model, where they neglect the contributions from the σ and assume the s–wave amplitude of the spectrum to be real. The basic idea of the spectator model is to make an ansatz for the decomposition of the quark–quark correlator function by replacing the sum with an effective spectator state with a definite mass and quantum numbers [90, 114, 134, 135]. By specializing the model to the case of $\pi^+\pi^-$ fragmentation with $P_1 = P_{\pi^+}$ and $P_2 = P_{\pi^-}$, the spectator has the quantum numbers of an on–shell valence quark with a constituent mass $m_q = 340\,\mathrm{MeV}$. By considering the interference between the ρ^0 resonance and a s–wave background as shown in the interference diagram Figure 2.25, one can obtain the amplitude $A_{\mathrm{UT}}^{\sin(\phi_{R\perp}+\phi_S)}$ as a function of Bjorken–x and the invariant mass M_h of the two–pion system. The different curves drawn in Figure 2.26 stands for the different theoretical predictions on the distribution functions and the fragmentation functions: The solid and dashed lines refer to the weaker or stronger $q\rho q$ couplings in

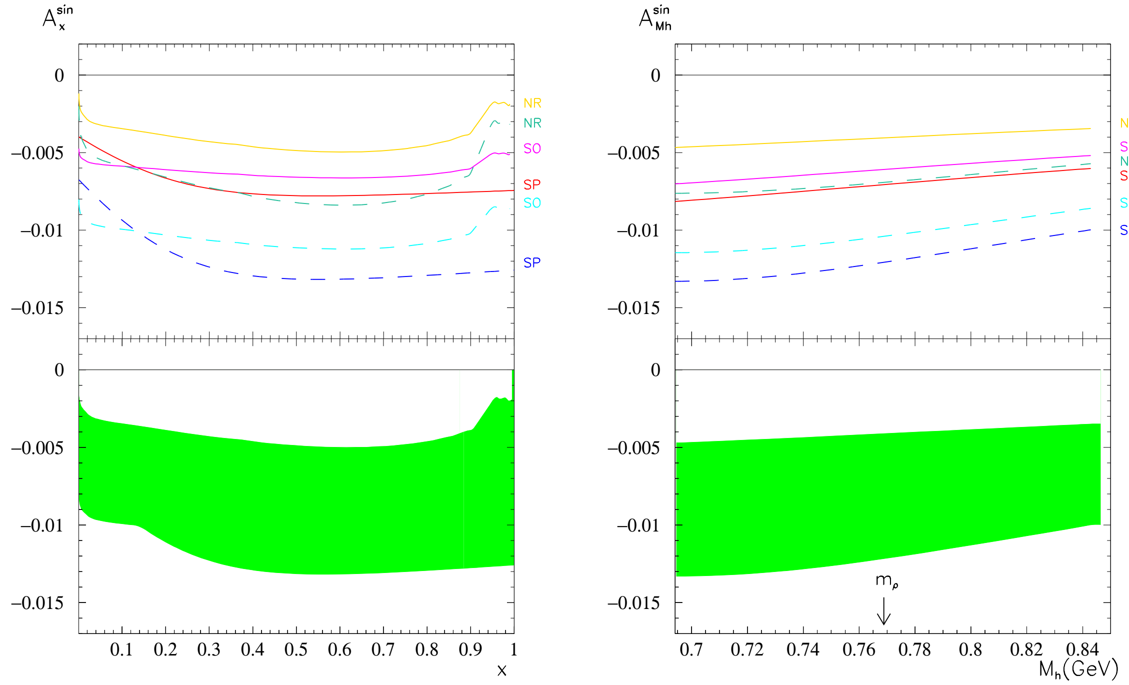

(a) (b)

Figure 2.26: The amplitude $A_{\mathrm{UT}}^{\sin(\phi_{R\perp}+\phi_S)}$ obtained from the model of Ref. [116].

the FF, respectively. For each parametrization, three different choices of DF are shown. The label SP refers to the DF calculated in the spectator model [90]. The label NR indicates that f_1 and g_1 are taken consistently from the leading–order parameterizations of Ref. [136] and Ref. [137], respectively, with $h_1 = g_1$. The label SO indicates the same parameterization but with the Soffer inequality saturated, *i.e.*, $h_1 = (f_1 + g_1)/2$. In the lower plot of each figure in Figure 2.26 the “uncertainty band” is shown as a guiding line. This amplitude needs to be multiplied by -1 in order to be consistent with the Trento Conventions [53]. In this model, the dihadron fragmentation function is almost proportional to the imaginary part of the ρ^0 resonance, *i.e.*, a Breit–Wigner peaked at the ρ^0 mass. Hence, it does not predict the sign change of the amplitude around ρ^0 mass, which is contrary to what Ref. [111] suggested,

Bacchetta and Radici presented a new model, similar to “spectator” model, for the dihadron fragmentation functions [117]. They tuned the parameters of their model to the output of the PYTHIA event generator for the two–hadron semi–inclusive DIS production at HERMES kinematics. By doing so, they can fix the parameters of the model and make predictions for other unknown fragmentation functions (*e.g.*, the unpolarized dihadron fragmentation function shown in Figure 2.27 and the polarized dihadron fragmentation

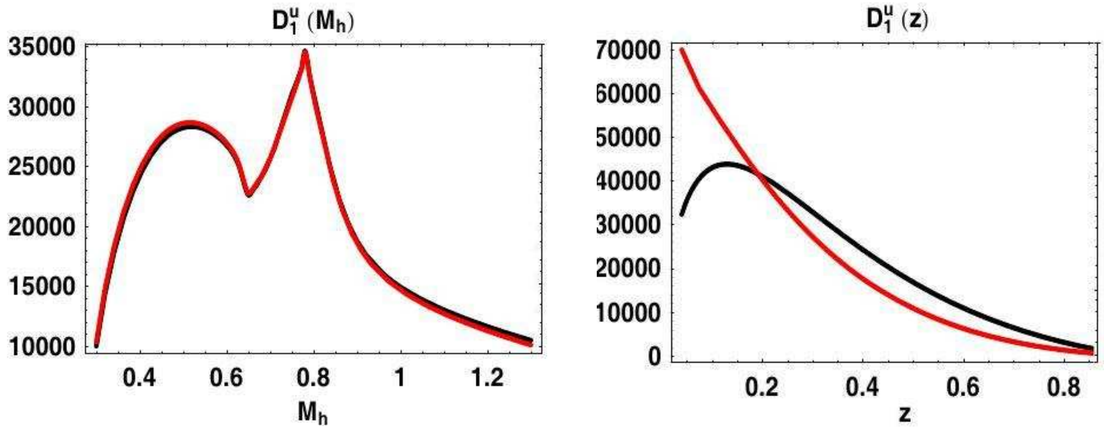

Figure 2.27: The unpolarized u quark dihadron fragmentation functions predicted by Ref. [117] at different Q^2 [125], as a function of M_h and z. $Q^2 = 2.5\,\mathrm{GeV}^2$ (black line) corresponds to the HERMES kinematics and $Q^2 = 100\,\mathrm{GeV}^2$ (red line) to the Belle kinematics.

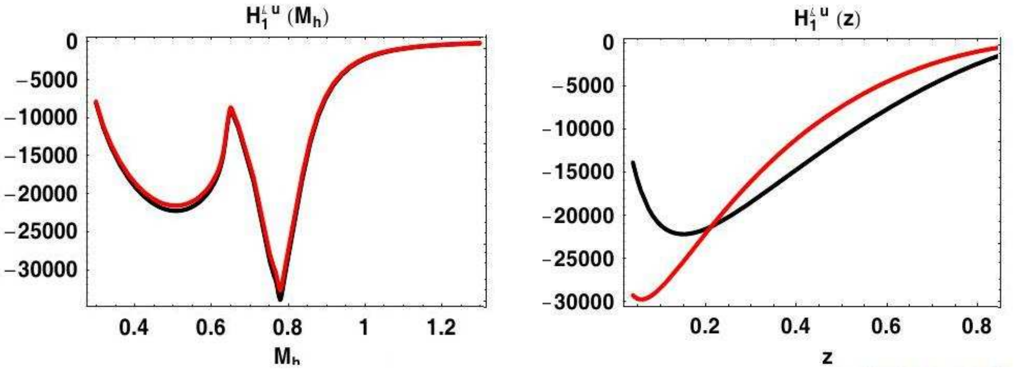

Figure 2.28: The polarized u quark dihadron fragmentation functions predicted by Ref. [117] at different Q^2 [125], as a function of M_h and z. $Q^2 = 2.5\,\mathrm{GeV}^2$ (black line) corresponds to the HERMES kinematics and $Q^2 = 100\,\mathrm{GeV}^2$ (red line) to the Belle kinematics.

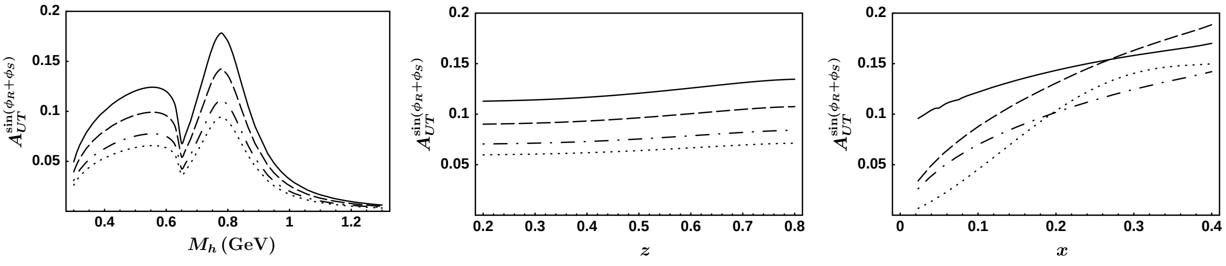

Figure 2.29: The amplitude $A_{\mathrm{UT}}^{\sin(\phi_{R\perp}+\phi_S)}$ as calculated in Ref. [117] versus $M_{\pi\pi}$, x and z. calculated for HERMES kinematics. The different lines correspond to different models of the transversity distribution function: dotted lines from Ref. [100], dash–dotted line from Ref. [99], dashed line from Ref [86], and solid line from Ref. [98].

function shown in Figure 2.28). With the isospin symmetry assumption, the unpolarized dihadron fragmentation function and the polarized dihadron fragmentation function for the different quark flavor are:

$$D_1^{\triangleleft,u} = D_1^{\triangleleft,\bar{u}} = D_1^{\triangleleft,d} = D_1^{\triangleleft,\bar{d}}, \tag{2.98}$$

$$H_1^{\triangleleft,u} = H_1^{\triangleleft,\bar{u}} = H_1^{\triangleleft,d} = H_1^{\triangleleft,\bar{d}}. \tag{2.99}$$

For a single–spin asymmetry in the azimuthal distribution of $\pi^+\pi^-$ pairs in semi–inclusive measurement of DIS on a transversely polarized proton and deuteron targets at HERMES and COMPASS experiments, the model predicted the amplitude $A_{\mathrm{UT}}^{\sin(\phi_{R\perp}+\phi_S)}$ which depends on the invariant mass M_h, Bjorken–x and z. In Figure 2.29 the predicted asymmetry amplitudes for the proton target at HERMES kinematics were plotted. In this model, the fragmentation function is almost proportional to the imaginary part of the p wave, *i.e.*, it has peaks at the ρ^0 mass and around 0.5 GeV, because the imaginary part of the ω resonance is also taken into account: the $\omega \to 3\pi$ channel. This gives rise to an additional contribution to the fragmentation function in the region around $M_{\pi\pi} \approx 0.5\,\mathrm{GeV}$, which explains the strong dependence on the invariant mass. This model does not predict the sign of the amplitude and uses the sign of the HERMES data as presented in Chapter 4 as input. The predicted deuteron target asymmetry amplitudes are only 10% of those on the proton target. Based on this dihadron fragmentation function model, Ref. [138] also made predictions of the same behavior (*e.g.*, see Figure 2.30) for the transversely polarized proton, deuteron and neutron targets at HERMES and COMPASS kinematics, Here different transversity distribution functions from SU(6) quark–diquark model [139] and pQCD based counting rules [140] were used. The shapes and sizes of the predicted asymmetry amplitudes are almost at the same level, even for the different transversity distribution models. This means that the asymmetry amplitudes will be determined mainly

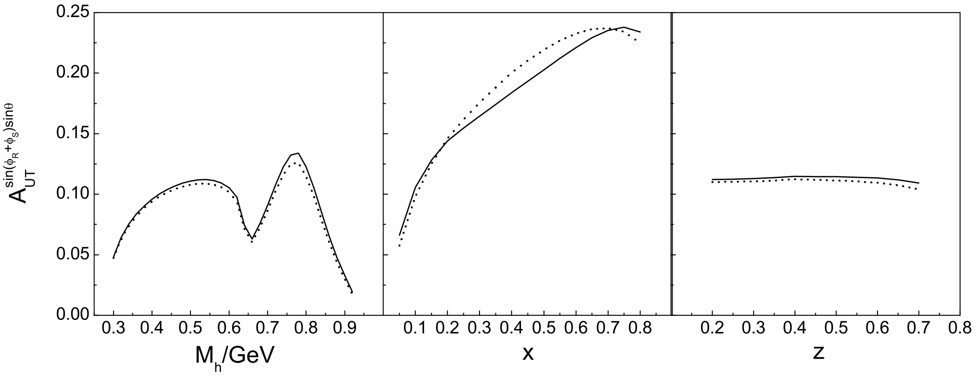

Figure 2.30: $A_{\mathrm{UT}}^{\sin(\phi_{R\perp}+\phi_S)\sin\theta}$ predicted by Ref. [138] at HERMES kinematics for a transversely polarized proton target as a function of M_h, x and z respectively. The solid lines and dotted lines correspond to the results evaluated from SU(6) quark–diquark model [139] and pQCD based counting rules [140], respectively.

by the dihadron fragmentation function. The predicted amplitudes in Figure 2.30 and Figure 2.29 correspond to the asymmetry amplitudes in Eq. (2.93) and Eq. (2.82), respectively. Their relative sizes should follow the relation of Eq. (2.95). The evolution of the dihadron fragmentation function were studied in Ref. [124, 125], which is essential to connect the experimental data among different kinematics in different experiments.

2.5 Summary

In the theoretical framework, this chapter briefly introduced the transversity distribution in Sec. 2.1 and Sec. 2.2, and also the related fragmentation functions in semi–inclusive measurement of deep inelastic scattering process. The property of transversity was emphasized in Sec. 2.2, which was followed by the Sec. 2.3 and Sec. 2.4. Theoretical explanation on why and how the processes of one–hadron and two–hadron semi–inclusive DIS can access this less known distribution function was given. Since in the analysis in this thesis we used the two–hadron semi–inclusive DIS process to measure transversity, the dihadron fragmentation functions were specially treated in more details, including partial wave expansion and model predictions. The amplitude $A_{\mathrm{UT}}^{\sin(\phi_{R\perp}+\phi_S)\sin\theta}$ of the single transverse target–spin asymmetry A_{UT} in Eq. (2.93) involves the transversity and the s–p wave interference dihadron fragmentation function. It has been demonstrated to potentially give substantially nonzero effects. Due to the large differences between the different models, it is important to actually measure this physics quantity and test the theoretical models. The extraction of the amplitude $A_{\mathrm{UT}}^{\sin(\phi_{R\perp}+\phi_S)\sin\theta}$ from the HERMES measurements will be discussed in Chapters 4 and 5.

Chapter 3

The HERMES Experiment

The HERMES experiment (**HERA** **ME**asurement of **S**pin) is a polarized deep inelastic scattering (DIS) experiment to study the spin structure of the nucleon. It ran at the HERA (**H**adron **E**lectron **R**ing **A**ccelerator) storage ring at DESY (**D**eutsches **E**lektronen-**SY**nchrotron) in Hamburg, Germany [1] from 1995 to 2007. Equipped with a forward spectrometer with a good particle identification in wide momentum range and a good tracking resolution, the atomic gas target unpolarized or transversely/longitudinally polarized, and the longitudinally polarized positrons or electrons from HERA, HERMES can access the full aspects of the nucleon structure with good precision. These various indispensable components in this experiment are described in the following, especially those parts relating with the work in this thesis. A laser–based Gain Monitoring System (GMS) for which I worked is also described in detail.

3.1 The HERA $e^{\pm}$ Storage Beam

HERA had two storage rings sharing an underground tunnel with a circumference of 6.3 km. A lepton beam and a proton beam can be accelerated to 27.5 GeV and 920 GeV respectively and stored. The HERA lepton storage ring can be filled with either electrons or positrons with momentum 27.5 GeV. HERA was the world's first high energy electron/positron storage ring which achieved longitudinal polarization. The physics processes are the same for positrons and electrons in most cases. So the term ”positron” will be used for both in this thesis. Both beams in two storage rings were brought into collision in two colliding experiments H1 and ZEUS (see Figure 3.1). The HERA–B experiment used only the proton beam until the year 2003 and the HERMES experiment used only the positron beam in all the period.

A small spin dependence of the emission probability of synchrotron radiation from charged particles enhances the population of the spin states of positions aligned and elec-

---

[1] HERA was an *e*-*p* collider but only the *e* beam is used by HERMES.

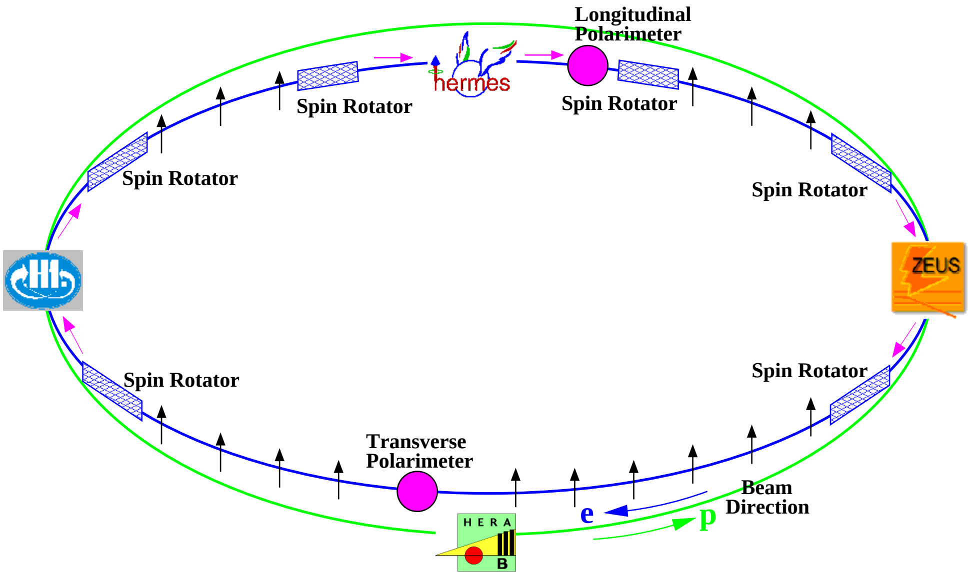

Figure 3.1: Schematic diagram of the HERA accelerator layout from 2001-2007 with the location of the four experiments. Also shown are the locations of the spin-rotators and the two polarimeters.

trons anti–aligned to the bending magnetic field [141]. This effect is called Sokolov–Ternov effect [142]. The positron beam in the high energy storage ring becomes transversely self–polarized. However, the direction of the beam polarization has to be longitudinal (*i.e.*, right– or left–handed) in order to be able to probe the basic asymmetries between the right– and left–handed quarks in the nucleons. The transverse polarization of the beam can be rotated into the longitudinal direction. Such a rotation was performed by a spin rotator consisting of interleaved horizontal and vertical bending magnets [143]. As shown in Figure 3.1, six spin rotators were installed up– and downstream for three experiments[2]. The upstream[3] spin rotator rotated the direction of the beam polarization into the beam direction, while the downstream one rotated the direction of the beam polarization back into the vertical direction.

The polarization was zero initially after injection and increases with time according to

$$P(t) = P_{max} \cdot (1 - e^{-t/\tau}), \tag{3.1}$$

$$P_{max} = \frac{8}{5\sqrt{3}}, \tag{3.2}$$

where P_{max} is the maximum polarization value in an ideal case, τ is a variable which

---

[2] Before 2001, there were only two spin rotators locating at the two sides of HERMES experiment.

[3] Upstream and downstream here mean with respect to the HERA positron beam direction.

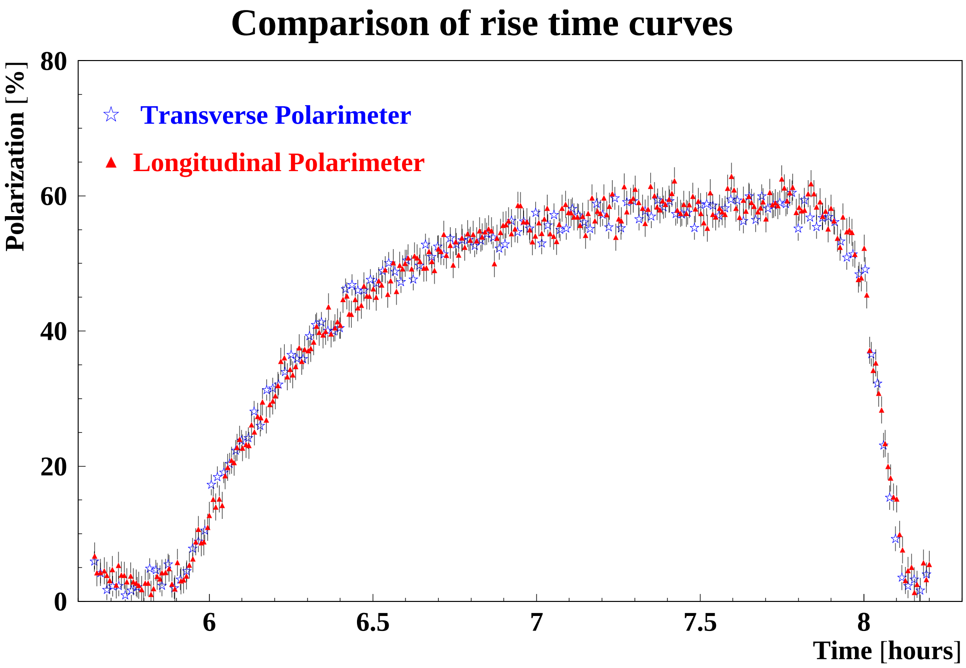

Figure 3.2: Comparison of risetime curve of transverse and longitudinal polarimeter.

accounts for the ring radius and the energy of the beam. Figure 3.2 shows time dependence of the measured beam polarization. As can be seen, the polarization rose up to 60 % in an hour.

Two polarimeters were installed to measure the beam polarization based on the spin dependence in Compton scattering of circularly polarized photons on positrons. The **longitudinal** polarimeter was located between the spin rotators close to the HERMES experiment. It measured the asymmetry in energy of the back–scattered photons between two helicity states of a laser beam [144]. The **transverse** polarimeter was located in the opposite position as shown in Figure 3.1. It measured the up–down spatial asymmetry of the back–scattered photons with respect to the orbital plane of the positrons for the two helicity states of a laser beam [145]. As we can see from Figure 3.2, the two polarimeters showed the consistent results. The beam polarization was typically greater than 50 % in the later years of the experiment, attaining values near 60 % for many fills of the storage ring. The direction of the longitudinal beam polarization was flipped about every one or several months and had the net beam polarization close to zero during one data taking year.

3.2 The Gas Target

The HERMES experiment was designed to run in parallel with the ZEUS and H1 collider experiments without significantly reducing the positron beam lifetime, which is of the order of 10 hours. This limited the target areal density to about 10^{15} H-atoms/cm^2 and excluded the use of any solid target material [146]. From the experience of the EMC experiment it was clear that the major source of systematic errors is associated with target polarization. Also the solid target has a high dilution factor. Therefore HERMES decided to use gas targets as they can be polarized to a high degree without or with only small dilution by unpolarized nuclei. The gas targets were also designed with a rapid polarization reversal. Therefore, it is an ideal choice to minimize systematic errors which originate in time dependent instrumental effects.

High luminosity is another requirement for a precision experiment. HERMES used the **storage cell** technique where polarized gas was fed into a T-shaped elliptical cell. The stored beam passed through the openings of the cell without interfering with the cell walls. The gas atoms undergo several hundred wall bounces before they leave the cell. In this way the density of the gas target was increased by a factor of about 100 compared to a free gas jet. By cooling the storage cell to low temperatures, the target density can be increased further [147].

In 1995, a longitudinally polarized ^{3}He target was used. Since 1996, the target apparatus for polarized hydrogen and deuterium has been in operation. During the years 1996–97 longitudinally polarized hydrogen ($H_{||}$) was used, while longitudinally polarized deuterium was employed in 1998–2000 ($D_{||}$), and from 2002 to 2005, transversely polarized hydrogen ($H_{\perp}$) has been used. Unpolarized gas target was also used during the end of each beam fill. From 2006 to the end of HERMES data taking, only unpolarized high density gas target was used.

3.2.1 Polarized Gas Target

The HERMES polarized hydrogen and deuterium targets, schematically shown in Figure 3.3, employed an atomic beam source (ABS) [148] that injected a polarized beam of H or D atoms into a thin–walled storage cell [149]. A sample of gas diffused from the center of the cell into a Breit–Rabi Polarimeter (BRP) [150] that measured the atomic polarizations, or into a Target Gas Analyzer (TGA) [151] that measured the relative atomic and molecular content of the gas. A magnet surrounding the storage cell provided a holding field defining the polarization axis and preventing spin relaxation by effectively decoupling the magnetic momenta of electrons and nucleons.

The target chamber shown in Figure 3.4 was evacuated by two turbo–molecular pumps with a combined speed of $4400\, l/s$. The chamber pressure was typically in the 10^{-7} mbar range during operation due to the high gas load from the atomic beam, which entered

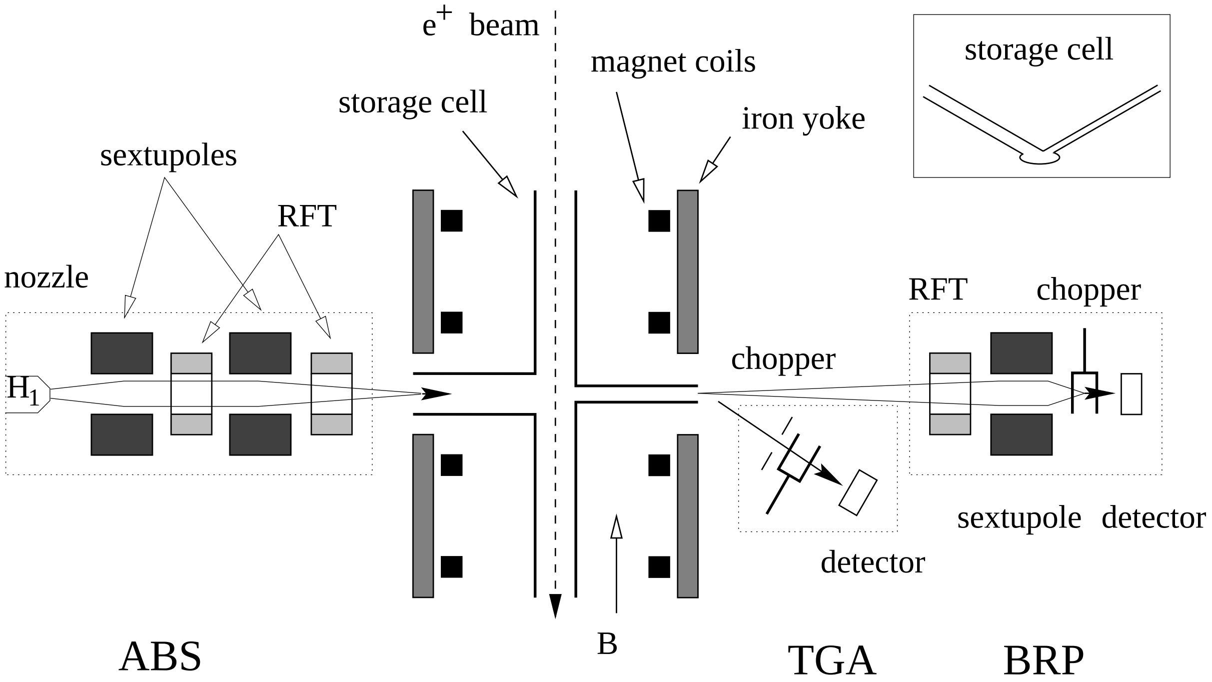

Figure 3.3: Schematic view of the HERMES polarized target. From left to right: Atomic Beam Source (ABS), target chamber with cell and magnet, and diagnostic system composed by Target Gas Analyzer (TGA) and Breit–Rabi Polarimeter (BRP). The locations of the radio–frequency transition (RFT) units are indicated.

the chamber from 30° above the horizontal plane. A 0.3 mm thick stainless steel exit window on the downstream end of the target chamber allows the scattered positrons and hadronic fragments to leave the target chamber and to be detected by the HERMES spectrometer [52]. For longitudinal running the storage cell and vacuum chamber were immersed in a longitudinal field generated by a superconducting magnet. The magnet field (up to 350 mT) provided optimum field uniformity over the length of the storage cell while providing a central gap for the beam to enter the cell. After the end of the longitudinal running in 2000, the HERMES target was modified for measurements with a hydrogen gas target in a transversely oriented magnetic holding field. A dipole magnet was built operating at a field value of B=297 mT. The magnet was used from 2001 to 2005. In these data taking periods, the polarization direction of the target was flipped with a fixed frequency.

The HERMES storage cell [149] was made of two 75 μm thin pure aluminum sheets, which were tightly spot–welded together. It was 400 mm long[4] and had an elliptical

---

[4] After 2006 the polarized target was removed and HERMES was running with the recoil detector and

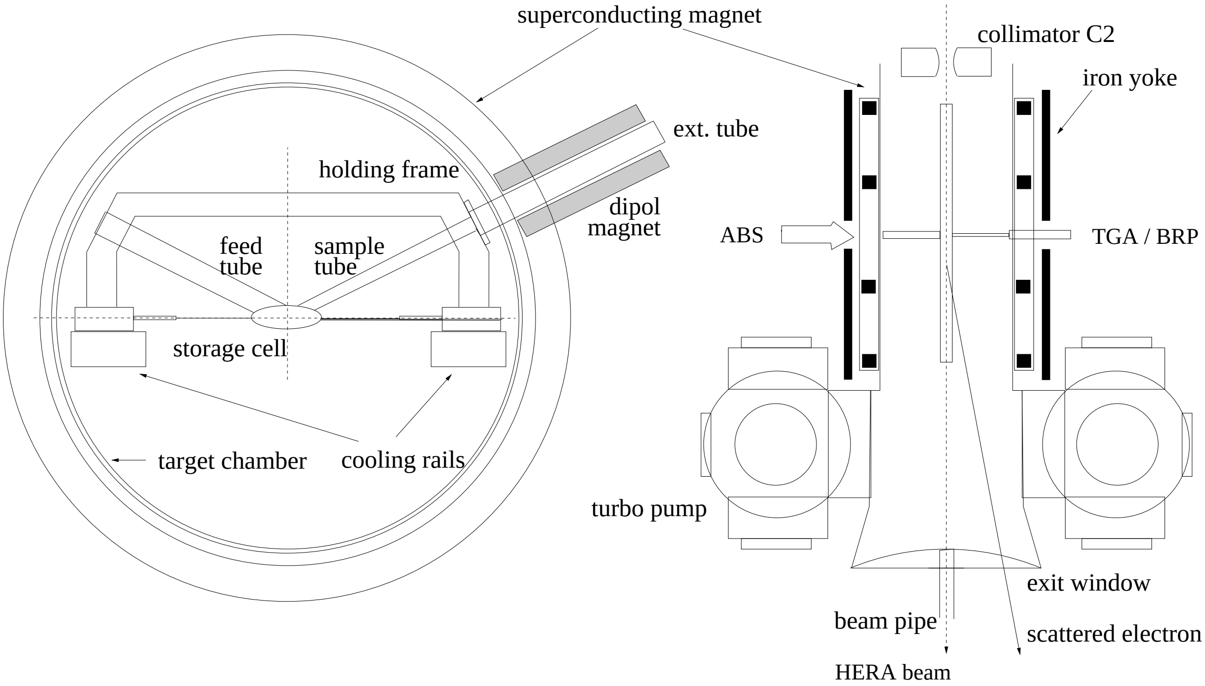

Figure 3.4: Longitudinal target chamber and magnet viewed from downstream with respect to the HERA beam direction (left), and from above (right).

cross–sectioned shape of $21 \times 8.9\,\text{mm}^2$.[5] The storage cell was mounted onto cooling rails, which were cooled by temperature regulated gaseous helium. The optimum operating temperature for hydrogen/deuterium target was found to be about 100/65 K. Due to thermal contraction of the cell when being cooled, the position of the cell center changed relative to the ABS and the BRP. From room temperature down to 100 K, the cell center moved by 0.9 mm. The alignment of the ABS and BRP relative to the cell center includes an offset to compensate for this effect at the target operating temperature. Two side tubes were connected to the beam tube, one to inject the polarized atoms and another smaller one to sample about 5% of the target gas and analyze it in the TGA and the BRP. The sample tube was tilted by 120° with respect to the axis of the injection tube to ensure that the sampled atoms had thermalized with the storage cell wall. A permanent dipole magnet around the sampling tube outside the target chamber extended the magnetic holding field of the target magnet to keep polarization (see Figure 3.4). In addition, a capillary near the location of the feed tube allowed injection of unpolarized gas into the cell.

---

unpolarized gas targets. The new target cell was with length 150 mm.

[5] Before December 1999, a larger tube with dimensions $29.8 \times 9.8\,\text{mm}^2$ was installed.

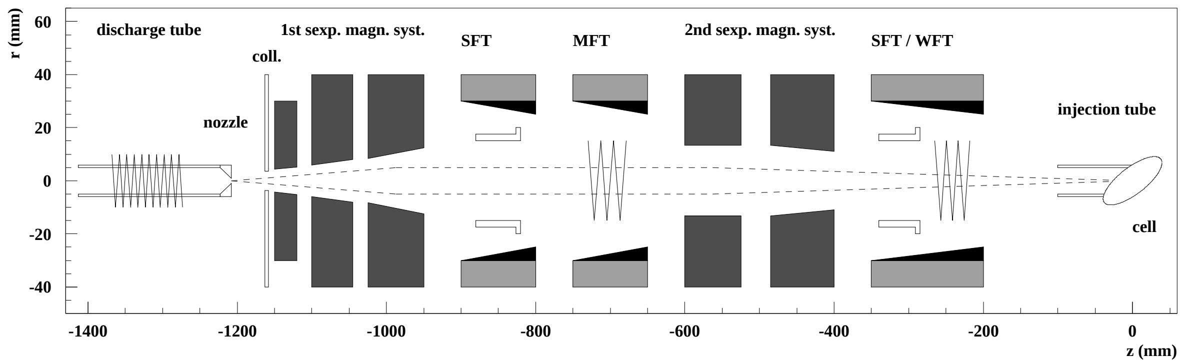

Figure 3.5: Schematic view (from downstream of the positron beam) of the HERMES ABS with dissociator and collimator for beam formation. Two sets of sextupole magnets were located along the beam axis as were the high–frequency transitions. The axis of the ABS was tilted by 30° downwards with respect to the horizontal plane.

The ABS was used to generate nuclear–polarized beams of hydrogen or deuterium atoms. Referring to Figure 3.5, Hydrogen (deuterium) molecules were dissociated via electron impact provided by a radio frequency (microwave) dissociator. The dissociated atoms expanded through a nozzle which was cooled down to 100 K by helium. An atomic beam of high intensity was formed after a skimmer and a collimator. The atomic beam was polarized by a set of sextupole magnets, which focused (deflected) atoms with positive (negative) electron spin, and by high frequency transition (HFT) units, which exchanged populations of certain hyperfine states of hydrogen/deuterium atoms. The HERMES ABS can provide a nuclear polarized beam of hydrogen (deuterium) atoms with an intensity of approximately $\approx 6.5 \times 10^{16}$ atoms/s ($\approx 4.5 \times 10^{16}$ atoms/s). Nuclear polarization values of 0.97 (0.92) at a degree of dissociation of 0.92 (0.95) for the hydrogen (deuterium) target had been reached. During the operation of the longitudinally polarized target, the nucleon spin state was changed every 60 s. For the transversely polarized target at first a spin flip interval of 60 s was used which was later increased to 90 s in order to reduce the dead time during the roughly 1 s long configuration changes.

The TGA [151] measured the atomic and molecular content of the gas extracted from the storage cell through the sample tube. It consisted of a pair of baffles, a chopper, a 90° off–axis quadrupole mass spectrometer (QMS) with a cross beam ionizer and a Channel Electron Multiplier (CEM) for single ion detection. The BRP [150] included two hyperfine transition units, a sextuple magnet system and the detector stage. It measured the relative populations n_i of the hyperfine states of hydrogen (or deuterium) atoms contained in the sample beam. From this measurement, the absolute atomic polarizations can be calculated by applying the knowledge of the target magnetic field strength. The average target polarization P_T as seen by the positron beam is given by the following equation:

$$P_T = \alpha_0 \alpha_r P_a + \alpha_0(1 - \alpha_r)\beta P_a \,, \tag{3.3}$$

where α_0 represents the initial fraction of nucleons in atoms in the gas injected by the ABS (or atomic fraction in the absence of recombination), α_r denotes the fraction of nucleons in atoms that have survived recombination, and $\beta = P_m/P_a$ represents the ratio of the nuclear polarization of the molecules P_m produced by recombination relative to the nuclear polarization of the atoms P_a. These values were calculated using the measurements of the TGA and BRP combined with various calibrations. The average value of target polarization for each data taking period can be found in Table 3.1 [152, 153].

Year	Type	Polarization	Fractional Uncertainty
1996	$H_\parallel$	0.759 ± 0.042	5.5%
1997	$H_\parallel$	0.850 ± 0.032	3.8%
1998	$D_\parallel$	0.856 ± 0.064	7.5%
1999	$D_\parallel$	0.832 ± 0.058	7.0%
2000	$D_\parallel$	0.845 ± 0.029	3.5%
2002	$H_\perp$	0.783 ± 0.041	5.2%
2003	$H_\perp$	0.795 ± 0.033	4.6%
2004.01-03	$H_\perp$	0.777 ± 0.039	5.0%
2004.04-07	$H_\perp$	0.721 ± 0.059	8.2%
2005.01-04	$H_\perp$	0.620 ± 0.090	16.0%
2005.04-11	$H_\perp$	0.730 ± 0.060	8.2%

Table 3.1: Target polarization values for different hydrogen and deuteron productions. The values are picked from the official HERMES target page [153]. The statistical uncertainty is negligible compared to the listed systematic uncertainty.

3.2.2 Unpolarized Gas Target

Alternatively to the injection of polarized atoms from the ABS, the storage cell can be filled with unpolarized gas using the unpolarized gas feed system (UGFS). Adjustable

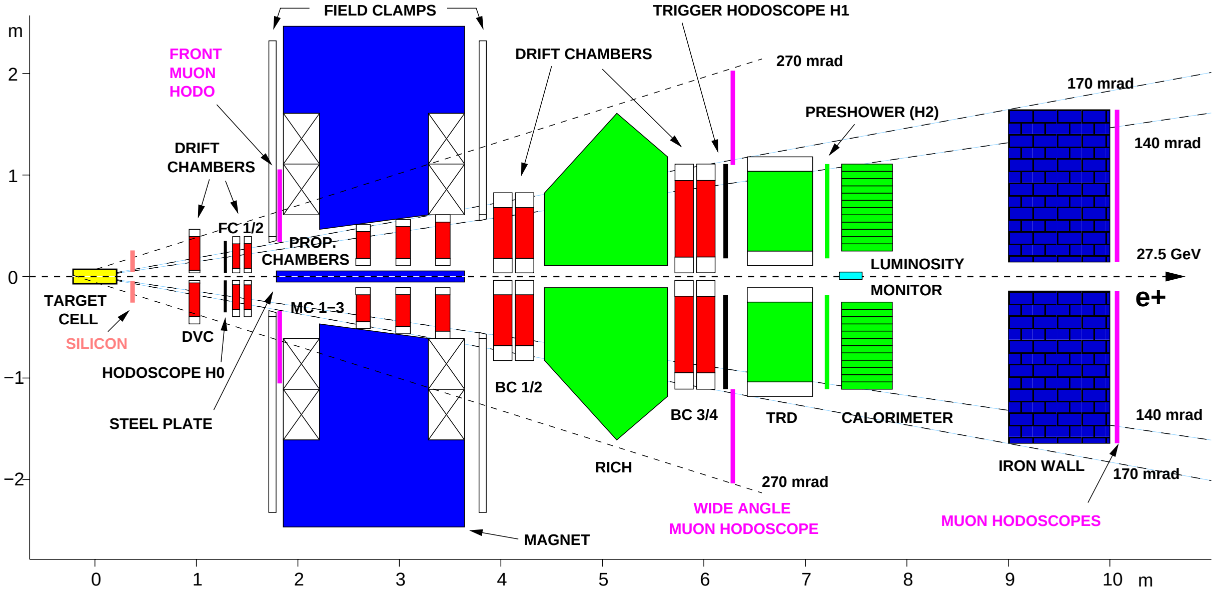

Figure 3.6: Side view of HERMES spectrometer configuration in the years 2001-2005.

densities and the possibility to inject the gas also into the target chamber (as opposed to the storage cell) furthermore allowed various calibration measurements necessary for the determination of the target polarization and the different contributions to its systematic uncertainty.

3.3 The HERMES Spectrometer

The HERMES spectrometer was a forward spectrometer with various novel technologies [52, 147]. It consisted of two symmetric halves above and below the horizontal plane in which the HERA beam pipes were located. A diagram of the spectrometer is shown in Figure 3.6. The coordinate system used by HERMES had the z axis along the beam momentum, the y axis vertical upwards, and the x axis horizontal, pointing towards the outside of the ring. Particles with scattering angles within $\pm 170\,\mathrm{mrad}$ in the horizontal direction and between $+(40 \sim 140)\,\mathrm{mrad}$ and between $-(40 \sim 140)\,\mathrm{mrad}$ in the vertical direction were accepted.

The front region before the spectrometer magnet consisted of a silicon strip detector, drift chambers (DVC, FC1/2), and a trigger hodoscope (H0). The region behind the magnet included drift chambers (BC1/2, BC3/4), a dual radiator Ring Imaging Čerenkov detector (RICH), a trigger hodoscope (H1), a Transition Radiation Detector (TRD), a pre-shower detector (H2), a luminosity detector, and a lead-glass calorimeter. A set of MultiWire Proportional Chambers (MWPC) (MC1–3) was installed in the gap of the magnet. A number of muon hodoscopes was also installed between the field clamps and the body of the magnet, and directly behind hodoscope H1, as well as behind a one meter thick iron wall.

DVC, FCs, MCs and BCs served for the tracking measurement. Particle IDentification (PID) was provided by H0, RICH, H1, TRD, H2, and the calorimeter. The luminosity monitor are necessary for absolute cross section measurement. The silicon strip detector, whose main purpose is to increase the acceptance for the decay products of Λ particles [154, 155], was installed. In the following, the parts related to the work in this thesis will be described in detail.

3.3.1 The Magnet

The HERMES spectrometer magnet with the length 2.2 m was of the H–type with field clamps in front as well as behind in order to reduce the fringe fields at the position of the drift chambers FC2 and BC1. The magnet provided a deflecting power of $\int Bdl = 1.3\,\mathrm{T{\cdot}m}$. The variation of the deflecting power within the acceptance was less than 10%. The gap between the pole faces enclosed the geometrical acceptance of $\pm(40 \sim 140)$ mrad in the vertical direction. In the horizontal direction ± 170 mrad plus another ± 100 mrad starting halfway through the magnet was provided. The pole faces were tilted parallel to the limits of the vertical angular acceptance. A massive iron plate in the symmetry plane shielded the positron and proton beams as they passed through the magnet. An effective magnetic shielding substantially reduced the effect of the magnet on the proton and positron beams. A correction coil with a deflecting power of 0.08 T·m was accommodated inside the shielding of the positron beam pipe. This coil was used to correct for the fringe fields and the imperfections of the magnetic shielding in this section of the iron plate. It was also used to compensate the transverse holding field of the target when operating with transverse polarization.

Magnetic model calculations were done with a good agreement with subsequent magnetic field measurements. The detailed field map was integrated into the track reconstruction algorithm.

3.3.2 Tracking System

The tracking system was to determine the event vertex, to measure the scattering angles (θ and ϕ) for kinematic reconstruction and to measure the particle momentum from the track deflection in the spectrometer dipole magnet. It also helped identifying the hits in the PID detectors associated with each track. In combination with the magnet, the tracking detectors can determine momenta of charged particles. For positrons with momenta between 3.5–27 GeV, the average angular resolution was 0.6–0.3 mrad and the average momentum resolution $\delta p/p$ was 0.7–1.3%, which was mainly limited by Bremsstrahlung

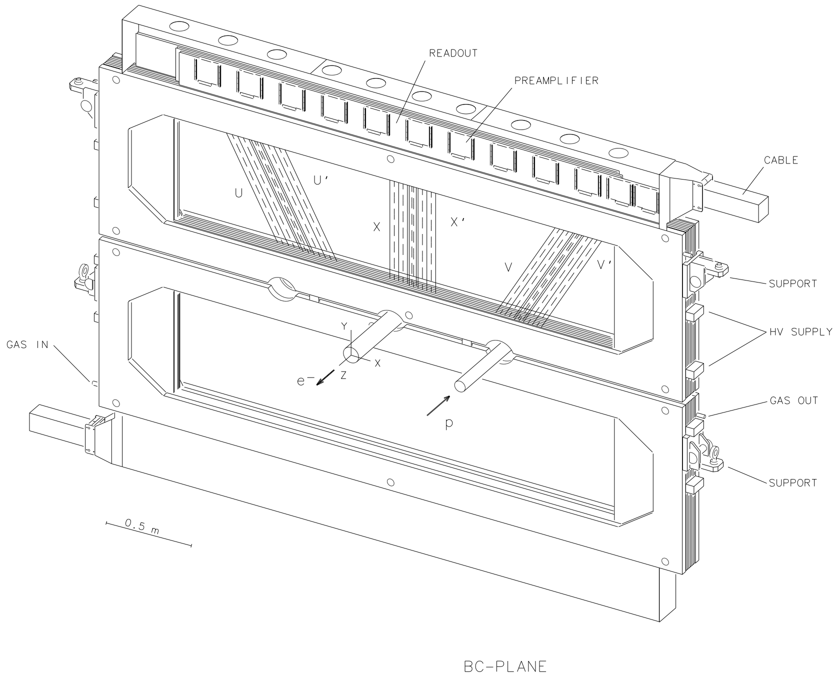

Figure 3.7: Schematic view of the BC chambers.

in the material of the target cell walls, the 0.3 mm thick stainless steel vacuum window.

The DVC [52] and FCs [156] were used to determine the event vertex in the target cell, as well as to measure the scattering angles and the initial trajectories of charged particles before the magnet. The BCs [157] were used to determine the trajectories of charged particles after the magnet, and to identify the hits in the PID detectors associated with each track. The DVC, FCs, and BCs consisted of conventional drift chambers of horizontal–drift type. Every chamber module contained six layers of drift cells (U, U′, X, X′, V, V′) (see Figure 3.7), each of which consisted of alternating anode–cathode wires between a pair of cathode foils. The cathode wires and foils were at negative high voltage with the anode sense wires at ground potential. The anode–cathode wires in the X and X′ planes were oriented in the vertical direction, while the ones in the U and U′ (V and V′) planes were tilted by 30° to left (right). U′, X′, and V′ planes were offset by half a cell width with respect to the corresponding U, X, and V planes in order to help solve left–right ambiguities. The gas mixture was the same for all the drift chambers: Ar:CO_2:CF_4 (90:5:5). The DC readout system consisted of Amplifier/Shaper/Discriminator (ASD) cards mounted onboard the drift chambers, driving ECL signals to LeCroy 1877 FastBus time–to–digital converters (TDCs). Some specifications of the tracking chambers are given below.

Drift Vertex Chamber

The width of the drift cells of the Drift Vertex Chamber (DVC) was 6 mm. The distance between two neighboring anode and cathode planes was 3 mm. The DVC had an active area of $474{\times}290\,\mathrm{mm}^2$. It consisted of two modules above and below the positron beam, and in total 1088 channels. The anode wires were made of gold–plated tungsten and had a diameter of $30\,\mu$m. The potential wires were made of gold–plated Be–Cu and had a diameter of $50\,\mu$m. The cathode planes were made of $34\,\mu$m thick, aluminized Mylar foils. A average spatial resolution of $220\,\mu$m per plane was reached by the DVC.

Front Chamber

The width of the drift cells was 7 mm. The distance between two neighboring anode and cathode planes was 4 mm. The FCs had an active area of $660{\times}180\,\mathrm{mm}^2$. Each chamber consisted of one module with 576 channels. The total number of channels was 2304. The anode wires were made of gold–plated tungsten and had a diameter of $20\,\mu$m. The potential wires were made of gold–plated Al and had a diameter of $76\,\mu$m. The cathode planes were made of $6.4\,\mu$m thick, double–sided aluminized Mylar foils. The single plane efficiency ranged from 97% near the anode wire to 99% at the center and edge of the cell. An average spatial resolution of $225\,\mu$m per plane was reached by the FCs.

Back Chamber

The width of the drift cells was 15 mm. The distance between two neighboring anode and cathode planes was 8 mm. The BC1 and BC2 (BC3 and BC4) had an active area of $1880{\times}520$ $(2890{\times}710)\,\mathrm{mm}^2$ and 768 (1152) channels per module. The total number of channels was 7680. The anode wires were made of gold–plated tungsten and have a diameter of $25.4\,\mu$m. The potential wires were made of gold–plated Be–Cu and had a diameter of $127\,\mu$m. The cathode planes were made of $25\,\mu$m thick C coated Kapton. The average BC plane efficiency was well above 99% for electron and positron tracks, and dropped to 97% when also hadronic tracks were considered. An average spatial resolution of 250 (275) μm per plane was reached by the BC1/2 (BC3/4).

Magnet Chamber

The proportional chambers inside the magnet (MC1/3) were originally intended to ensure that multi–track ambiguities could be resolved [158]. As it happened, chamber occupancies were low enough that this can be accomplished using the drift chambers alone. However, the MCs were found to be very useful for momentum analysis of low energy decay products that were deflected too much to reach the downstream tracking detectors. These tracks, which were called as *short–tracks*, did not enter the RICH and hence had no PID information. For these tracks the reconstruction program provided a coarse momentum

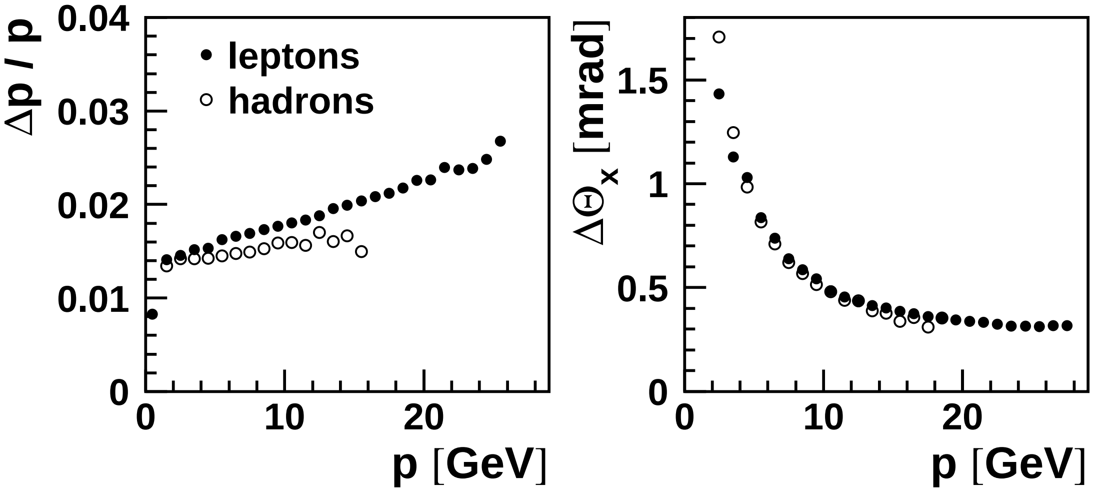

Figure 3.8: Tracking system resolution for lepton and hadron tracks for the detector configuration. In the left panel the relative momentum resolution is displayed, and the right panel shows the resolution in the horizontal scattering angle θ_x, both as a function of the track momentum p.

determination based on curvature of the tracks. For the work in this thesis, the long track is prerequisite due to the necessity of the PID information. Hence, MCs are not used.

Tracking Reconstruction

The tracking algorithm determined partial tracks before (front track) and after the magnet (back track). The track projections were found in a fast tree search and then combined to determine the particle momentum. The front and back tracks were associated by matching pairs that intersect in the center of the magnet within a given tolerance. For each associated pair, the front track was forced to agree with the magnet mid–point of the back track, and the front track was recomputed accordingly. This procedure improved the resolution of the front tracking system, which relied on the FC chambers. The precision of the front track was increased by adding an additional virtual point at the intersection of the forward extrapolation of the back track with the xy-plane at the middle of the magnet (force bridge technique). Using lookup tables the momentum of a charged particle was determined from the front and back track parameters. However, DVC was not used in the reconstruction algorithm in the analysis reported in this thesis. Multiple scattering in the spectrometer material leads to reduced resolutions. Figure 3.8 shows the resolutions for the Deuterium data sample as obtained form a Monte Carlo simulation of the entire spectrometer. With the threshold Čerenkov counter installed, a momentum resolution of $\delta p/p < 2.2\,\%$ and an angular resolution of $\delta\theta < 1.4\,\mathrm{mrad}$ for particles with $p > 2\,\mathrm{GeV}$ could be obtained. The resolutions became worse with the installation of a Ring Imaging

Čerenkov detector (RICH) in place of the threshold Čerenkov counter. The resolutions became $\delta p/p < 2.6$ % and $\delta\theta < 1.8$ mrad, because of some additional material introduced by RICH.

Target Transverse Magnet Correction

The transverse target holding field deflected the trajectory of the charged particle flying through the magnet field. Therefore the vertex and scattering angle reconstruction of the detected track have to be corrected. To do this the transverse magnet field had to be mapped which was only possible in the shutdown of 2003 after the implementation of additional correction coils [159]. The measured field map can be used for the productions. In 2002 a theoretical field map was calculated with the help of the magneto–static program MAFIA [160]. A survey of the magnet field along the z–axis and at certain positions along the x direction served as input for this calculation. Two different methods for the target magnet correction (TMC) are available, both using the track position information from the DVC and the FCs [161].

In target magnet correction 1 (TMC1), the correction on the particle track was applied based on reference tracks from a database. In a detailed tracking calculation a grid of trajectories covering the HERMES acceptance was computed in small steps of momentum, z–vertex and vertical and horizontal angles. From this set the trajectory closest to a measured particle track was selected, based on the tracking information from the DVC and FCs. The remaining deviations from the reference track in the data base are used in a linear interpolation to yield the corrected z–vertex and vertical scattering angle of the measured track. The true horizontal angle can then be computed from the position on FC2 by a simple relationship.

Target magnet correction 2 (TMC2) was based on a ray tracing procedure. Using the reasonable assumption that a trajectory which was in the beginning close to a reference trajectory will also be close to the reference trajectory at the end, a Taylor expansion for the final position in terms of the initial position can be performed. The coefficients provide a quick way to relate the initial position of a track to its final position with the help of a transfer function. For the determination of these transfer coefficients several reference particles had to tracked through the magnet field using the MIT–Raytrace program [162]. In order to correct the z–vertex position and the scattering angles the right transfer function, which depends on the particle momentum and the z–position from which the particle was assumed to originate, has to be found iteratively until convergence was achieved. Ref. [161] presents the detailed implementation of the two methods. By a Monte Carlo (MC) simulation of the HERMES detector, it was proved that the TMC methods significantly counteracted the dissolution of the target transverse magnet to the spectrometer resolutions [163, 164]. For the official data production, TMC2 is recommended for 2002 and 2005 data, while TMC1 for 2003 and 2004 data.

3.3.3 Particle Identification Detectors

The HERMES Particle IDentification (PID) system discriminated among different particles, such as positrons, pions, kaons and protons. The HERMES PID system has been designed to provide a factor of at least 10 in hadron suppression at the DIS trigger level to keep data acquisition rates reasonable. The rate of DIS positrons was much exceeded by that of hadrons from photo–production by a factor as high as 400:1 in certain kinematic regions. The system provided a hadron rejection factor (HRF) of at least 10^4 in offline analysis to keep the contamination of the positron sample by hadrons below 1% for the whole kinematic range. The HRF was defined as the total number of hadrons in the spectrometer acceptance divided by the number of hadrons misidentified as positrons. The PID system also discriminated among different hadrons, *e.g.*, pions, kaons and protons for the important semi–inclusive measurements that will allow the contribution of the valence and sea quarks to the nucleon spin to be isolated. The PID system consisted of four sub–systems: a lead–glass calorimeter, the plastic scintillator hodoscopes (H0/1/2), a transition radiation detector (TRD), and a Čerenkov detector (see Figure 3.6). The hodoscopes were initially only used for triggering purpose but can also be used for time–of–flight (TOF) measurement, which provided good PID for protons and pions in the momentum range up to 2.9 GeV/c and for kaons up to 1.5 GeV/c. The calorimeter and the hodoscopes were used in the first level trigger to select DIS events. The threshold Čerenkov was used in 1996–97 primarily for pion identification, while the Ring Imaging Čerenkov detector (RICH) was used thereafter to identify pions, kaons and protons. The rejection factor was estimated to be approximately 10 in the trigger. The TRD consisted of 6 modules in each half and provides an additional HRF of over 100 for 90% e^+ efficiency.

Čerenkov Detector

The Čerenkov detector was placed between BC1/2 and BC3/4. At the beginning, a threshold Čerenkov detector was used in HERMES to discriminate between pions and positrons [165]. It was operational from 1995 to 1997 and was replaced in 1998 by a dual radiator Ring Imaging Čerenkov (RICH) [166] detector. Both components utilized the principle of Čerenkov radiation [167]. Particles traversing a dielectric medium with refractive index n emit Čerenkov radiation if their velocity v_p was greater than the velocity $v_m = c/n$ of light in that medium. The opening angle of the wave front of the Čerenkov radiation can be calculated as,

$$\cos\theta = \frac{v_m}{v_p} = \frac{c}{nv_p} = \frac{1}{n\beta}, \tag{3.4}$$

where $\beta = v_p/c$ is the relative velocity (with respect to the velocity of light c) of the particle. Čerenkov radiation is emitted when $v_p > v_m$, which corresponds to a threshold momentum $p > \gamma mc/n$, where $\gamma = \frac{1}{\sqrt{1-\beta^2}}$. As the threshold momentum depends on the mass of the particle, different particles can be separated by observing the emitted Čerenkov radiation in the medium.

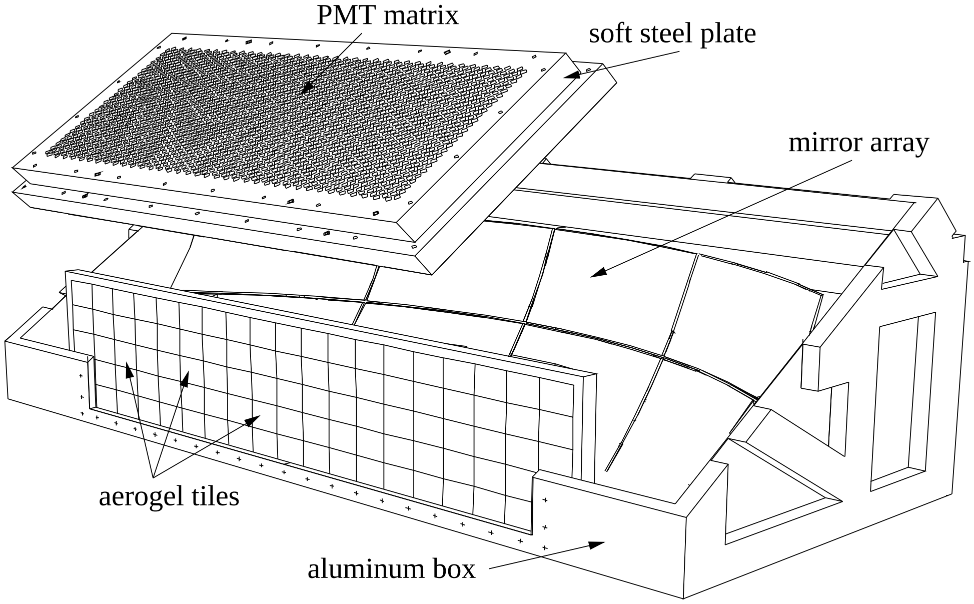

Figure 3.9: A cutaway schematic view of the (top) RICH counter.

Ring Imaging Čerenkov (RICH) Detector

After 1998, threshold Čerenkov detector was updated to RICH, which allows kaons and protons to be identified as well as pions [166, 168, 169]. The RICH used a novel two–radiator design to achieve separation of pions, kaons and protons over the entire kinematic range of interest. The first radiator consists of aerogel tiles mounted just behind the entrance window (see Figure 3.9) and the second radiator was C_4F_{10} gas. The aerogel tiles were 1.1 cm thick and they were stacked in five layers for a total length of 5.5 cm. A mirror array with a radius of curvature of 220 cm focused the Čerenkov photons onto 1934 photomultiplier tubes of 1.92 cm diameter per detector half, which yielded a pixel size 2.33 cm and an angular resolution of about 8 mrad.

The photomultiplier signals only provide a pulse if there was a hit above threshold, but do not provide pulse–height information. As shown in Figure 3.10, the RICH detector identified pions, kaons, and protons in the momentum range $2 < p < 15\,\mathrm{GeV}/c$. The pattern of Čerenkov photons emitted by tracks passing through the aerogel or the gas radiators on the photomultiplier matrix was associated with tracks using inverse ray tracing. Several methods [170] were developed for RICH PID.

In method Inverse Ray Tracing (IRT) for each particle track, the photon emission angle was computed with different Particle Type Hypothesis (PTH). With denotation of

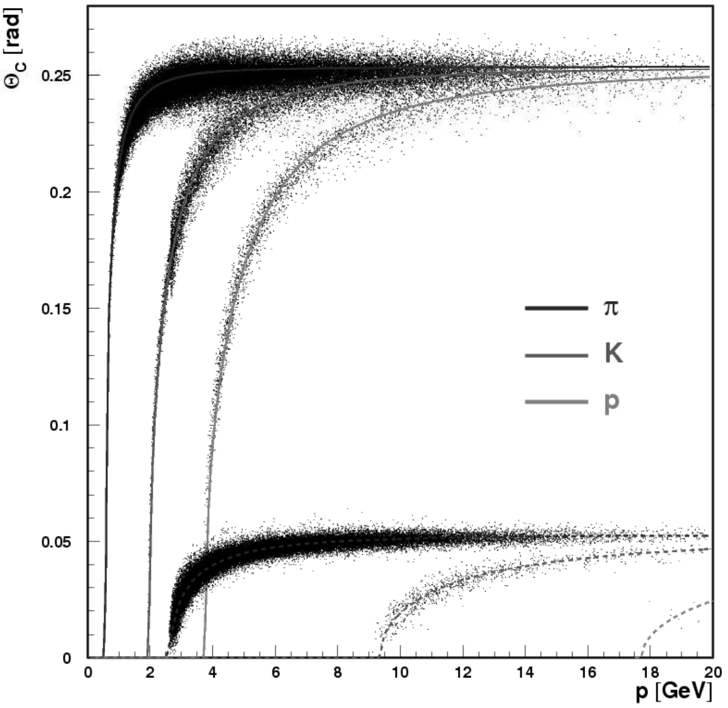

Figure 3.10: Čerenkov angles associated with the three particle hypotheses as a function of the particle momentum. The characteristic angles of Čerenkov light emitted in the aerogel (n=1.03) are given by the solid lines. The characteristic angles for emission in the gas (n=1.0014) are shown as the dashed lines. The corresponding histogram entries are experimentally determined angles of a sample of hadrons.

aerogel as a and gas as g, the average Čerenkov angles $\langle\theta\rangle^{a,g}_{\pi,K,p}$ were calculated for each radiator (a,g) and PTH (π,K,p) by including only photons with emission angles within $2\,\sigma_\theta$ about the theoretically expected emission angle $\theta^{\mathrm{theo};a,g}_{\pi,K,p}$, where $\sigma_\theta \simeq 8\,\mathrm{mrad}$ was the single photon resolution. This procedure rejected background photons, and photons due to other tracks or the other radiator. Figure 3.10 shows the distribution of angles in the two radiators as a function of the particle momentum. Based on the Gaussian likelihood,

$$\mathcal{L}^{a,g}_i = \exp\left[-\left(\theta^{\mathrm{theo};a,g}_i - \langle\theta\rangle^{a,g}_i\right)^2 \frac{1}{2\sigma^2_{\langle\theta\rangle^{a,g}_i}}\right] \tag{3.5}$$

a particle hypothesis $i = \pi, K, p$ with the largest total likelihood $\mathcal{L}^{\mathrm{tot}}_i = \mathcal{L}^a_i \cdot \mathcal{L}^g_i$ was assigned to each hadron track. Another method Direct Ray Tracing (DRT) preformed a Monte Carlo simulation of the RICH's response to a track with the kinematics of the candidate track. Many emitted photons were generated and the hit patterns on the PMTs were simulated for each PTH. By comparing the simulated hit pattern and the observed hit pattern, the likelihood of each PTH can be calculated. The most likely hypothesis was chosen as the suggested type of this track.

The disadvantage [171] of IRT and DRT algorithms was that it considered only a single track at one time. If, for example, there are two tracks in the same detector half, the PMT hits from the both tracks are included in the observed hit pattern but only one track at one time was recognized. The combined particle type hypothesis (CPTH) was devised recently, which would evaluate the likelihood with combination of PTHs for all the tracks in the detector half for one event. A CPTH, called event–level tracing (EVT), was created by adding together the hit patterns for individual tracks from DRT. Due to some practical reason, the data in years 2002–2003 have not been filtered with this new algorithm, but it does not matter very much for the analysis in this thesis since the dominant statistics are from years 2004–2005.

Identification efficiencies and probabilities for contamination of hadron populations from mis–identification of other hadrons [172] were estimated with a Monte Carlo simulation which had been calibrated with "electron tune", which matches Čerenkov opening angle and number of PMT hits from single electron/positron tracks, and "hadron tune", which compares tracks decayed from experimentally reconstructed ρ^0, ϕ, K_s^0 meson and Λ hyperon. Two tunes provides the estimate of the systematic uncertainty

The Calorimeter

The function of the calorimeter was to provide a first level trigger for scattered positrons, based on energy deposition in a localized spatial region; to suppress hadrons by a factor of $\geq$10 at the first level trigger and $\geq$100 in the off–line analysis; to measure the energy of positrons and also of photons from radiative processes or from π^0 and η decays. In some analysis which needs photon information, the calorimeter also provided a rough position measurement of the positrons and photons.

The solution chosen to meet these requirements consisted of radiation resistant F101 lead–glass blocks arranged in two walls of 420 blocks each above and below the beam (see Figure 3.11). Čerenkov light produced by electromagnetic showers was detected by Philips XP3451 photomultipliers (PMTs) of 7.5 cm diameter viewing from the rear side. The radiation length of F101 lead–glass was 2.78 cm, Moliere radius 3.28 cm, critical energy 17.97 MeV, refractive index 1.65, and density 3.86 g/cm^3. The area of the front face of the blocks was $9 \times 9\,\mathrm{cm}^2$, and the length 50 cm, which corresponded to about 18 radiation lengths. The blocks were arranged into two 42×10 arrays, one above and the other below the positron beam. They were polished, wrapped with 50 μm thick aluminized mylar foils, and covered with a 125 μm thick tedlar foil to provide light isolation.

Each lead–glass block was calibrated within $\sim$ 1% at DESY in a 3 GeVpositron beam incident at the center of the block [173]. The ratio E/p was expected to be close to unity, independently of the positron/photon energy, where E was the measured energy and momentum p was determined by tracking in the magnet. But for hadrons, as expected

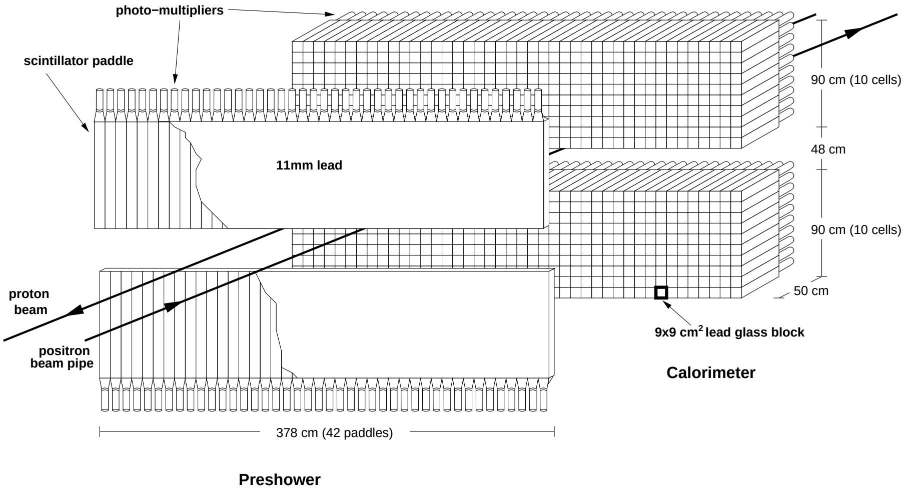

Figure 3.11: Schematic view of the calorimeter and the pre–shower detector.

the ratio was less than unity. The performance of a 3×3 array of counters showed [174] an energy response to positrons linear within 1%, over the energy range 1–30 GeV. The energy resolution can be parameterized as

$$\sigma(E)/E\ [\%] = (5.1 \pm 1.1)/\sqrt{E} + (1.5 \pm 0.5). \tag{3.6}$$

Contrary to leptons, hadrons lose only a small fraction of their energy, due to nuclear interactions and ionization losses dE/dx. Since positrons lose almost all of their energy, the total deposited energy E measured by the calorimeter was close to the momentum p of the lepton measured with the spectrometer. This allows a good discrimination of leptons from hadrons in the distribution of E/p as can be seen in Figure 3.13.

To prevent radiation damage of the lead glass, both calorimeter walls were moved away vertically from the beam pipe by 50 cm when the beam was injected. The monitoring of gain and ageing was achieved using a Gain Monitoring System (GMS) [175]. Radiation damage to the lead–glass was also monitored indirectly using TF1 [174] blocks placed behind the calorimeter. This material was much more sensitive to radiation damage than F101. No variation had been observed in their response, indicating that the effect of radiation damage was negligible.

Hodoscopes

A forward trigger scintillator (H0) placed directly upstream of the front drift chambers was introduced to eliminate a large number of showers generated by the proton beam by distinguishing forward and backward going particles using the time of flight between the front and rear scintillators. This front trigger detectors consisted of a single sheet of standard plastic scintillator, 3.2 mm thick (0.7% of a radiation length). A scintillator hodoscope (H1) and Pb–scintillator pre–shower counter (H2) provided trigger signals and particle identification information. Both counters were composed of vertical scintillator modules (42 each in the upper and lower detectors), which were 1 cm thick and $9.3\times91\,\mathrm{cm}^2$ in area. The individual panels were read out by PMTs away from the beam pipe as sketched in Figure 3.11.

In addition to providing a fast signal that was combined with the calorimeter, H0 and H1 to form the first level trigger, the H2 counter provided important discrimination between positrons and hadrons. This was accomplished with a passive radiator that initiates electromagnetic showers that deposited typically much more energy in the scintillator than minimum ionizing particles. This results in energy losses of 20∼40 MeV for positrons whereas hadrons deposited only around 2 MeV, as shown in Figure 3.13. A PRF of ∼10 was possible with 95% efficiency for positron detection.

Transition Radiation Detector

Transition Radiation (TR) [176] is produced by relativistic charged particles when they cross the interface of two media of different dielectric constants. The emitted radiation is the homogeneous difference between the two inhomogeneous solutions of Maxwell's equations of the electric and magnetic fields of the moving particle in each medium separately. In other words, since the electric field of the particle is different in each medium, the particle has to *shake off* the difference when it crosses the boundary. The total energy loss of a charged particle on the transition depends on its Lorentz factor $\gamma = E/mc^2$ with equation of

$$E = \frac{2}{3}\alpha\omega_p\gamma, \tag{3.7}$$

where ω_p is the plasma frequency of the medium. Mostly the radiation is directed forward, peaking at an angle of the order of $\frac{1}{\gamma}$ relative to the particle's path. The intensity of the emitted radiation is roughly proportional to the particle's energy E. The characteristics of this electromagnetic radiation makes it suitable for particle discrimination, particularly of positrons and hadrons in the momentum range between 1 GeV/c and 100 GeV/c. The transition radiation photons produced by positrons have wavelengths in the X–ray range, with energies typically from 5 to 15 keV. However, the number of produced photons per interface crossing is very small. Usually several layers of alternating materials or composites are used to collect enough transition radiation photons for an adequate measurement.

Each of the upper and lower halves of the spectrometer contained six TRD modules with an active area of $325\times75\,\mathrm{cm}^2$. As shown in figure 3.12, each module consisted of a radiator and a proportional wire chamber to detect the TR photons. In addition, there were two flush gaps on either side of each detector through which CO_2 was flowed to reduce the diffusion of oxygen and nitrogen into the chamber. CO_2 was used in the flush gaps because it was easily removed from the chamber gas during re–circulation. The radiators consisted of a pseudo–random but predominantly two–dimensional array

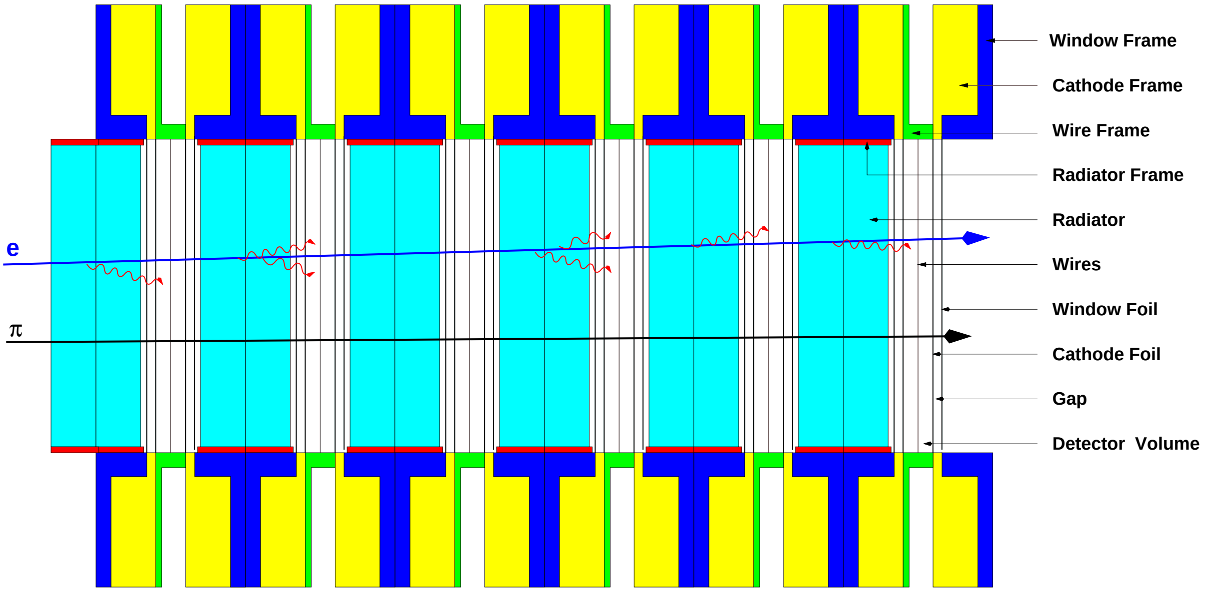

Figure 3.12: The upper half of the TRD with a positron and a pion track. The opening angles of the transition radiation produced by the lepton are exaggerated.

of polyethylene fibers with 17–20 μm diameter. The proportional chambers had a wire spacing of 1.27 cm, used Xe:CH$_4$ (90:10) gas, and were 2.54 cm thick. Xe/CH$_4$ (90:10) was used as the detector gas because of its efficient X–ray absorption.

Both positrons and hadrons deposit energy in the detectors. At HERMES energies only leptons emit a large enough amount of transition radiation to be detected. The emitted energy for a lepton with the same energy as a pion was about 270 times larger. Due to ionization losses dE/dx in the chamber gas all particles deposit some energy in the wire chamber. In general, leptons leave approximately 2.5 times the amount of energy of pions, allowing for a separation by the energy deposition in the TRD modules. In Figure 3.13 a typical response to leptons and hadrons is shown. Plotted is the truncated mean which was the averaged signal calculated from 5 modules, discarding the module with the largest response. This procedure reduces significantly the Landau tail of the hadronic response. Using a combined probability of positron and hadron from the responses of 6 modules, a PRF of 1460±130 (489±25) was reached with 90(95)% positron efficiency. Photon can leave a signal in a cluster of blocks which does not coincide with a track reconstructed in the HERMES acceptance. By weighting the centroid of each block of a cluster with the logarithm of the corresponding energy, a position resolution of about 0.5 cm for photons was achieved [177].

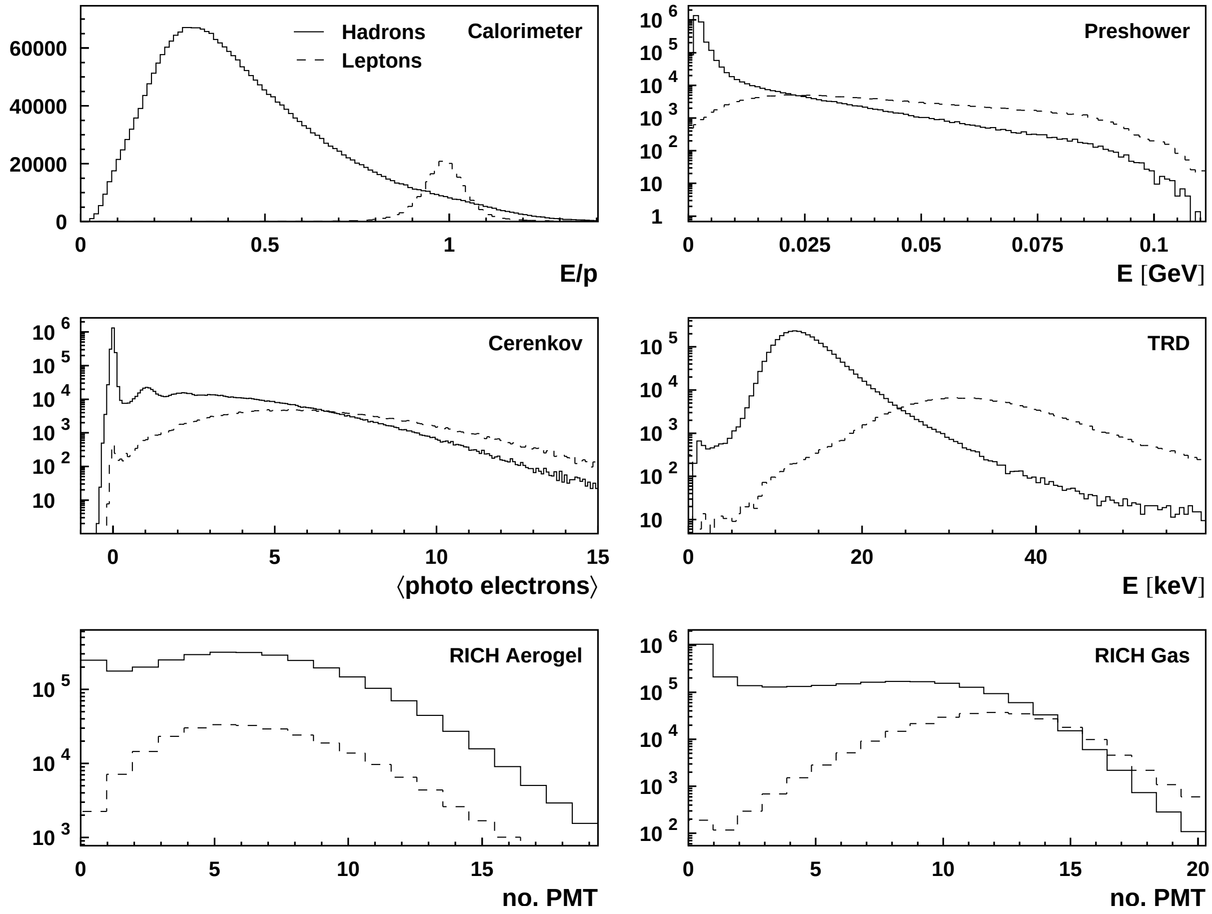

Figure 3.13: Typical PID detector responses. The truncated mean is shown in the case of the TRD. The relative size of the lepton (dashed line) and hadron distributions (solid line) was scaled to the flux ratio in the respective data–taking periods to give a better idea of the level of contamination possible from each detector. The flux ratio of positrons to hadrons was typically $\sim 10\,\%$ for these data.

PID System

The responses of the PID detectors are plotted in Figure 3.13. The identification of hadrons and leptons was based on a Bayesian algorithm that uses the conditional probability $P(A|B)$ defined as the probability that A is true, given that B was observed. For each track the conditional probability $P(H_{l(h)}|E,p,\theta)$ that the track is a lepton (hadron) is calculated as

$$P(H_{l(h)}|E,p,\theta) = \frac{P(H_{l(h)}|p,\theta)\; P(E|H_{l(h)},p)}{\sum_{i=l,h} P(H_i|p,\theta)\; P(E|H_i,p)}\,. \tag{3.8}$$

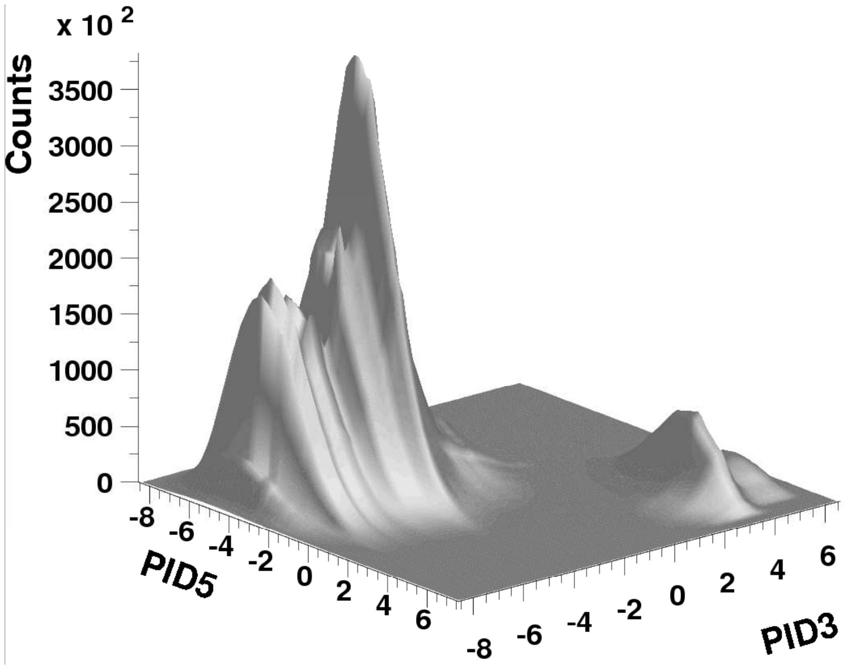

Figure 3.14: Two–dimensional distribution of PID values for all particles in the acceptance.

Here $H_{l(h)}$ is the hypothesis that the track is a lepton (hadron), E the response of the considered detector, and p and θ are the track's momentum and polar angle. The parent distributions $P(E|H_{l(h)}, p)$ of each detector (*i.e.*, the typical detector responses) were extracted from data with stringent restrictions on the other PID detectors to isolate a particular particle type. In a first approximation, uniform fluxes $P(H_l|p,\theta) = P(H_h|p,\theta)$ are assumed so that the ratio

$$\log_{10} \frac{P(H_l|E,p,\theta)}{P(H_h|E,p,\theta)} \tag{3.9}$$

reduces to:

$$\mathrm{PID}_{det} = \log_{10} \frac{P(E|H_l,p)}{P(E|H_h,p)} \,. \tag{3.10}$$

The quantity PID_{det} is defined for the calorimeter (*cal*), the pre–shower detector (*pre*), the Čerenkov detector (*cer*) (the RICH detector (*ric*) since 1998), and the TRD (*trd*). In the case of the RICH and the TRD this ratio is the sum over the PID values of the two radiators and the six TRD modules, respectively. The PIDs are defined as

$$\mathrm{PID2} \equiv \mathrm{PID}_{cal} + \mathrm{PID}_{pre}, \tag{3.11}$$

$$\mathrm{PID3} \equiv \mathrm{PID}_{cal} + \mathrm{PID}_{pre} + \mathrm{PID}_{ric}, \tag{3.12}$$

$$\mathrm{PID5} \equiv \mathrm{PID}_{trd} = \sum_{i=1}^{6} \mathrm{PID}_{trd,i}. \tag{3.13}$$

The distribution of PID5 versus PID3 is shown in Figure 3.14, where the leptons (small bump) are seen to be clearly separable from the hadrons (large peak). PID3 + PID5 can be used as criterion to separate hadrons and leptons. Since RICH installation, criterion (PID3 + PID5) > 1 was applied to be the lepton selection with the efficiency above 97% and a hadron contamination below 0.01%. For hadrons the value (PID3 + PID5) < 0 was chosen, yielding an efficiency of 99% with a contamination below 1% [155].

3.3.4 Luminosity Monitor

The luminosity measurement[178] was based on the elastic scattering of beam positrons from target gas electrons $e^+e^- \rightarrow e^+e^-$ (Bhabha scattering) and the annihilation into photon pairs $e^+e^- \rightarrow \gamma\gamma$ for a positron beam, the process $e^-e^- \rightarrow e^-e^-$ (Møller scattering) for an electron beam. The cross sections are known precisely, including radiative corrections, *e.g.*, $e^+e^- \rightarrow e^+e^-\gamma$, $e^+e^- \rightarrow \gamma\gamma\gamma$. The scattered particles exited the beam pipe at z=7.2 m and were detected in coincidence by two small calorimeters with a horizontal acceptance of 4.6 to 8.9 mrad, which was limited by the size of the beam aperture in the magnet shielding plate. Due to the high radiation background in the region very near to the beam, the calorimeter consisted of Čerenkov crystals of $\mathrm{NaBi(WO_4)_2}$, which have a very high radiation hardness on the order of $7 \cdot 10^5$ Gy.

3.3.5 Trigger

The function of the trigger system is to distinguish interesting events from background with high efficiency, and initiate digitization and readout of the detector signals. HERMES required physics triggers corresponding to deep inelastic positron scattering, photo–production processes (where no positron was detected) and additional triggers for detector monitoring and calibration.

The DIS trigger selected electron/positron events by requiring hits in the three scintillator hodoscopes (H0, H1, and H2) together with sufficient energy deposited in two adjacent columns of the calorimeter, in coincidence with the accelerator bunch signal (HERA clock). The requirement of hits in H0 and H1 suppressed neutral particle background. The calorimeter had a high efficiency for electromagnetic showers, but relatively low efficiency for hadronic showers. The calorimeter threshold was set at 1.4 GeV (3.5 GeV for the first period in 1995). The purity of the DIS trigger was good for a high calorimeter threshold (3.5 GeV) and acceptable for a low threshold (1.4 GeV).

The photo–production trigger detected hadrons such as K, ρ, D^0, J/ψ and Λ^0 that were produced at low Q^2 and decay to two or more charged particles. Typically the scattered positron angle was too small for detection. The trigger required two detected charged particle tracks, as identified by the three hodoscopes and the BC1 chamber as well as the HERA Clock. The back chamber requirement eliminated those showers originating in the upstream collimators, which were confined near the beam pipe and hit the tips of the hodoscopes but not the wire chambers which were well shielded by the magnet steel. Approximately one third of the photo–production triggers had reconstructable tracks.

3.4 Gain Monitoring System

The stability of the part PID detectors was monitored by the Gain Monitoring System (GMS) [175], which can help the shift crews to rapidly diagnose and repair hardware failures. The GMS also monitored other detectors equipped with PMTs like the luminosity monitor, the trigger hodoscopes and the beam polarimeter, giving a total of 952 PMTs. The GMS was used to measure the gain of the PMTs, which is related to the condition of the detector itself and of the signal readout chain.

3.4.1 Configuration of the System

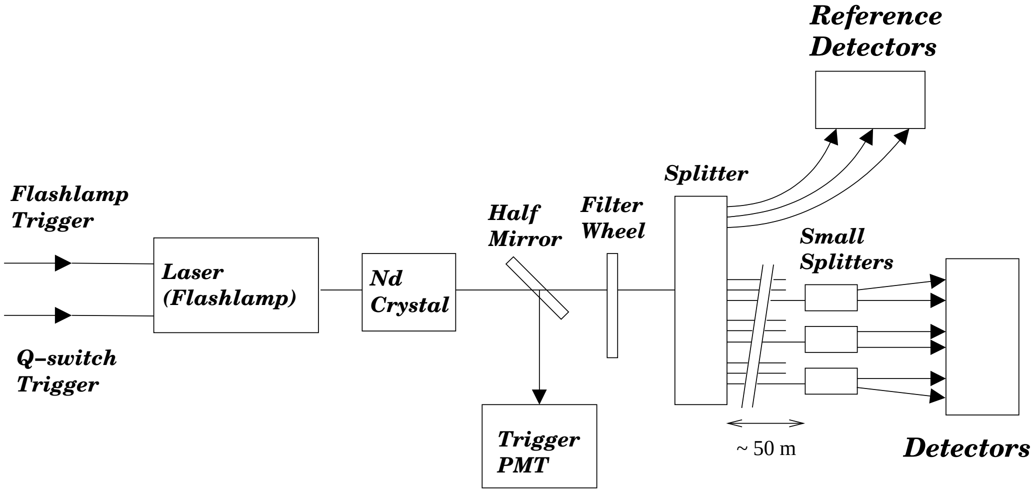

Figure 3.15: Layout of the GMS system.

Figure 3.15 shows the configuration of the system. It used a Nd:YAG laser with a 532 nm wavelength as the light source. A light filtering system, consisting of a rotating wheel (see Figure 3.16(a)) with several attenuation plates, varied the intensity of light source, which can be clearly seen in Figure 3.16(b). In Figure 3.16(a), the indicated holes are aligned along the radii of the motorized wheel. The attenuation filters are attached to the large, outermost holes. The small holes are coupled with fixed LED / photo-transistor pairs (shown as (1) in Figure 3.16(a)), whose signals are used for filter identification and laser triggering. An optical coupler (shown as (2) in Figure 3.16(a)) carries the filtered light to the main optical fiber. The filtered light pulses were sent to an

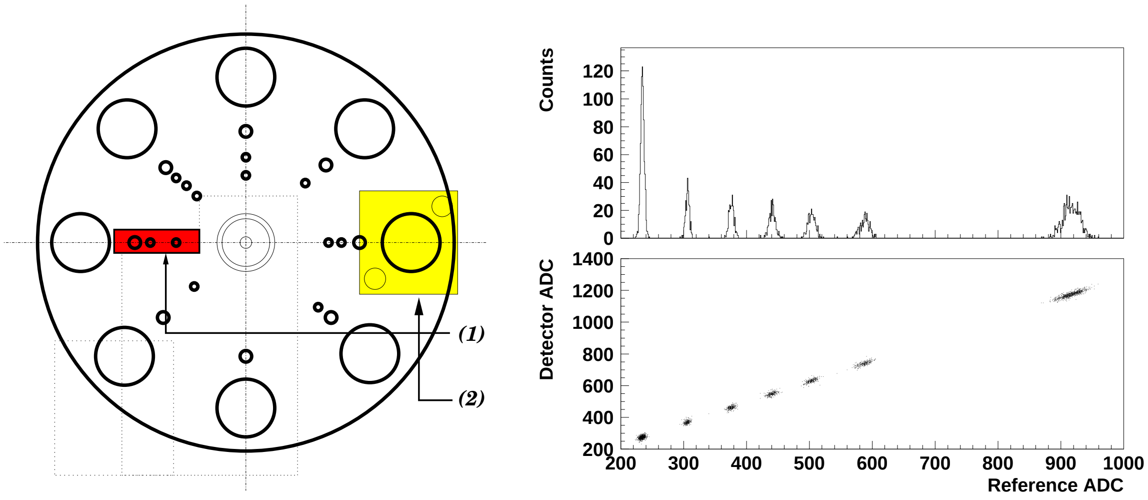

(a) (b)

Figure 3.16: (a): Cross section of the light filtering system. (b): The upper panel shows a typical ADC histogram recorded by one of the reference detectors. The lower panel shows the typical correlation between the responses of a monitored detector and a reference detector.

optical splitter (1x16), where the light density of each output channel can be adjusted by the equipped attenuators in order to cover the dynamic range of the ADCs used in different detector system. After splitting, the light pulses are sent to the monitored detectors and also to an array of reference detectors via optical fiber networks with additional smaller splitters. A partially–reflecting mirror between the laser and the light filtering system sends a reflection of each laser pulse to a trigger PMT. Its signal was used to generate a GMS trigger for recording the calibration events and also monitor the laser output level. The PMTs were continuously monitored during HERMES data taking. A laser trigger, which was determined by the trigger lamp (shown as (1) in Figure 3.16(a)), the beam bunch interval and the HERA clock, synchronized with the bunch structure of the HERA electron beam prevented any interference between the laser–calibration events and real DIS events. The GMS event rate is about 3 Hz.

The GMS has three reference detectors: PIN1, PIN2 and PIN4. PIN photo-diodes (S1190, Hamamatsu Corp.) are used for this purpose because of the very small temperature dependence of their gain in the wavelength region of interest. Detector gain is evaluated by comparing the responses of the monitored detectors to those of the reference detectors. As the reference detectors are located far away from the experimental area, they are not subject to the sources of instability that might affect the monitored detectors, such as the effects of stray magnetic fields, background radiation, damage due to nearby beam losses, and so on.

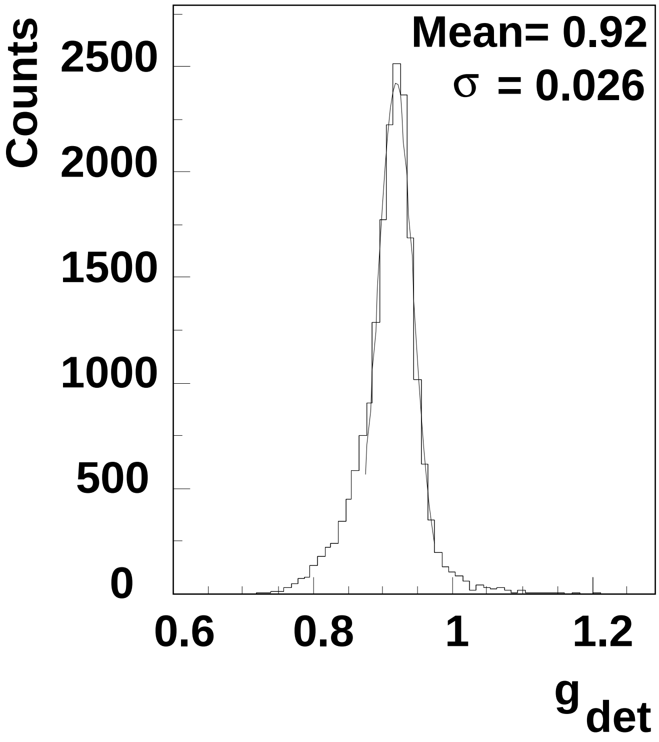

Figure 3.17: Distribution in relative gain measured event–by–event for one of the calorimeter PMTs. The data were collected during a 10–run period where the experimental conditions were stable. The data are superimposed with a Gaussian fit, yielding an intrinsic relative gain resolution of about 3%.

3.4.2 Gain Monitoring

A relative gain is defined as:

$$g_{det} \equiv \frac{R_{det}}{R_{ref}} = \frac{G_{det}}{G_{ref}} \cdot \beta_{det}, \tag{3.14}$$

where R is the response of a PMT to N^{γ} incoming photons, and the gain $G = R/N^{\gamma}$. $\beta_{det} \equiv N^{\gamma}_{det}/N^{\gamma}_{ref}$ is the ratio of the number of incoming photons between the monitored detector and reference detector. In real analysis, the relative gain is evaluated by averaging the responses R_{det} and R_{ref} over a sample of the GMS events:

$$g_{det} \equiv \frac{\sum_i R^i_{det}}{\sum_i R^i_{ref}}, \tag{3.15}$$

where the index i runs over all GMS events recorded in the time interval of the measurement. The resolution of this averaged relative gain is roughly $\sigma/\sqrt{N}$, where σ is the intrinsic resolution in relative gain of a single–event GMS measurement, and N is the

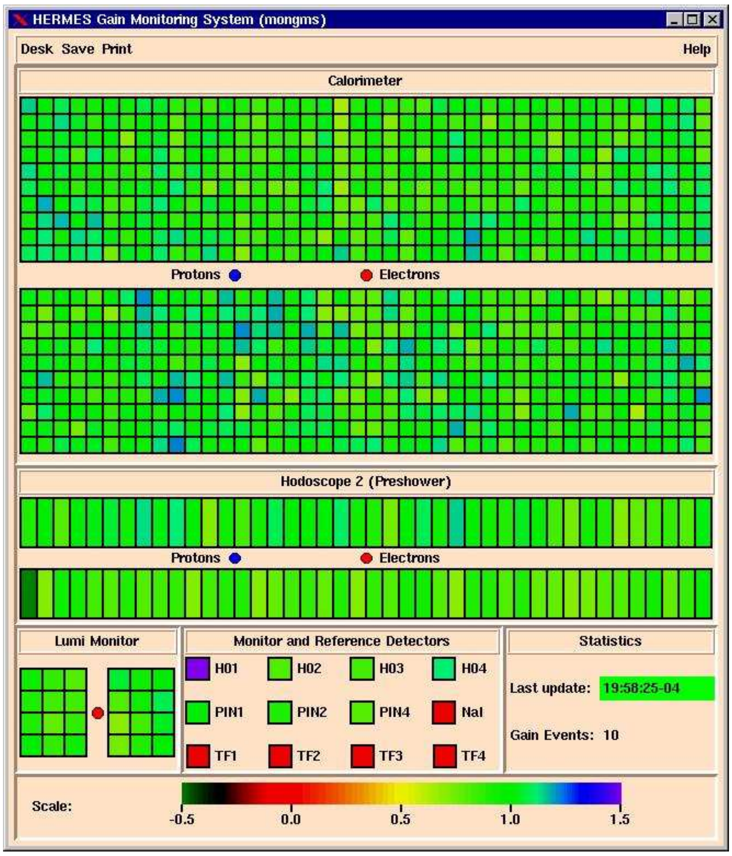

Last update: 19:58:25-04

Gain Events: 10

Figure 3.18: The GMS online monitoring client. All the monitored channels are displayed for the shift crew. As explained by the color scale at the bottom, colors other than green indicate deviation of a PMT gain from its latest recorded reference value. For example, the red squares indicates the current malfunctioning PMTs in the detectors.

total number of the GMS events used in the calculation. By analyzing a sample of the GMS events during a span of data taking, we can get the relative gains of PMTs with the time dependence.

As the histogram of relative gain measurements for the electromagnetic calorimeter shown in Figure 3.17, the intrinsic resolution of the relative gain determination was obtained by applying a Gaussian fit to the relative gains. Each relative gain is determined by a single GMS event from a sample of the GMS events. The standard deviation σ was found to be about 3 %. This intrinsic resolution is due to the light propagation and distribution systems (*e.g.*, spatial variation of the light pulses).

In the gain monitoring, the relative gains were actually normalized to the "initial" relative gains, which were acquired when PMTs were in good condition. The initial

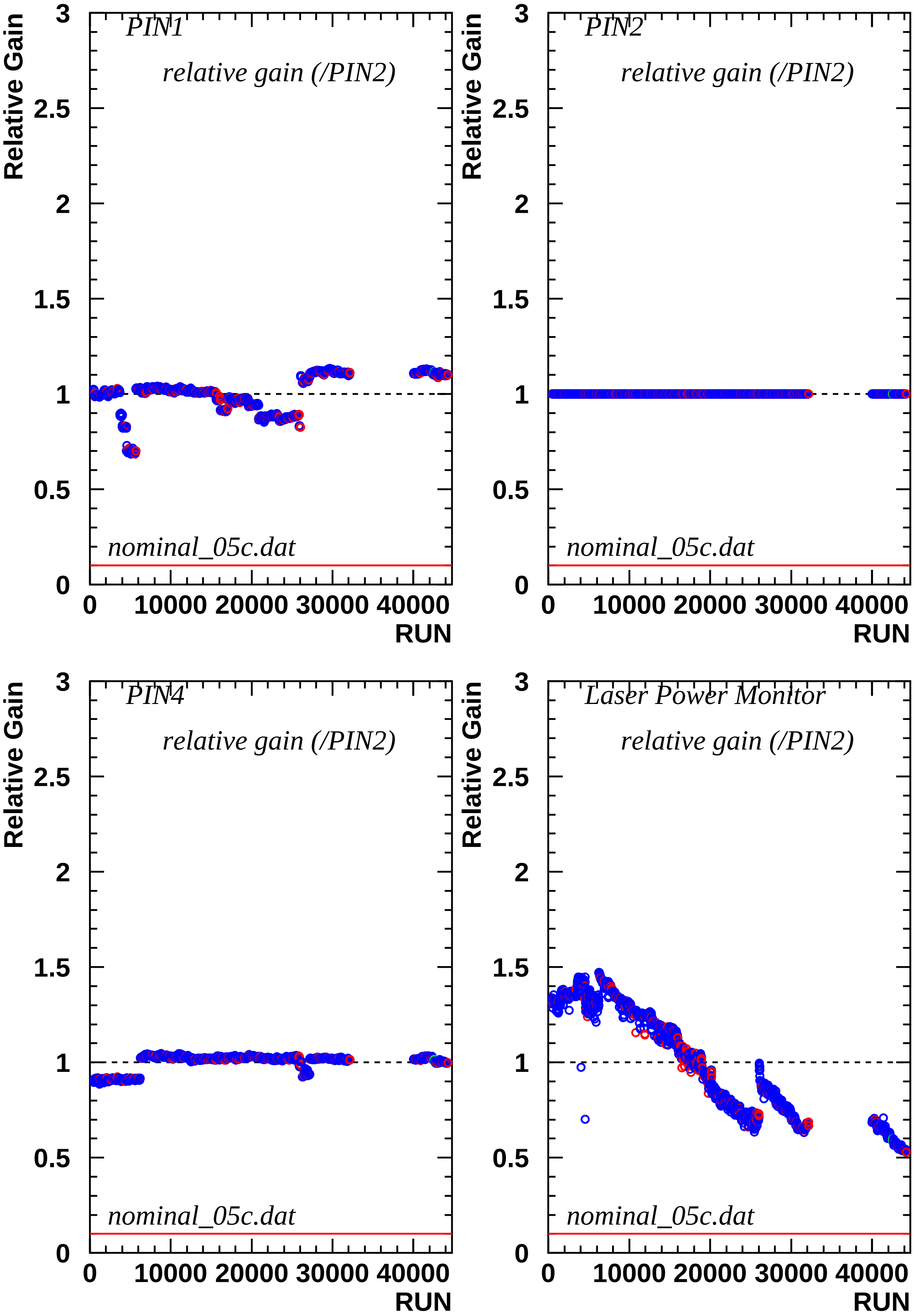

Figure 3.19: The normalized relative gains of the reference detectors (PIN1, PIN2 and PIN4) and the laser power monitor in one data taking period 2005. The reference detector PIN2 was used for normalization. “run” numbers are increased with the time of data taking, which will be explained in Sec. 3.5.

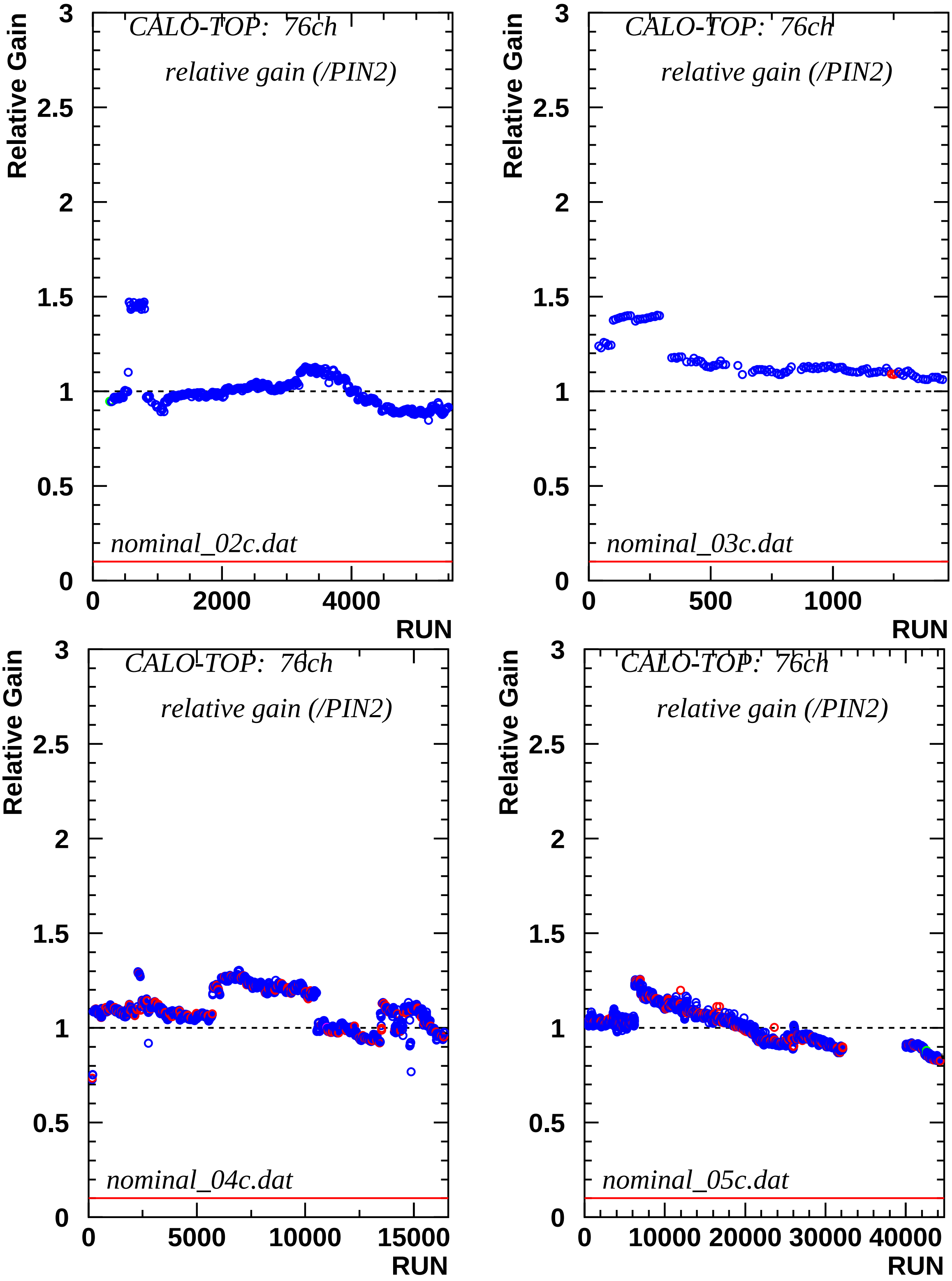

Figure 3.20: The normalized relative gains of a channel in the top half of the calorimeter detector in years 2002–2005. Here the reference detector PIN2 was used for normalization. "run" numbers are increased with the time of data taking.

relative gains were updated every a few months. Online monitoring system was to provide a real–time (20–30 s) information of the normalized relative gains of detectors, which was used to diagnose the detector problems, such as High Voltage (H.V.) trips or readout chain failures. Figure 3.18 is the online monitoring software for the shift crew to frequently check the working condition of all the channels.

Figure 3.19 shows the normalized relative gains of three reference detectors (PIN1, PIN2 and PIN4) and the laser power monitor in one data taking period 2005. The relative gains were normalized by the gains of PIN2. The status of three reference detectors are mostly very stable, except a little fluctuation in the reference detector PIN1. The laser power was decreasing in a long period because of the decline of the laser flashlamp. The average life time of the flashlamp was about 3 months. Hence, the laser flashlamp was replaced several times during one data taking period, judging on the quality of the laser.

Figure 3.20 shows the representative measurement of the ratios of the current relative gains to the initial values "nominal data" during the data taking period of 2002–2005. The "nominal data" was taken as the averaged relative gain in each data taking year. The fluctuations of the normalized relative gains correspond to the changes of the spectrometer during the data taking, such as the condition of the beam and the spectrometer, and the changes on the GMS system. The blue point indicates the transversely polarized hydrogen run and the red point is the unpolarized run. The steady relative gains in Figure 3.20 shows the stable data taking of the transversely polarized hydrogen target runs.

The similar plot to Figure 3.20, which shows the normalized relative gains of part of the channels to represent all the 952 monitored channels, were reported every week to the collaboration to present the status of the monitored PID detectors during the latest one week. During offline analysis, the GMS data were analyzed to provide data–quality checks on the detector responses. As will be discussed in Sec. 4.1, the data quality bit 17 gives the number of dead blocks in the calorimeter and bit 18 gives the number of dead blocks in the luminosity monitor and in the pre–shower hodoscopes (H2), which are monitored by the GMS. The GMS system provides the data qualities of the calorimeter, H2 and luminosity detectors, which produce necessary criteria of the positron–hadron separation and the luminosity measurement. Hence, the GMS provides the important information of data qualities of the data production.

3.5 Data Acquisition and Processing

The backbone of the Data AcQuisition (DAQ) system was constructed in Fastbus. It consisted of 10 front–end crates, an event collector crate, and an event receiver crate, connected to the online workstation cluster via two SCSI interfaces. CERN Host Interfaces (CHI) acted as Fastbus masters, and their performance was enhanced by Struck Fastbus Readout Engines (FRE) containing two Motorola 96002 DSPs.

The drift chambers were read out by LeCroy multi–hit, multi–event 16–bit 96 channel

TDCs (model 1877). Charge from the photomultipliers and from the TRD was digitized by LeCroy multi–event 64 channel 1881M multi block ADCs. These ADCs and the TDCs were capable of sparsifying the data, *i.e.*, online suppressing channels with pedestal levels from the readout. The magnet chamber readout was instrumented with the LeCroy VME based PCOS4 system. The vertex chamber data arrived from the detector as a 16 bit ECL STR330/ECL data stream and were processed in one of the VC DSPs. Double buffering was implemented in the dual DSPs of the Fastbus masters. Event collection on one DSP was done in conjunction with readout from the second DSP to the DAQ computer. In addition to the standard readout, a series of asynchronous independent events from the luminosity monitor and from monitoring equipment could be read out at rates exceeding 5 kHz. One VME branch with 4 crates and three CAMAC branches with 9 crates were used for these events.

The data were arranged into the following time structure:

- *Burst:* Events were grouped into *bursts*, defined as the interval between two successive reads of the experiment scalers. A burst was roughly 10 seconds long. Data quality was checked on the burst level.

- *Run:* The size of the files stored on disk and tape was adjusted so that an integral number of *runs* can fit on a tape. At high instantaneous luminosity, one run can be as short as 10 minutes. A run was the basic unit of data for analysis. Calibration constants were applied at the run level, although not all detectors were calibrated with this time granularity.

- *Fill:* Runs were grouped into *fills*, which were simply defined as data collected during a given fill of the electron beam in the storage ring. A fill is typically 8 hours.

Each event associated with a trigger condition went to the DAQ data stream as a single event record. Scaler events were recorded approximately every burst in which all the scalers in the experiment were read out. Each period of time between scaler events defined a burst. A data file corresponding to a run was ended either automatically whenever 450 Mbytes of information had been collected, or manually by the shift crews. The output of the DAQ data stream was written in EPIO (experimental physics input output) format to staging disks over the course of a fill of the storage rings and copied fills to storage silos on the DESY main site. In parallel, they were stored on local DLT tape drives for redundancy. The dead time during standard running was typically well below 10% and the downtime due to the data acquisition system was estimated to be below 1%.

The recorded data are processed through a production chain including the main production, the slow control production and the micro data summary tape (μDST) production. The main production is to decode raw data collected online and reconstruct events based on existing detector calibrations. The slow control production is responsible for collecting and synchronizing data from the raw slow control files and expert files containing offline calibrations. The slow control data means the calibration data, such as GMS data.

The μDST production aims to produce a single data file for each run which contains the tracking data from the main production for selected events, the relevant slow control data from the slow control production, and the data quality information. These files can be reliably used for physics analysis without concern for the details of the data collection. The produced μDST files are labelled by 4 characters consisting of the last two digits of the corresponding year, a letter indicating the production, and an index number. For example, 05c1 means the first version of the c–production in the year 2005. Productions with a higher version (for a given year) are assumed to be of a higher quality. Detector calibrations from previous data taking period are applied in the first μDST production (a–production). Using a–production to re–calibrate the detector produces next μDST production(b–production). In c–production, additional corrections and improved calibrations are taken into account. The index number is increased with each slow control production with improved slow control information. The data analysis presented in the next chapter is based on the c–productions from 2002 to 2005.

Chapter 4

Data Analysis

In the years 2002–2005, the HERMES experiment collected data with a transversely polarized hydrogen target. The extraction of azimuthal single–spin asymmetry amplitudes from the accumulated semi–inclusive DIS events is presented in this chapter. In Sec. 4.1 and Sec. 4.2, several criteria are set up in order to ensure a high quality of the data before semi–inclusive events are identified from the reconstructed tracks by certain geometry and kinematic requirements. The obtained count rates of semi–inclusive events are used to form a single–spin asymmetry depending on the azimuthal angles in Sec. 4.3. With a two–dimensional fit the unique azimuthal modulations of the dihadron fragmentation effect are extracted. In Sec. 4.4, systematic effects from different sources are investigated in detail to estimate influences on the extraction results. The acceptance effects on the asymmetry moments are discussed in Sec. 4.5, where the method to extract the amplitudes from the HERMES data was chosen so as to minimize the acceptance effects. The systematic uncertainties from the acceptance were estimated.

4.1 Data Quality

Not all the events in the μDST file can be used in physics analysis, since some of the recorded events were measured when some detectors were not working properly or other parts of the experiment had some problem. The information about the performance of the experiment relating instrument is stored based on burst level (cf. Sec. 3.5). To ensure a high Data Quality (DQ) in each recorded burst, several measured quantities are checked for consistency. The checklist includes:

- the rate of the luminosity monitor
- the beam current
- the beam polarization

- the status of the target
- the data acquisition system
- the information from the shift logbook
- malfunctioning PID detectors
- high voltage trips in the wire chambers.

For each burst, 32–bit pattern was set, of which each bit corresponds to one of the information and is set to 1 if the related part was working properly. For each data production, a burst list with the information of the data quality is provided by HERMES data quality group. Table 4.1 listed the corresponding information for each bit for the data during the years 2002–2005. Details about the data quality checks can be found in Rf. [179] and on the HERMES μDST data quality web page [180].

This work requires a hexadecimal bit pattern 0xFFFFFFFD, where the most right–hand digit corresponds to the binary bit numbers from 0 to 3 shown in Table 4.1. Here only bit number 1 is loosed. Bit number 1 asks the reasonable beam polarization, which is not the requirement for this target single–spin asymmetry analysis. Some specific data quality settings, which need to be more clarified, are:

- bit number 5: the luminosity rate. In 2005 reasonable luminosity rate ($1\,\mathrm{Hz} \leq L \leq 100\,\mathrm{Hz}$) is required. During the years 2002–2004 ($1\,\mathrm{Hz} \leq L \leq 50\,\mathrm{Hz}$) is imposed.
- bit number 28: beam polarization is measured in recent 5 min. Bit set 1 is needed since in the present analysis an unpolarized beam is preferred. In order to make the whole dataset averagely zero beam polarization, the accurate measurement of the beam polarization is important.
- bit number 31: no dead blocks in calorimeter. In the year 2002 one block dead in the calorimeter is allowed, in which the calorimeter suffered from ageing. It caused several failures of PMT units. An elaborate study showed that one dead unit does not influence semi–inclusive azimuthal asymmetries of charged hadrons [163]. In other 3 years, no dead block is allowed in the calorimeter.

4.2 Event Selection

After the DIS triggered data passed the data quality selection on the burst level, a set of selections based on the event level were also applied in the analysis chain. First of all, each track in the event has to be in the effective HERMES spectrometer detection area. Secondly, with the information from particle identification we can identify the

BIT	Quality	value	explanation	SET
0	DAQ iTargetBit	4‖8	nuclear polarization states	1
1	Beam rPolFit	(30, 80)	reasonable beam polarizations	0
2	DAQ rDeadCorr		select reasonable dead time	1
3	DAQ rLength	(0, 11]	burst length	1
4	Beam rMdmCurr	(5, 50]	beam current value	1
5	Beam rLumiFitBstGai	(1, 50]	luminosity rate	1
6	Quality iuDSTbad		drop first burst in a run	1
7	Quality iuDSTbad		drop bad uDST records	1
8	Quality iuDSTbad2		drop no PID bursts	1
9	Quality iExpment	1	Logbook: analyzable burst	1
10	Quality iExpMode	2	select two state target	1
11	Quality iExpMode	0‖16	unpolarized target	1
12	Quality iExpMode	<0	Logbook: no Logbook DQ info	1
13	Quality iExpMode	3	3–state target	1
14	Quality iExpMode	4	special 2–state mode target	1
15	Unpol iGasType	>0	no unpolarized data	1
16	Target		no bad target DQ	1
17	Quality bCaloDead		no dead block in calorimeter	1
18	Qaulity bH2LumiDead		no dead block in H2 or Lumi	1
19	Qaulity iTrdDQ		no TRD bad burst	1
20	HVtrip		no HV trips in FC and BC	1
21	Daq iRun		no bad RICH	1
22	HVTrip		no HV trips in RICH	1
23	ABS rAlpha0		fixed polarization value	1
24	ABS rAlphaR		fixed polarization value	1
25	Quality bCereDQ		no RICH bad infomation	1
26		empty		1
27	ABS CalCarryOver		fixed polarization value	1
28	Beam iPolFitGap	$\|T_{Gap}\| \leq 300$	beam pol. meas. within 5 min.	1
29	Target rPol	empty		1
30	DAQ rDeadCorr21	[0.5, 1.0]	select reasonable dead time	1
31	Quality bClaoDead		no dead block in calorimeter	1

Table 4.1: Data quality bit pattern for polarized burst lists. The resulting bit pattern is 0xFFFFFFFD.

	charged particles
origin vertex position	$\lvert z_{\mathrm{vertex}}\rvert \leq 18\,\mathrm{cm}$
track passed the fiducial volume cut	($iSelect$ & 0x0100) == 0
front field clamp position (z=172 cm)	$\lvert x\rvert < 31\,\mathrm{cm}$
septum plate position(z=181 cm)	$\lvert y\rvert > 7\,\mathrm{cm}$
rear field clamp position (z=383 cm)	$\lvert y\rvert < 54\,\mathrm{cm}$
rear clamp position (z=383 cm)	$\lvert x\rvert \leq 100\,\mathrm{cm}$
	$\lvert y\rvert \leq 54\,\mathrm{cm}$
calorimeter position (z=738 cm)	$\lvert y\rvert \leq 108\,\mathrm{cm}$

Table 4.2: Geometric restrictions applied for all charged tracks. The coordinate was defined in Sec. 3.3. The positions of the various components of the spectrometer were plotted in Figure 3.6.

positron and different hadrons with a quite reliable efficiency (cf. Sec. 3.3). Finally, the kinematics selections will be considered in two phases: The first step is to put DIS kinematics requirements on all the candidate events, and the second step is to apply the semi–inclusive DIS restrictions to the final detected hadrons.

4.2.1 Geometry Restrictions

The geometry restrictions, including fiducial volume cuts and additional geometry requirements listed in Table 4.2, take into account the following consideration on the particle tracks:

- Fiducial volume cut requires that the track is inside the volume of the calorimeter, and the truncated mean pulse height for the TRD was corrected for gas pressure.
- The reconstructed original vertex z_{vertex} of the track is restricted to the target cell region.
- Additional fiducial volume cuts ensure that the track reconstruction was not influenced by the edges of the HERMES spectrometer. The vertical and horizontal positions of the track are checked at the locations of several detector components which limit the HERMES acceptance.

These requirements are aimed to suppress the background of the ambiguous track measurement.

4.2.2 Particle Identification

Particle identification is a crucial specification for an experiment measurement. With particle identification we can access the physical quantities which are not able to be studied without it. Better particle discrimination can also significantly improve the accuracy of the measurement results.

Lepton–Hadron Separation

As introduced in Sec. 3.3.3, the PID system at HERMES experiment provides a clear separation between leptons and hadrons with efficiency higher than 99% and with less than 1% contamination [155]. The following cuts were put to the data analysis in order to discriminate the leptons and hadrons:

$$\begin{aligned} \text{leptons}: &\qquad PID_3 + PID_5 > 1, && (4.1) \\ \text{hadrons}: &\qquad -100 < PID_3 + PID_5 < 0. && (4.2) \end{aligned}$$

Hadron Identification

The hadron identification are performed by the Čerenkov detector (cf. Sec. 3.3.3). During the data taking period, the RICH detector was used to discriminate among pions, kaons and protons. Based on the different PTH method [170] (cf. Sec. 3.3.3), the total likelihood $\mathcal{L}_i^{\text{tot}} = \mathcal{L}_i^a \cdot \mathcal{L}_i^g$ defined in Eq. (3.5) is assigned to the track. By defining the quality parameter

$$\text{rQp} = \log_{10} \frac{\mathcal{L}_{h_1}^{\text{tot}}}{\mathcal{L}_{h_2}^{\text{tot}}} \tag{4.3}$$

as the the logarithm of the likelihood ratio of the most and the second most likely hadron types, h_1 and h_2, we can use the criterion that rQp should be positive if the identification is successful. Once the identification algorithm could not find a most probable hadron type, the quality parameter rQp is set to zero. In this analysis we required two pion production. From Čerenkov angles distribution versus particle momentum in two different layers shown in Figure 3.10, we can see that pion can be selected out under the condition momentum $p > 1\,\text{GeV/c}$. Hence we select the pion candidate with the cuts:

$$\begin{aligned} \text{RICH} \quad PID &= 3 \quad \text{(Pion)}, && (4.4) \\ rQp &> 0, && (4.5) \\ p &> 1\,\text{GeV}/c, && (4.6) \end{aligned}$$

in the RICH algorithm.

	inclusive DIS	semi–inclusive DIS
four momentum transfer	$Q^2 > 1\,\mathrm{GeV}^2$	$Q^2 > 1\,\mathrm{GeV}^2$
invariant mass of the final state	$W^2 > 4\,\mathrm{GeV}^2$	$W^2 > 10\,\mathrm{GeV}^2$
fractional energy transfer	$0.1 < y < 0.85$	$0.1 < y < 0.85$
Bjorken scaling variable	$0.023 < x < 0.4$	$0.023 < x < 0.4$
exclude exclusive channel		$M_X > 2\,\mathrm{GeV}$
total energy of the final states		$E_{\mathrm{tot}} < 28\,\mathrm{GeV}$
invariant mass of $\pi^+\pi^-$ pair		$0.25\,\mathrm{GeV} < M_{\pi\pi} < 2\,\mathrm{GeV}$

Table 4.3: The kinematic cuts for the selection of inclusive and semi–inclusive DIS events.

4.2.3 Kinematic Selections

Based on the particle identification, we can select the events that consist of the scattered DIS lepton and the produced final hadron pair, *i.e.*, $\pi^+\pi^-$ pair, with a set of kinematic cuts listed in Table 4.3. The selections can be grouped into two categories: inclusive DIS cuts and semi–inclusive DIS cuts, which can be used to filter the experimental data to acquire the needed DIS sample for luminosity spectator and the semi–inclusive $\pi^+\pi^-$ DIS samples for data analysis, respectively.

Inclusive DIS Process Selections

Before make any selections, the events sample should at first have the mark of DIS trigger, numbered as trigger 21 (cf. Sec. 3.3.5). Among the DIS triggered events, we choose those events which contain at least one detected lepton. Then pick one of the leptons in each event as the candidate of DIS lepton and check the resulting kinematic variables with the inclusive cuts in Table 4.3. For inclusive DIS events, it can also be used for the luminosity normalization as described later. The motivation of the selections are:

- A four–momentum transfer $Q^2 > 1\,\mathrm{GeV}^2$, *i.e.*, larger than the squared proton mass, is required for scattering processes in the deep inelastic region.

- The invariant mass of the final hadronic state W has to be in the region $W^2 > 4\,\mathrm{GeV}^2$. This selection is to remove the processes of the excitation states of proton, *i.e.*, N and Δ resonances, which are almost lower than 2 GeV.

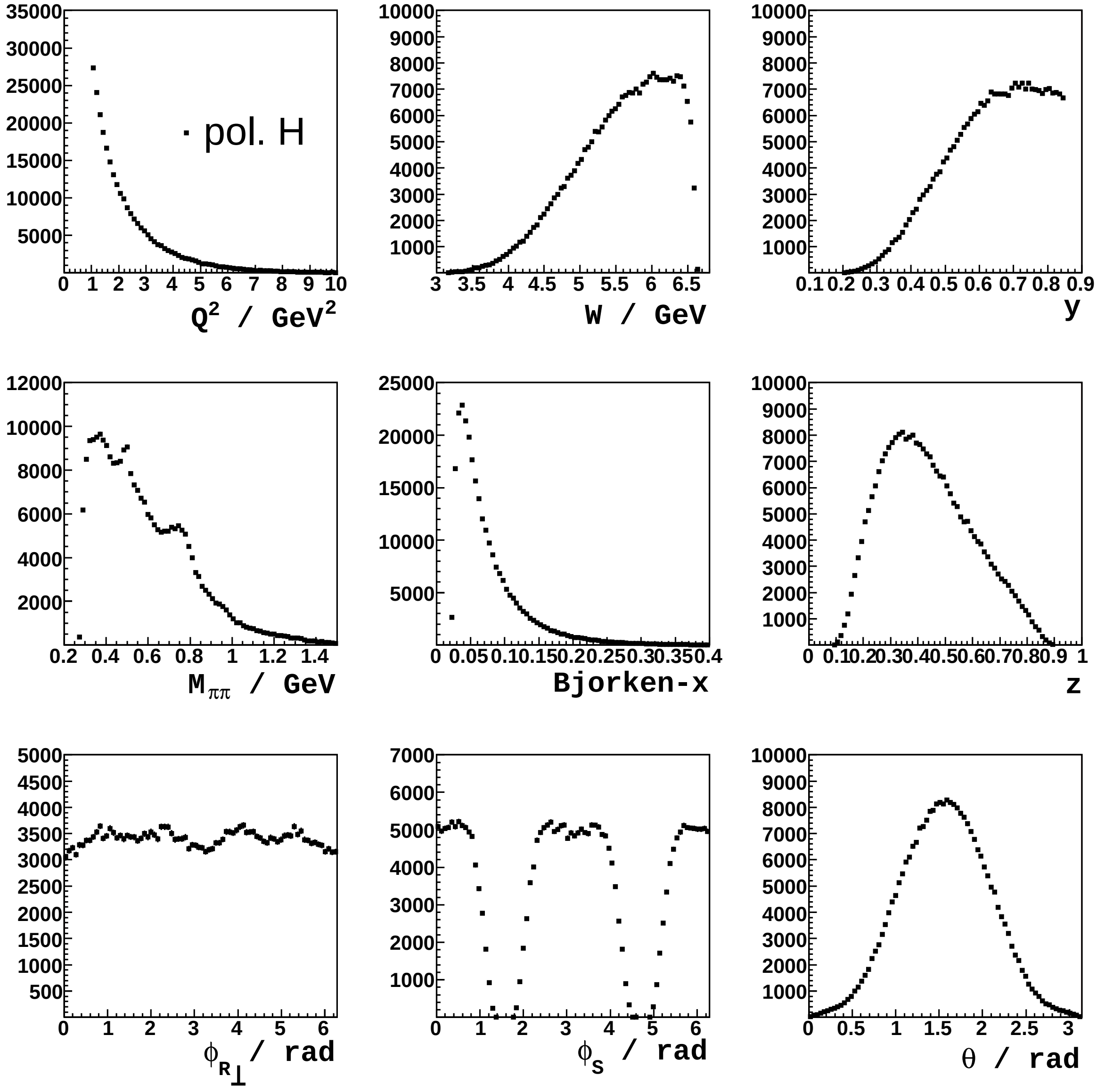

Figure 4.1: The distribution of the kinematic variables for the transversely polarized target data in the years 2002–2005.

- The fractional energy transfer y has the upper limit to eliminates DIS events from a region with a large contribution to the cross section by higher order QED effects, *e.g.*, bremsstrahlung. This limit discards leptons with momentum lower than 4.1 GeV, where $y = 0.85$. On the other hand, the restrictions on W and Q^2, the lowest possible value of y is 0.07. It is however excluded by a lower cut of $y > 0.1$.

- Bjorken scaling variable x range is determined by the HERMES acceptance and by the cuts on Q^2 and W.

If more than one lepton exists in the same event after the geometry and DIS kinematic cuts, only the one with the highest momentum is chosen as the DIS lepton candidate.

Semi–Inclusive DIS Process Selections

To choose the $\pi^+\pi^-$ data sample, the DIS event has to contain at least one combination of the RICH–identified $\pi^+\pi^-$. The required semi–inclusive DIS cuts in Table 4.3 ensure the cleanness of the DIS $\pi^+\pi^-$ sample. In addition to the inclusive cuts, more strict kinematic conditions were applied to the semi–inclusive data. The details about those cuts are described in the following:

- The invariant mass of the final hadronic state W is required to be $W^2 > 10\,\mathrm{GeV}^2$, whose lower limit is higher than that of the inclusive DIS cut. Higher cut is to strictly remove those target excitation processes, which do not belong to deep inelastic scattering and to ensure that the fragmentation process happens. This higher cut also helps improving the separation between the hadrons carrying the information of the struck quark from the hadrons which come from the target remnant [181].

- The constraint was placed on the missing mass: $M_x > 2\,\mathrm{GeV}$. This excludes the contribution of the exclusive two–pion channels, for which factorization in distribution and fragmentation functions cannot be applied. The cut on 2 GeV is a better choice than 0 GeV, since it removes the resonance around the proton mass with the momentum resolution of the HERMES spectrometer [35].

- The $\pi^+\pi^-$ pair invariant mass $M_{\pi\pi}$ is upward limited by the HERMES kinematics. The lower limit 0.25 GeV is the sum of two pions' invariant mass $2m_\pi$. Practically this can be automatically satisfied.

All possible combinations of detected $\pi^+\pi^-$ pair will be treated as separate semi–inclusive event. The total number of selected inclusive and semi–inclusive events are listed in Table 4.4, where RICH algorithm IRT was used in data 2002–2003 and EVT was used in data 2004–2005. Figure 4.1 shows the kinematic distributions after all the selections.

	2002	2003	2004	2005	2002–2005
# of DIS events	679353	348818	2277665	4840647	8146483
$\langle P_B \rangle$	0	0.303	-0.039	-0.034	-0.020
# of SIDIS $\pi^+\pi^-$ events	22914	10676	76612	172222	282424

Table 4.4: The number of the selected DIS events used for luminosity normalization and the net beam polarization obtained from DIS samples during the years 2002–2005. The number of the selected semi–inclusive $\pi^+\pi^-$ events are also listed, where RICH algorithm IRT was chosen for data 2002–2003 and EVT for data 2004–2005.

In the ϕ_s distribution on the bottom center of Figure 4.1, the events number is zero at $\phi_s = \frac{\pi}{2}$ and $\phi_s = \frac{3\pi}{2}$. That is because that the target polarization axis is always along the z–axis. So $\phi_s = \frac{\pi}{2}$ or $\phi_s = \frac{3\pi}{2}$ means that the lepton scattering plane is horizontal, that is ,on the xy–plane (see Figure 2.2). In such case, there are no triggers because the scattered lepton is blocked by the horizontal plate in the magnet.

4.2.4 Lepton Beam Polarization

The measurement of the asymmetry A_{UT} requires the unpolarized lepton beam, *i.e.*, with zero polarization. But at HERMES experiment, the longitudinally polarized HERA positron beam are utilized (cf. Sec. 3.1). When the net beam polarization is zero during the whole period of data collection, the beam longitudinal polarization effect can be cancelled out. To achieve that, the number 28 bit in the data quality bit pattern was set 1 (cf. Sec. 4.1) in order to ensure that the net beam polarization is zero.

Specially in the data taking year 2002 the beam polarization in HERA storage ring was not optimized just after a major upgrade [121]. So the polarization of each lepton in the beam was randomly distributed and the net beam polarization is considered to be 0. Furthermore in 2003, the beam polarization of about one eighth of the data samples were wrongly set to -1%, while in fact they have larger polarizations (about 10–20%). The events with fake beam polarization value were discarded in data analysis. In Table 4.4, the net beam polarization of the whole data set in years 2002–2005 can be found quite small and slightly negative. The systematic studies on the nonzero beam polarization in Sec. 4.4.2 concludes that it is negligible.

In fact, even if the average beam polarization is nonzero, the cross section σ_{LT} and σ_{LU} at leading twist do not contribute to the transverse single–spin asymmetry A_{UT}, thanks to the integration over the transverse momentum $\boldsymbol{P_{h\perp}}$ [113, 122]. Another argument is that due to the unique azimuthal angle dependence, the extracted amplitude $A_{\mathrm{UT}}^{\sin(\phi_{R\perp}+\phi_S)\sin\theta}$ will not be affected by the beam polarization [121]. In Sec. 4.4.2, the amplitudes $A_{\mathrm{UT}}^{\sin(\phi_{R\perp}+\phi_S)\sin\theta}$ extracted from different nonzero beam polarization samples were compared and found to be a consistent for all the beam helicity stats.

4.3 Extraction of the Asymmetry Amplitudes

The basic ideas and methods of extracting the asymmetry amplitudes from experimental data will be discussed in this section.

4.3.1 Transverse Single–Spin Asymmetry

The transverse single target–spin asymmetry A_{UT}, as theoretically defined in Eq. (2.93), can be measured in the experiment by the following equation (cf. Appendix C)

$$A_{\mathrm{UT}} = \frac{1}{\langle|\boldsymbol{P_T}|\rangle} \frac{N^{\uparrow}/N_{\mathrm{DIS}}^{\uparrow} - N^{\downarrow}/N_{\mathrm{DIS}}^{\downarrow}}{N^{\uparrow}/N_{\mathrm{DIS}}^{\uparrow} + N^{\downarrow}/N_{\mathrm{DIS}}^{\downarrow}}. \tag{4.7}$$

Here, $N^{\uparrow(\downarrow)}$ is the number of the selected $\pi^+\pi^-$ pair events when the target is either polarized upwards (↑) or downwards (↓). Both these numbers are normalized to the numbers of inclusive DIS events $N_{\mathrm{DIS}}^{\uparrow(\downarrow)}$ [1] with the correspondingly polarized target. $\langle|\boldsymbol{P_T}|\rangle$ is the weighted absolute target polarization value with the luminosity constant. In this work, the average value of the proton polarization was 0.74 ± 0.06. Appendix C shows the details how the formula Eq. (4.7) is derived. It was argued that Eq. (4.7) is well established if the target polarization is balanced. As shown in plot 4.2, the net zero target polarization is nicely guaranteed, as the target polarization flips frequently, *i.e.*, every 60 s (cf. Sec. 3.2).

In Appendix C, the pion pair detection efficiency in HERMES spectrometer was assumed to fulfill the requirement in Eq. (C.8). But due to the operation of the transverse holding magnet field, the above condition is not completely fulfilled, which means the asymmetry and the extracted amplitude might be affected by the distorted acceptance from the transverse target magnet. For instance, this effect can be seen in Figure 4.3, which shows the two–dimensional distribution of the azimuthal angles $\phi_{R\perp}$ versus ϕ_S (defined in Eq. (2.73a) and Eq. (2.2), respectively), the two kinematic variables that A_{UT} directly depends on. For the distribution in the left plot, the events for both target polarization states are summed up, such that the contribution from σ_{UT} cancels (see

---

[1] Luminosity monitor (cf. Sec. 3.3.4) in HERMES spectrometer is designed for luminosity measurement. But in this work using the DIS events for normalization is safer than the luminosity counting by the luminosity monitor, because the combined positron (year 2002–2004) and electron (year 2005) beam data were used in analysis. In this case, there needs special treatment in combining the counting on the luminosity from positron and electron data.

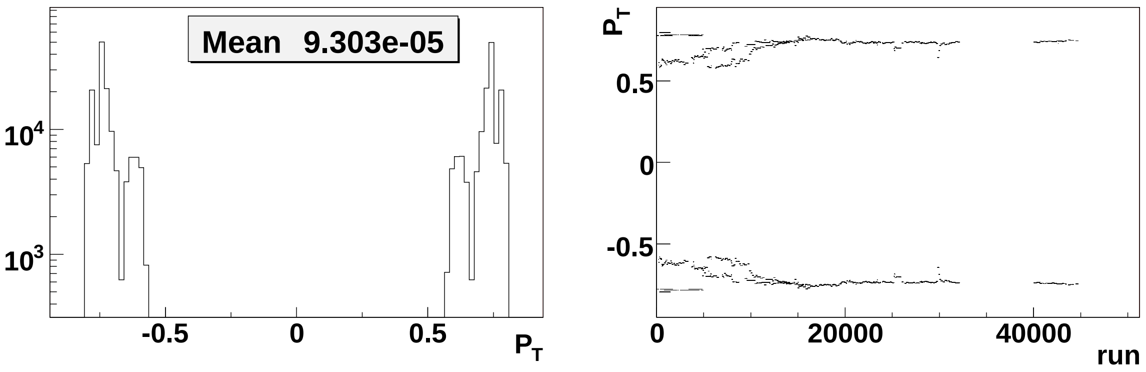

(a) (b)

Figure 4.2: Figure 4.2(a) shows the target polarization distribution of the whole dataset. Figure 4.2(b) presents the target polarization versus run number. The average target polarization is $\langle P_T \rangle = 0.0001$. The two plots show how well the target polarizations were balanced both in measurement time and in polarization value.

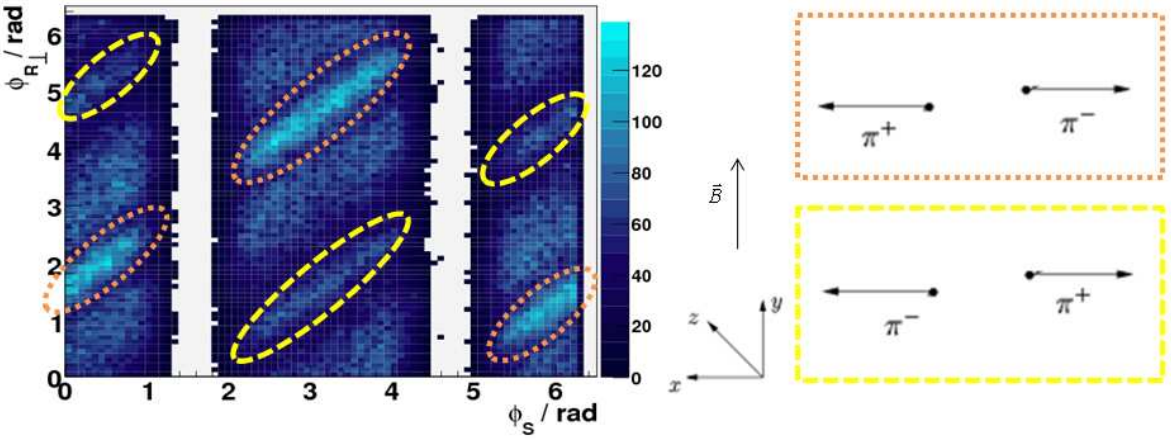

Figure 4.3: The left plot is the measured distribution of the azimuthal angles $\phi_{R\perp}$ versus ϕ_S for the transversely polarized hydrogen data. The dotted and dashed line area are positively correlated, where the two pions are in the same half of the spectrometer. The right one is a simplified picture of the HERMES transverse magnet effect to the two pions. Here the beam direction goes into the paper (z–axis) and the magnet field direction is along y–axis. Two possible x–components of the relative momenta of the $\pi^+\pi^-$ pairs are shown, which correspond to the area with the same line in the left plot, respectively.

Eq. (2.92b)) and also the unpolarized cross section σ_{UU} (Eq. (2.92a)) is independent of both $\phi_{R\perp}$ and ϕ_S. Therefore, the complicated distribution in left plot can be entirely attributed to the limited geometrical spectrometer acceptance, *i.e.*, using a 4π acceptance detector this distribution would be homogeneous. The gaps in the ϕ_S distribution and the diagonal patterns are due to the gap in the geometrical acceptance between the top and bottom parts of the spectrometer, as discussed in Figure 4.1 (cf. Sec. 3.3). The large difference in the number of events in the encircled parts of the distribution with different line is just related to the effect of the transverse target magnet on the way of outgoing charged particle tracks when they are in the same half of the detector. The outside area are the events with the two tracks in different halves of the detector. The schematic picture of the HERMES transverse magnet on the right plot in Figure 4.3 explains how this effect takes place. With the specified configuration in the right plot, π^+ is always bent to left side and π^- to right side. Depending on both $\phi_{R\perp}$ and ϕ_S, the magnet either bends both particles towards each other (the right–up configuration) or away from each other (the right–down configuration). In the first situation one or both of the pions can be bent into the detector acceptance, in the latter situation one or both can be bent out of the detector acceptance, which can largely decrease the statistics. Later in Sec. 4.5.7, the single–spin asymmetry amplitudes based on different corrections for the target magnet field were compared. It proved that the target transverse magnet does not contribute additional asymmetries to the single–spin amplitude A_{UT}.

The asymmetry amplitude $A_{\mathrm{UT}}^{\sin(\phi_{R\perp}+\phi_S)\sin\theta}$ in Eq. (2.93) depends on the characteristic azimuthal angles $(\phi_{R\perp}+\phi_S)$ and θ. So the events were binned in terms of the two angles in two dimensions. For events with the same values of ϕ_S, the absolute positions of the particles in the detectors are different in the different target polarization states. Their absolute positions are the same only when the values of ϕ_S in the two target polarization states differ by π. To calculate the asymmetry of the azimuthal angles, one should use the following equation:

$$A_{\mathrm{UT}}(\phi_{R\perp}+\phi_S,\theta)=\frac{1}{\langle|\boldsymbol{P_T}|\rangle}\frac{N^{\uparrow}(\phi_{R\perp}+\phi_S,\theta)/N^{\uparrow}_{\mathrm{DIS}}-N^{\downarrow}(\phi_{R\perp}+\phi_S+\pi,\theta)/N^{\downarrow}_{\mathrm{DIS}}}{N^{\uparrow}(\phi_{R\perp}+\phi_S,\theta)/N^{\uparrow}_{\mathrm{DIS}}+N^{\downarrow}(\phi_{R\perp}+\phi_S+\pi,\theta)/N^{\downarrow}_{\mathrm{DIS}}}, \quad (4.8)$$

where ϕ_S is calculated by Eq. (2.2). So in this thesis, we will use $\phi_{R\perp}+\phi_S$ to stand for the two target polarization states: $\phi_{R\perp}+\phi_S$ when the polarization direction is up and $\phi_{R\perp}+\phi_S+\pi$ when the polarization direction is down. In the following sections we will discuss two different approaches, named as **least squares fit** and **maximum likelihood fit** to directly extract the single–spin asymmetry amplitudes. The performance of the two fitting methods is also investigated.

4.3.2 Least Squares Fit

The method of Least Squares (LS) [182] is based on the fact that if $x_1, \cdots, x_n$ are n independent Gaussian random variables with the same mean but different σ_i. Let's take

$\hat{\mu}$ as the estimate of the mean value of the variables x_i. The sum $\sum_i^n (x_i - \hat{\mu})^2/\sigma_i^2$ follows the χ^2 probability density function (p.d.f.) with $n-1$ degrees of freedom. Let's consider a set of N independent measurement y_i at known points x_i. The measurement y_i is assumed to be Gaussian distributed with mean $F(x_i; \boldsymbol{a})$ and known variance σ_i^2. The estimator for the mean of the parameters $\boldsymbol{a}$ is given by the LS method as the point in the parameter space where

$$\chi^2 = \sum_{i=1}^{n} \frac{(y_i - F(x_i; \boldsymbol{a}))^2}{\sigma_i^2} \tag{4.9}$$

is at its minimum. The estimator for the variance of the parameters $\boldsymbol{a}$ is given by the tangent planes of the contour in the parameter space defined by

$$\chi^2(\boldsymbol{a}) = \chi^2_{min} + 1. \tag{4.10}$$

This method has been used within HERMES in many previous published analysis works. In this work, we extract the interested azimuthal amplitudes in terms of two–dimensional $(\phi_{R\perp} + \phi_S)$ and θ fit. Let's first assume a simple case of the fit function $F(\phi_{R\perp} + \phi_S, \theta)$. The quantity χ^2 is given by

$$\chi^2 = \sum_{i,j} \frac{(A_{\mathrm{UT}}^{i,j} - F((\phi_{R\perp} + \phi_S)_i, \theta_j; \boldsymbol{a}))^2}{\sigma^2(A_{\mathrm{UT}}^{i,j})} \tag{4.11}$$

where i and j denotes the bin number in $(\phi_{R\perp} + \phi_S)$ and θ, respectively. $\sigma^2(A_{\mathrm{UT}})$ is the variance of the calculated asymmetry A_{UT}. We could bin the data sample into the two azimuthal dimensions with a suitable bin size, in order to have the sufficient statistics. As the number of detected events (for $N > 10$) in each bin follows the Poisson p.d.f., the variance of the number of the grouped events is

$$\sigma^2(N) = N. \tag{4.12}$$

The arguments $(\phi_{R\perp} + \phi_S)$ and θ entering into the fit function $F(\phi_{R\perp} + \phi_S, \theta)$ in Eq. (4.11) can be taken as the average of the events in each bin, and the variance $\sigma^2(A_{\mathrm{UT}})$ can be approximated by the first–order Taylor expansion around the estimate for the mean of $\langle |\boldsymbol{P_T}| \rangle$, $N_{\mathrm{DIS}}^{\uparrow\downarrow}$, and $N^{\uparrow\downarrow}$,

$$\begin{aligned}
\sigma^2(A_{\mathrm{UT}}) \;\approx\; & (\frac{\partial A_{\mathrm{UT}}}{\partial N^{\uparrow}})^2 \cdot \sigma^2(N^{\uparrow}) + (\frac{\partial A_{\mathrm{UT}}}{\partial N^{\downarrow}})^2 \cdot \sigma^2(N^{\downarrow}) \\
& + (\frac{\partial A_{\mathrm{UT}}}{\partial N_{\mathrm{DIS}}^{\uparrow}})^2 \cdot \sigma^2(N_{\mathrm{DIS}}^{\uparrow}) + (\frac{\partial A_{\mathrm{UT}}}{\partial N_{\mathrm{DIS}}^{\downarrow}})^2 \cdot \sigma^2(N_{\mathrm{DIS}}^{\downarrow}) \qquad (4.13) \\
= \;& \frac{4}{\langle |\boldsymbol{P_T}| \rangle^2} \frac{N^{\uparrow} N^{\downarrow} N_{\mathrm{DIS}}^{\uparrow} N_{\mathrm{DIS}}^{\downarrow}}{(N^{\uparrow} N_{\mathrm{DIS}}^{\downarrow} + N^{\downarrow} N_{\mathrm{DIS}}^{\uparrow})^4} (N^{\uparrow} N^{\downarrow} N_{\mathrm{DIS}}^{\uparrow} \\
& + N^{\uparrow} N^{\downarrow} N_{\mathrm{DIS}}^{\downarrow} + N^{\uparrow} N_{\mathrm{DIS}}^{\uparrow} N_{\mathrm{DIS}}^{\downarrow} + N^{\downarrow} N_{\mathrm{DIS}}^{\uparrow} N_{\mathrm{DIS}}^{\downarrow}) \qquad (4.14)
\end{aligned}$$

where the variance of the target polarization is neglected and taken as systematic uncertainty (cf. Sec. 5.1).

The LS method has an advantage [164] that the fitted minimum value of χ^2 can be used as a goodness–of–fit statistic. Another good point is that by using the asymmetry formula Eq. (4.7), the detection efficiency is cancelled out. However it also has an obvious disadvantage that an additional systematic uncertainty is introduced from the arbitrary choice of the bin width and the variance σ^2 is biased when the actual number of detected events is small. Hence the fitted results of the parameters $\boldsymbol{a}$ will also be biased.

It was argued that in binned fitting of the asymmetries, the statistical uncertainty of the fitting parameter will not be affected by the statistics when the number of events per bin is larger than 100 [183]. In this work the statistics of pion pair events in each bin can reach to around 250, which is quite sufficient.

4.3.3 Maximum Likelihood Fit

We suppose that a set of independently measured quantities x_i follows a p.d.f. $f(\boldsymbol{x};\boldsymbol{a})$, where $\boldsymbol{a} = (a_1, \cdots, a_n)$ is a set of parameters to be determined. The estimators $\hat{\boldsymbol{a}}$ for the mean of $\boldsymbol{a}$ is given by the method of maximum likelihood (ML) [182] as the point in the parameter space where the likelihood function

$$L(\boldsymbol{a}) = \prod_{i=1}^{N} f(\boldsymbol{x}_i;\boldsymbol{a}) \tag{4.15}$$

is maximized. It is usually easier to work with the negative logarithm

$$-\ln L(\boldsymbol{a}) = -\sum_{i=1}^{N} \ln f(\boldsymbol{x}_i;\boldsymbol{a}) \tag{4.16}$$

and then it can be minimized for the same parameter values $\boldsymbol{a}$. The ML estimators can be found by solving the likelihood equations,

$$-\frac{\partial \ln L(\boldsymbol{a})}{a_i} = 0, \qquad i = 1, \cdots, n. \tag{4.17}$$

We will only be interested in the maximum of L and in ratios of L at different values of the parameters; hence any multiplicative factors that do not involve the parameters of interest estimate may be dropped. The estimator for the inverse covariance matrix is given by

$$(\hat{V}^{-1})_{ij} = -\left.\frac{\partial^2 \ln L}{\partial a_i \partial a_j}\right|_{\hat{\boldsymbol{a}}}. \tag{4.18}$$

In this work, with the indication of the kinematic variables by $\boldsymbol{x}$ including azimuthal angles $(\phi_{R\perp} + \phi_S)$ and θ and target polarization $\boldsymbol{P_T}$, the event distribution function can be written as

$$N(\boldsymbol{x}, \boldsymbol{P_T}, t; \boldsymbol{a}) = \mathbb{L}(t)\varepsilon(\boldsymbol{x}, \boldsymbol{P_T})\sigma_{UU}(\boldsymbol{x})[1 + \boldsymbol{P_T}(t)A_{\mathrm{UT}}(\boldsymbol{x}; \boldsymbol{a})], \tag{4.19}$$

where $\mathbb{L}(t)$ is the luminosity, t is the measurement time and ε is the detection efficiency. By substituting t with $\boldsymbol{P_T}$ [184]

$$\mathbb{L}(\boldsymbol{P_T})\mathrm{d}\boldsymbol{P_T} = \sum_{\boldsymbol{P_T} < \boldsymbol{P_T}(t) < \boldsymbol{P_T} + \mathrm{d}\boldsymbol{P_T}} \mathbb{L}(t)\mathrm{d}t \tag{4.20}$$

the event distribution function will be modified as:

$$N(\boldsymbol{x}, \boldsymbol{P_T}; \boldsymbol{a}) = \mathbb{L}(\boldsymbol{P_T})\varepsilon(\boldsymbol{x}, \boldsymbol{P_T})\sigma_{UU}(\boldsymbol{x})[1 + \boldsymbol{P_T}A_{\mathrm{UT}}(\boldsymbol{x}; \boldsymbol{a})]. \tag{4.21}$$

The normalization can be formulated as

$$\mathcal{N}(\boldsymbol{a}) = \iint N(\boldsymbol{x}, \boldsymbol{P_T}; \boldsymbol{a})\mathrm{d}\boldsymbol{x}\mathrm{d}\boldsymbol{P_T}. \tag{4.22}$$

Then the likelihood function in terms of the p.d.f for the ML fit can be illustrated as

$$L(\boldsymbol{a}) = \prod_{i=1}^{N} \frac{N^{W_i}(\boldsymbol{x}_i, \boldsymbol{P_T}_i; \boldsymbol{a})}{\mathcal{N}^{W_i}(\boldsymbol{a})}, \tag{4.23}$$

where W_i is the event weights, which can be set to separate event relying on the event weight, *e.g.*, RICH PID efficiency (cf. Sec. 4.5.6) and lepton beam polarization (cf. Sec. 4.4.2). By the assumption that the detection efficiency ε is independent with target polarization $\boldsymbol{P_T}$, Eq. (4.22) can be approximated as

$$\begin{aligned}\mathcal{N}(\boldsymbol{a}) &= \int \mathrm{d}\boldsymbol{x} \left\{\varepsilon(\boldsymbol{x})\sigma_{UU}(\boldsymbol{x}) \int \mathrm{d}\boldsymbol{P_T} \left\{\mathbb{L}(\boldsymbol{P_T})\left[1 + \boldsymbol{P_T}A_{\mathrm{UT}}(\boldsymbol{x}; \boldsymbol{a})\right]\right\}\right\} \\ &= \int \mathrm{d}\boldsymbol{x} \left\{\varepsilon(\boldsymbol{x})\sigma_{UU}(\boldsymbol{x}) \left\{\int \mathrm{d}\boldsymbol{P_T}\mathbb{L}(\boldsymbol{P_T}) \cdot [1 + \frac{\int \mathrm{d}\boldsymbol{P_T}\mathbb{L}(\boldsymbol{P_T})\boldsymbol{P_T}}{\int \mathrm{d}\boldsymbol{P_T}\mathbb{L}(\boldsymbol{P_T})} \cdot A_{\mathrm{UT}}(\boldsymbol{x}; \boldsymbol{a})]\right\}\right\}.\end{aligned} \tag{4.24}$$

The normalization formula will be independent from the estimators $\boldsymbol{a}$ and can be omitted in the likelihood maximization, if the whole dataset has the net zero polarization

$$\int \mathrm{d}\boldsymbol{P_T}\mathbb{L}(\boldsymbol{P_T})\boldsymbol{P_T} = 0. \tag{4.25}$$

As shown in Figure 4.2, the above term is well satisfied. Therefore, with neglect of the terms which have no dependence on the estimator $\boldsymbol{a}$, the negative logarithm likelihood formula can be simplified from Eq. (4.23) as

$$-\ln L(\boldsymbol{a}) = -\sum_{i=1}^{N} W_i \ln\left[1 + \boldsymbol{P_T}_i A_{\mathrm{UT}}(\boldsymbol{x}_i; \boldsymbol{a})\right]. \tag{4.26}$$

But it needs to test the HERMES acceptance effect which is due to the transverse magnet field as in the LS method.

As binning is unnecessary in applying the ML method, it does not have the disadvantage in the bin size effect, which the LS method has. Furthermore, ML method has an advantage to easily perform the estimate to the RICH non–pion contamination to the $\pi^+\pi^-$ production, by using the event weights (cf. Sec. 4.5.6). In this work the two fitting methods were both implemented and their comparisons show that their results are same. The LS method can provide the goodness–of–fit of the fit results. So we choose LS fit results as final results in this work, in order to present the direct impression of the fitting efficiency.

4.3.4 Extraction of the Amplitude

In the discussion of the LS fit in Sec. 4.3.2, the asymmetry is computed in bins of the kinematic variables, the dependence on which are studied. In this work, the fully differential asymmetry for two–hadron semi–inclusive DIS depends on 9 kinematic variables: x, y, z, $M_{\pi\pi}$, $|\boldsymbol{P_{h\perp}}|$, $\phi_{R\perp}$, ϕ_S, ϕ_h, and θ, as defined in Eq. (B.2) and Eq. (B.3). Due to the limited statistics, it is not possible to determine the amplitudes $A_{\mathrm{UT}}^{\sin(\phi_{R\perp}+\phi_S)\sin\theta}$ of the asymmetry with full dependence on all the relevant variables. By the integration over $|\boldsymbol{P_{h\perp}}|$, we can have simpler kinematic dependent formula in Eq. (2.92a) and Eq. (2.92b). So derived from Eq. (2.81), Eq. (2.92a) and Eq. (2.92b) and, the measured asymmetry in Eq. (4.7) can be modulated as

$$A_{\mathrm{UT}}(\phi_{R\perp}+\phi_S,\theta) = \sin(\phi_{R\perp}+\phi_S)\frac{A_{\mathrm{UT}}^{\sin(\phi_{R\perp}+\phi_S)\sin\theta}\sin\theta + A_{\mathrm{UT}}^{\sin(\phi_{R\perp}+\phi_S)\sin 2\theta}\sin 2\theta}{1+\dfrac{D_{1,\mathrm{UL}}^{sp}}{D_{1,\mathrm{UU}}}\cos\theta + \dfrac{D_{1,\mathrm{LL}}^{pp}}{D_{1,\mathrm{UU}}}\dfrac{1}{4}(3\cos^2\theta-1)}, \tag{4.27}$$

where the amplitudes $A_{\mathrm{UT}}^{\sin(\phi_{R\perp}+\phi_S)\sin\theta}$ and $A_{\mathrm{UT}}^{\sin(\phi_{R\perp}+\phi_S)\sin 2\theta}$ are defined in Eq. (2.93) and Eq. (2.94). Here we assumed that Eq. (2.98) is tenable. Therefore, all the θ–dependent terms are taken into account in the asymmetry parameterization form:

$$A_{\mathrm{UT}}(\phi_{R\perp}+\phi_S,\theta) = \sin(\phi_{R\perp}+\phi_S)\frac{a_1\sin\theta + a_2\sin(2\theta)}{1+a_3\cos\theta + a_4\dfrac{1}{4}(3\cos^2\theta-1)}\ , \tag{4.28}$$

where each parameter corresponds to the terms in Eq. (4.27), with $a_1 \equiv A_{\mathrm{UT}}^{\sin(\phi_{R\perp}+\phi_S)\sin\theta}$ and $a_2 \equiv A_{\mathrm{UT}}^{\sin(\phi_{R\perp}+\phi_S)\sin 2\theta}$. The measured asymmetry is binned in $(\phi_{R\perp}+\phi_S)$ and in θ.

Due to the too many free parameters in the parameterization equation, the statistical uncertainties of the asymmetry amplitudes of interest increase. To decrease the number of free parameters again, the binning in θ was antisymmetrized around $\theta = \pi/2$ (cf. Figure 4.4), such that one can obtain the following nonlinear fit function:

$$A_{\mathrm{UT}}(\phi_{R\perp}+\phi_S,\theta') = \sin(\phi_{R\perp}+\phi_S)\frac{a_1\sin\theta'}{1+A_2\dfrac{1}{4}(3\cos^2\theta'-1)}\ , \tag{4.29}$$

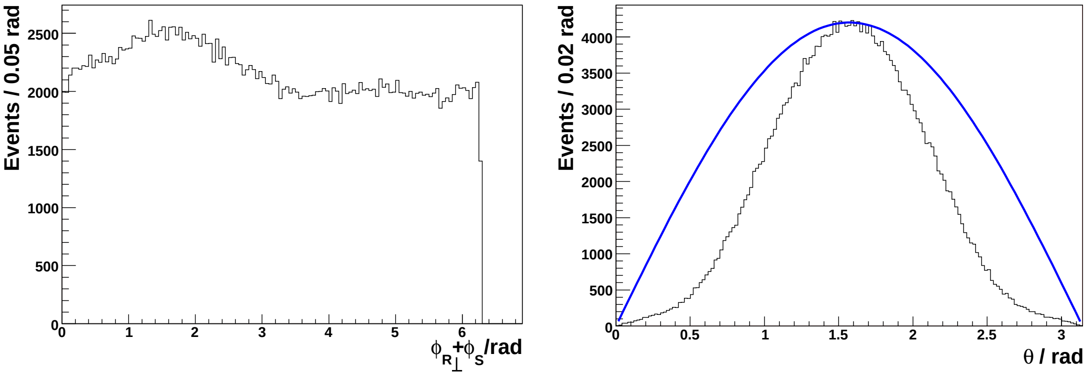

Figure 4.4: The azimuthal angles $\phi_{R\perp}+\phi_S$ ($\phi_{R\perp}+\phi_S+\pi$) for positive (negative) target polarization (cf. Eq. (4.8)) and θ distributions in the bin $0.250\,\text{GeV} < M_{\pi\pi} < 0.400\,\text{GeV}$. The sine curve in the right plot shows the ideal θ dependence of the cross section in 4π acceptance.

with $\theta' \equiv ||\theta - \pi/2| - \pi/2|$ in the range $\theta' \in [0, \frac{\pi}{2}]$, and $A_2 \equiv D^{pp}_{1,\text{LL}}/D_{1,\text{UU}}$. In this expression, all contributions to σ_{UU} and σ_{UT}, which are odd with respect to $\theta = \pi/2$, are cancelled.

In the mass region less than $1\,\text{GeV}/c^2$, the contribution of *pp*–wave interference component is presumably small. Assuming that the unknown A_2 contribution is trivial, we can have the fit function

$$A_{\text{UT}}(\phi_{R\perp} + \phi_S, \theta') = A_{\text{UT}}^{\sin(\phi_{R\perp}+\phi_S)\sin\theta} \sin(\phi_{R\perp} + \phi_S)\sin\theta', \tag{4.30}$$

which is called the **simm–nonlinear fit** function in this thesis. In LS fit, we group the data in 2-dimension (**2–D**) of $(\phi_{R\perp} + \phi_S)$ and θ'. In ML fit, no binning is needed. The conjecture of trivial A_2 will be tested using Monte Carlo technique in Sec. 4.5.4.

With the consideration on the statistic low limits in the LS fit for each bin, the bins limits of the different kinematic quantities, used in the analysis, are listed in Table 4.5. The invariant mass covers the range where there is mainly the interference between *s*– and *p*–wave channels of the two hadron production. We focused our efforts on the study of the asymmetry amplitude from the *s*–*p* interference fragmentation, as indicated in Eq. (2.93). The asymmetry amplitude has dependence on the azimuthal angles $(\phi_{R\perp} + \phi_S)$ and θ, whose distributions can be found in Figure 4.4 as an example in one bin $0.250\,\text{GeV} < M_{\pi\pi} < 0.400\,\text{GeV}$. We see the different distributions in $(\phi_{R\perp} + \phi_S)$ and θ, instead of the ideal flat and sine distribution, respectively, due to the spectrometer acceptance. The effects from these limits will be investigated in Sec. 4.4 and Sec. 4.5.

The program MINUIT [185] is used which determines the minimum of the figure–of–merit function by scanning the parameter space. The goodness of the fit can be estimated by the reduced–χ^2 which is the minimum of χ^2 divided by the number of degrees of freedom (ndf). For the two–hadron asymmetries, each kinematic bin in Table 4.5 is split up into

semi–inclusive bins	1	2	3	4	
$M_{\pi\pi}$ bin limits [GeV]	0.250	0.400	0.550	0.770	2.000
x bin limits	0.023	0.040	0.055	0.085	0.400
z bin limits	0.000	0.340	0.440	0.560	1.000

Table 4.5: Bin limits of the kinematic quantities used in the analysis.

8×8 bins in the azimuthal angles $(\phi_{R\perp}+\phi_S)$ and θ'. The $(\phi_{R\perp}+\phi_S)$ bins are equidistant, but the widths of azimuthal θ' bins is adjusted in order to obtain the same level of the statistics in each bin. Using 2–D binning fit, we can extract the asymmetry amplitudes.

In applying ML method, in order to study the kinematic dependence of the asymmetry amplitude, the same kinematic variable bins as listed in Table 4.5 were adopted. In each kinematic bin, the likelihood function Eq. (4.26) can be computed by introducing the amplitude parameterization equation, *e.g.*, Eq. (4.30). Program MINUIT were used to minimize the negative logarithm likelihood function.

4.3.5 Comparison between LS fit and ML fit

The comparison between LS fit and ML fit is helpful to check whether the estimated amplitudes by the LS fit is biased due to the statistic deficit and whether the LS fit can be safely used.

In addition to the 2–D fit and ML fit with the simm–nonlinear function Eq. (4.30), another simpler LS fit method is devised in order to test the performance of the LS fit. As the asymmetry is proportional to $\sin(\phi_{R\perp}+\phi_S)\sin\theta'$ in Eq. (4.30), a simpler way is to group the data in $\sin(\phi_{R\perp}+\phi_S)\sin\theta'$ bin. By binning in this way, we can fit the asymmetry using a linear fit function

$$A_{\mathrm{UT}}(\sin(\phi_{R\perp}+\phi_S)\sin\theta') = A_{\mathrm{UT}}^{\sin(\phi_{R\perp}+\phi_S)\sin\theta}\sin(\phi_{R\perp}+\phi_S)\sin\theta' , \tag{4.31}$$

which is called the **linear fit** function in this work. This fitting method has an advantage of more even distribution than that of the polar angle θ. So it is simpler to be implemented in the analysis.

The LS and ML fitting results are in Figure 4.5. In LS method, the results extracted from the 8×8 2–D binning fit and from the linear binning fit in 50 equidistant $\sin(\phi_{R\perp}+\phi_S)\sin\theta'$ bins. The ML simm–nonlinear fitting results are consistent with both LS fitting results. Therefore, the three sets of the fitting results are compared and all results are consistent. The reduced–χ^2 ranges from 0.75 to 1.45. Therefore, we can verify the validity of the LS fit in this work and the consistency between two fitting methods.

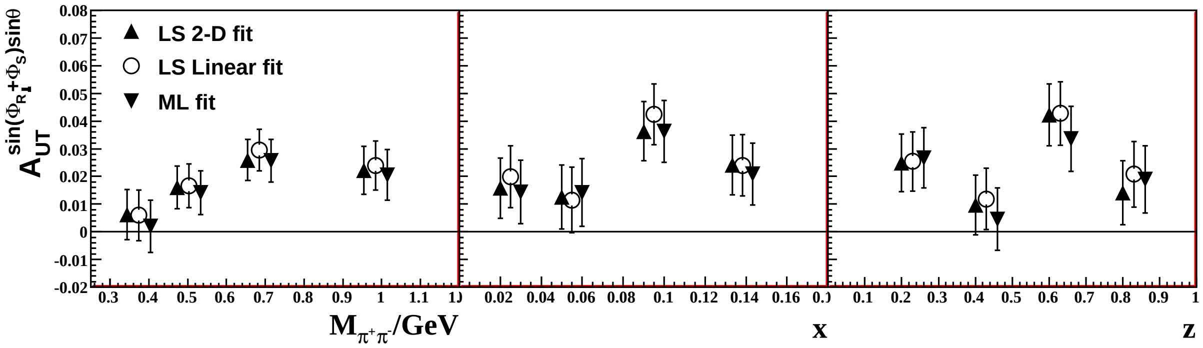

Figure 4.5: The comparison of the asymmetry amplitudes fitted by LS and ML methods, using the simm–nonlinear fit function Eq. (4.30), for the data in years 2002–2005. The LS fits were performed in 8×8 (64) two–dimension (2–D) azimuthal angle bins and 50 $\sin(\phi_{R\perp} + \phi_S) \sin\theta'$ equidistant bins. Note that the corresponding kinematic positions for the amplitudes are just displayed for schematic illustration.

4.3.6 Binning Effect

In this section, the binning effect in LS fit will be checked. As shown in the last section, the asymmetry amplitudes from the LS 2–D fit and the LS linear fit are consistent. Hence, we can test the binning effect using the LS linear fit. This fitting method was chosen because of it's convenience in implementing binning owing to the relatively even distribution of $\sin(\phi_{R\perp} + \phi_S) \sin\theta'$ than the polar angle θ (cf. Figure 4.4). By varying the number of equispaced bins, we can test the variation of the fitting results and the goodness–of–fit with the reduced–χ^2. Then we can fix the bin numbers by choosing the best reduced–χ^2 value, which were supposed to approximate to 1.

Figure 4.6 shows the extracted x–dependence of the asymmetry amplitudes and the corresponding reduced–χ^2 values at the different numbers of the bins, where the simpler asymmetry parameterization function Eq. (4.31) was employed. The fitting results are almost not affected by the change of the bin numbers, both for the central values and for the statistical uncertainties. The reduced–χ^2 values basically do not fluctuate. They are a little scattered at small bin numbers, but approaching to 1 when the bin numbers are increased.

But the linear fit can only be available when the fit function is proportional to $\sin(\phi_{R\perp} + \phi_S) \sin\theta'$. It was also testified that the extracted asymmetry amplitudes in 2–D LS fit with 8×10, 10×8 and 10×10 bins are also consistent. Therefore, thanks to the sufficient statistics, we could safely ignore the binning effect when the bin numbers is moderate, *e.g.*, 8×8 bins.

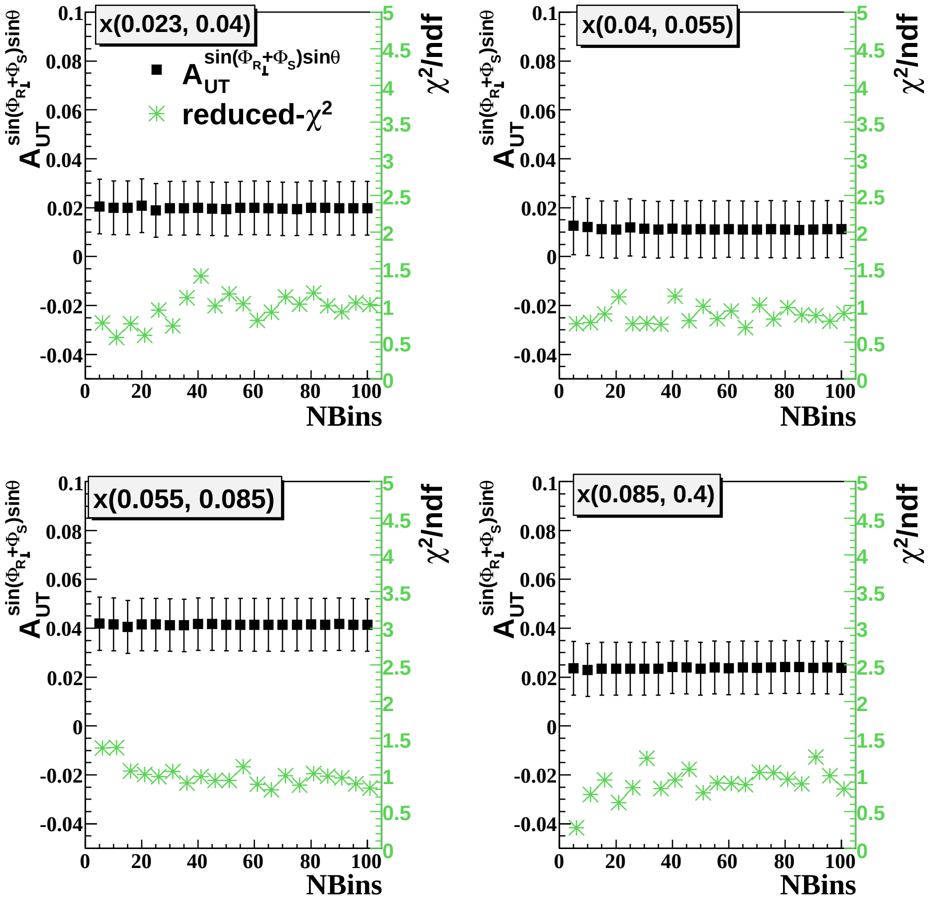

Figure 4.6: The extracted asymmetry amplitudes and the corresponding reduced–χ^2 versus the number of the bins in the $\sin(\phi_{R\perp} + \phi_S)\sin\theta'$. The four panels are corresponding to the different Bjorken–x bins, respectively.

4.3.7 Constant Part in the Fit Function

As discussed in Sec. 4.3.1, a constant C should vanish in the fit function for a correct luminosity normalization in the measurement of the asymmetry. If the constant part is not negligible, the fake asymmetry will be introduced in the simm–nonlinear fit function Eq. (4.30), in which the constant part is omitted. In this section, we will test whether the constant part is negligible in the fit function and whether the event rates in two target spin states are well normalized to the luminosity.

From Eq. (4.30), we derive the asymmetry function with constant C:

$$A_{\mathrm{UT}}(\phi_{R\perp} + \phi_S, \theta') = C + A_{\mathrm{UT}}^{\sin(\phi_{R\perp}+\phi_S)\sin\theta} \sin(\phi_{R\perp} + \phi_S)\sin\theta' \; . \tag{4.32}$$

In the same way as the discussion in Sec. 4.3.4, we can do the LS 2-D fit, the LS linear fit and the ML fit using the fitting function Eq. (4.32) with a constant C.

Bins		8 × 8 binning LS 2–D Fit			50 bins LS Linear Fit			ML Method	
		C	$\mathcal{A}$	χ^2/ndf	C	$\mathcal{A}$	χ^2/ndf	C	$\mathcal{A}$
$M_{\pi\pi}$	1	-0.005 ± 0.005	0.006 ± 0.009	0.966	-0.005 ± 0.005	0.006 ± 0.009	0.963	-0.007 ± 0.006	0.002 ± 0.009
	2	-0.002 ± 0.005	0.016 ± 0.008	1.381	-0.002 ± 0.005	0.017 ± 0.008	0.960	-0.005 ± 0.005	0.014 ± 0.008
	3	0.002 ± 0.005	0.026 ± 0.007	0.753	0.002 ± 0.005	0.030 ± 0.008	1.203	0.001 ± 0.005	0.026 ± 0.008
	4	0.010 ± 0.006	0.022 ± 0.009	1.323	0.010 ± 0.006	0.024 ± 0.009	1.024	0.009 ± 0.006	0.021 ± 0.009
x	1	0.001 ± 0.007	0.016 ± 0.011	1.064	0.001 ± 0.007	0.020 ± 0.011	1.156	0.003 ± 0.008	0.014 ± 0.011
	2	0.003 ± 0.008	0.013 ± 0.012	0.983	0.003 ± 0.008	0.012 ± 0.012	0.991	-0.005 ± 0.008	0.014 ± 0.012
	3	0.012 ± 0.007	0.036 ± 0.011	1.429	0.012 ± 0.007	0.042 ± 0.011	0.924	0.012 ± 0.007	0.036 ± 0.011
	4	0.003 ± 0.007	0.024 ± 0.011	0.893	0.004 ± 0.007	0.024 ± 0.011	0.759	0.000 ± 0.007	0.021 ± 0.011
z	1	0.008 ± 0.007	0.025 ± 0.010	1.148	0.008 ± 0.007	0.025 ± 0.010	1.054	0.004 ± 0.008	0.027 ± 0.011
	2	0.000 ± 0.007	0.010 ± 0.011	0.915	0.000 ± 0.007	0.012 ± 0.011	1.078	0.000 ± 0.008	0.005 ± 0.011
	3	-0.007 ± 0.007	0.042 ± 0.011	0.776	-0.007 ± 0.007	0.043 ± 0.011	0.662	-0.011 ± 0.008	0.034 ± 0.012
	4	0.018 ± 0.007	0.014 ± 0.012	0.991	0.018 ± 0.007	0.021 ± 0.012	0.992	0.018 ± 0.008	0.019 ± 0.012

Table 4.6: The fitting results by LS method and ML method, using the fit function Eq. (4.32), for the data in years 2002–2005. The LS fit were performed in 8×8 (64) two–dimension (2–D) azimuthal angle bins and 50 $\sin(\phi_{R\perp} + \phi_S)\sin\theta'$ equidistant bins. Here, the symbol $\mathcal{A} = A_{\mathrm{UT}}^{\sin(\phi_{R\perp}+\phi_S)\sin\theta}$ is the extracted asymmetry amplitude.

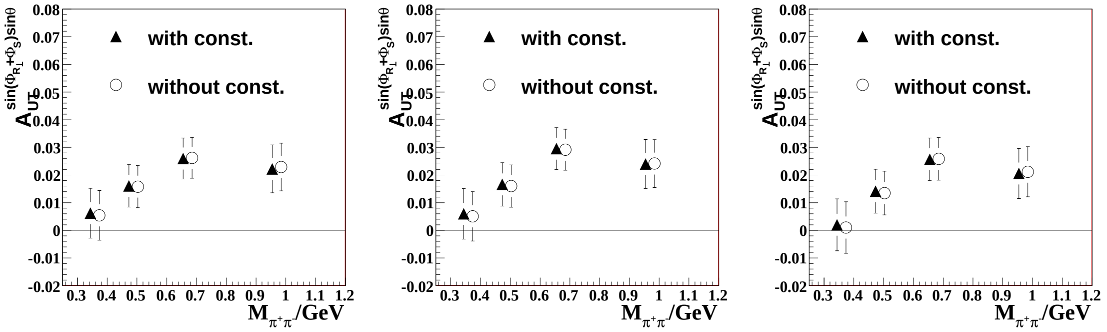

(a) LS 2–D fit (b) LS linear fit (c) ML fit

Figure 4.7: The comparison of the extracted invariant mass $M_{\pi\pi}$ dependent asymmetry amplitudes between the fit formula with the constant part (Eq. (4.32)) and without the constant part (Eq. (4.30)). Plots 4.7(a), 4.7(b) and 4.7(c) are the fitting results with LS two–dimension (2–D) fit, LS linear fit, and ML fit. Note that the corresponding kinematic positions for the amplitudes are displayed only for schematic illustration.

As can be seen from Table 4.6, the fitting constant part C in the asymmetry parameterization formula is very small compared with the amplitude part in each of the three methods of the fitting. Hence it is safe to neglect the constant part in the asymmetry formula. The comparison on the asymmetry amplitudes and their dependence on the invariant mass $M_{\pi\pi}$ are shown in Figure 4.7 for the three types of the fitting methods: 8×8 binning 2–D fit, 50 bins linear fit and ML fit. All the results are consistent within each group, and also for all fitting results. We skipped showing the comparison of the asymmetry amplitudes for the dependence on the other kinematic variables. They show the similar results. The zero asymmetry contribution from the constant part testified the good luminosity normalization in this analysis, and the constant part can be omitted safely in the fit function.

We extracted the asymmetry amplitudes using LS and ML method with the simm-nonlinear fit function. The sizes and statistical uncertainties of the asymmetry amplitudes can be obtained, and the fitting results are robust to the different fitting methods. But due to the detector acceptance limitation, the measured asymmetry might be affected. Then the additional asymmetries could be introduced and the extracted azimuthal amplitudes would be biased. So it is important to evaluate the HERMES acceptance effect using Monte Carlo simulation. In addition, other systematic uncertainties in the measurement also need to be investigated and estimated.

4.4 Studies of Systematic Errors

The systematic studies on the possible sources of the influences of experimental uncertainties will be extensively discussed in this section. Without special mention, the 2-D LS fit with the simm-nonlinear fit function will be used in the later part of this thesis.

4.4.1 Data Taking Period Comparison

The data analyzed in this paper were recorded during a period that extends the years from 2002 to 2005. During the four years, changes of the HERMES spectrometer, *e.g.*, in the alignment or the efficiencies of the detectors, may occur and can influence the extracted asymmetry amplitudes. The difference of the kinematic variables among the different years were compared and the distributions of some variables showed a slightly discrepancy, especially in the comparison between 2004 and 2005 [186]. Here the extracted amplitudes in different data taking periods are compared in order to check whether the changes will affect the results of the amplitudes significantly.

To test the consistency of the two samples, a Student's t test can be used if the two samples are with Gaussian distribution and their Gaussians have the same variance[2]. A Student's t variables can be constructed as

$$t = \frac{\bar{X_1} - \bar{Y_1}}{s}, \tag{4.33}$$

where

$$s^2 = \frac{(n_1 - 1)s_1^2 + (n_2 - 1)s_2^2}{n_1 + n_2 - 2} \left(\frac{1}{n_1} + \frac{1}{n_2} \right), \tag{4.34}$$

Here s^2 is the unbiased estimator of the variances, n is number of samples, 1(2) stands for different group of samples. The statistical significance level associated with the t value calculated in this way is the probability whether the means are different under the null hypothesis of equal means. As n approaches infinity, *e.g.*, $n \gtrsim 45$, Student's–t distribution approaches the standard normal distribution. In this case, variable t can be simplified as

$$t = \frac{\bar{X_1} - \bar{Y_1}}{\sqrt{\hat{\sigma_1}^2 + \hat{\sigma_2}^2}}, \tag{4.35}$$

The sum of the squared t–values follows the χ^2 distribution

$$\chi^2 = \sum_i t_i^2, \tag{4.36}$$

which can be used to test whether the two samples follow the same distribution.

As the statistics in years 2002 and 2003 are low, we split the whole data set into 3 groups: 2002–2003 data, 2004 data and 2005 data. The t–test is done by comparing the

---

[2] Even if the p.d.f is not Gaussian, this test is still a good approximation [187].

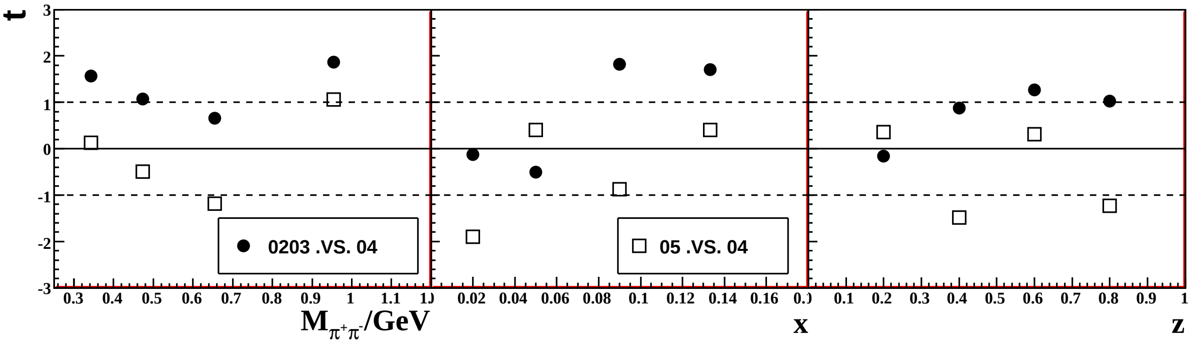

Figure 4.8: The t–value of the student's–t test in the amplitudes extracted from 3 groups of data set: 2002–2003 years data, 2004 year data and 2005 year data.

results in 2002–2003 and 2005 with 2004 results, as shown in Figure 4.8. The t–values of 2002–2003 data and 2004 data, in the dependence on $M_{\pi\pi}$, x and z are almost positive, which means the extracted amplitudes from 2002–2003 data are larger than those from 2004 data. The χ^2 values in $M_{\pi\pi}$, x and z plots are 7.54, 6.46 and 3.46 with n.d.f=4, which give the probabilities 89.0%, 83.3% and 51.6% that the two amplitudes are with different distribution. Hence the results between 2002–2003 data and 2004 data with dependence on $M_{\pi\pi}$ and x are less consistent. The z results are very consistent. The t–test between 2004 data and 2005 data shows more consistent behaviors. They fluctuate around zero and do not show any systematic trend. The χ^2 values in $M_{\pi\pi}$, x and z plots are 2.79, 4.67 and 3.92, which give the inconsistency probabilities 40.0%, 67.0% and 58.4%. Hence these two set of amplitudes are relatively more consistent. Due to the high statistics in 2004 and 2005 as given in Table 4.4, the amplitudes are mainly dominated by these two years data. Therefore, the asymmetry amplitudes are mostly determined from the consistent data taking periods.

4.4.2 Beam Polarization Effect

As discussed in Sec. 4.2.4, the beam polarization has to be balanced to net zero in order to avoid the contribution from the beam longitudinal polarization effect to the measured asymmetry (cf. Eq. (2.79)). However, in this measurement where the longitudinally polarized beam is used, this condition is not perfectly satisfied. In this work, the net beam polarization -0.020 ± 0.001 (cf. Table 4.4) has been reached, which is very close to zero. Sec. 4.2.4 also argued that even with nonzero beam polarization, taken advantage of the integration over the transverse momentum $\boldsymbol{P_{h\perp}}$ and the unique azimuthal angle dependence of the asymmetry amplitude, the results will not be influenced. As will be proved in Sec. 4.5.3, the incomplete detection of the transverse momentum $\boldsymbol{P_{h\perp}}$ in HERMES acceptance will not affect the final extracted amplitudes. That means the nonzero beam polarization will not produce any fake asymmetry amplitude. In this section, we will check how the asymmetry amplitudes would be changed, with adjusted beam polarizations which are purely negatively polarized, purely positively polarized and well balanced, respectively.

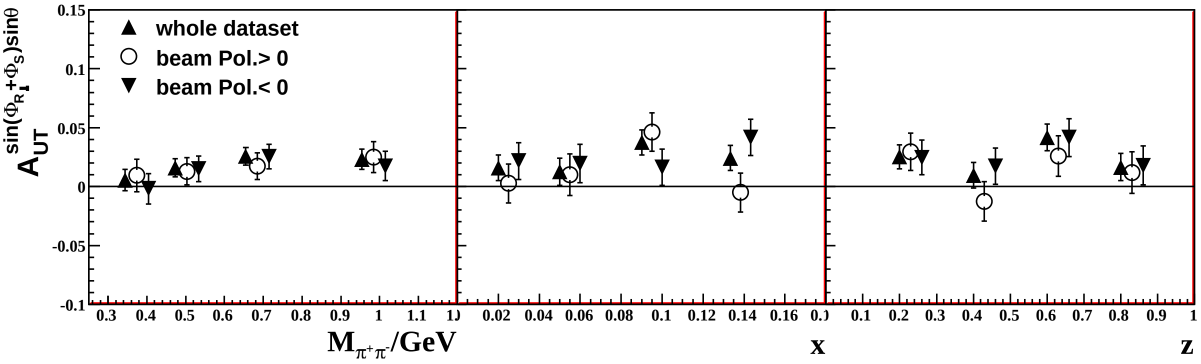

Figure 4.9: The extracted amplitudes with the whole dataset, with only positive beam polarization data and with only negative beam polarization data. “beam Pol. >0” only takes into account the events with positive longitudinal polarization, and “beam Pol. <0” with negative longitudinal polarization. The simm–nonlinear fit method was used.

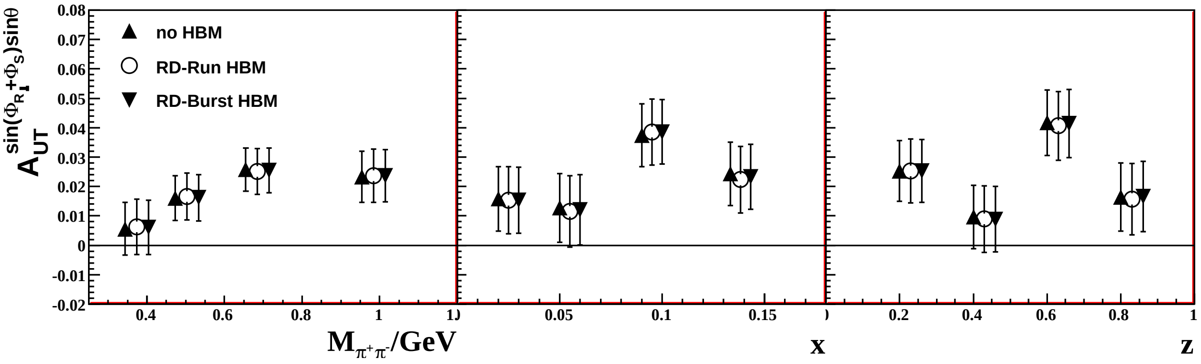

Figure 4.10: The asymmetry amplitudes extracted from the data with two helicity balance methods (HBM). Random drop (RD) on run (RD–Run) and burst (RD–Burst) level are performed, respectively. The results without HBM also are given.

Figure 4.9 shows the extracted amplitudes $A_{\rm UT}^{\sin(\phi_{R\perp}+\phi_S)\sin\theta}$ with only positive beam helicity and negative beam helicity. The amplitude with positive or negative single beam helicity state always fluctuates above or below the amplitude from the combined beam helicity states, and no identical tendency was found for either the positive or negative beam helicity state. The 3 sets of the asymmetry amplitudes are consistent within the statistical uncertainty.

The Figure 4.10 gives the comparison among the results with different levels of the net beam polarization. The whole dataset has the net beam polarization -1.8% as in Table 4.4. The data with random drop (RD) beam helicity balance method (HBM) on run and burst level has net beam polarization around the level of 0.5% (cf. Figure D.1) and 0.00005% (cf. Figure D.2), respectively. The details in implementation of RD HBM are explained in Appendix D. After many times of the random drop operations, the mean value and the standard deviation of the extracted amplitudes with RD–Run HBM or RD–Burst HBM can be estimated by Gaussian curve. Mean values are plotted in Figure 4.10, and the systematic uncertainties in both HBMs are nearly 0, compared with the size of the amplitudes (cf. Figure D.2 and Figure D.2). The statistical uncertainties are identical for each extraction and the average value of these statistical uncertainties were used as the statistical errors in Figure 4.10. With the extracted amplitudes from no HBM data included in Figure 4.10, the different results are consistent with each other. The systematic effect from the beam polarization is therefore negligible.

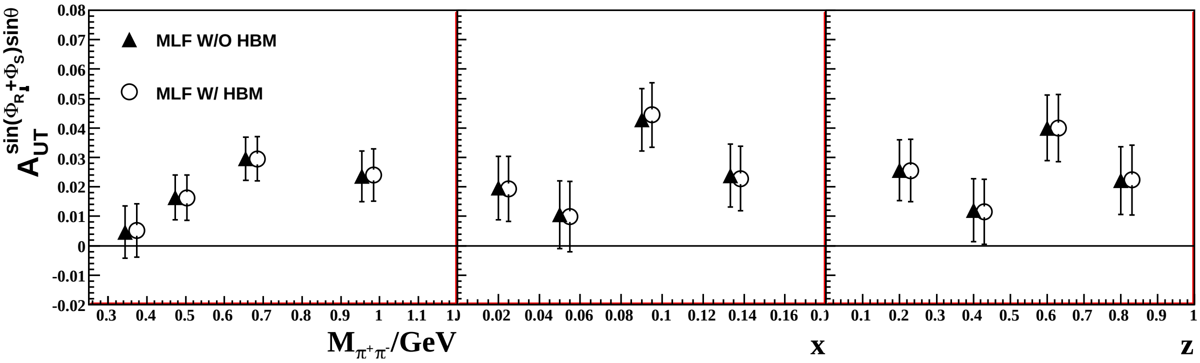

Figure 4.11: The asymmetry amplitudes extracted with ML fit to the simm–nonlinear function, taking into account a beam helicity balance weight (W/ HBM). The ML fit results without HBM (W/O HBM) are also presented for comparison.

Another way to balance the two states of the beam helicity is to put an event weight in the ML fit. From the discussion in Sec. 4.3.3, an event weight W_i can be applied to each event in likelihood function Eq. (4.26). We define a factor

$$a = \frac{\langle|\overrightarrow{P}_B|\rangle}{\langle|\overleftarrow{P}_B|\rangle}, \tag{4.37}$$

where the →(←) is the helicity direction. The event weight for different helicity state can be set as

$$\overrightarrow{W}_i = \begin{cases} 1, & \text{if } a > 1: \\ \frac{1}{a}, & \text{if } a < 1. \end{cases} \quad , \quad \overleftarrow{W}_i = \begin{cases} \dfrac{1}{a}, & \text{if } a > 1: \\ 1, & \text{if } a < 1. \end{cases} . \tag{4.38}$$

The extracted amplitudes using ML fit with the beam helicity correction factor a were presented in Figure 4.11, with the comparison with the ML fit results without helicity balance factor. We can see that no significant change of the amplitudes after the correction at all. The beam polarization effect is less than an absolute value of 0.001 and is negligible.

4.4.3 Target Magnet Field Correction

The LS fit and ML fit in this work require the identical HERMES acceptance in the cases of different target polarizations. But it is not the case in reality and there is difference in the HERMES detection acceptance between two target sates as discussed in Sec. 4.3.1. The transverse magnet field around the target cell region not only biases the acceptance of the spectrometer, but also influences the measurement of the parameters of the tracks, which are the polar angle θ, the azimuthal angle $\phi_{R\perp} + \phi_S$, the momentum and the position. This is due to the bend of the passing charged particles. As introduced in Sec. 3.3.2, the measurement of the bent tracks was performed with Transverse Magnet Corrections: TMC1 and TMC2.

The official TMC1 and TMC2 are both performed only in 2004 and 2005 data, and in year 2002 (2003) only TMC1 (TMC2) was applied. For the analysis data selections, the TMC1 (TMC2) was suggested and chosen for 2005 (2004) data officially. The Figure 4.12 presents the extracted amplitudes for the whole data set with TMC and with no TMC. We can see the consistent results by the comparison.

To check the effect of the TMC, we need to check the effect of the TMC between different TMC methods. Hence we have to separate the comparison for different data taking periods and here only the comparisons for 2005 data, without TMC, with TMC1 and with TMC2 are given. Figure 4.13 shows the extracted amplitudes $A_{\mathrm{UT}}^{\sin(\phi_{R\perp}+\phi_S)\sin\theta}$ with the dependence on $M_{\pi\pi}$, x and z using 2005 data, with no TMC, with TMC1, and with TMC2. When the transverse magnet is on, the TMC should be implemented in the track measurement. Although the extraction of the asymmetry amplitudes with no TMC applied should not be taken as seriously as the results with TMC, the three results are consistent within the uncertainties. The difference between the TMC1 and TMC2 results could also be used as an estimate of the systematic uncertainty of the TMC effect. The

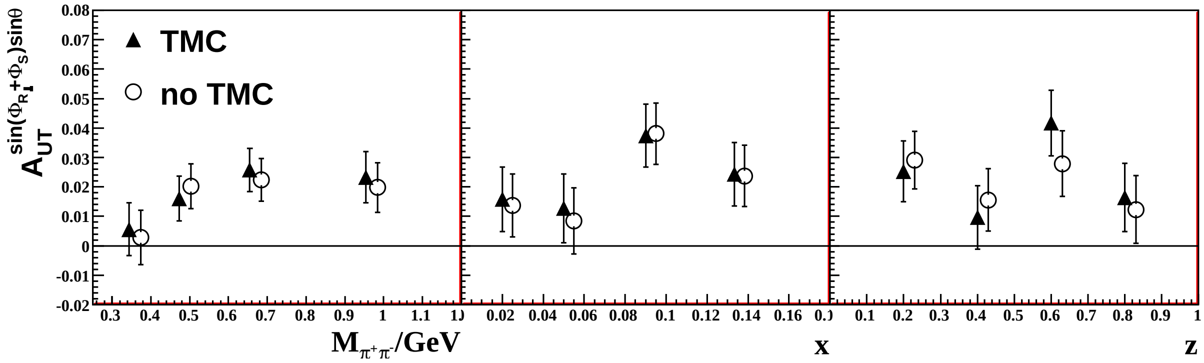

Figure 4.12: The extracted asymmetry amplitudes in the whole data set with TMC method and with no TMC. Here 2002/2005 used TMC1 method and 2003/2004 used TMC2 method.

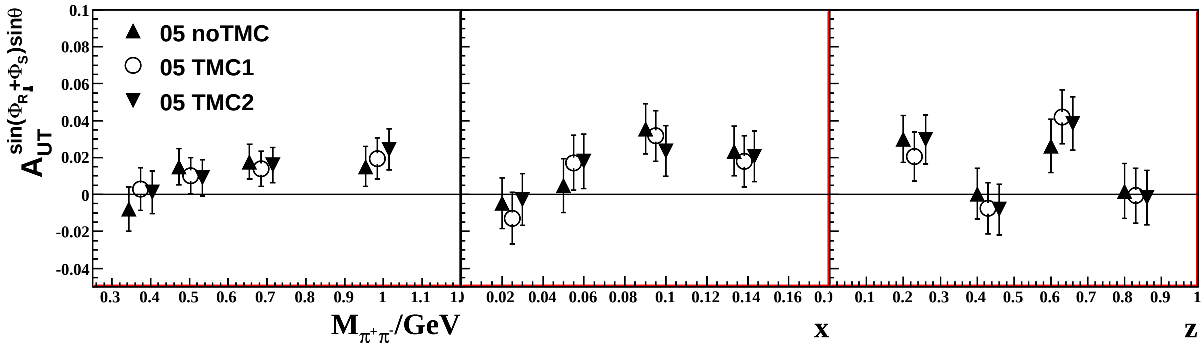

Figure 4.13: The extracted asymmetry amplitudes in 2005 data with no TMC, with TMC1 and with TMC2.

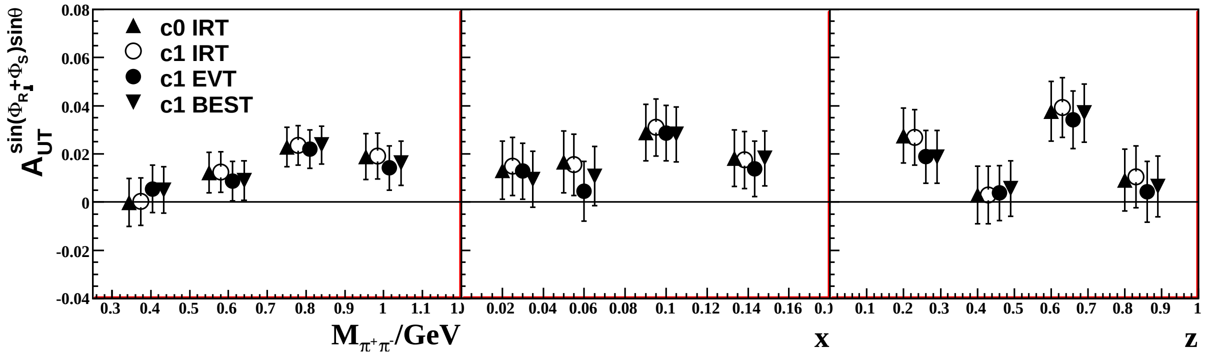

Figure 4.14: Amplitudes $A_{\rm UT}^{\sin(\phi_{R\perp}+\phi_S)\sin\theta}$ versus $M_{\pi\pi}$, x, and z, extracted with simm–nonlinear fit method from the 4 kinds of real data in years of 2004–2005. The different datasets includes c0 IRT data, c1 IRT data, c1 EVT data and c1 BEST data.

different TMC would shift the events to the neighbour azimuthal bins, and then might change the calculated asymmetries and the extracted amplitudes. If the statistics in the bins are too small, the extracted amplitudes would be influenced significantly. Hence, to estimate the systematic uncertainty of the TMC methods, high statistical Monte Carlo simulation data are more suitable than the experimental data. We will discuss the detailed study in MC data in Sec. 4.5.7.

4.4.4 RICH Algorithm Comparison

As mentioned in Sec. 3.3.3, we have the IRT, DRT and EVT algorithms to determine the hadron type from RICH PMT hit patterns. The above systematic studies are basically performed using data with IRT RICH algorithm. In this section we will show that the asymmetry amplitudes is not dependent on the different RICH algorithms and it is safe to use RICH–IRT data to study the systematic effects.

In Figure 4.14 4 asymmetry amplitude results are compared, which are extracted from c0 IRT production, c1 IRT production, c1 EVT production and c1 BEST production in years 2004–2005. The c0 and c1 represent different versions of c–production in the off–line analysis chain. BEST production means the best information between IRT and DRT for each track. But in real data, DRT was never tuned good enough for data analysis. This is the reason why DRT data was not considered in this work. The 4 groups of values are totally consistent and no identical trend of the systematic effect is found. We understand that EVT algorithm can improve the identification of hadron type for multi–tracks in one RICH detector half. In this work, π is highly dominant and the non–pion contamination on the pion pairs does affect the final results, which can be justified later in Sec 4.5.6.

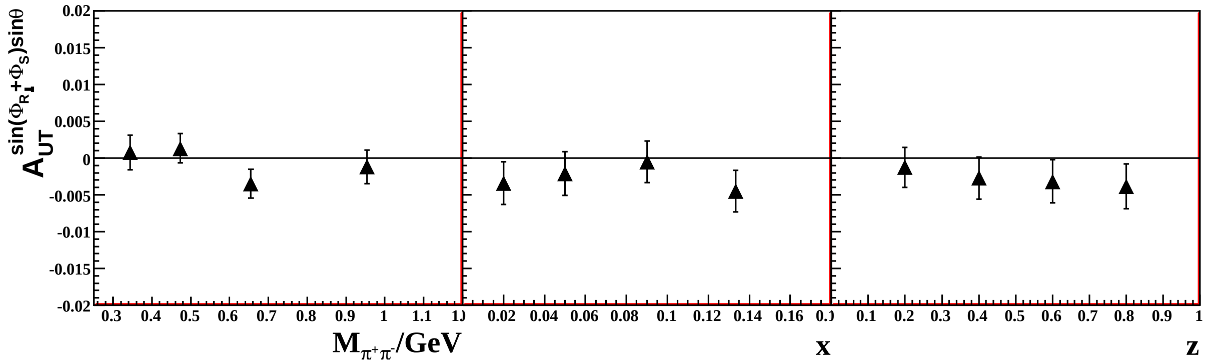

Figure 4.15: Amplitudes $A_{\mathrm{UT}}^{\sin(\phi_{R\perp}+\phi_S)\sin\theta}$ versus $M_{\pi\pi}$, x, and z, extracted with simm–nonlinear fit method from the real data, which were uniformly randomly assigned the target spin. The high statistics is due to re–using the same real data several times.

4.4.5 Zero Asymmetry Check

The real data is also used to check the extraction method with the dataset to which zero asymmetry is assigned. In order to improve the statistics, the real data were reused several times, the random target spin states were reassigned with the uniform distribution. As described in Sec. 4.5.9, the results are shown in Figure 4.15. The same conclusion can be drawn as the zero asymmetry amplitudes in Figure 4.33. Hence, this is another way to prove that the HERMES acceptance effect cannot generate non–zero asymmetries, and the fitting methods also will not bring in non–zero asymmetries.

4.5 Monte Carlo Simulation

The two sets of data, in 4π acceptance data and the HERMES acceptance, were generated in order to study the HERMES acceptance, which are based on the Pythia Monte Carlo (MC) simulation [188, 189]. Specially, a version of Pythia was used where the cross sections of the process implemented in Pythia were tuned to HERMES data [190]. Apart from the simple assumption on the experimental acceptance effect as in Appendix C, the measured number of events is always convoluted with the experimental acceptance ϵ, *i.e.*,

$$N^{\uparrow(\downarrow)}(\phi_{R\perp},\phi_S,\theta,M_{\pi\pi}) \propto \int \mathrm{d}\,x\ \mathrm{d}\,y\ \mathrm{d}\,z\ \mathrm{d}^2\,\boldsymbol{P_{h\perp}}\,\epsilon(x,y,z,\boldsymbol{P_{h\perp}},\phi_{R\perp},\phi_S,\theta,M_{\pi\pi}) \\ \times\,\sigma_{U\uparrow(\downarrow)}(x,y,z,\boldsymbol{P_{h\perp}},\phi_{R\perp},\phi_S,\theta,M_{\pi\pi}), \tag{4.39}$$

such that ϵ does not necessarily drop out of the expression for the asymmetry (Eq. (4.7)). This implies that one might not be able to directly compare the results measured at

HERMES to results measured in a detector with full 4π coverage or equivalently to a theoretical prediction that does not take the HERMES acceptance into account. Therefore, the influence of the limited HERMES acceptance on the results is investigated in this section.

By introducing the parton distribution function and the dihadron fragmentation models to the asymmetry A_{UT} (*e.g.*, the ratio of the integrations of Eq. (2.92b) and Eq. (2.92a)), the MC data with the transverse spin dependence can be derived from the unpolarized Pythia MC simulation. In Sec. 4.5.2, with the implementation of the theoretical models for the asymmetry amplitude $A_{\mathrm{UT}}^{\sin(\phi_{R\perp}+\phi_S)\sin\theta}$, the HEREMS acceptance effect on the extracted asymmetry amplitude is evaluated. Later Sec. 4.5.3 and Sec. 4.5.4 discuss the HERMES acceptance effect on the asymmetry, *i.e.*, the azimuthal angles ϕ_h and θ dependence. In Sec.4.5.5, the contribution from the unpolarized p–wave fragmentation function to the asymmetry and the extracted amplitude are evaluated and the effect will be taken as a part of the systematic uncertainties. Another important issue in MC simulation, which is studied in Sec.4.5.6, is to estimate how much the hadron contamination in RICH detector would pollute the extracted amplitude.

4.5.1 MC Data with the Transverse Spin Dependence

In order to investigate the influence of the HERMES acceptance on the asymmetry A_{UT} and the azimuthal amplitudes, one needs the MC simulation, where the relating physics mechanism is included. This requires that the MC generator can simulate the two–hadron cross section both for σ_{UU} and for σ_{UT}. However, the transversity and dihadron fragmentation function (DiFF) has not yet been implemented in Pythia MC code and it is beyond the scope of this work to write a completely new MC code. So another method as a substitution was used.

Using the HERMES tuned Pythia MC code, which does not have σ_{UT} implemented, the unpolarized dihadron lepto–production data were generated. In order to introduce the target polarization dependent asymmetry to the MC unpolarized data, the target spin states were assigned for each event according to an expression for the asymmetry equation A_{UT}. With a random number *rand*, which has $rand \in (0, 1)$, the target polarization $\boldsymbol{P_T}$ were taken as, in C–like fashion,

$$\boldsymbol{P_T} = (rand < 0.5\ (1 + A_{\mathrm{UT}}(x, y, z, M_{\pi\pi}, \phi_{R\perp}, \phi_S, \phi_h, \theta))),. \tag{4.40}$$

If $\boldsymbol{P_T}$ is true, the target spin will be assigned up as 1; If $\boldsymbol{P_T}$ is false, the target spin is down as -1. It is thus possible, for a given model of A_{UT}, to generate a sample of DIS data with a realistic spin distribution with 4π acceptance and the HERMES acceptance. In Figure 4.16, the comparisons of the distributions are shown for all kinematic variables that the asymmetry depends on. The comparison is between the selected experimental polarized hydrogen data (summing events of the both target polarization states) and the

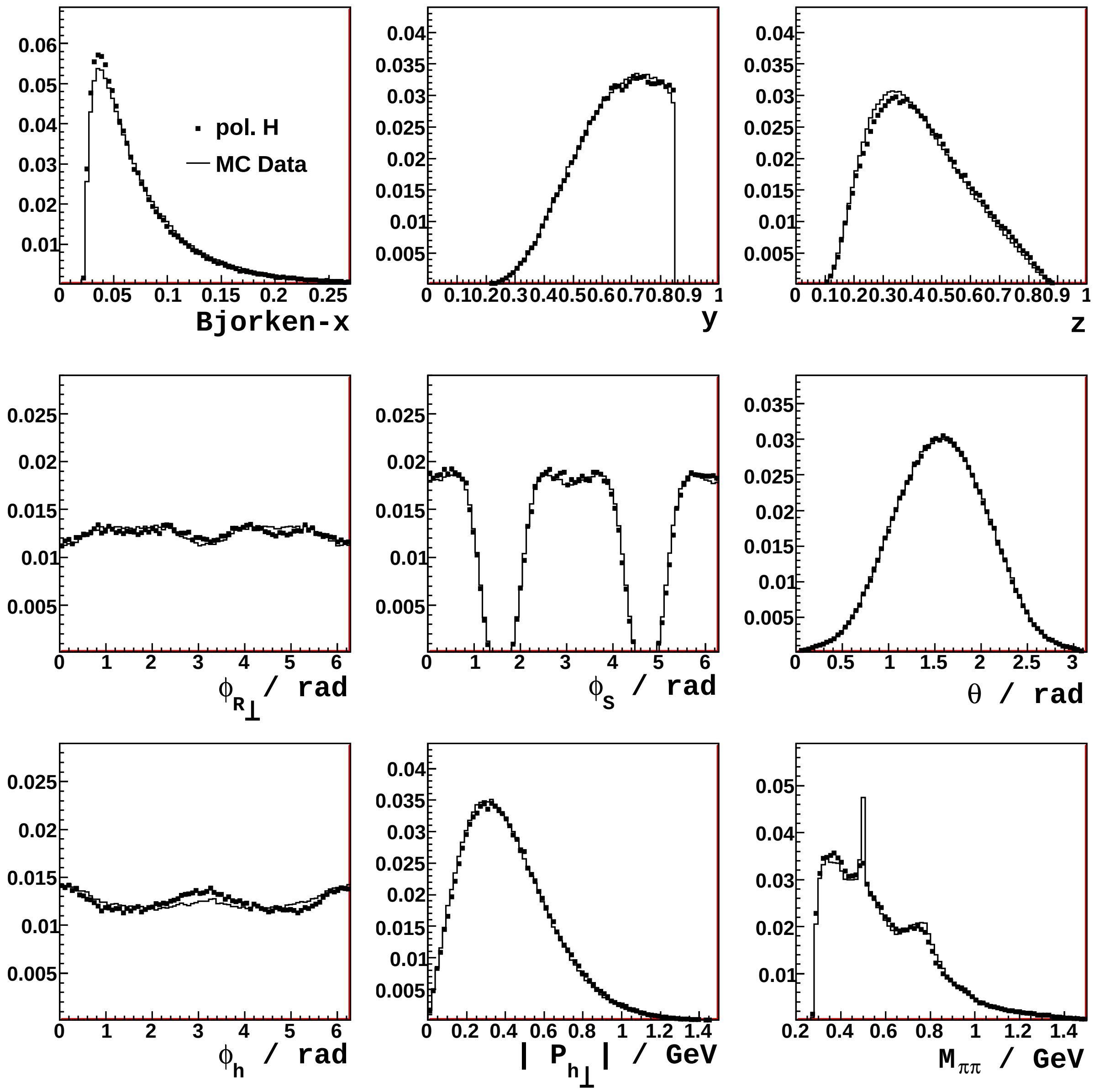

Figure 4.16: Normalized event distributions for semi–inclusive $\pi^+\pi^-$ DIS productions in 9 independent kinematic variables that the asymmetry A_{UT} depends on. The points represent the distributions of the selected polarized hydrogen data (summing the events of the both target polarization states) as same data used in the analysis shown in Figure 4.1. The histograms represent the distributions of the Pythia MC simulation, taking into account the HERMES acceptance.

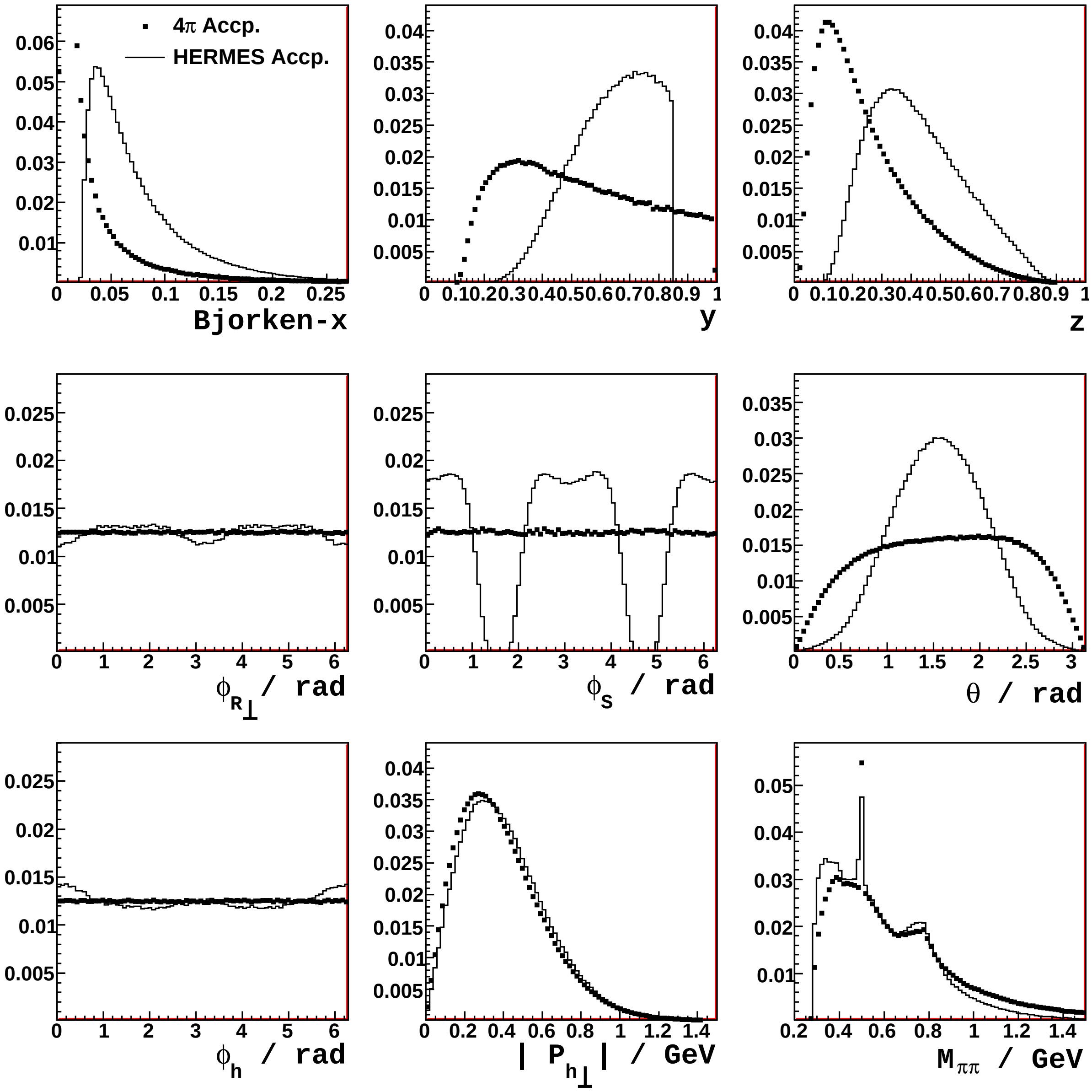

Figure 4.17: Normalized event distributions for semi–inclusive $\pi^+\pi^-$ DIS productions in 9 independent kinematic variables that the asymmetry A_{UT} depends on. The points represent the distributions of the Pythia MC simulation data in **4π acceptance** without any kinematic cuts. The histograms represent the distributions of the Pythia MC simulation data within the HERMES acceptance.

modified Pythia MC data mentioned above. The various experimental distributions are well reproduced by the MC simulation. The two peaks in the $M_{\pi\pi}$ invariant–mass distribution correspond to the $\rho^0(770)$ resonance and the $K_s^0(498)$ resonance. The Figure 4.17 shows the different distributions of the events in the 9 kinematic variables in 4π MC data and the MC data in the HERMES acceptance. Specially in 4π MC data, there are ideal flat distributions in azimuthal angles $\phi_{R\perp}$, ϕ_S, ϕ_h and the sine–like curve distribution in θ.

For the ϕ_h and θ distribution, we will discuss specifically in Sec. 4.5.3 and Sec. 4.5.4.

4.5.2 Acceptance Effect to the Amplitude

To perform acceptance studies, a model prediction for the asymmetry A_{UT} is needed for Eq. (4.40). In practice, it was assumed that there are no other contributions to the asymmetry, *i.e.*, in Eq. (4.28) a_2, a_3 and a_4 are zero. The parameterization then can be written as:

$$\begin{aligned} A_{\mathrm{UT}} &= \sin(\phi_{R\perp}+\phi_S)\sin\theta\ A_{\mathrm{UT}}^{\sin(\phi_{R\perp}+\phi_S)\sin\theta} \\ &= -\sin(\phi_{R\perp}+\phi_S)\sin\theta\frac{B(y)}{A(y)}\sqrt{1-\left(\frac{2m_\pi}{M_{\pi\pi}}\right)^2}\frac{\sum_q e_q^2 h_1^q(x) H_{1,q}^{\sphericalangle,sp}(M_{\pi\pi},z)}{\sum_q e_q^2 f_1^q(x) D_{1,q}(M_{\pi\pi},z)}, \end{aligned} \tag{4.41}$$

where m_π is the π invariant mass $m_\pi = 139.57\,\mathrm{MeV}$ and the amplitude $A_{\mathrm{UT}}^{\sin(\phi_{R\perp}+\phi_S)\sin\theta}$ in Eq. (2.93) in case of $\pi^+\pi^-$ productions was used. For the DiFFs $D_{1,q}(M_{\pi\pi},z)$ and $H_{1,q}^{\sphericalangle,sp}(M_{\pi\pi},z)$, parameterizations were taken from Ref. [117]. For the distribution functions $f_1(x)$ and $h_1(x)$, parameterizations were taken from Ref. [136] and Ref. [86], respectively (corresponding to the dashed line in Figure 2.29).

For the purpose of comparison, the MC data in 4π acceptance were filtered with the same kinematic selections as what we did in MC HERMES acceptance data. As we can see, the parameterization Eq. (4.41) used to assign the target spin is the same with the simm–nonlinear fit function Eq. (4.30). Using the no–constant–part 8×8 binning simm–nonlinear fit, the asymmetry amplitudes in MC data simulated in a 4π acceptance and in the HERMES acceptance are compared in Fig 4.18 and all the values are listed in Table 4.7. The overall amplitudes for each kinematic dependence are also calculated. All the values are confirmed by the ML fit to the same MC data, which are not given explicitly in this thesis.

The figure shows that for the $M_{\pi\pi}$ dependence and for the z dependence there is a clear difference in the values of the extracted amplitudes. This can be caused by the fact that the coverage of the variables that are integrated over[3] are different for the two data sets. It can be easily seen form the difference of the average values of those variables

---

[3] Note that an asymmetry is integrated over certain variables, separately in the numerator and denominator of the asymmetry equation, *e.g.*, $A(x_1) = \frac{\int \mathrm{d}\,x_2\ \mathrm{d}\,x_3 \ldots\ \sigma_{\mathrm{UT}}(x_1,x_2,x_3,\ldots)}{\int \mathrm{d}\,x_2\ \mathrm{d}\,x_3 \ldots\ \sigma_{\mathrm{UU}}(x_1,x_2,x_3,\ldots)}$.

Bins		Results in 4π acceptance				Results in HERMES acceptance				Amplitudes Difference	Scale c_i (%)
		$\mathcal{A}_{4\pi}$	$\langle M_{\pi\pi}\rangle/$ GeV	$\langle x\rangle$	$\langle z\rangle$	$\mathcal{A}_{\mathrm{HERMES}}$	$\langle M_{\pi\pi}\rangle/$ GeV	$\langle x\rangle$	$\langle z\rangle$		
$M_{\pi\pi}$	1	0.107	0.344	0.095	0.307	0.094	0.344	0.083	0.369	0.013	11.8
	2	0.144	0.478	0.095	0.338	0.125	0.475	0.080	0.387	0.019	17.3
	3	0.148	0.661	0.094	0.355	0.119	0.657	0.076	0.431	0.029	26.4
	4	0.090	1.055	0.092	0.400	0.093	0.944	0.072	0.523	-0.003	-2.73
	All	0.121	0.719	0.094	0.361	0.110	0.591	0.078	0.423	0.011	10.0
x	1	0.062	0.719	0.033	0.318	0.058	0.699	0.033	0.397	0.004	3.28
	2	0.092	0.719	0.047	0.347	0.094	0.694	0.047	0.436	-0.002	-1.64
	3	0.133	0.719	0.069	0.370	0.122	0.689	0.068	0.453	0.011	9.02
	4	0.216	0.717	0.156	0.379	0.196	0.683	0.135	0.479	0.020	16.4
	All	0.148	0.719	0.094	0.361	0.122	0.691	0.075	0.444	0.026	21.3
z	1	0.128	0.708	0.088	0.238	0.092	0.631	0.064	0.275	0.036	29.5
	2	0.160	0.724	0.099	0.387	0.117	0.694	0.072	0.389	0.043	35.2
	3	0.182	0.729	0.103	0.495	0.128	0.718	0.080	0.496	0.054	44.3
	4	0.180	0.738	0.100	0.651	0.168	0.731	0.088	0.662	0.012	9.84
	All	0.148	0.719	0.094	0.361	0.122	0.691	0.075	0.444	0.026	21.3

Table 4.7: The extracted simulated amplitudes $A_{\mathrm{UT}}^{\sin(\phi_{R\perp}+\phi_S)\sin\theta}$, $\mathcal{A}_{4\pi}$ in 4π acceptance and $\mathcal{A}_{\mathrm{HERMES}}$ in HERMES acceptance, by LS simm–nonlinear fit. Owing to the high statistics of MC data, the statistical uncertainties were small enough. The average kinematic $M_{\pi\pi}$, x and z are listed in each kinematic bin. The scale factor c_i is defined in Eq. (4.42).

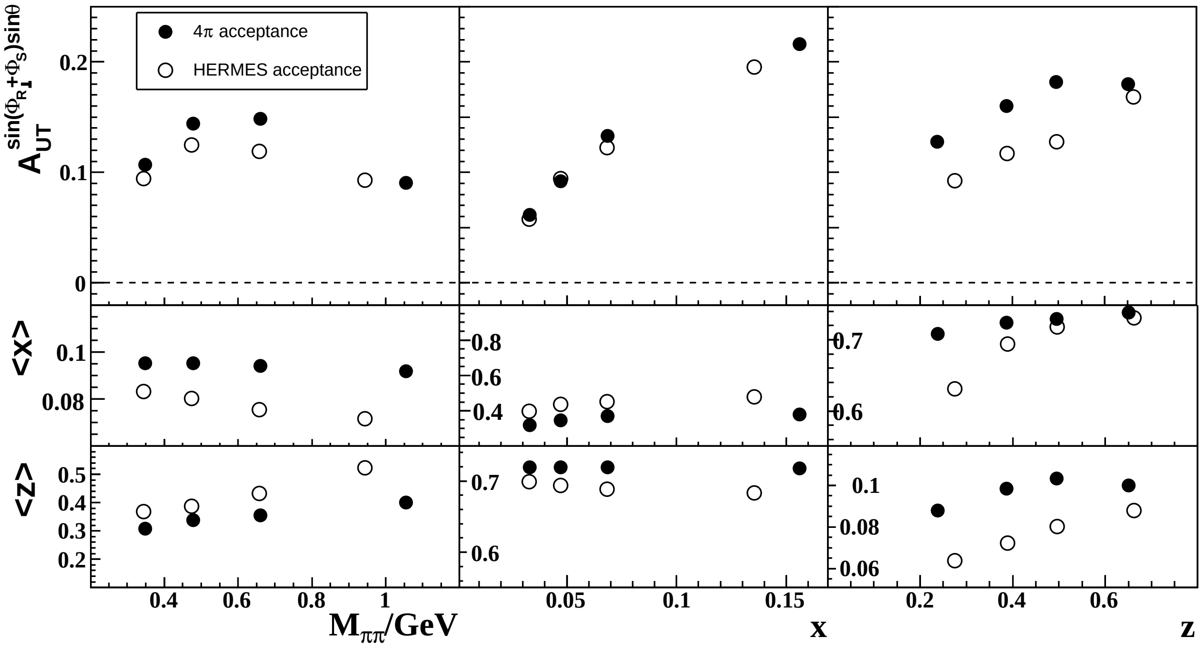

Figure 4.18: The asymmetry amplitude $A_{\mathrm{UT}}^{\sin(\phi_{R\perp}+\phi_S)\sin\theta}$ as a function of $M_{\pi\pi}$, x and z as evaluated with the model predictions: the DiFFs in Ref. [117], the parton distribution functions $f_1^q(x)$ in Ref. [136] and $h_1^q(x)$ in Ref. [86]. The simulations in a 4π acceptance are compared to those in the HERMES acceptance. The statistical error bars were too short to be seen, because of the high statistics of the MC samples. The bottom panels indicate for each data point the corresponding average values $\langle M_{\pi\pi}\rangle$, $\langle x\rangle$ and $\langle z\rangle$. All the numbers can be found in Table 4.7.

in the lower panels in Figure 4.18. Especially the differences in the average values of x for the $M_{\pi\pi}$ dependence and for the z dependence are significant and the influences by the HERMES acceptance can be attributed to the differences in the average x values, which were proved in Ref. [121] with more studies. Since the transversity distribution function $h_1(x)$ is the only unknown part, which depends on Bjorken–x in $A_{\mathrm{UT}}^{\sin(\phi_{R\perp}+\phi_S)\sin\theta}$, this comparison mostly relies on the chosen model of $h_1(x)$. Combined with the fact that most models for $h_1(x)$, are approximately linear in the x range of HERMES experiment (cf. Sec. 5.3.1), it is concluded that this evaluation of the acceptance effect is less model dependent. It is thus possible to give an overall estimate of the systematic uncertainty for each of the kinematic bins, making use of the comparison shown in Figure 4.18. The relative sizes of 4π results to the HERMES acceptance results are taken as the acceptance effect. As the listed numerical results in Table 4.7, we can see that the underestimation of the measured amplitudes is up to 25% for the $M_{\pi\pi}$ dependence, a negligible effect for the x dependence and an up to 43% underestimation for the z dependence.

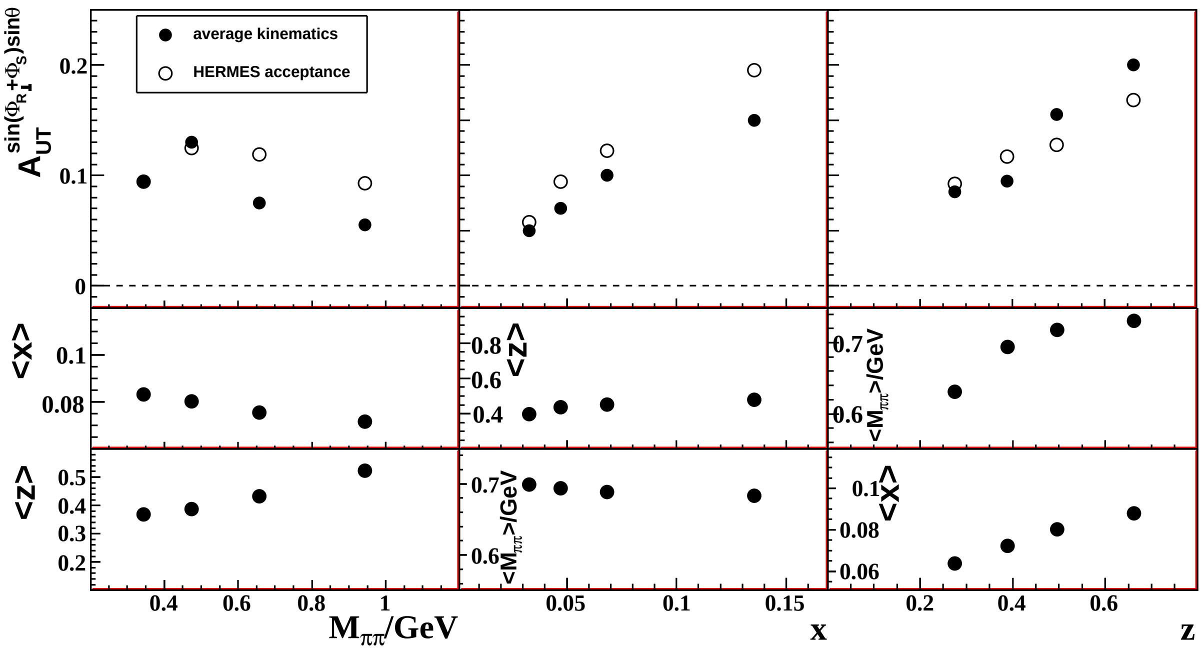

Figure 4.19: The asymmetry amplitude $A_{\mathrm{UT}}^{\sin(\phi_{R\perp}+\phi_S)sin\theta}$ as a function of $M_{\pi\pi}$, x and z as evaluated with the model prediction (the same models used in Sec. 4.5.2). A comparison is shown between the model prediction at the average kinematics within the HERMES acceptance to the model prediction evaluated by a MC study within the HERMES acceptance.

To better understand the bigger acceptance effect in $M_{\pi\pi}$ and z dependence, another study is devised to calculate the asymmetry at the averaged values of the kinematic variables of MC data within the HERMES acceptance. If the asymmetry is linearly dependent on the kinematic variables within the range that the variables are integrated over, the asymmetry of this calculation should be of the same size of that of the MC study within the HERMES acceptance. Figure 4.19 shows the comparison between two model predictions of the asymmetry amplitudes. We can see that the difference appears to be smaller than that in Figure 4.18, but still they are not totally in agreement. At the same averaged kinematic values, two groups of the asymmetry amplitudes are still different, especially at $M_{\pi\pi}$ and z dependence plots. In MC study, the asymmetry is extracted from the kinematic bins where data are scattered based on the statistics. But the model calculation of the asymmetry only at the averaged values can have the same amplitudes as the MC simulation, only if the kinematic dependence of the asymmetry is linear. As indicated in Figure 2.29 and Figure 2.30, in the kinematic range at HERMES, x and z dependence is approximately linear. But $M_{\pi\pi}$ dependence is obviously non–

linear, with strong peaks at $M_{\pi\pi} \approx 0.5\,\mathrm{GeV}$ and $\rho^0(770)$ region. Thus the disagreement in Figure 4.19 can be understood as the effect of the non–linearity of the $M_{\pi\pi}$ dependence of the asymmetry.

Therefore, in theory one could make an acceptance correction to the extracted asymmetry amplitudes based on this study. However, because this study highly relies on the theoretical models and the model itself has quite large inherent uncertainties, we will only take this effect as a part of the systematic uncertainties. A scaling systematic uncertainty can be calculated from the acceptance effect to the asymmetry. The factor is taken as the ratio of the difference of the extracted asymmetry in 4π acceptance and that in HERMES acceptance to the extracted overall asymmetry of that kinematic dependence. The scaling factor is calculated by

$$c_i = \frac{\mathcal{A}^i_{4\pi} - \mathcal{A}^i_{\mathrm{HERMES}}}{\mathcal{A}^{All}_{\mathrm{HERMES}}} \ , \tag{4.42}$$

where i is the bin index number and $\mathcal{A}^{All}_{\mathrm{HERMES}}$ is the total asymmetry amplitude which is integrated over all the kinematics in the whole kinematic range. Compared with using the ratio of the difference to the asymmetry amplitude in the same kinematic bin, this method can better avoid the influence from the limited statistics of the real data. The scaling factor c_i is also listed in Table 4.7. The scaling factor will be taken as the systematic uncertainties of the measured asymmetry amplitudes.

4.5.3 Azimuthal Angle ϕ_h Acceptance

From Figure 4.17, we can see the incomplete ϕ_h in HERMES acceptance, if comparing with that in 4π acceptance. Hence, the integration of the transverse momentum dependent polarized cross section (cf. Appendix B) over the transverse momentum of the pion pair $\boldsymbol{P_{h\perp}}$ might be biased and furthermore would bring additional asymmetry to the measured one. Since the ϕ_h–dependent terms in Eq. (B.2) and Eq. (B.3) will not necessarily disappear after integrated over $\boldsymbol{P_{h\perp}}$, the final extracted $\sin(\phi_{R\perp} + \phi_S)$ momenta would be changed considerably.

To evaluate this acceptance effect, the model predictions for the sizes and dependencies of all these ϕ_h–dependent terms are needed. The effect on the amplitude $A_{\mathrm{UT}}^{\sin(\phi_{R\perp}+\phi_S)}$, which is directly related to the measured amplitude $A_{\mathrm{UT}}^{\sin(\phi_{R\perp}+\phi_S)\sin\theta}$ with a factor $\frac{\pi}{4}$ in Eq. (2.95), is then used to estimate the corresponding contribution as part of the systematic uncertainties. Following the same strategy as in Sec. 4.5.1, target spin states were assigned again to the unpolarized Pythia MC dihadron lepto–production data according to the model for the asymmetry A_{UT} including all ϕ_h–dependent terms. However, no such transverse momentum dependence information exists, *e.g.*, most of the involved transverse momentum dependence distribution functions and fragmentation functions are yet completely unknown. But as a good substitution, a very general model can be used, in which the sizes and dependencies of these terms are varied between reasonable bounds. For the transverse–momentum dependence of all the distribution and fragmentation functions appearing in A_{UT}, a Gaussian Ansatz was used as the Eq. (B.4). After taking into account the Gaussian Ansatz for the convolution integrals, the expressions for $\mathrm{d}^9\sigma_{\mathrm{UU}}$ and $\mathrm{d}^9\sigma_{\mathrm{UT}}$ are given as Eq. (B.5) and Eq. (B.6). For the parton distribution functions $f_1(x)$, $h_1(x)$ and for the fragmentation functions $D_1(M_{\pi\pi}, z)$ and $H_1^{\sphericalangle,sp}(M_{\pi\pi}, z)$, the same models were used as in Sec. 4.5.2.

The ϕ_h–dependent terms were implemented such that the corresponding asymmetry amplitudes $A_{\mathrm{UT}}^{\sin(a\phi_h+b\phi_{R\perp}+c\phi_S+\frac{d}{2}\pi)}$ depend on x, z, and $\boldsymbol{P_{h\perp}}$ according to:

$$\begin{aligned}\frac{1}{2}A_{\mathrm{UT}}^{\sin(a\phi_h+b\phi_{R\perp}+c\phi_S+\frac{d}{2}\pi)} &\equiv \frac{\iiint \mathrm{d}\,\phi_h\ \mathrm{d}\,\phi_{R\perp}\ \mathrm{d}\,\phi_S \sin(a\phi_h + b\phi_{R\perp} + c\phi_S + \frac{d}{2}\pi)\ \mathrm{d}^9\,\sigma_{\mathrm{UT}}}{\iiint \mathrm{d}\,\phi_h\ \mathrm{d}\,\phi_{R\perp}\ \mathrm{d}\,\phi_S\ \mathrm{d}^9\,\sigma_{\mathrm{UU}}} \\ &= C_N\ z^{\alpha_N}\ x^{\beta_N}\ f_N(|\boldsymbol{P_{h\perp}}|) \qquad (4.43)\end{aligned}$$

with N identifying the various terms in the polarized cross section, C_N a constant scaling factor, α_N, $\beta_N \in [0.1, 3]$ and a, b, c and d are either zero or integers depending on N. Similarly, asymmetry amplitudes $A_{\mathrm{UU}}^{\sin(a\phi_h+b\phi_{R\perp}+c\phi_S+\frac{d}{2}\pi)}$ were introduced for the ϕ_h–dependent terms in the unpolarized cross section. All amplitudes were chosen to be independent of θ[4]. Apart from the fact that all these different amplitudes of the polarized and unpolarized cross section increase nonlinearly with increasing x and z, the choices for α_N and β_N are quite arbitrary, but were found not to influence the final conclusions. The values of the scaling factors C_N in Eq. (4.43) were derived from the averaged amplitudes, which were randomly chosen in the range $[-0.1, 0.1]$, *i.e.*,

$$\frac{\int A_{\mathrm{UU/T}}^{\sin(a\phi_h+b\phi_{R\perp}+c\phi_S+\frac{d}{2}\pi)}\ \mathrm{d}^9\,\sigma_{\mathrm{UU}}}{\int \mathrm{d}^9\,\sigma_{\mathrm{UU}}} \in [-0.1, 0.1] \qquad (4.44)$$

where the integral is performed over all 9 dimensions and integration ranges were used corresponding to those used in the analysis as

$$\begin{aligned} M_{\pi\pi} &\in [0.5, 1]\ \mathrm{GeV}, \\ |\boldsymbol{P_{h\perp}}| &\in [0, \infty]\ \mathrm{GeV}, \\ y &\in [0.10, 0.85], \\ z &\in [0.1, 1.0], \\ x &\in [Q^2_{\mathrm{min}}/(y(s-M^2)), 0.4] = [1/(y(s-M^2)), 0.4]. \qquad (4.45)\end{aligned}$$

Each resulting parameterization of A_{UT} had to satisfy the positivity limit $|A_{\mathrm{UT}}| < 1$.

To estimate the systematic uncertainty, the amplitude $A_{\mathrm{UT}}^{\sin(\phi_{R\perp}+\phi_S)}$ was extracted 1000 times from the same Pythia dataset, similar in size to the real data, but each time with spin states randomly chosen according to their probability calculated from randomly chosen values for α_N, β_N, and C_N for each of the ϕ_h–dependent terms. As an example in

---

[4] Eq. (2.95) shows a constant ratio of $A_{\mathrm{UT}}^{\sin(\phi_{R\perp}+\phi_S)}$ to $A_{\mathrm{UT}}^{\sin(\phi_{R\perp}+\phi_S)\sin\theta}$.

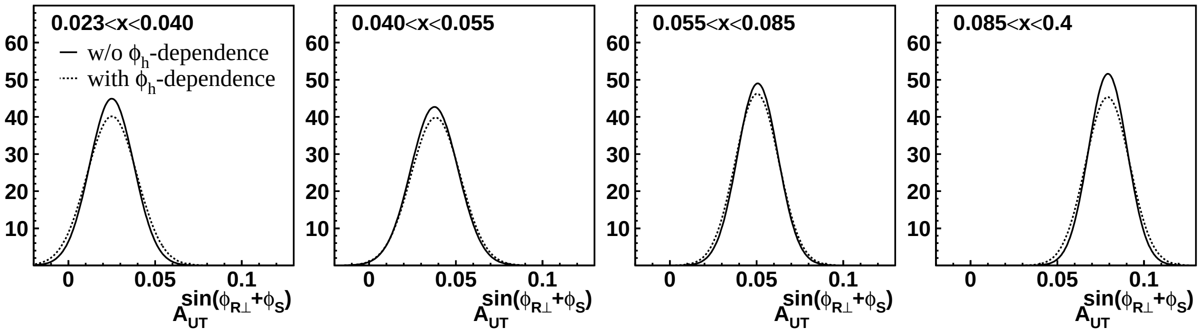

Figure 4.20: Gaussian fits to the distributions of simulated values of $A_{\mathrm{UT}}^{\sin(\phi_{R\perp}+\phi_S)}$ without (solid histograms) and with (dashed histograms) a contribution of ϕ_h–dependent terms to A_{UT}. The reduced–χ^2 values of the fits are in the range 0.50–1.1. The different panels correspond to different Bjorken–x bins as indicated.

the Bjorken–x dependence shown in Figure 4.20, the distribution obtained in the extracted amplitudes $A_{\mathrm{UT}}^{\sin(\phi_{R\perp}+\phi_S)}$ was compared to a similarly obtained distribution, but which had only $A_{\mathrm{UT}}^{\sin(\phi_{R\perp}+\phi_S)}$ implemented. On average the implementation of the ϕ_h dependence resulted in a distribution which has the same average value, but which is 10% broader [121], independent of the $M_{\pi\pi}$, z or x bin considered. Thus this effect is found to be small compared to the other effect of the acceptance described above.

4.5.4 Polar Angle θ Acceptance

The relative momentum of two pion determines the polar angle θ, since θ is defined in the center–of–mass system of them (cf. Figure 2.22). The RICH detector in HERMES PID system requires the particle momentum $P > 1$ GeV/c, in order to discriminate pion from other particles. So this distorted the θ statistical distribution from the ideal sine curve. In this section, the incomplete acceptance of θ (cf. Figure 4.17) in HERMES spectrometer is studied in order to investigate its influence to the extraction of the asymmetry amplitude $A_{\mathrm{UT}}^{\sin(\phi_{R\perp}+\phi_S)\sin\theta}$. Also it is important to check the validity of Eq. (2.95), as it needs the integration over $\cos\theta$ in the numerator and denominator, separately. Therefore, if the numerator and the denominator of the asymmetry A_{UT} are integrated over θ within the limited HERMES spectrometer, the terms in Eqs. (2.92), other than the s–p wave DiFF, can still contribute to the amplitude in Eq. (2.93), which can be avoided for a detector with a complete coverage of the polar angle θ.

To study this effect in MC simulation, two different transverse target–spin modulations on the MC data with HERMES acceptance were applied. The first one only considers the simple θ dependence, *i.e.*, the first term of Eq. (2.92b), just the same as used in Sec. 4.5.2. The second one includes full θ–dependent terms as Eq. (4.27). Thus, the target spin is

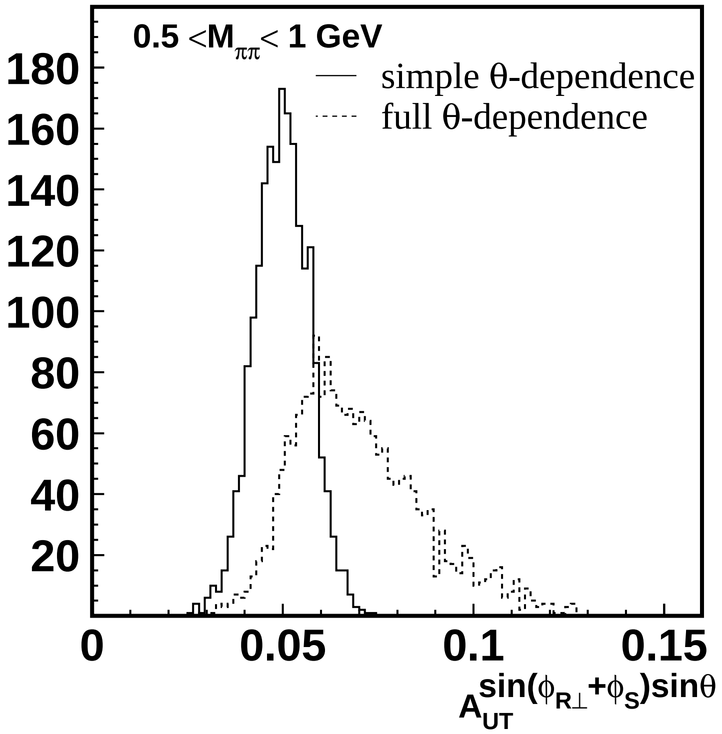

Figure 4.21: Distributions of simulated values of $A_{\rm UT}^{\sin(\phi_{R\perp}+\phi_S)\sin\theta}$ without (solid line) and with (dashed line) θ–dependent contributions of the fragmentation functions $D_{1,\rm UL}^{sp}$, $D_{1,\rm LL}^{pp}$ and $H_{1,\rm LL}^{\sphericalangle,pp}$ to $A_{\rm UT}$.

set following the asymmetry equation

$$A_{\rm UT} = \sin(\phi_{R\perp}+\phi_S)\frac{A_{\rm UT}^{\sin(\phi_{R\perp}+\phi_S)\sin\theta}\sin\theta + A_{\rm UT}^{\sin(\phi_{R\perp}+\phi_S)\sin 2\theta}\sin 2\theta}{1+\dfrac{D_{1,\rm UL}^{sp}}{D_{1,\rm UU}}\cos\theta+\dfrac{D_{1,\rm LL}^{pp}}{D_{1,\rm UU}}\dfrac{1}{4}(3\cos^2\theta-1)}. \tag{4.46}$$

$A_{\rm UT}^{\sin(\phi_{R\perp}+\phi_S)\sin\theta}$ is modeled as the Sec. 4.5.2 and the fragmentation function $H_1^{\sphericalangle,pp}$ related amplitude $A_{\rm UT}^{\sin(\phi_{R\perp}+\phi_S)\sin 2\theta}$ modeled as

$$A_{\rm UT}^{\sin(\phi_{R\perp}+\phi_S)\sin 2\theta} = C\, z^{\alpha}\,\frac{\sum_q e_q^2 h_1^q(x)}{\sum_q e_q^2 f_1^q(x)}, \tag{4.47}$$

where C was varied in accordance with the limit expressed by Eq. (4.44). According to the boundaries given in Sec. 2.4.3, the fragmentation functions $D_{1,\rm UL}^{sp}$ and $D_{1,\rm LL}^{pp}$, which appear in Eq. (2.92a), can be of the same order of magnitude as D_1. The values of the fragmentation function ratios $D_{1,\rm UL}^{sp}/D_{1,\rm UU}$ and $D_{1,\rm LL}^{pp}/D_{1,\rm UU}$ were varied randomly, within the following boundaries:

$$-\frac{3}{2} \le D_{1,\rm UL}^{sp}/D_{1,\rm UU} \;\le\; \frac{3}{2}\,, \tag{4.48}$$

$$-1 \le D_{1,\rm LL}^{pp}/D_{1,\rm UU} \;\le\; 2\,. \tag{4.49}$$

These boundaries are needed to ensure the positivity of the cross section. Finally, for each chosen set of values a scan was made to ensure that they also satisfy the constraint $|A_{\mathrm{UT}}| < 1$.

After 1000 times of operation on the two sets of the MC data, the asymmetry amplitude $A_{\mathrm{UT}}^{\sin(\phi_{R\perp}+\phi_S)\sin\theta}$ were extracted using LS 2-D simm-nonlinear fit many times. The histograms of the extracted amplitudes from simple (solid line) and complete (dashed line) θ–dependent MC data in Figure 4.21 show the obviously different behaviors: the central values of the two histograms are shifted and the dashed distribution is much broader. The differences show that the effect of the θ–dependent terms can be quite sizable, and should be estimated as part of the systematic uncertainties.

Hence the θ'–dependent term in Eq. (4.29) can not be neglected. The value of the fit parameter a_1 depends on the value of A_2. A systematic uncertainty can be assigned to the extracted value a_1 by studying its response to the scan of A_2. The parameter A_2 was varied within its positivity limits, given by the Eq. (2.90c)

$$-\frac{3D_{1,\mathrm{UU}}^{pp}}{2D_{1,\mathrm{UU}}} \leq A_2 \leq \frac{3D_{1,\mathrm{UU}}^{pp}}{D_{1,\mathrm{UU}}}, \tag{4.50}$$

where $D_{1,\mathrm{UU}}^{pp}$ indicates the pure p–wave component of the dihadron unpolarized fragmentation function $D_{1,\mathrm{UU}}$. The size of this component are estimated using the Pythia MC event generator tuned to HERMES kinematics in next Section. The values for a_1 are obtained from the central fitted value between the upper and lower fitted a_1 values, when varying A_2 between its upper and lower bounds.

4.5.5 p–Wave DiFF D_1^{pp} Estimation

We follow the way of modeling dihadron fragmentation function in Ref. [117] to estimate the relative size of the component of the pure p–wave unpolarized DiFF in the unpolarized DiFF. Taking the advantage of the unpolarized two–pion MC production, taking into account the HERMES acceptance as explained in Sec. 4.5, the invariant mass spectrum can be generated, which are plotted in Figure 4.22. The prominent channels contributing to this production are the followings [182]:

1. $q \to \pi^+\pi^- X_1$: fragmentation into an "incoherent" $\pi^+\pi^-$ pair that we will call, in the following, "background";

2. $q \to \rho\ X_2 \to \pi^+\pi^- X_2$: fragmentation into a ρ resonance then decaying into $\pi^+\pi^-$, responsible for a peak at $M_h \sim 770$ MeV (14.81%);

3. $q \to \omega\ X_3 \to \pi^+\pi^- X_3$: fragmentation into a ω resonance then decaying into $\pi^+\pi^-$, responsible for a small peak at $M_h \sim 782$ MeV (0.31%);

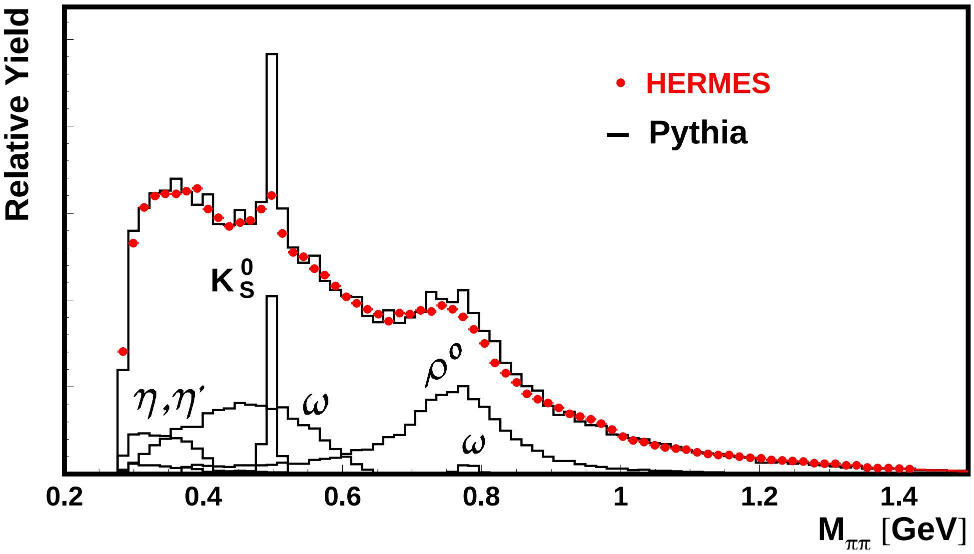

Figure 4.22: The normalized counts of semi–inclusive $\pi^+\pi^-$ productions in bins of $M_{\pi\pi}$ from the MC data with HERMES acceptance (the histogram) and from real analyzed data (the points). The contributions of the prominent channels are also indicated separately.

4. $q \to \omega\ X'_4 \to \pi^+\pi^- X_4$ with $X_4 = \pi^0\ X'_4$: fragmentation into a ω resonance then decaying into $\pi^+\pi^-\pi^0$ (π^0 unobserved), responsible for a broad peak around $M_h \sim$ 500 MeV (8.65%);

5. $q \to \eta\ X'_5 \to \pi^+\pi^- X_5$ with $X_5 = \mathcal{X}\ X'_5$: fragmentation into a $\eta(547)$ or $\eta'(958)$ then decaying into $\pi^+\pi^-\mathcal{X}$ ($\mathcal{X}$ unobserved), responsible for a peak around $M_h \sim$ 350 MeV (2.05%);

6. $q \to K^0\ X_6 \to \pi^+\pi^- X_6$: fragmentation into a K^0 resonance then decaying into $\pi^+\pi^-$, responsible for a narrow peak at $M_h \sim$ 498 MeV (3.41%).

Pions in the channels 2 and 3 are obviously produced in relative p wave, since they come from the decay of a vector meson. In the channel 4, each charged pion can be in a relative p wave with respect to the other one or to π^0, the net result being that there is a fraction of $\pi^+\pi^-$ pairs that is produced in a relative s wave. In the following, we will neglect this fraction and assume that all charged pairs in the channel 4 are produced in p wave. Then we could estimate the value of the pure p–wave component of the dihadron fragmentation function $D_{1,\mathrm{UU}}$, by multiplying $\frac{4}{3}$[5] with the ratio of the yields in the pure

---

[5] This is due to the factor of $\frac{3}{4}$ for the pure p–wave fragmentation function in the unpolarized two–hadron cross section in Eq. (2.92a).

p–wave channel and the total two pion yields:

$$\frac{D^{pp}_{1,\mathrm{UU}}(M_{\pi\pi}, z)}{D_{1,\mathrm{UU}}(M_{\pi\pi}, z)} = \frac{4N^{pp}_{\pi\pi}(M_{\pi\pi}, z)}{3N_{\pi\pi}(M_{\pi\pi}, z)} \ . \tag{4.51}$$

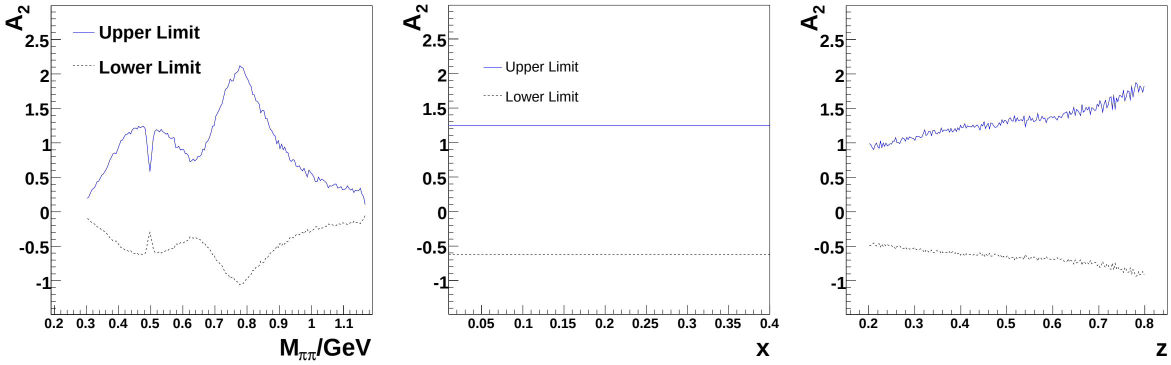

Figure 4.23: A_2 bounds with dependence on $M_{\pi\pi}$, x and z. The upper and lower limits of Eq. (4.50) are indicated, separately. Since fragmentation function is independent of x, the boundary is constant in the whole x range.

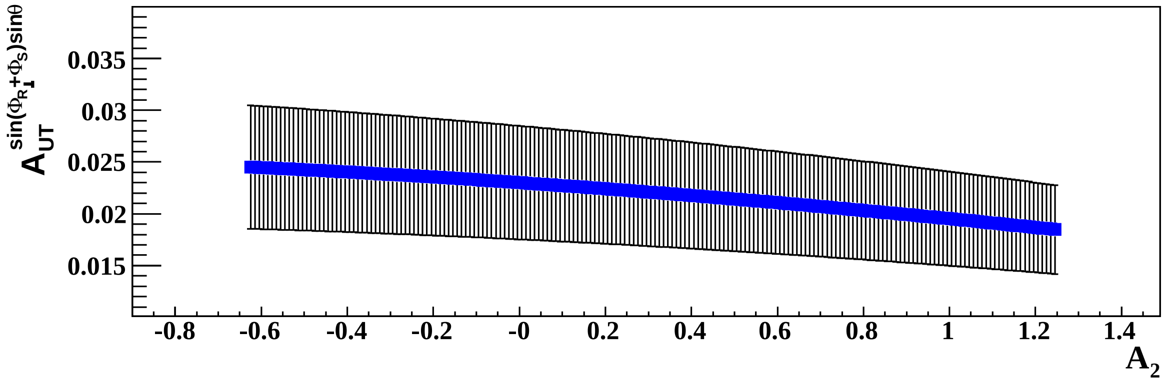

Figure 4.24: The extracted amplitudes with the total real data set with the variation of A_2 inside its bound.

Plots in Figure 4.23 show the bounds for A_2 with dependence on $M_{\pi\pi}$, x and z. The A_2 boundaries of different kinematic dependence are calculated with the selections of the corresponding kinematic bins as in Table 4.5. The cut off of the curves in Figure 4.23 is due to low statistics in that range and the boundary cannot be calculated from MC data. But the kinematic coverages of the curves are enough for all the averaged values of kinematic variables in the bins (cf. Table 5.1). Note that in Figure 4.22, MC simulation excessively produces $\pi^+\pi^-$ pairs around $K^0(498)$ resonance compared with the real HERMES data. It can be understood that the MC generator was tuned to the single–hadron multiplicity at HERMES experiment. Only to tune the two–hadron multiplicity of MC data to that of real data can resolve this problem. But in fact this extra K^0 MC yields would not affect the scan analysis. For x– and z–dependent study, the $K^0(498)$ is out of the $M_{\pi\pi}$ range as indicated in Table 4.5. And for $M_{\pi\pi}$–dependent study, thanks to the narrow resonance of $K^0(498)$, the averaged $M_{\pi\pi}$ values in Table 4.7 are all out of the $\pm 2\sigma$ mass window of the $K^0(498)$ resonance. Hence, the inconsistent multiplicity around $K^0(498)$ resonance would not influence the scan study.

The absolute value of the upper limit is twice the absolute value of the lower limit, as given by the Eq. (4.50). For different kinematic bins, by varying A_2 in the corresponding bound with small steps, a series of a_1 can be fitted correspondingly, with a fixed A_2 parameter in each step. The variation of the fitted a_1 then can be used to estimate the effect from the p–wave DiFF D_1^{pp}. As an example, the changes of a_1 in the overall bin are plotted in Figure 4.24 as a function of the variation of A_2, which was scanned within the MC evaluated bounds. We can see the flat decreasing trend of the fitting a_1 when A_2 increases. The median of these a_1 samples were taken as the final result of the extract asymmetry amplitude $A_{\mathrm{UT}}^{\sin(\phi_{R\perp}+\phi_S)\sin\theta}$, and the standard deviation of this flat distribution, which is a factor of $1/2\sqrt{3}$ of the difference between the maximum and the minimum a_1, was assigned as the systematic scanning uncertainty. So the data in 2002–2005 are used to extract the asymmetry amplitudes as final results. Table 4.8 lists the scan results with LS fit. The results of the A_2 scan study is confirmed by those fitted with ML fit. The fitted asymmetry and the statistical errors will be taken as final extracted asymmetry results and the scan errors as the asymmetrical uncertainties.

4.5.6 RICH Non–Pion Contamination

In this analysis, the efficiency of the pion identification in RICH detector is quite crucial. With MC simulation on the RICH detector [191], we can estimate the efficiency of RICH detector and apply the correction in the extraction.

We define the number of the particles N_t^i where t is the true particle type (*e.g.*, π, K and p) and i is the identified particle type by RICH. Then we can have the identification probability

$$Q_t^i \equiv \frac{N_t^i}{\sum_s N_s^i}, \tag{4.52}$$

where $Q_t^i \in [0,1]$ means the probability that the identified particle of type i are in fact

Bins		LS scan fit			
		$\mathcal{A}$	stat. error	reduced–χ^2	scan. error
$M_{\pi\pi}$	1	0.010	±0.009	0.703	±0.001
	2	0.012	±0.007	1.324	±0.001
	3	0.024	±0.007	0.850	±0.002
	4	0.019	±0.008	0.965	±0.001
	all	0.016	±0.004	0.851	±0.002
x	1	0.015	±0.010	0.883	±0.001
	2	0.002	±0.011	1.030	±0.001
	3	0.035	±0.010	1.379	±0.004
	4	0.020	±0.010	0.936	±0.001
	all	0.018	±0.005	0.866	±0.002
z	1	0.018	±0.010	1.035	±0.001
	2	0.010	±0.010	0.636	±0.001
	3	0.036	±0.010	1.040	±0.005
	4	0.012	±0.009	0.836	±0.001
	all	0.018	±0.005	0.866	±0.002
overall		0.018	±0.005	0.866	±0.002

Table 4.8: The extracted amplitudes $\mathcal{A}$ ($A_{\mathrm{UT}}^{\sin(\phi_{R\perp}+\phi_S)\sin\theta}$), the corresponding statistical uncertainty (stat. error) and systematic uncertainty (scan. error) from the scan of A_2 within the positivity bounds using LS fit. The latest production in 2002–2005 are used. Also the reduced–χ^2 in LS fit is given. The overall bin means extracting the asymmetry amplitude from the whole kinematic region $0.5\,\mathrm{GeV}/c^2 < M_{\pi\pi} < 1.0\,\mathrm{GeV}/c^2$, $0.023 < x < 0.400$ and $0.000 < z < 1.000$.

particle of type t. Then we could make the matrix Q

$$Q = \begin{pmatrix} Q_\pi^\pi & Q_K^\pi & Q_p^\pi \\ Q_\pi^K & Q_K^K & Q_p^K \\ Q_\pi^p & Q_K^p & Q_p^p \end{pmatrix} \tag{4.53}$$

The Q–matrix can be extracted from MC data, which simulate the RICH detection and HERMES acceptance. We set

$$W_i = Q_{i,\pi}^{j1} Q_{i,\pi}^{j2}, \tag{4.54}$$

where $j1, j2 \in \{\pi, K, p\}$ and W_i is the probability in event i that the identified two hadrons $j1$ and $j2$ by RICH are truly the pion pair. By using ML fit, W_i can be regarded as the event weight in the p.d.f as in Eq. (4.26). From the Čerenkov angles plot in Figure 3.10, it can be seen that in the momentum range $1\,\mathrm{GeV}/c < p < 2\,\mathrm{GeV}/c$, RICH cannot discriminate kaon and proton, but can identify pion. Hence, in this range identified kaon and proton are not credible and the event weight W_i will only take into account the identified pion:

$$W_i = Q_{i,\pi}^{\pi} Q_{i,\pi}^{\pi}. \tag{4.55}$$

This is applicable, because for the momentum of particle in the momentum range $1\,\mathrm{GeV}/c < p < 2\,\mathrm{GeV}/c$ in real data, RICH identified pions are as much as $N_\pi/N \sim 92\%$ in the final hadrons. For momentum region $p > 2\,\mathrm{GeV}/c$, pion, kaon and proton can be differentiated by RICH, and Eq. (4.55) is used.

The identification efficiency of the RICH detector are influenced by the following items:

- **PID algorithms: IRT, DRT and EVT** described in Sec. 3.3.3 are in fact one of the identification techniques. In the selection of the real data in this analysis only IRT was utilized, because it shows more stable performance than other choices.

- **The quality parameter** rQ_p is defined as the ratio of the highest and the second highest possible type, as defined in Eq. (4.3). A cut on it will affect the particle identification performance. Here we choose the cut at $rQ_p > 0$.

- **The momentum of the passing particle** has a relation with the emission angle of the Čerenkov photon. So, the momentum is directly related to the resolution of the RICH detector. When the Čerenkov angle is small, the resolution becomes worse. The Q–matrix will be generated for each momentum of the hadron.

- **The number of the particles** in the same half of the RICH detector (cf. Sec. 3.3.3). When the tracks are more than 1, the Čerenkov rings will be contaminated among them and the efficiency then will be influenced. In this work, the number of the tracks in one half is grouped as $n = 1$, $n = 2$ and $n > 2$.

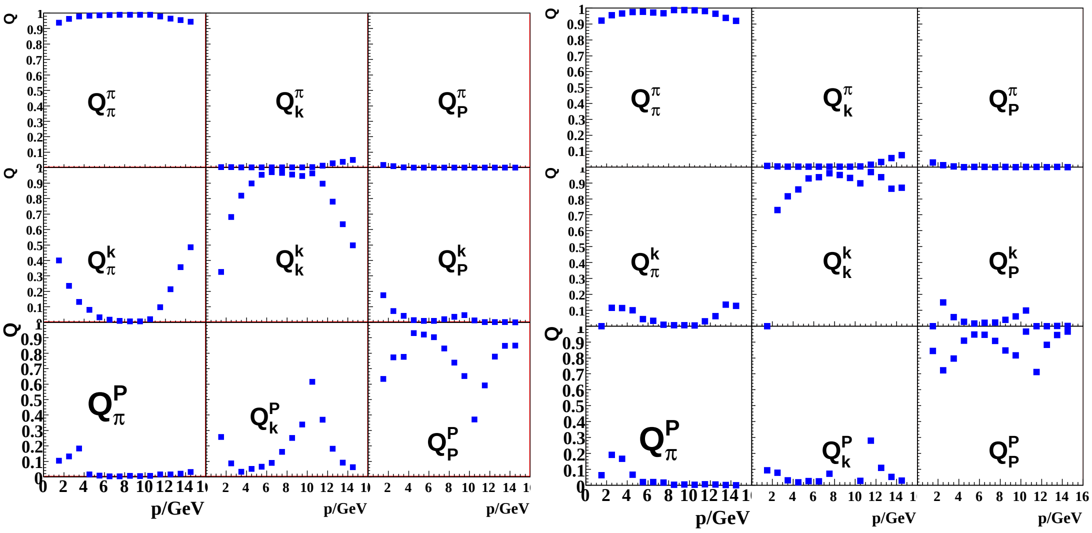

Figure 4.25: Extracted elements in Q–matrix versus the particle momentum p. The values corresponds to only one track in one half of RICH detector, that is $n = 1$. Left plot is from IRT MC simulation, and right plot is from EVT MC simulation.

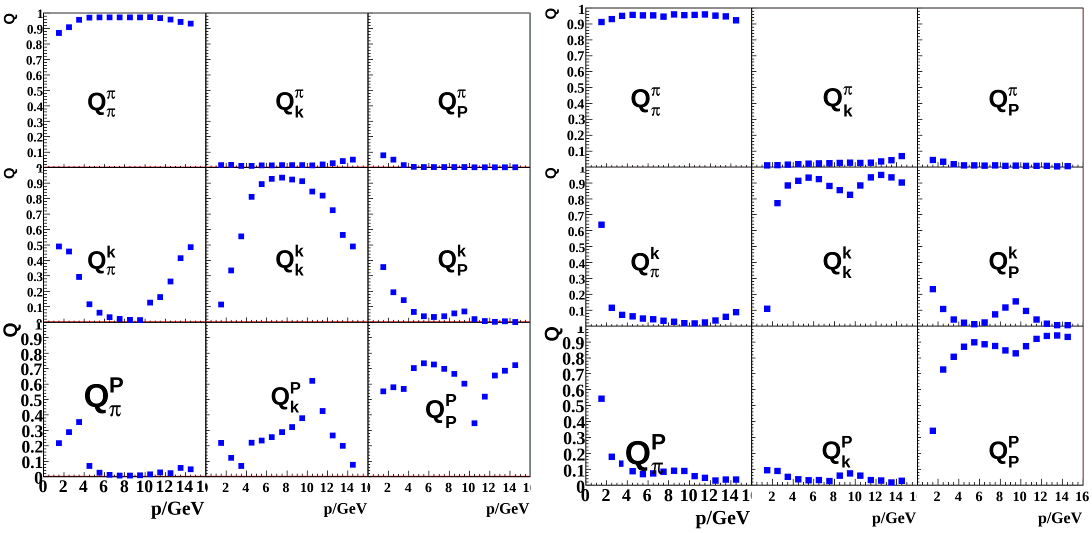

Figure 4.26: Extracted elements in Q–matrix as Figure 4.25, but with $n = 2$. Left plot is from IRT MC simulation, and right plot is from EVT MC simulation.

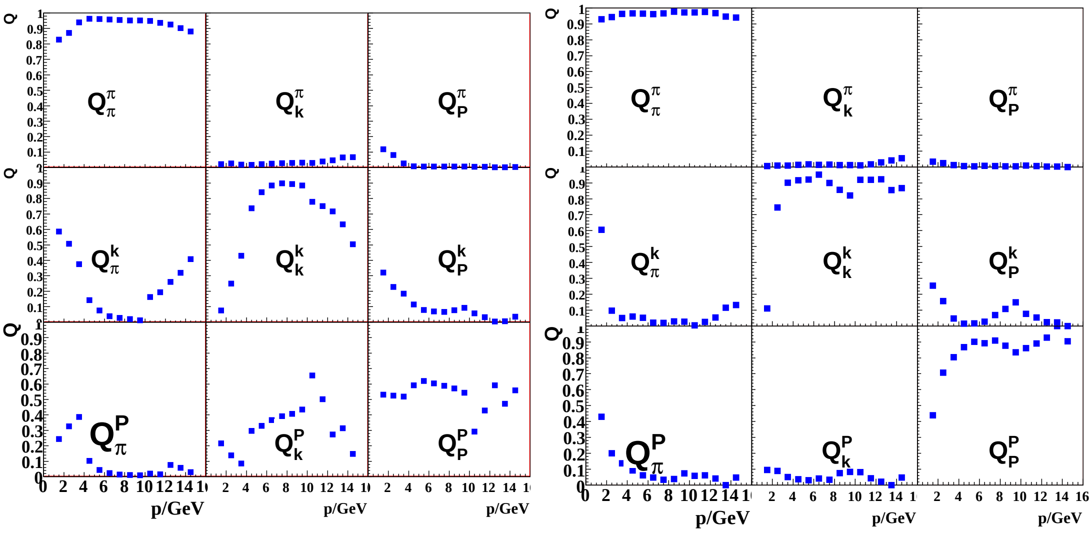

Figure 4.27: Extracted elements in Q–matrix as Figure 4.25, but with $n > 2$. Left plot is from IRT MC simulation, and right plot is from EVT MC simulation.

New MC data are used for this purpose of the study, where the RICH detector and the semi–inclusive two–hadron production with HERMES acceptance are simulated. By counting the number of the tracks in MC data in the different momentum bins and in the bins of the number of tracks in the same half of the RICH, we can evaluate the Q–matrix. Since the statistics of final particles with momentum larger than 15 GeV/c is very small, the momentum is grouped into 14 bins with step of 1 GeV/c from 1 GeV/c to 14 GeV/c. The particles with momentum larger than 15 GeV/c will be combined into the last bin (14 GeV/c∼15 GeV/c). Figs. 4.25, 4.26 and 4.27 show the extracted momentum–dependent Q–matrix with the number of the tracks $n = 1, 2, > 2$ within the same half of the RICH detector, respectively. The left plots are from RICH algorithm IRT, and the right plots are from RICH algorithm EVT. The decreasing efficiency can be seen when the Q–matrices among $n = 1$, $n = 2$ and $n > 2$ are compared. It is easily understandable that the more tracks in the same half of RICH detector, the more contamination among the simultaneous passing particles. But we can clearly see the improvement of the EVT efficiency compared with IRT plots, especially for tracks $n > 1$.

To apply the RICH efficiency correction (also called RICH unfolding), we selected the real data with the same selections as those described in Sec. 4.2, only loosing the requirement of the hadron type on the RICH PID in Eq. (4.4). Assigning the two hadrons in each event with the corresponding Q value based on the RICH identified hadron type, we could have the event weight:

$$W_i = \begin{cases} Q^{\pi}_{i,\pi} Q^{\pi}_{i,\pi}, & \text{if } 1\,\mathrm{GeV}/c < p < 2\,\mathrm{GeV}/c\ ; \\ Q^{j1}_{i,\pi} Q^{j2}_{i,\pi}, \quad (j1, j2 \in \pi, K, p), & \text{if } p > 2\,\mathrm{GeV}/c\ . \end{cases} \tag{4.56}$$

Taking the asymmetry parameterization in Eq. (4.29) and the likelihood function in Eq. (4.26), we have the following likelihood function

$$-\ln L(\boldsymbol{\phi_{R\perp}}+\boldsymbol{\phi_S},\boldsymbol{\theta'}) = -\sum_{i=1}^{N} W_i \ln\left[1+\boldsymbol{P_T}_i\sin(\phi_{R\perp i}+\phi_{S i})\frac{a_1\sin\theta'_i}{1+A_2\frac{1}{4}(3\cos^2\theta'_i-1)}\right], \tag{4.57}$$

where A_2 takes 0 in the unfolding procedure (known as simm–nonlinear asymmetry parameterization).

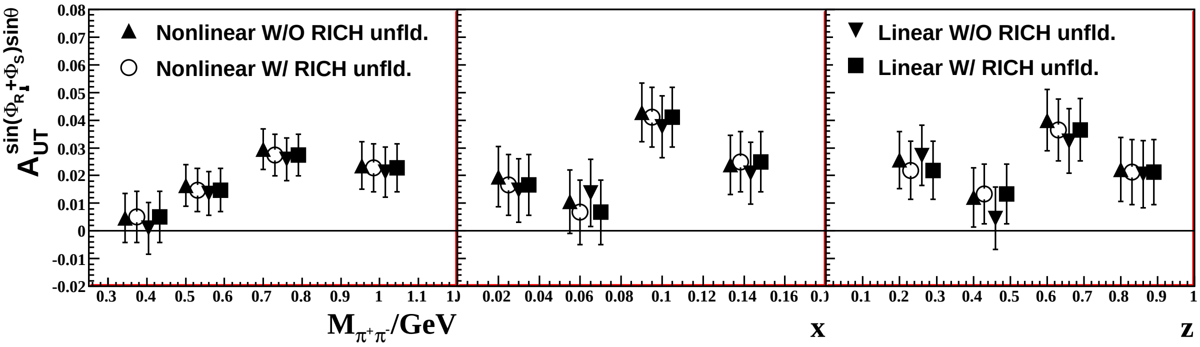

Figure 4.28: The comparisons of the extracted amplitudes from IRT data between the ML fittings with and without RICH unfolding, using simm–nonlinear asymmetry function (as Eq. (4.30)) and linear asymmetry function (as Eq. (4.31)).

The fitting results from pure IRT data by simm–nonlinear fit method without and with RICH unfolding are compared in Figure 4.28. We see their consistent amplitudes in the whole $M_{\pi\pi}$, x and z bins. Also the compared extraction method is the linear fit method (cf. Sec. 4.3.7) without and with RICH unfolding. The more sizable difference between the results without and with RICH unfolding in linear ML fit, but less difference between those results in simm–nonlinear ML fit. It is possible due to the advantage in simm–nonlinear fit that it cancels the θ–odd parts in the asymmetry formula in Eq. (4.28), and hence could obtain cleaner amplitudes. The same unfolding is also performed for EVT data in years 2004–2005. Figure 4.29 shows the comparison between the results with unfolding and without unfolding. The results before and after the RICH unfolding within simm–nonlinear ML fit do not indicate significant effect. The difference between the asymmetry amplitudes before and after the RICH unfolding is less than an absolute value 0.003(0.001) for IRT(EVT) data. As the EVT data of the years 2004–2005 would contribute the most statistics in the final results, it suggests that the extracted asymmetry amplitudes are quite robust to the RICH mis–identification.

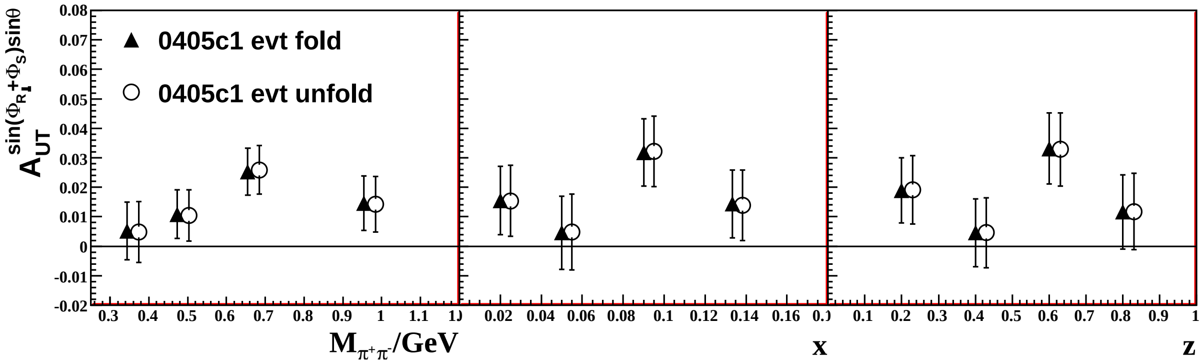

Figure 4.29: The comparisons of the extracted amplitudes from EVT data in years 2004–2005 between with and without RICH unfolding, using LS simm–nonlinear fitting function (as in Eq. (4.29) with $A_2 = 0$).

4.5.7 Target Magnet Field Correction

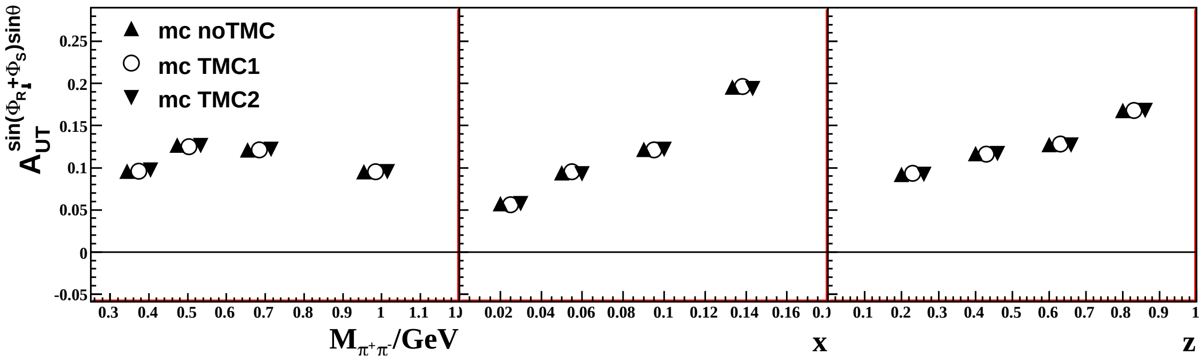

Figure 4.30: The extracted amplitudes in MC data with no TMC, with TMC1 and with TMC2. The statistical uncertainties are too small to see here.

As discussed in Sec. 4.4.3, the TMC effect need to be investigated using high statistics MC data. In the study on the MC data which include the transverse magnet field in the target cell, the asymmetry is applied following Eq. (4.41), and the TMCs were also applied. The extracted asymmetry amplitudes were compared, among the cases of with no TMC, with TMC1 and with TMC2. As shown in Figure 4.30, the TMC effect is negligible with the absolute contribution smaller 0.002. But it should be aware that the MC estimation is model dependent. Combining with the comparison done in the real data in Sec. 4.4.3, we can conclude the TMC effect is negligible in the current work.

4.5.8 Misalignment Effect

The detector position and the beam position are not exactly the same as designed, but there is some shifts in both. These differences, called "misalignment effect", have to be taken into account in the reconstruction of the track information. Hence in practice there are some systematic uncertainties from the determination of the actual detector position and the beam position, which can affect the kinematic quantities and would bias the extracted amplitudes. Ref. [192] found that the misalignment of the spectrometer could produce a $\cos\phi_h$ modulation asymmetry in the hadron yield.

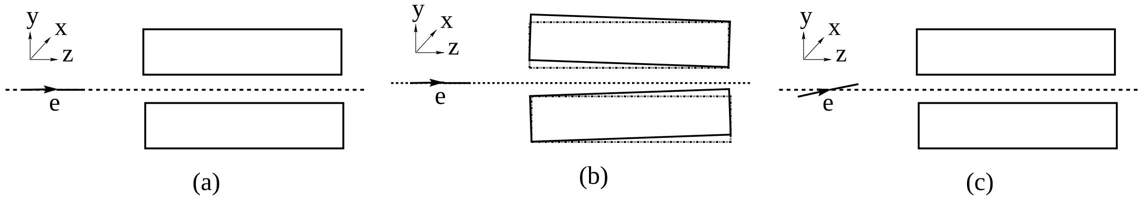

Figure 4.31: Schematic drawings of the misalignment of the spectrometer and of the beam: (a) the spectrometer and the beam in their ideal places; (b) misalignment of the two spectrometer halves; (c) misalignment of the beam.

2002–2004	x–slope (mrad)	y–slope (mrad)	x–offset (cm)	y–offset (cm)
top spectrometer	−0.18	−0.62	0.30	−0.08
bottom spectrometer	−0.42	−0.49	0.29	−0.11
beam	−0.041	−0.13	0.005	0.046

Table 4.9: The measured misalignment of the spectrometer [193] and the beam [164] relative to the coordinate system in the laboratory during the years 2002–2005.

The beam can be shifted or tilted away from the z–axis as shown in Figure 4.31. The measurement of the beam misalignment was performed by Ref. [164, 194]. There are two kinds of detector misalignment: internal misalignment and external one. Internal means relative shifts and rotations of detectors with respect to each other; external means that the detectors are shifted and rotated as a whole with respect to a reference coordinate system. The internal misalignment of the HERMES spectrometer is determined several times per year with enough statistics. Hence it can be safely omitted from the systematic

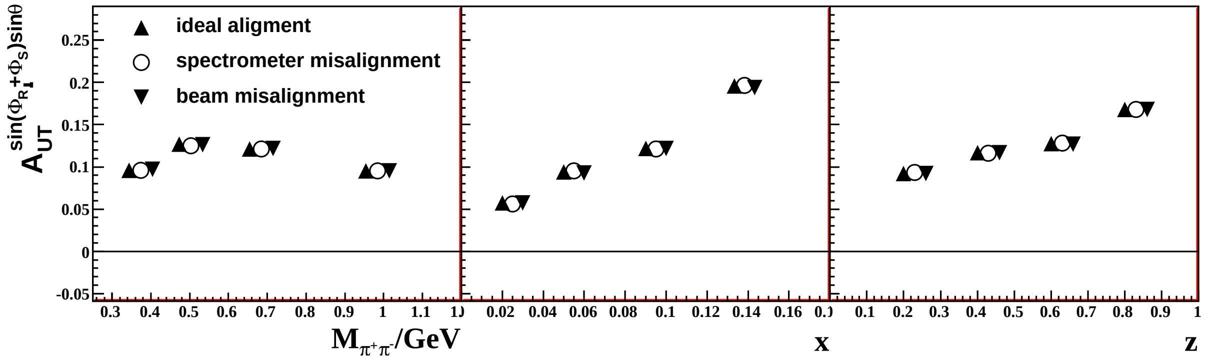

Figure 4.32: Comparison of the amplitudes $A_{\rm UT}^{\sin(\phi_{R\perp}+\phi_S)\sin\theta}$ extracted from MC simulations using either a perfectly aligned spectrometer and beam, a misaligned spectrometer or a misaligned beam. The differences are observed to be negligible.

study. The external misalignment of the spectrometer are illustrated in Figure 4.31 and has been determined in Ref. [193]. The results of the misalignment of the spectrometer and the beam are listed in Table 4.9.

In order to study the effect of the misalignment on the amplitude $A_{\rm UT}^{\sin(\phi_{R\perp}+\phi_S)\sin\theta}$ extracted from HERMES data, three different Pythia MC productions were used, whose asymmetry $A_{\rm UT}$ was implemented as Eq. (4.41). One production was used where both the spectrometer and the beam are perfectly aligned, *i.e.*, without any deviations with respect to their ideal positions. Secondly, another Monte–Carlo production was created where a misaligned spectrometer was used in the MC simulation according to the values given in Table 4.9. The third production takes into account the misalignment of the beam. For this production, only the x–slope θ_x and the y–slope θ_y were taken into account. This was done by using $\boldsymbol{k}/|\boldsymbol{k}| = (\sin\theta_x, \sin\theta_y, \sqrt{1-\sin^2\theta_x-\sin^2\theta_y})$ instead of $\boldsymbol{k}/|\boldsymbol{k}| = (0,0,1)$ for the beam momentum $\boldsymbol{k}$. The results of the three simulations are shown in Figure 4.32 and are consistent within the statistical uncertainty. In fact, according to the present simulations any systematic effect due to misalignment of the spectrometer or the beam on the extracted amplitudes should be smaller than 0.002 (absolute).

4.5.9 Fake Asymmetry Check

In order to verify the validity of the developed extraction method, the amplitudes were extracted from the data, with uniformly randomly assigning target spin state to the unpolarized MC data, taking into account the HERMES acceptance. The results are shown in Figure 4.33. The extracted amplitudes are consistent with zero. These results indicate that the HERMES acceptance effect cannot generate non–zero asymmetries, and

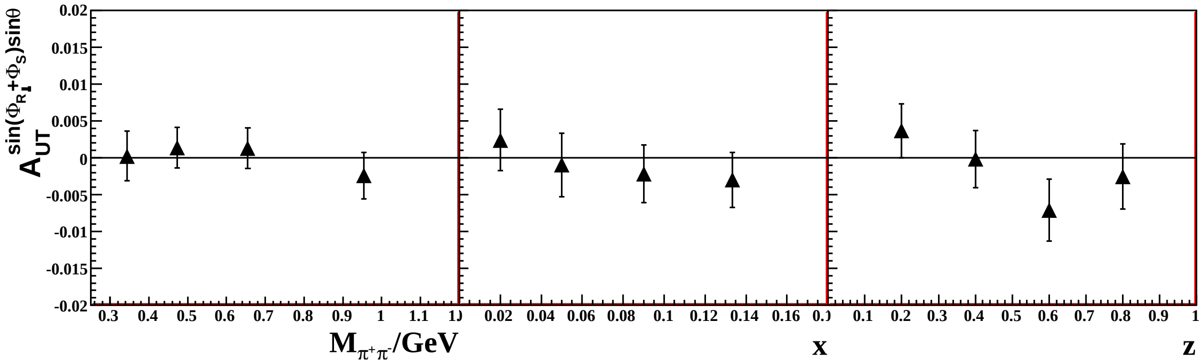

Figure 4.33: Amplitudes $A_{\mathrm{UT}}^{\sin(\phi_{R\perp}+\phi_S)\sin\theta}$ versus $M_{\pi\pi}$, x, and z, extracted with simm–nonlinear fit method from the unpolarized MC data, taking into account the HERMES acceptance.

the fitting method also will not bring in non–zero asymmetries. The acceptance effects only influence the size of the non–zero asymmetry by the convolution with the kinematic variables (cf. Eq. (4.39)).

Chapter 5

Discussion on Results

Using the transversely polarized target data in years from 2002 to 2005, the single transverse target–spin asymmetry amplitude $A_{\mathrm{UT}}^{\sin(\phi_{R\perp}+\phi_S)\sin\theta}$ was extracted as a function of $M_{\pi\pi}$, x and z. As suggested by the relevant theory explained in Chapter 2, this amplitude is related to the less known transversity distribution h_1 and the unknown s–p wave interference fragmentation function $H_1^{\sphericalangle,sp}$. The data analysis was extensively explained in Chapter 4. This chapter will sum up all the analyses in Chapter 4 and discuss what we can learn from the results. Also, other possible ways to probe transversity are presented for comparison.

5.1 Single Transverse Spin Asymmetry Amplitude

The measured asymmetry is based on events integrated over $\boldsymbol{P_{h\perp}}$ (within the acceptance), which considerably simplifies an eventual extraction of h_1 and $H_1^{\sphericalangle,sp}$, since in this case $h_1 H_1^{\sphericalangle,sp}$ appears in the expression for the amplitudes as a simple product (cf. Sec. 2.4.1) instead of in a convolution integral over transverse momentum. Due to the incomplete coverage on the polar angle θ of the HERMES acceptance (cf. Sec. 4.5.4), a θ azimuthal related term of p–wave DiFF D_1^{pp} affects the extracted amplitude $A_{\mathrm{UT}}^{\sin(\phi_{R\perp}+\phi_S)\sin\theta}$ (cf. Sec. 4.5.5). By scanning the possible values of this effect within the positive limit, the median value of the fitted results of the amplitudes was chosen as the final results of the interested amplitude. The corresponding statistical uncertainty is taken as the statistical uncertainty of the final amplitude. Due to the limited statistics of the polarized HERMES data, the amplitudes were only studied with the dependence on the $M_{\pi\pi}$, x and z. The kinematics bins were defined in Table 4.5. In the overall bin, x bin and z bins, $M_{\pi\pi}$ were restricted in $0.5\,\mathrm{GeV} < M_{\pi\pi} < 1.0\,\mathrm{GeV}$.

In this analysis the fitting methods, *e.g.*, the choice of ML fit and LS fit, the constant part in the fit function, and the binning choice in LS fit, did not influence the results significantly, as discussed in Sec. 4.3. All the ML fit results confirmed the LS fit results. The final results were taken from the LS fit, since the LS fit can provide the statistics of goodness–of–fit. The systematic effects were fully studied, most of which only contributed trivially to the measurement. The measurements in different data taking periods were compared. Their results did not show a systematic trend and only showed the statistical fluctuations. The beam polarization, which has a good balance between two helicity states in real data, was found not to affect the extracted asymmetry amplitudes. The efficiency in RICH hadron identification was studied using MC method, and the RICH unfolding showed no sizable systematic effect from the non–pion contamination. Target magnet correction (TMC) methods were compared and found to be consistent in the extraction. TMC does not bring systematic uncertainty. Misalignment of the beam and the spectrometer was also found to be a negligible effect to the asymmetry amplitude.

But there are also some significant systematic effects which have to be taken in account as systematic uncertainties. They include:

- **Target Polarization**
  The average value of the target polarization in years from 2002 to 2005 is estimated to be [153]: $\langle |\boldsymbol{P_T}| \rangle = 0.74 \pm 0.06$. A relative systematic uncertainty of $0.06/0.74 \simeq 8.1\%$ was assigned to the extracted amplitude due to the uncertainty in determining the target polarization value.

- **Acceptance Effect**
  Till now, no polarized dihadron fragmentation information is available in the MC event generator. By the technique of assigning the target spin state with the azimuthal modulation and the kinematic dependence to the HERMES tuned Pythia MC unpolarized data based on the theoretical model, the overall HERMES acceptance effect on the extracted amplitudes were studied. The study of the acceptance effects were elaborated in Sec. 4.5.2. The results showed in Table 4.7 that the overall acceptance effect is an underestimation of the real amplitude by up to 21%, including an underestimation of the amplitudes in the measurement up to 25% for the $M_{\pi\pi}$ dependence, negligible effect on the x dependence and up to 43% deflation in the z dependence. Although one could make an acceptance correction to the extracted amplitude results, we finally choose to take the effect as a part of the systematic uncertainties, because the estimation of the effect is based on the theoretical model and the model itself still has large inherent uncertainties. Hence, the scaling systematic uncertainties based on the factor c_i in Eq. (4.42) are taken into account.

- **p–wave DiFF D_1^{pp} Effect**
  In Sec. 4.5.3, the limited coverage on ϕ_h was found to have no significant effect on the extracted amplitudes. But the incomplete acceptance on polar angle θ resulted in the additional non–zero contribution from another angle θ related term: p–wave DiFF D_1^{pp}. With unpolarized data from the HERMES tuned MC simulation, taking

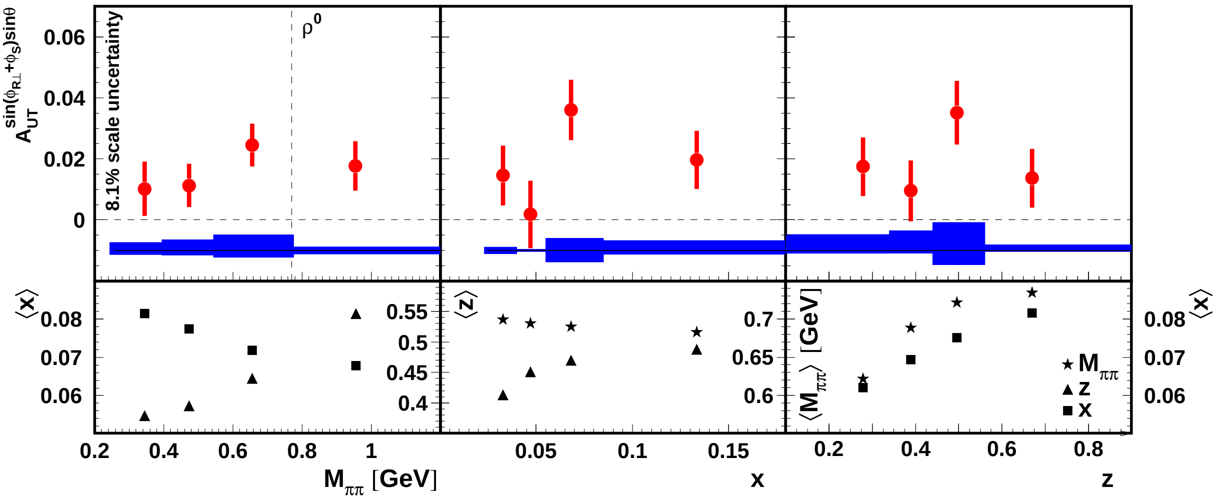

Figure 5.1: The extracted amplitudes $A_{\mathrm{UT}}^{\sin(\phi_{R\perp}+\phi_S)\sin\theta}$ in kinematic variables $M_{\pi\pi}$, x and z bins. The bottom panels show the average values of the variables that were integrated over. For the dependence on x and z, $M_{\pi\pi}$ was constrained to the range $0.50\,\mathrm{GeV} < M_{\pi\pi} < 1.0\,\mathrm{GeV}$. The numerical results and additional systematic uncertainties are listed in Table 5.1. A relative scale uncertainty of 8.1% arises from the uncertainty in the target polarization. Other contributions to the systematic uncertainty are summed in quadrature and represented by the asymmetric error band.

into account the HERMES acceptance, the boundary of the ratio $A_2 = D_{1,\mathrm{LL}}^{pp}/D_{1,\mathrm{UU}}$ could be estimated. Then by varying A_2 within the bounds, the effect related with the p–wave DiFF D_1^{pp} was evaluated as the standard deviation of a series of the fitted amplitudes $A_{\mathrm{UT}}^{\sin(\phi_{R\perp}+\phi_S)\sin\theta}$ with fixed A_2 parameter each time. The median of the flat distributed a_1 samples was taken as the estimated mean value of the measured asymmetry amplitude $A_{\mathrm{UT}}^{\sin(\phi_{R\perp}+\phi_S)\sin\theta}$. The numerical results by LS fit were given in Table 4.8, which is confirmed with those fitted with ML fit.

The summarized results of the asymmetry amplitude $A_{\mathrm{UT}}^{\sin(\phi_{R\perp}+\phi_S)\sin\theta}$, as functions of $M_{\pi\pi}$, x, and z, are given in Figure 5.1, where the relative scale of 8.1% from the target polarization measurement are indicated. The asymmetric error band contains the combined systematic uncertainties from the HERMES acceptance effect and scan study. The numerical results of the asymmetry amplitude $A_{\mathrm{UT}}^{\sin(\phi_{R\perp}+\phi_S)\sin\theta}$ are listed in Table 5.1, which includes the systematic uncertainties, the reduced–χ^2 from fitting and the average kinematic values.

The extracted azimuthal amplitude $A_{\mathrm{UT}}^{\sin(\phi_{R\perp}+\phi_S)\sin\theta}$ from HERMES data, summed over the HERMES acceptance, *i.e.*, $0.5\,\mathrm{GeV} < M_{\pi\pi} < 1.0\,\mathrm{GeV}$, $0.023 < x < 0.4$ and

bin boundaries	$A_{\mathrm{UT}}^{\sin(\phi_{R\perp}+\phi_S)\sin\theta}$	$\langle M_{\pi\pi}\rangle$ / GeV	$\langle x\rangle$	$\langle y\rangle$	$\langle z\rangle$	$\langle Q^2\rangle$ / GeV^2	χ^2/n.d.f.
0.25 GeV< $M_{\pi\pi}$ <0.40 GeV	$0.010 \pm 0.009\,_{\mathrm{stat}} \pm 0.001\,_{\mathrm{scan}} + 0.002\,_{\mathrm{acc}}$	0.344	0.081	0.615	0.377	2.413	0.703
0.40 GeV< $M_{\pi\pi}$ <0.55 GeV	$0.012 \pm 0.007\,_{\mathrm{stat}} \pm 0.001\,_{\mathrm{scan}} + 0.003\,_{\mathrm{acc}}$	0.473	0.077	0.628	0.395	2.371	1.324
0.55 GeV< $M_{\pi\pi}$ <0.77 GeV	$0.024 \pm 0.007\,_{\mathrm{stat}} \pm 0.002\,_{\mathrm{scan}} + 0.004\,_{\mathrm{acc}}$	0.655	0.072	0.650	0.440	2.298	0.850
0.77 GeV< $M_{\pi\pi}$ <2.00 GeV	$0.019 \pm 0.008\,_{\mathrm{stat}} \pm 0.001\,_{\mathrm{scan}} - 0.000\,_{\mathrm{acc}}$	0.954	0.067	0.679	0.544	2.272	0.965
0.023< x <0.040	$0.015 \pm 0.010\,_{\mathrm{stat}} \pm 0.001\,_{\mathrm{scan}} + 0.001\,_{\mathrm{acc}}$	0.698	0.033	0.734	0.416	1.232	0.883
0.040< x <0.055	$0.002 \pm 0.011\,_{\mathrm{stat}} \pm 0.001\,_{\mathrm{scan}} - 0.000\,_{\mathrm{acc}}$	0.692	0.047	0.659	0.452	1.604	1.030
0.055< x <0.085	$0.035 \pm 0.010\,_{\mathrm{stat}} \pm 0.004\,_{\mathrm{scan}} + 0.002\,_{\mathrm{acc}}$	0.687	0.068	0.630	0.467	2.214	1.379
0.085< x <0.400	$0.020 \pm 0.010\,_{\mathrm{stat}} \pm 0.001\,_{\mathrm{scan}} + 0.003\,_{\mathrm{acc}}$	0.680	0.133	0.592	0.484	4.031	0.936
0.000< z <0.340	$0.018 \pm 0.010\,_{\mathrm{stat}} \pm 0.001\,_{\mathrm{scan}} + 0.005\,_{\mathrm{acc}}$	0.623	0.062	0.717	0.277	2.242	1.035
0.340< z <0.440	$0.010 \pm 0.010\,_{\mathrm{stat}} \pm 0.001\,_{\mathrm{scan}} + 0.006\,_{\mathrm{acc}}$	0.687	0.070	0.668	0.390	2.301	0.636
0.440< z <0.560	$0.036 \pm 0.010\,_{\mathrm{stat}} \pm 0.005\,_{\mathrm{scan}} + 0.008\,_{\mathrm{acc}}$	0.718	0.075	0.630	0.496	2.323	1.040
0.560< z <1.000	$0.012 \pm 0.009\,_{\mathrm{stat}} \pm 0.001\,_{\mathrm{scan}} + 0.002\,_{\mathrm{acc}}$	0.732	0.080	0.592	0.666	2.355	0.836
0.5 GeV< $M_{\pi\pi}$ <1.0 GeV 0.023< x <0.400 0.0< z <1.0	$0.018 \pm 0.005\,_{\mathrm{stat}} \pm 0.002\,_{\mathrm{scan}} + 0.004\,_{\mathrm{acc}}$	0.689	0.072	0.653	0.455	2.304	0.866

Table 5.1: The extracted amplitudes $A_{\mathrm{UT}}^{\sin(\phi_{R\perp}+\phi_S)\sin\theta}$ with statistical uncertainties (stat), the systematic uncertainties from the A_2 scan (scan) and from the experimental acceptance (acc). The average values of the kinematic variables and the reduced–χ^2 values of LS fit in each bin are listed. A relative scale uncertainty from target polarization are not given.

$0 < z < 1$, is $A_{\mathrm{UT}}^{\sin(\phi_{R\perp}+\phi_S)\sin\theta} = 0.018 \pm 0.005_{\,\mathrm{stat}} \pm 0.002_{\,\mathrm{scan}} + 0.004_{\,\mathrm{acc}}$ with an additional 8.1% scale uncertainty coming from the uncertainty in the determination of the target polarization. The mean values of the kinematic variables are $\langle x\rangle = 0.072$, $\langle y\rangle = 0.653$, $\langle Q^2\rangle = 2.304\,\mathrm{GeV}^2$, $\langle z\rangle = 0.455$, and $\langle|\boldsymbol{P_{h\perp}}|\rangle = 0.421\,\mathrm{GeV}$. The overall amplitude is non–zero with high probability (at $4\,\sigma$ confidence level). The extracted amplitudes with dependence on $M_{\pi\pi}$, x, and z shown in Figure 5.1 are positive over the entire range of all three variables. The dashed vertical line in $M_{\pi\pi}$–dependence plot indicates the position of the $\rho^0(770)$ invariant mass 0.776 GeV [182]. The amplitude around the mass of $\rho^0(770)$ is most likely to be non–zero. The reduced–χ^2 values for the fits to the data set are in the range 0.636–1.379.

5.2 Discussion on the Results

The measured amplitudes $A_{\mathrm{UT}}^{\sin(\phi_{R\perp}+\phi_S)\sin\theta}$ in Figure 5.1, which shows the dependence on $M_{\pi\pi}$, x, and z, can be related with the x dependence of the two distribution functions involved, $h_1(x)$ and $f_1(x)$, as well as with the $M_{\pi\pi}$ and z dependence of the dihadron fragmentation functions $H_1^{\sphericalangle,sp}(z, M_{\pi\pi}^2)$ and $D_1(z, M_{\pi\pi}^2)$ (see Eq. (2.93)). These dependencies can be used to compare with the model predictions and verify their feasibility. But it should be noted that, due to the limited HERMES spectrometer acceptance and the applied kinematic selections, the dependencies shown in Figure 5.1 are correlated with each other, as indicated by the simultaneous dependencies on the other variables illustrated in the bottom panels of Figure 5.1.

The non–zero result of the asymmetry amplitude $A_{\mathrm{UT}}^{\sin(\phi_{R\perp}+\phi_S)\sin\theta}$ suggests that both the transversity distribution function h_1 and the dihadron fragmentation function $H_1^{\sphericalangle,sp}$ are non–zero. Therefore, the semi–inclusive lepto–production of $\pi^+\pi^-$ pairs on a transversely polarized hydrogen target can be used to extract transversity h_1, in combination with an independent measurement of presently unknown dihadron fragmentation function $H_1^{\sphericalangle,sp}$. There exists already some evidence that the transversity distribution could be non–zero, which will be presented later in Sec. 5.3.1. But the present measurement provides the first indication ever that the dihadron fragmentation function $H_1^{\sphericalangle,sp}$ is non–zero (with the conference level $4\,\sigma$).

5.2.1 Comparison with Other Measurements

The first try to study transversity and dihadron dihadron fragmentation function was performed [195] using the dihadron semi–inclusive DIS process in the data collected in earlier years from 1998 to 2000 at HERMES experiment. At that time, HERMES did not have a transversely polarized target yet and was operated with a longitudinally polarized deuterium targets instead. The reason that the longitudinally polarized target data can be used to access transversity, is due to the different polarization reference in experiment and in theory [196]. In experiment, the longitudinal polarization direction is along the incident lepton, but in theory the term "longitudinal" means the polarization direction with respect to the direction of the virtual photon. Since there is a angle between the incident lepton and the virtual photon θ_γ, the polarized cross section difference $\mathrm{d}^7\,\sigma^\ell_{\mathrm{UL}}$ is given, at subleading twist, by [197]:

$$\begin{aligned} \mathrm{d}^7\sigma^\ell_{\mathrm{UL}} &= -\sum_q \frac{\alpha^2 e_q^2}{2\pi s x y^2}\,\sin\phi_R \sin\theta \left\{ |\boldsymbol{S_L}|\, V(y)\, \frac{|\boldsymbol{R}|}{Q}\left[\frac{Mx}{M_h}\, h_L\, H_1^{\sphericalangle} + \frac{1}{z}\, \mathrm{g}_1\, \widetilde{G}^{\sphericalangle}\right] \right. \\ &\qquad \left. -|\boldsymbol{S_T}|\, B(y)\, \frac{|\boldsymbol{R}|}{M_h}\, h_1\, H_1^{\sphericalangle} \right\}, \end{aligned} \tag{5.1}$$

where

$$V(y) = 2\,(2-y)\,\sqrt{1-y}, \qquad B(y) \;=\; 1-y. \tag{5.2}$$

The unpolarized cross section $\mathrm{d}^7\,\sigma_{\mathrm{UU}}$ is the same as the Eq. (2.92a). Here we have the longitudinal polarization $\boldsymbol{S_L}$ ($\boldsymbol{S_L} = \cos\theta_\gamma \boldsymbol{P_L} \approx \boldsymbol{P_L}$, $\boldsymbol{P_L}$ is the longitudinal polarization.) and a part proportional to the transverse polarization $\boldsymbol{S_T} \approx \sin\theta_\gamma |\boldsymbol{S_L}|$. The distribution function h_L, which is directly related to h_1 [198, 199], and the fragmentation function $\widetilde{G}^{\sphericalangle}$ both contribute only at subleading twist, such that at leading twist the only contribution of Eq. (5.1) to the asymmetry A^ℓ_{UL} [1] comes from the term containing the product $h_1 H_1^{\sphericalangle}$. This is the same product as the one in the measured asymmetry in this work. So the product $h_1 H_1^{\sphericalangle}$ can also be obtained by measuring the amplitude $A_{\mathrm{UL}}^{\sin\phi_{R\perp}} = \frac{\pi}{4} A_{\mathrm{UL}}^{\sin\phi_{R\perp}\sin\theta}$. This amplitude is shown in Figure 5.2 and 5.3 as a function of $M_{\pi\pi}$ in panels representing several bins in x and z, respectively, using the hadron pairs of unidentified oppositely charged hadrons. The average target polarization $|\boldsymbol{P_L}|$ of 0.84 ± 0.04. For all panels, the amplitude is consistent with zero given the size of the statistical uncertainties.

However, the results here are consistent with the results of the work in this thesis. At leading twist, the amplitudes $A_{\mathrm{UL}}^{\sin\phi_{R\perp}\sin\theta}$ and $A_{\mathrm{UT}}^{\sin(\phi_{R\perp}+\phi_S)\sin\theta}$ have:

$$A_{\mathrm{UL}}^{\sin\phi_{R\perp}\sin\theta} = -\sin\theta_\gamma A_{\mathrm{UT}}^{\sin(\phi_{R\perp}+\phi_S)\sin\theta}. \tag{5.3}$$

In HERMES acceptance, $\langle\sin\theta_\gamma\rangle < 0.09$. From the results in Figure 5.1, $A_{\mathrm{UT}}^{\sin(\phi_{R\perp}+\phi_S)\sin\theta}$ can be safely assumed to be smaller than 0.1. Then the amplitude $A_{\mathrm{UL}}^{\sin\phi_{R\perp}\sin\theta}$ should be less than 0.009, which is consistent with the results in Figure 5.2 and 5.3. Compared with the obtained data in this thesis, these results in Figure 5.2 and 5.3 cannot contribute much knowledge to our understanding due to the relatively large statistical uncertainties and the small value of the amplitudes. Maybe the only value lies in that these results indicate a small contribution of $A^{\gamma^*}_{\mathrm{UL}}$ to A^ℓ_{UT}, at leading twist. It should also be noted

---

[1] The ℓ in the asymmetries A^ℓ_{UT} and A^ℓ_{UL} means the polarization direction referring to the incident lepton, and the γ^* in the asymmetries $A^{\gamma^*}_{\mathrm{UT}}$ and $A^{\gamma^*}_{\mathrm{UL}}$ means the polarization direction referring to the virtual photon.

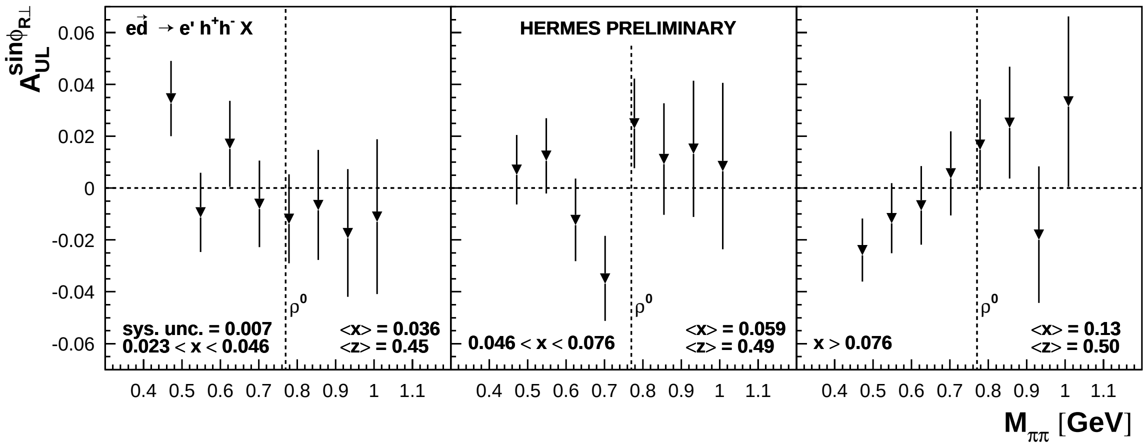

Figure 5.2: The amplitude $A_{\mathrm{UL}}^{\sin\phi_{R\perp}}$ versus the invariant mass $M_{\pi\pi}$ as obtained from HERMES data in years from 1998 to 2000, using a deuterium target. The amplitude is shown in three panels of increasing x, as indicated. The quoted systematic uncertainty of 0.007 is a scale uncertainty due to the uncertainty in the target polarization. The dashed vertical lines indicate the mass of the ρ^0 resonance (0.78 GeV).

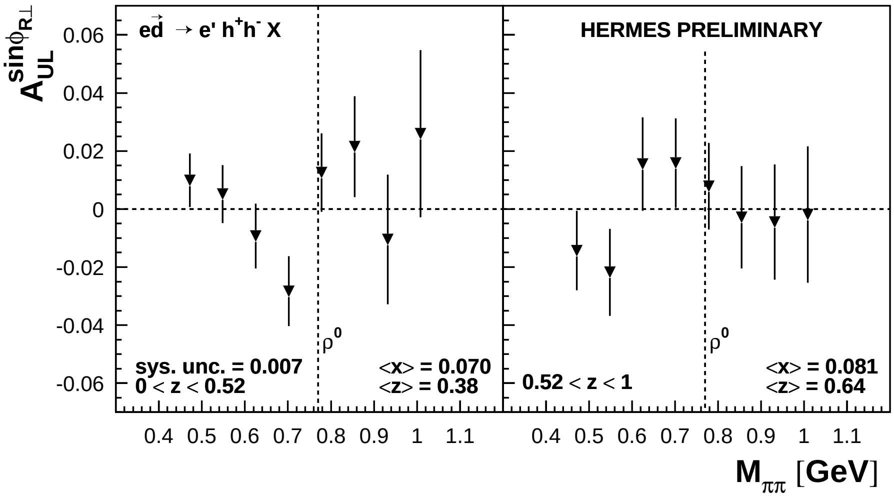

Figure 5.3: The amplitude $A_{\mathrm{UL}}^{\sin\phi_{R\perp}}$ versus the invariant mass $M_{\pi\pi}$, as in Figure 5.2, but here shown in two panels at different z regions.

that for the HERMES $A_{\text{UL}}^{\sin\phi_{R\perp}}$ data no pion identification was made, which complicates the interpretation. Furthermore, a deuteron target was used, for which the expected asymmetries are significantly smaller [117, 138].

The pioneering attempt at HERMES on the study of this thesis is presented in Refs. [200–203]. In that work, the magnitude of the dihadron fragmentation functions D_1^{sp} and D_1^{pp} in the denominator were ignored in the extraction of the azimuthal amplitude, *i.e.*, they were assumed to be zero. Later, the influence from the D_1^{sp} and D_1^{pp} was considered [121] and was parameterized as one additional parameter in the LS fit to extract the azimuthal amplitude. The 2005 data became available for analysis after that, which can improve the statistics doubly. However, when the 2-parameter method was applied to 2005 data, it showed some difficulties in converging. The reason may be that the HERMES data cannot evaluate the unpolarized dihadron fragmentation function well. The current work then developed a new way to evaluate the effects of the unpolarized dihadron fragmentation functions D_1^{sp} and D_1^{pp} in the denominator to the extracted amplitude. Here a systematic uncertainty was assigned to the measured amplitude, when scanning D_1^{pp} with the positive bounds, instead of fit as a free parameter. The prior and current results are consistent within statistical uncertainties. But by including 2005 data, the current work has smaller statistical uncertainties.

Another process related to the dihadron fragmentation function was studied at HERMES experiment. Using the longitudinally polarized lepton beam and the unpolarized hydrogen and deuterium targets, the dihadron semi–inclusive DIS cross section difference $\mathrm{d}^7\sigma_{\text{LU}}$ can be written as:

$$\mathrm{d}^7\sigma_{\text{LU}} = -\sum_a \frac{\alpha^2 e_a^2}{2\pi Q^2 y}\,|\boldsymbol{S_L}|\,W(y)\,\sin\phi_R\,\sin\theta\,\frac{|\boldsymbol{R}|}{Q}\left[\frac{Mx}{M_h}\,e\,H_1^{\sphericalangle} + \frac{1}{z}\,f_1\,\widetilde{G}^{\sphericalangle}\right], \tag{5.4}$$

where

$$W(y) \,=\, 2\,y\,\sqrt{1-y}\;. \tag{5.5}$$

The fragmentation function $\widetilde{G}^{\sphericalangle}$ can only contribute significantly in subleading twist. Taking the unpolarized dihadron cross section in Eq. (2.92a), the asymmetry A_{LU}^{ℓ} can be used to determine the product of $eH_1^{\sphericalangle}$, where $e(x)$ is the unknown twist–3 distribution function and $H_1^{\sphericalangle}$ is the dihadron fragmentation function, which was studied in this thesis. The HERMES proton target data and deuterium target data in years from 1996 to 2005 were used to extract the amplitude $A_{\text{LU}}^{\sin\phi_R\sin\theta}$, by selecting the $\pi^+\pi^-$ pairs. The asymmetry A_{LU}^{ℓ} can be parameterized as :

$$\begin{aligned} A_{\text{LU}}^{\ell}(\phi_R,\theta) &\propto a_1 + \frac{a_2\sin\phi_R\sin\theta}{1-a_3\cos\phi_R\sin\theta} \\ &\approx a_1 + a_2\sin\phi_R\sin\theta + \frac{a_2a_3}{2}\sin(2\phi_R)\sin^2\theta, \end{aligned} \tag{5.6}$$

where a_1 is constant, $a_2 \equiv A_{\text{LU}}^{\sin\phi_R\sin\theta}$ and $a_3 \equiv D_{1,\text{UL}}^{sp}/D_{1,\text{UU}}$. A linear fitting function was used

$$A^{\ell}_{\mathrm{LU}}(\phi_R,\theta) \quad = \quad p_1 + p_2 \sin\phi_R \sin\theta + p_3 \sin(2\phi_R)\sin^2\theta. \tag{5.7}$$

The measured asymmetry amplitude is $A_{\mathrm{LU}}^{\sin\phi_R \sin\theta} = 0.0012 \pm 0.0055_{\mathrm{stat}}$ for the proton target and $A_{\mathrm{LU}}^{\sin\phi_R \sin\theta} = 0.0070 \pm 0.0046_{\mathrm{stat}}$ for the deuterium target. With the high statistics, the both results gave small amplitudes (less than 0.01) and consistent with zero. These results are not inconsistent with the extracted amplitudes in this thesis, as here the size of the amplitude $A_{\mathrm{LU}}^{\sin\phi_R \sin\theta}$ is directly related to the twist–3 distribution function $e(x)$. Assuming that the overall value of the amplitude in the thesis is on the level of 0.02 (cf. Sec. 5.1), the size of transversity should be 20 times larger than the twist–3 distribution $e(x)$, if we compare the both overall values of the amplitude in proton target. In this A_{LU} analysis, the amplitudes in the proton target and the deuterium target are both small and consistent. Hence, it is difficult to judge their relative sizes. But it is possible that the size in deuterium target is larger than that in proton target, which should be interpreted as the different behaviors of the distribution function $e(x)$ in proton and neutron.

The preliminary results for the amplitude $A_{\mathrm{UT}}^{\sin(\phi_{R\perp}+\phi_S)}$ on a transversely polarized ^{6}LiD target were obtained by the COMPASS collaboration [204]. The COMPASS collaboration uses a slightly different convention for the asymmetry [205–208]. They consider the asymmetry A_{RS}, defined as:

$$A_{RS} = \frac{A_{\mathrm{UT}}^{\sin(\phi_{RS})}}{D_{NN} f P} = \frac{-A_{\mathrm{UT}}^{\sin(\phi_R+\phi_S)}}{D_{NN}}, \tag{5.8}$$

where f ($\approx$ 0.37) is the target dilution factor, P ($\approx$ 0.50) is the target polarization and D_{NN} is the y–dependent depolarization factor $D_{NN} = (1-y)/(1-y+y^2/2)$. The angle ϕ_{RS} is defined as $\phi_{RS} \equiv \phi_R + \phi_S - \pi$ and the asymmetry $A_{\mathrm{UT}}^{\sin(\phi_{RS})}$ is defined as $A_{\mathrm{UT}}^{\sin(\phi_{RS})} \equiv f P A_{\mathrm{UT}}^{\sin(\phi_R+\phi_S-\pi)}$. In the beginning the hadron identification was not applied and the value of A_{RS} is presented for all the hadron pairs lepto-production in COMPASS data from 2002-2004 as shown in Figure 5.4 in bins of x, $M_{\pi\pi}$, and z [205–207]. The error bars show the statistical error. The measured asymmetry amplitudes are compatible with zero, within the small statistical error. Recently, the information from the Ring Imaging Čerenkov detector (RICH) [204] became available to distinguish pions, kaons and protons for the data from 2003 and 2004. The pion pairs were selected and the asymmetry amplitudes A_{RS} were presented in Figure 5.5 with dependence on x, $M_{\pi\pi}$, and z [208]. The sizes of the asymmetry are still small and below 1%.

The COMPASS result is different from the measurement in this thesis, where a proton target was used and a significant non–zero two–hadron asymmetry amplitudes were presented. However, this does not mean that the two measurements are inconsistent, since the results from the two collaborations cannot be directly compared. Firstly, the COMPASS collaboration measured the amplitude $A_{\mathrm{UT}}^{\sin(\phi_{R\perp}+\phi_S)}$ using a deuteron target.

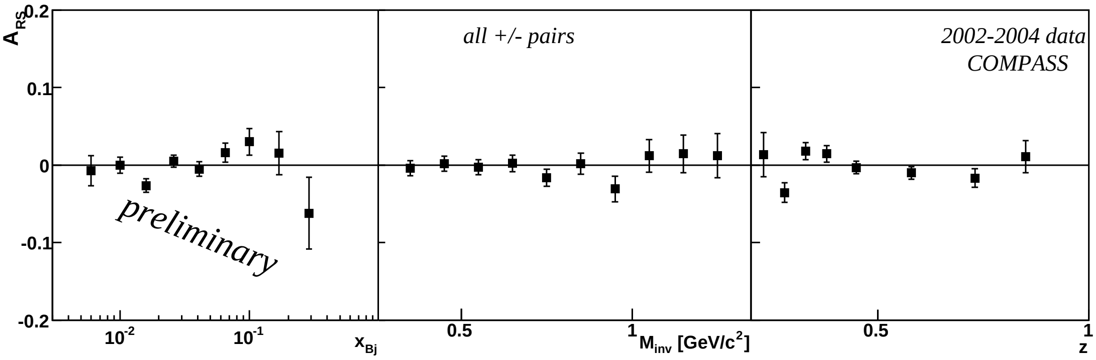

Figure 5.4: The two–hadron asymmetry amplitude A_{RS} against x, the invariant mass of the hadron pair M_{inv}, and z for all oppositely charged hadron pairs from 2002-2004 COMPASS data. No hadron identification was applied. The error bars represent the statistical uncertainty only.

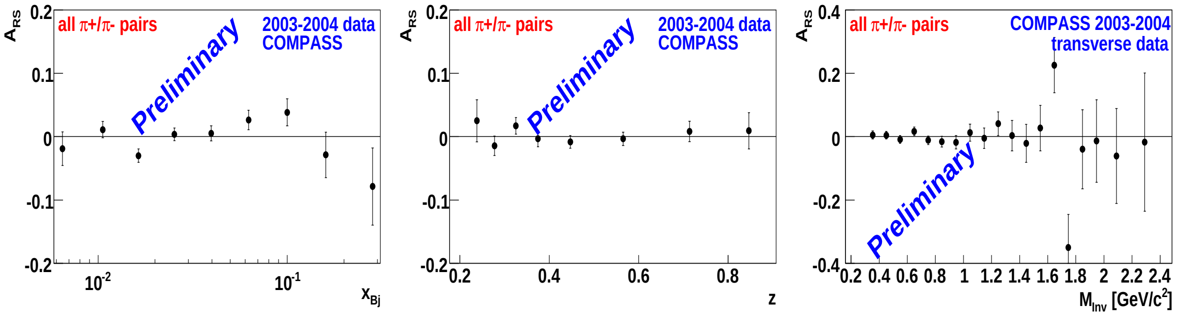

Figure 5.5: Measured asymmetry amplitudes A_{RS} of $\pi^+\pi^-$ pairs from COMPASS data in 2003-2004 with hadron identification. The asymmetries are shown as a function of x, z and M_h. The error bars represent the statistical uncertainty only.

This can result in much smaller asymmetries [117, 138] compared to those measured on a proton target, due to cancellation effects between the transversity distribution of u quarks and d quarks. This observation is also consistent with the small Collins asymmetry measured by the COMPASS collaboration on a deuteron target [43] and the measurement of $A_{\mathrm{UL}}^{\sin\phi_{R\perp}}$ at HERMES experiment as described at the beginning of this section. In 2007, COMPASS was taking data with a transversely polarized proton target [209] where the asymmetries are expected to be larger as the results in this thesis. This will facilitate the comparison with the present results in this thesis. Together with the deuteron data presented by COMPASS experiment, a separation of the asymmetries originating from u and d quarks shall then be possible. Finally, the COMPASS collaboration extracted the amplitude using a linear ϕ_{RS}–dependent fit [209]. Hence, integrating both the numerator and the denominator over θ within the detector acceptance will not justify this linear fit, since in the COMPASS analysis the requirement is made that both $z_1 > 0.1$ and $z_2 > 0.1$, which influences the coverage in the angle θ (cf. Sec. 4.5.4). The omission of the θ dependence in the denominator of the asymmetry makes the comparison more complicate.

5.2.2 Comparison with Model Predictions

Since the fragmentation function $H_1^{\sphericalangle,sp}$ requires the interference between s and p waves, it is supposed to be sizable in the regions where spin–1 resonances are presented, assuming the rest of the spectrum to be in an s–wave. As can be seen in Figure 4.22, in the invariant–mass range $0.5\,\text{GeV} < M_{\pi\pi} < 1.0\,\text{GeV}$, the ρ^0 and ω resonances are present and give large contributions to the spectrum. The available theoretical models related with the dihadron fragmentation function $H_1^{\sphericalangle,sp}$ discussed in Sec. 2.4.4 indicate that the effect should be non–zero and maximal in the vicinity of the ρ^0 mass [111, 116, 117]. The relatively large value of the amplitude of the third data point in the $M_{\pi\pi}$ panel in Figure 5.1 provides a positive support for this expectation.

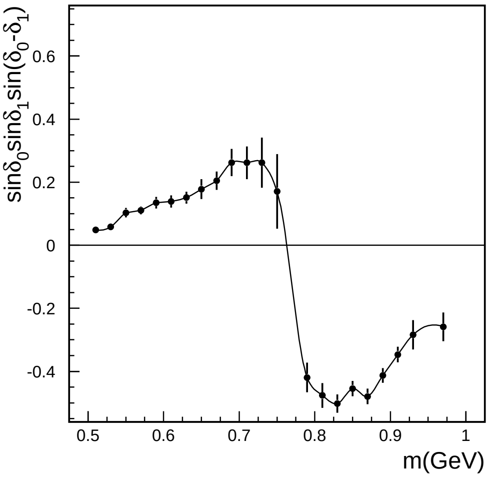

Figure 5.6: The phase factor $\sin\delta_0 \sin\delta_1 \sin(\delta_0 - \delta_1)$ with the invariant mass dependence.

Jaffe's model [111, 112] predicted a sign change of the dihadron fragmentation function $H_1^{\sphericalangle,sp}$ approximately at the ρ^0 mass (as seen in Figure 5.6). Then the amplitude $A_{\text{UT}}^{\sin(\phi_{R\perp}+\phi_S)\sin\theta}$ would also show such a sign change there. Such a distinct behavior is obviously negated based on this study, since the amplitude are always positive in the whole kinematic range, without any hint to change the sign at the vicinity of the ρ^0 mass.

Radici, Jakob and Bianconi's model [116] did not suggest the sign change around the ρ^0 mass, which is supported by this work. But their predicted amplitudes are very small.

Developing from this model, Bacchetta and Radici [117] can give a quantitative prediction for the full kinematic dependence of both dihadron fragmentation functions $H_1^{\sphericalangle,sp}$ and D_1 that are needed to calculate the amplitude $A_{\mathrm{UT}}^{\sin(\phi_{R\perp}+\phi_S)\sin\theta}$ (cf Sec. 2.4.4). Their model was used in MC simulation in this study and worked effectively in the systematic studies. By the study in Sec. 4.5.2, we could evaluate the predicted amplitude in MC simulation, taking into account the HERMES acceptance, and compare them with the extracted amplitude from real data. In principal, this kind of comparison is the best way for comparison of the theoretical prediction with the experimental measurement. In fact, they already made a prediction for the amplitude evaluated at the kinematics of the HERMES experiment. It was given in a different form in Figure 2.29 from the model prediction in Figure 5.7. Firstly, the model–predicted amplitudes here include HERMES acceptance effect, which cannot be thoroughly brought into the integration of the asymmetry amplitudes. For instance, the limited acceptance of azimuthal angle and the momentum restriction of the final particles are difficult to be taken into account in theoretical calculation. Hence, a part of the HERMES acceptance effect was ignored for the amplitude shown in Figure 2.29. But as we have pointed out the difference between 4π acceptance and HERMES acceptance discussed in Sec. 4.5.2, these effects are not negligible, which the difference between the Figure 5.7 and Figure 2.29 can also qualify. Note also that in Figure 2.29 the amplitude $A_{\mathrm{UT}}^{\sin(\phi_{R\perp}+\phi_S)}$ is shown, whereas Figure 5.7 presents the amplitude $A_{\mathrm{UT}}^{\sin(\phi_{R\perp}+\phi_S)\sin\theta}$. These differ by a factor $\pi/4$ according to Eq. (2.95) (within a 4π acceptance).

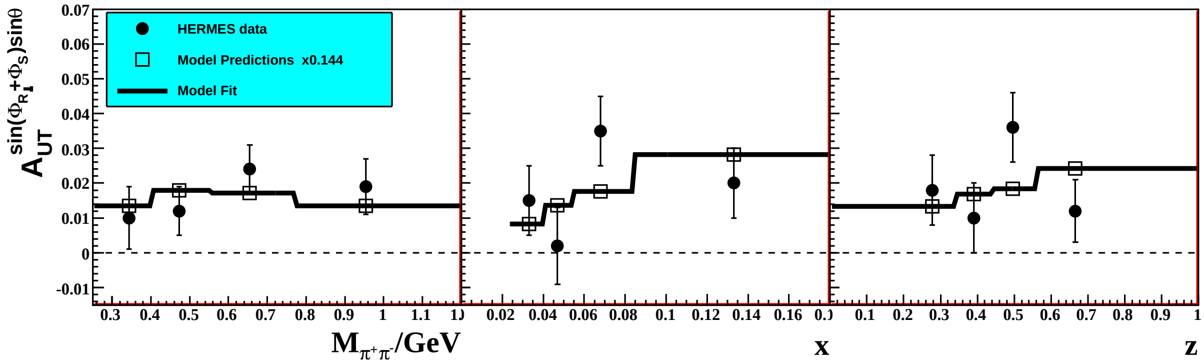

Figure 5.7: The extracted amplitude $A_{\mathrm{UT}}^{\sin(\phi_{R\perp}+\phi_S)\sin\theta}$ from real data (taken from the data in Figure 5.1), and the model predictions of the asymmetry amplitudes within the HERMES acceptance using the MC simulation (taken from the HERMES acceptance data in Figure 4.18). The model–predicted asymmetry amplitudes are multiplied with the global fitting scale in Table 5.2. The solid line shows the global fit to the real data. The obtained overall scaling factor is in Table 5.2.

dependence	scale factor	reduced–χ^2
$M_{\pi\pi}$	0.150 ± 0.034	0.764
x	0.144 ± 0.040	1.751
z	0.135 ± 0.037	1.861
global	0.144 ± 0.021	1.202

Table 5.2: The fitted scaling factors of the model predictions in HERMES acceptance (taken from the HERMES acceptance data in Figure 4.18) to the measured amplitudes as shown in Figure 5.7 to the HERMES data.

The comparison between the model prediction and the real measurement in HERMES acceptance is shown in Figure 5.7 where the model–predicted amplitudes were taken from the HERMES acceptance results in Figure 4.18 or Table. 4.7. The model–predicted amplitudes are generally larger than the HERMES results. In order to estimate how much the amplitude is overestimated and to compare the shape of the amplitudes as a function of $M_{\pi\pi}$, x, or z, the model–predicted amplitudes were fitted to the real data results, using an overall scaling factor as a free parameter. This fit was performed globally and separately for the three kinematic dependencies. The fitted results are indicated in Figure 5.7 as the solid lines. The fitted scaling factors and the reduced–χ^2 of the fits are given in Table 5.2. The extracted scaling factors for the three dependencies are consistent with each other, and also with the globally fitted factor, which indicates that the model overestimates the data by a factor of 7. In Refs. [117, 125, 210] it was already argued that the model probably overestimates the effect of interferences, that is, the model overestimates the dihadron fragmentation function $H_1^{\sphericalangle,sp}$. Ref. [125] argued that in this asymmetry amplitudes only a part of the s–p interference $\pi^+\pi^-$ pairs contribute. The fitting results in Table 5.2 indicate that it could be only 14.4%.

The theoretical model in the transversity distribution function has been fitted to the existing world experimental data (cf. Sec. 5.3.1). For the different choices of the models in the transversity distribution function, we see similar distributions of the amplitudes in Figure 2.29 and Figure 2.30. Hence, for the comparison with model prediction on the amplitude $A_{\mathrm{UT}}^{\sin(\phi_{R\perp}+\phi_S)\sin\theta}$, the mechanism on the dihadron fragmentation function plays a key role in interpreting the behavior of the asymmetry. But combined with the information of the dedicated measurement on the dihadron fragmentation function, transversity can be extracted from the current results and narrow down the information on transversity with other transversity related experimental data (cf. Sec. 5.3.1).

5.3 Other Options to Access Transversity

Transversity cannot be accessed in inclusive DIS process, which had made us turn to semi–inclusive DIS process to study transversity. Besides the semi–inclusive DIS process, the hadron-hadron collisions have also potential to be connected with transversity. Other than the measurement of the two–hadron lepto–production, possible processes, which may be related to transversity, will be depicted in this section. As discussed above, the processes can be categorized into two groups.

5.3.1 Lepton–Nucleon Reactions

The first category of reactions which can access transversity is the lepton-nucleon reactions. This was mostly covered in Chapter 2. Besides those described with details in Chapter 2, there are some other candidate lepto-production processes which can involve transversity.

Lepto–Production of One Hadron

As discussed in Sec. 2.3, one–hadron semi–inclusive DIS with unpolarized lepton beam and transversely polarized nucleon target, $l + N^{\uparrow} \rightarrow l + N + X$, can be used to probe the transversity. The single–spin asymmetry for this process is related to the **convolution** of the transversity distribution function and the Collins fragmentation function. The Sivers function also will contribute to the asymmetry in a convolution with the unpolarized fragmentation function, but with different azimuthal Fourier component from the Collins part. That difference makes us possible to separate the two azimuthal moments. Firstly preliminary results on the single–spin asymmetry in pion lepto-production was reported by the SMC [211]. The SMC results were with large uncertainties due to small statistics.

From 2002, the HERMES Collaboration installed the transversely polarized target and published their first results on the Collins single–spin asymmetry [40] through π lepto-production. Later the most recent preliminary results with higher statistics were also released [41] through π and K lepto-production with data from 2002–2005. These results are shown in Figure 5.8; The measured Collins amplitude is positive for π^+, and negative for π^-. This sign difference is consistent with $h_1^u > 0$ and $h_1^d < 0$, which is also in agreement with model predictions (cf. Sec.2.2). Also, the magnitude of the π^- amplitude appears to be comparable or larger than the one for π^+. This leads to the conclusion that the disfavoured Collins fragmentation function has a substantial magnitude with an opposite sign compared to the favoured Collins fragmentation function. That is because that the azimuthal moments are related to the following combinations of distribution and fragmentation functions: (here fav≡favored and dis*equiv*disfavored) [212]:

$$\langle \sin(\phi_h + \phi_S) \rangle^{\pi^+} : \quad 4h_1^u H_1^{\perp \mathrm{fav}} + h_1^d H_1^{\perp \mathrm{dis}}, \tag{5.9}$$

$$\langle \sin(\phi_h + \phi_S) \rangle^{\pi^-} : \quad 4h_1^u H_1^{\perp \mathrm{dis}} + h_1^d H_1^{\perp \mathrm{fav}}. \tag{5.10}$$

Taking into account that one expects from model predictions $|h_1^d| < |h_1^u|$, the first terms in Eq. (5.9) and Eq. (5.10). This would then imply that the data require a large disfavored Collins functions, with $H_1^{\perp \mathrm{dis}} \approx -H_1^{\perp \mathrm{fav}}$. The opposite sign of the favored and disfavored Collins function can be understood within the context of the string model of fragmentation (see *e.g.*, [213]). If a favored pion is formed from the first string break, the second string break will result in a disfavored pion. Due to momentum conservation, this second disfavored pion will have transverse momentum in the opposite direction compared to the favored pion. As a consequence the Collins fragmentation function obtains the opposite sign [214, 215]. The last point is that for charged kaons no statistically significant non–zero Collins amplitudes are found. However, the Collins amplitudes for K^+ are consistent to the π^+ amplitudes within statistical accuracy.

The data sample of semi–inclusive DIS events, used to obtain the results that are shown in Figure 5.8, is slightly contaminated with pions that result from the decay of exclusively produced vector mesons. In Figure 5.9, the fraction of exclusively produced vector mesons is shown as determined using the Pythia Monte–Carlo simulation [106]. Recent studies [163] indicate that the asymmetry produced by this contribution is small and does not bias the results presented in Fig 5.8. This implies that the exclusively produced vector mesons only give rise to a dilution of the measured asymmetries. The corrections for the dilution were found to be very small in all kinematic bins except for π–mesons in the highest z bins. For the results shown here, the correction was not implemented.

The COMPASS collaboration at CERN also published the results for the single–spin asymmetry of unidentified charged hadrons on a transversely polarized ^{6}LiD target [42, 43] and later reported the results for identified pions and kaons as well [44]. They measured very small asymmetries that are consistent with zero within the statistical uncertainty. The difference with the HERMES results could be due to cancellation effects between the single–spin asymmetries on a proton and a neutron target.

In order to extract transversity from the single–spin asymmetries in one-hadron semi–inclusive DIS, a separate measurement of the Collins fragmentation function is needed. This function can be obtained from e^+e^- scattering ($e^+e^- \to h_1 h_2 X$), as was accomplished by the Belle collaboration at KEK [216] and recently updated with higher statistics [217, 218]. Anselmino et al. [49] firstly extracted the transversity distribution function for u and d quarks from a global analysis of the results from the HERMES [40], COMPASS [42, 43] and Belle [216] collaborations. The light color band in Figure 5.10 shows the uncertainty of the fit. Later with new data from HERMES [41], COMPASS [44] and Belle [217] collaboration, Anselmino et al. [219] made a new global fit to the transversity, as shown in Figure 5.10. The new fit constrains both the $h_1^u(x)$ and $h_1^d(x)$ quite well and diminishes

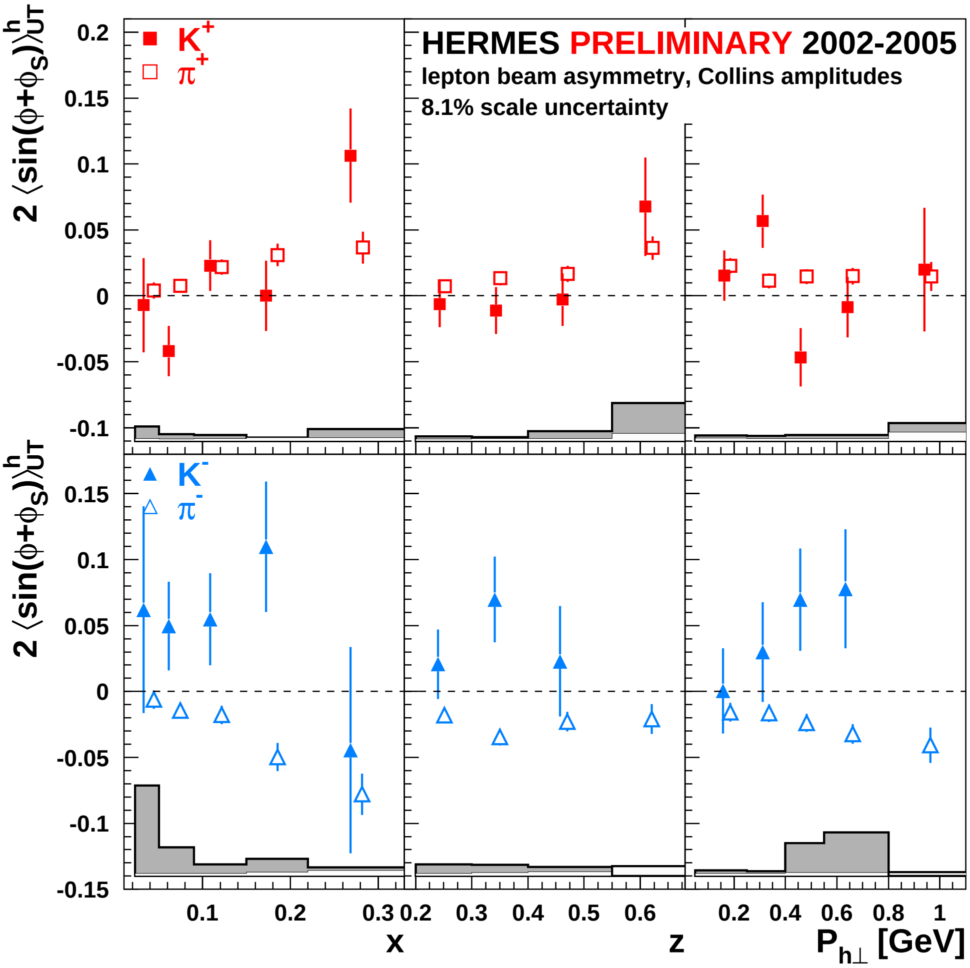

Figure 5.8: Collins moments for semi–inclusive DIS produced charged pions (open symbols, as labelled) and charged kaons (closed symbols, as labelled) as a function of x, z and $P_{h\perp}$ as measured by HERMES [41]. The error bars represent the statistical uncertainty. The systematic uncertainty is indicated separately as a dark grey histogram in the lower part of each panel.

the uncertainties. The new fitted $h_1^u(x)$ is larger than the old fitted result and $h_1^d(x)$ is consistent with the old fitted result. The fitting results show that $h_1^u(x) > 0$ and $h_1^d(x) < 0$, which is consistent with the model predictions (cf. Figure 2.11). The values of transversity $h_1^u(x)$ and $h_1^d(x)$ are found to be considerably smaller than the Soffer bound (cf. Eq. (2.49)) which is indicated as the blue line in Figure 5.10. As shown in Figure 5.11, the extracted transversity is comparable with most of the model predictions.

The E06–010/E06–011 experiment in Hall A at JLab is also planning to measure the single–spin asymmetry of charged pions to access transversity of the neutron, using

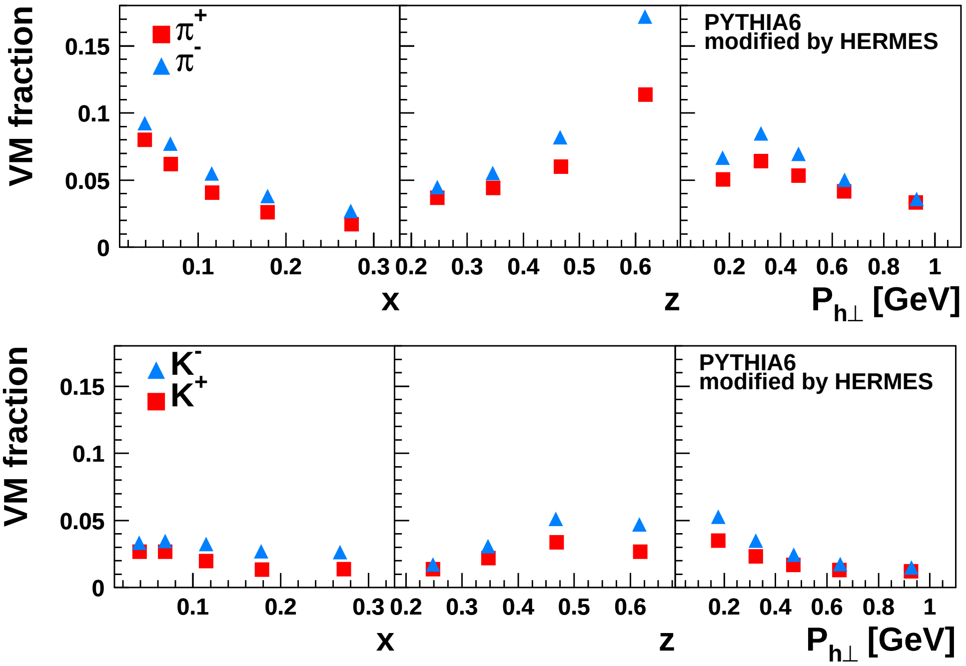

Figure 5.9: Simulated fractions of charged π–mesons and charged K–mesons originating from exclusively produced diffractive vector meson production and decay. The fractions are determined using the Pythia Monte–Carlo simulation, tuned for the HERMES kinematics.

6 GeV electron beam and a transversely polarized ^{3}He target [223]. This would be a complementary measurement of transversity to the proton target results at HERMES and the deuteron target results at COMPASS. Besides that, the CLAS collaboration in Hall B at JLab is planning to study transversity [224], using the future upgraded 12 GeV CEBAF accelerated electron beam with a polarized NH$_3$ target. The theoretical predictions were already made on the JLab experiments [49, 225].

Lepto-Production of One Spin–1 Hadron

Semi–inclusive DIS production of spin–one hadrons, $l + N^{\uparrow} \to l + \ h^{J=1} + X$, (*e.g.*, ρ, ω, ϕ and $K^{\star}$) has also been studied and proposed as an alternative method to measure the transversity distribution [226–229]. The polarized cross section [78] after integration over the transverse momentum $\boldsymbol{P}_{h\perp}$ is

$$\mathrm{d}^6\sigma_{UT} = -\sum_q \frac{\alpha^2 e_q^2}{2\pi s x y^2}\,(1-y)\,|\boldsymbol{S}_{\perp}|\,\sin 2\theta\,\sin(\phi_R+\phi_S)\,h_1^q(x)\,H_{1LT}^q(z), \tag{5.11}$$

where θ, ϕ_R, ϕ_S are with the same definitions as those in the two–hadron semi–inclusive DIS process (cf. Sec. 2.4). Here the asymmetry of Eq. (5.11) contains the transversity

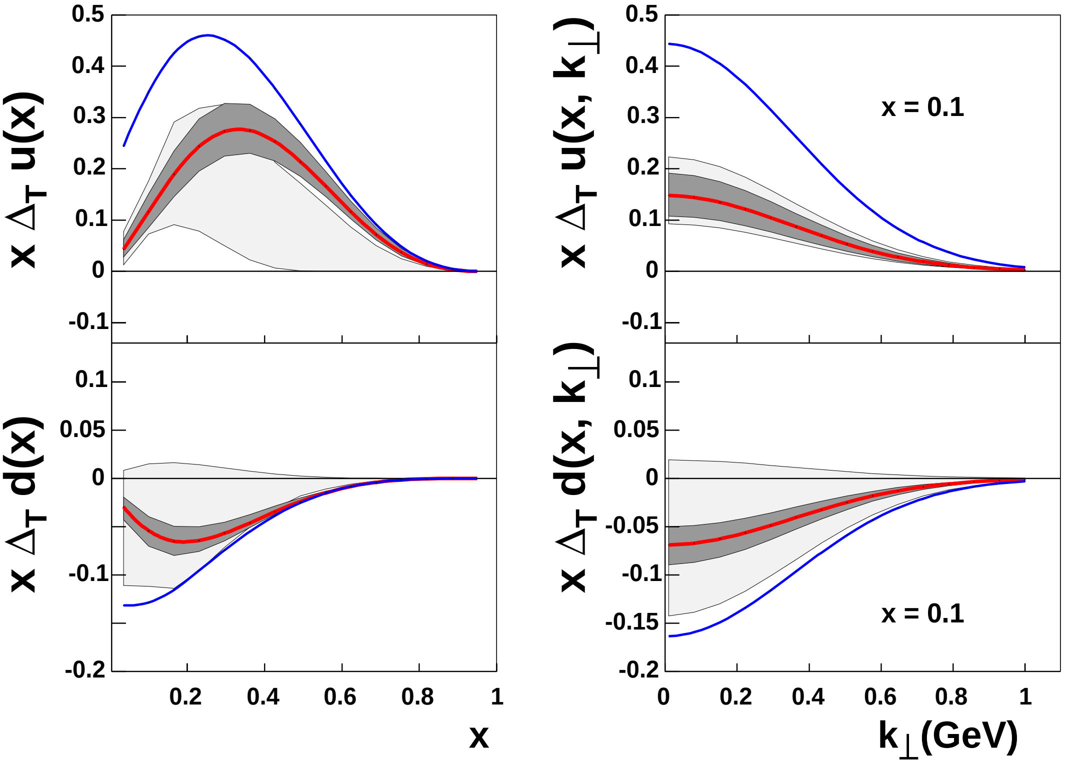

Figure 5.10: The transversity distribution (here indicated as Δ_T instead of h_1) for u and d quarks from a global analysis presented in Ref. [219], as a function of Bjorken-x and $k_\perp$ at a fixed value of Bjorken-x. The thick red curve presents the fitted transversity distribution and the grey shaded band shows the uncertainties from the fit. The thick blue curve represents the Soffer bound [79] for the value of the transversity distribution function. The light band shows the uncertainties of the old fit from Ref. [49]. The x dependence shown on the left is a result from a fit to the experimental data, the $k_\perp$ dependence on the right is chosen to be the same as that of the unpolarized distribution functions, but not from the fit. The shaded area on the right only represents the uncertainty of the fit.

distribution h_1 multiplied by the chiral–odd T–odd fragmentation function $H_{1LT}^q(z)$. The transverse polarization of the struck quark is transferred to a certain polarization state which can be analyzed by polarimetry on the final decay products. In this sense, the vector meson production represents just a specific contribution to the more general case of two–hadron production near the vector meson mass. Note that $H_{1LT}^q(z)$ corresponds to the pp sector of Eqs. (2.92). For instance, the reaction $ep \to e\rho^0 X(\rho^0 \to \pi^+\pi^-)$ is actually just a part of the more general reaction $ep \to e\pi^+\pi^- X$, which was studied in this thesis. Hence, as an extensive work apart from the single–spin asymmetry of the two-pion lepto-production measured in this thesis, a very preliminary measurement of the asymmetry of

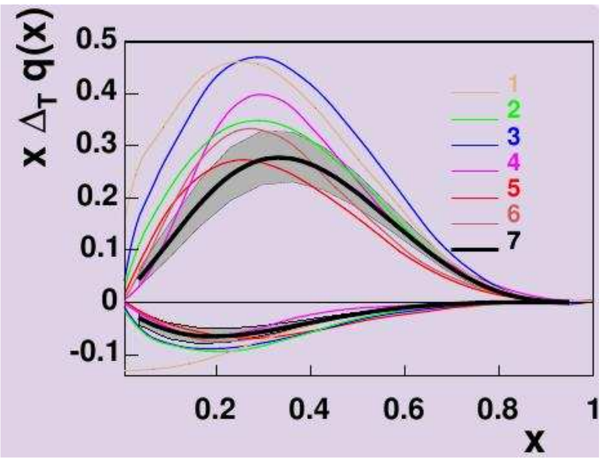

Figure 5.11: The transversity distributions for u and d quarks in proton from different model predictions as a function of Bjorken-x. Lines 1–6 are from Ref. [98], Ref. [99], Ref. [86], Ref. [220], Ref. [221], and Ref. [222], respectively. Line 7 is from the global analysis presented in Figure 5.10. The shaded band shows the uncertainty of the fit.

the ρ^0 lepto-production was also preformed. Even with quite high statistics of the ρ_0 meson lepto-production, the result did not show any evidence of non-zero asymmetry. That could be due to the huge background of non–resonant pion pairs, which will probably dilute the results. Till now, no experiment ever reported the measurement of this asymmetry.

Lepto-Production of Transversely Polarized Hadron

Transversity can be accessed through the process: $l + N^{\uparrow} \to l + h^{\uparrow} + X$, if the transverse spin of the struck quark is transferred to the produced spin–half hadron, which is called **transverse spin transfer**. Here transverse means orthogonal to the $\gamma^* h$ plane. The transverse polarization of the produced hadron can then be directly related to transversity h_1 and an unknown twist–two chiral–odd transversity fragmentation function $H^h_{1,q}$ [104, 105, 230]. For example in the transversely spin transfer of Λ production in the process: $l + p^{\uparrow} \to l + \Lambda^{0\uparrow}\,(\overline{\Lambda}^{0\uparrow}) + X$, where $\Lambda^0\,(\overline{\Lambda}^0) \to p\,(\overline{p}) + \pi^-\,(\pi^+)$, the Λ transverse polarization P_Λ can be written [231] as:

$$P^{\uparrow}_{\Lambda} = |P_T| \frac{2(1-y)}{1+(1-y)^2} \frac{\sum_q e_q^2 h_1^q(x) H^{\Lambda}_{1,q}(z)}{\sum_q e_q^2 f_1^q(x) D^{\Lambda}_{1,q}(z)} \tag{5.12}$$

The challenge of such a measurement is the determination of the polarization of the produced hadrons. In case of a two–particle decay of the produced hadron, this can be achieved through the analysis of the angular distributions in the parity violating decay. The unique azimuthal modulation of this transversity related asymmetry were given in Ref. [101]. First preliminary results of Λ^0 $(\overline{\Lambda}^0)$ productions have been obtained by the

COMPASS experiment [232–234] and the HERMES collaboration [235]. Both experiments found that the values for the transverse Λ^0 ($\overline{\Lambda}^0$) polarization are consistent with zero, which mainly is due to the large statistical uncertainties of those measurements. Higher precision results are needed in order to conclude whether or not this process can be used to access transversity. At HERMES experiment, the small acceptance for Λ^0 together with the complex decay angular distribution analysis will not allow the extraction of the azimuthal asymmetries amplitudes from the complete HERMES data sample on a transversely polarized proton target. However, the possible explanation on this small transverse spin transfer is that the u quark polarization in Λ^0 hyperon is presumably small. But the semi-inclusive DIS measurement with transversely polarized proton target at HERMES is u quark dominant.

5.3.2 Hadron–Hadron Reactions

The second class of reactions probing the quark transversity is hadron-hadron reaction with at least one of the two colliding particles in a transverse polarization state. In the case where both initial hadrons are transversely polarized, Drell–Yan production is supposed to be the most favourable reaction for studying the transversity distributions. For the single transversely polarized case, transversity may also emerge. Especially, a similar mechanism as the process studied in this thesis is possible to be studied at RHIC experiments.

Drell–Yan Processes

A promising candidate process for a measurement of the transversity distribution h_1 is Drell–Yan production (cf. Figure 5.12): $N^\uparrow + N^\uparrow \to l^+ + l^- + X$. To lowest order in QCD, the lepton pairs originates from a virtual photon $\gamma^\star$. A systematic study [39, 236] of this process firstly introduced the transversity distribution in theory. The advantage of this process is that no fragmentation functions are involved, as the production of the lepton pair from the quark annihilation ($q\bar{q} \to l^+l^-$) is described by QED and can be precisely calculated. The double spin asymmetry for this process is sensitive to the product of the quark and antiquark transversity distribution functions, which has been proposed to measure using the colliding polarized protons at RHIC [237]. Since there is no gluon transversity distribution for spin-half hadrons, the Drell–Yan process has the advantage that to lowest order there is no partonic subprocess which involves a gluon in the initial state. But till now no experimental data about this process is available. That is because the transversely polarized antiquark density in the nucleon is presumably rather small; there is no splitting term $g \to q\bar{q}$ in the evolution equations for the transversity [103], so a vital source for the generation of antiquarks is missing. Then this transverse double–spin asymmetry is expected to be suppressed [76, 238]. Generally gluons usually strongly contribute to the unpolarized cross sections which is in the denominator of the asymmetry,

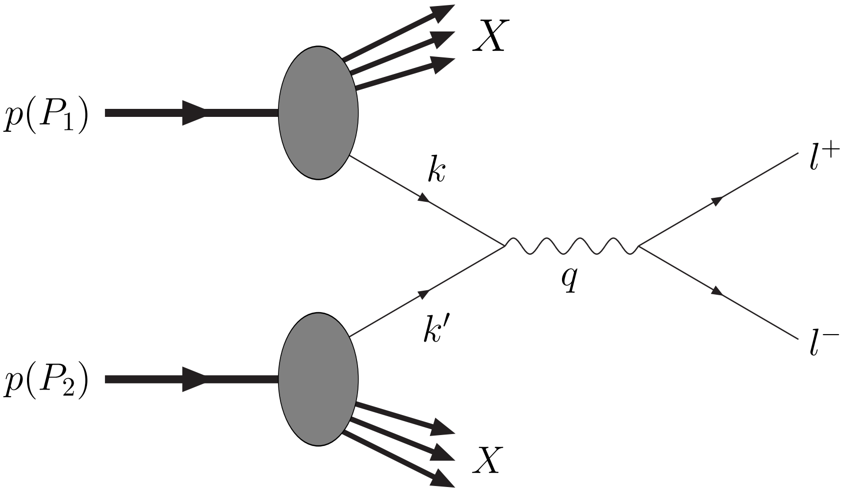

Figure 5.12: Drell–Yan dilepton production.

whereas they are absent for transversity in the numerator, as discussed above. For the *pp* collisions experiment at RHIC, the transverse double spin asymmetries are quite small for RHIC kinematic conditions, *i.e.*, of the order of 1–2% only [239, 240].

Since the transversity distributions for antiquarks in the proton are presumably small, the PAX collaboration at GSI [241] uses the collisions of polarized proton and polarized antiproton, which can avoid this problem. In this case, the double–spin asymmetry is sensitive to the product of two quark transversity distribution functions. Model calculations predict values for the asymmetry in PAX kinematics range of 30–40% [242, 243]. But the biggest challenge for the PAX collaboration will be to reach the intended transverse polarization for the antiproton beam of $P_{\bar{p}} = 0.2$–0.3 [244, 245].

However, the Drell–Yan process: $N + N^{\uparrow} \rightarrow l^+ + l^- + X$, with one colliding hadron polarized might also be used to study transversity. This nonzero single–spin asymmetries for dimouons Drell–Yan production could be related to the product of the transversity distribution function with the Boer–Mulders function, which describes the distribution of transversely polarized quarks in an unpolarized nucleon [246]. Transversity can then be extracted from the asymmetry in combination with measurements of the unpolarized Drell–Yan process, which can be used to obtain the Boer–Mulders distribution function. This process could be measured by the PAX experiment or the RHIC experiments.

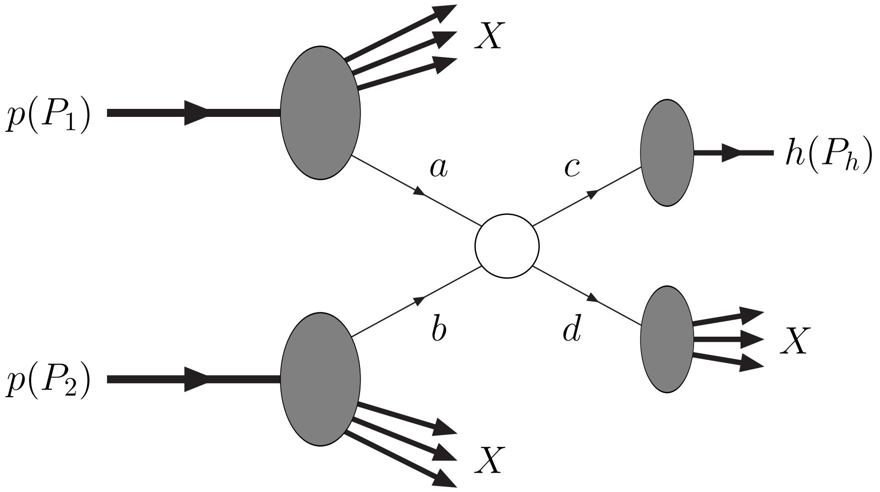

Figure 5.13: Hadron-hadron reaction with the inclusive hadro-production of a hadron h, *e.g.*, π.

Transverse Single–Spin Asymmetries of One Hadron

Surprisingly the large single transverse spin asymmetries A_N of the inclusive hadro-production in the process of Figure 5.13, *e.g.*, $p^{\uparrow}p \rightarrow \pi X$, have been observed experimentally [247–251] over many years from 70s. However, these experiments were performed at relatively low energies ($\sqrt{s} \leq 6$ GeV), such that it is not obvious that the cross sections can be factorized in terms of the distribution and fragmentation functions. In 1991 the E704 experiment at Fermilab extended to higher energies ($\sqrt{s} = 19.4$ GeV) and observed up to 40% single–spin asymmetries in inclusive pion hadro-production with a transversely polarized proton to higher p_T [252, 253]. More recently, nonzero single–spin asymmetries were also observed at RHIC ($\sqrt{s} = 200\,\text{GeV}$) by the STAR [254, 255], BRAHMS [256, 257] and PHENIX [258] experiments. However, at mid–rapidity the PHENIX collaboration measured the transverse single–spin asymmetries consistent with zero [259].

Sizeable A_N was not expected in collinear pQCD at leading twist due to the chiral properties of the theory [260]. This large asymmetries then prompted a lot of new developments in pQCD, such as the introduction of transverse momentum dependence (TMD) correlated with the spin degree of freedom. Sivers *et al.* had suggested that the single–spin asymmetries could originate, at leading twist, from the intrinsic motion of quarks in the colliding protons [46, 261, 262], which is called Sivers effect. A different mechanism was proposed by Collins [45], which is called Collins effect. Higher twist (twist-3) effects arising from quark-gluon correlation effects beyond the conventional twist-2 distribution have also been considered as a possible origin of the single–spin asymmetries [263–265]. Ref. [45] claimed that the asymmetries are mainly the result of the Collins effect, where there is a convolution of transversity with the Collins fragmentation function. But recently it was shown that in the process $p^{\uparrow}p \to \pi X$, the Collins mechanism is suppressed [266]. As a consequence, several unknown distribution and fragmentation functions need to be evaluated in order to reach a full understanding of these asymmetries. An eventual extraction of transversity from these measurement is still not clear and need the inputs of different mechanisms from other experiments.

Note that in proton–proton collision experiment, two Bjorken-x's are involved as two partons collides. It is important to identify them event–by–event. Inclusive pion measurement cannot do it. Coincidence measurement is required to perform a kinematically complete measurement.

Transverse Single–Spin Asymmetries of Two Hadrons

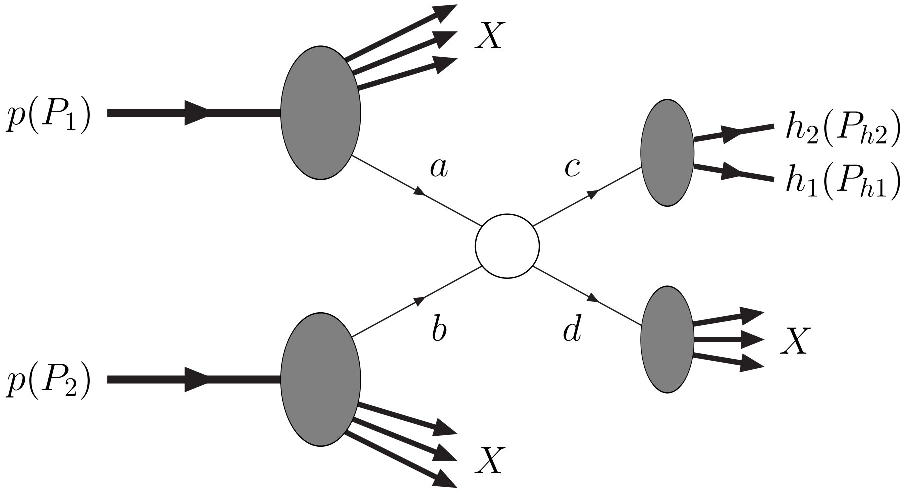

Figure 5.14: Hadron-hadron reaction with the inclusive hadro-production of hadron pairs h_1h_2, *e.g.*, $\pi\pi$.

A mechanism analogous to the one investigated in this thesis in pp reactions can offer another promising way to access the transversity. It was firstly suggested in Ref. [111, 112] that the transversity can be studied by the two–hadron hadro–production process: $p^{\uparrow}p \to h_1h_2X$, as shown in Figure 5.14. As the two–hadron DIS process studied in this thesis, the transverse single–spin asymmetry of this process is also related to the product of the transversity h_1 and the dihadron fragmentation function $H_1^{\sphericalangle}$. The measurement of this transverse single–spin asymmetry was proposed at RHIC experiments [237] and the study is recently ongoing at PHENIX experiment [267]. However, owing to many potential contributions to this process, the uncertainty of this measurement still exists.

5.4 Summary

The single transverse spin asymmetry amplitude $A_{\mathrm{UT}}^{\sin(\phi_{R\perp}+\phi_S)\sin\theta}$ was measured at HERMES experiment for the first time in the world. The values with statistical uncertainties and systematic uncertainties are given in Table 5.1. The results are significantly non–zero, at the conference level of 4σ. This implies that both transversity h_1 and the dihadron fragmentation function $H_1^{\sphericalangle,sp}$ are non–zero. The amplitudes were extracted as a function of $M_{\pi\pi}$, x and z. The present results rule out the sign change around the ρ^0 mass range predicted by the Jaffe's model [111, 112]. The measurement of the amplitudes with DIS can be used to extract transversity, by the combination with the dihadron fragmentation function which could be measured by the Belle [217], BaBar [268] and BES [269] collaboration. The work in this thesis is consistent with other related measurement at HERMES.

There are also other ways to access transversity, which can be used to pin down the mechanism of transversity. Transversity has been studied also in one–hadron lepton DIS process and extracted from the Collins asymmetry. But the extracted transversity is still with large uncertainties. There are also other possible ways to probe transversity, such as Drell–Yan process and single transverse spin asymmetry in pp collision, but till now no available data exist.

Chapter 6

Conclusion

The spin physics is one of the fundamental topics in nowadays research frontier in particle and nuclear physics. As mentioned as “proton spin problem”, part of proton spin contribution is missing till now. At leading twist order, in the nucleon structure, transversity is less studied in experiment and theory compared with other two distribution functions: the quark density distribution and the helicity distribution. Transversity was extracted from the world data of measurement of one hadron transverse target–spin asymmetry in lepton semi–inclusive deep inelastic scattering and measurement of Collins fragmentation function. The transverse target–spin asymmetry of two hadron production, which is presented in this thesis, is another complementary way to access transversity. In this asymmetry, transversity is multiplied with the unknown dihadron fragmentation function. This thesis presents the world first measurement of this two hadron transverse target–spin asymmetry at the HERMES experiment. This asymmetry can be used to extract transversity in an independent way by combination with the measurement of the dihadron fragmentation function.

Taking advantage of the longitudinally/transversely polarized atomic target and the longitudinally polarized positron/electron beam, HERMES experiment can measure the different aspects of nucleon spin structure. In the work of this thesis, only transversely polarized target was used to study the transverse target–spin asymmetry of two hadron lepto–production. RICH detector provided the nice separation among protons, kaons and pions. The performance of the detectors were monitored by GMS system, which helps detector maintenance, malfunction analysis and data–quality evaluation.

The asymmetry reported in this thesis was systematically studied and the extracted amplitude $A_{\mathrm{UT}}^{\sin(\phi_{R\perp}+\phi_S)\sin\theta}$ is positive with the value $0.018 \pm 0.005(\mathrm{stat})^{+0.004}_{-0.002}(\mathrm{syst})$ in the overall kinematic range. The amplitudes with dependence on $M_{\pi\pi}$, x and z were studied, which facilitates comparison with theoretical studies and extraction of transversity from these data. The dependence on $M_{\pi\pi}$ suggests a consistently positive in the whole kinematic range, which disfavors the theoretical model by Jaffe. The result showed a large asymmetry around the resonance of $\rho(770)$, which is consistent in shape with the model from Radici and Alessandro. Although the later model well predicted the asymmetry amplitude in shape, which was adopted to study systematic uncertainties in this analysis, the size of the HERMES data is smaller than the prediction. By applied a scaling factor, the predicted amplitude $A_{\mathrm{UT}}^{\sin(\phi_{R\perp}+\phi_S)\sin\theta}$ becomes consistent with the present results. It should be noted that the estimated systematic uncertainties are model dependent. With the information of the dihadron fragmentation function, which is planned to be measured at the Belle experiment, transversity can be extracted from this measurement.

This measurement is consistent with the HERMES results of the azimuthal amplitude $A_{\mathrm{UL}}^{\sin\phi_{R\perp}}$ and the azimuthal amplitudes $A_{\mathrm{LU}}^{\sin\phi_R\sin\theta}$. The preliminary results measured by the COMPASS collaboration on the same asymmetry amplitude from the deuteron target are not inconsistent with this measurement and its future measurement on the transversely proton target can be more directly compared with the results in this thesis. The analogous mechanism in *pp* collisions at RHIC experiments could be measured. It will be complementary to the measurements in lepto-production process. For the moment, no data are available yet.

Appendix A

Notations and Conventions

Units Natural units $\hbar = c = 1$ are used throughout. For the basic unit of charge we use the magnitude of the charge of the electron: $e > 0$.

Metric Tensor The conventions will follow the review paper [54]. The metric tensor is definded as:

$$g^{\mu\nu} = g_{\mu\nu} = \begin{pmatrix} 1 & 0 & 0 & 0 \\ 0 & -1 & 0 & 0 \\ 0 & 0 & -1 & 0 \\ 0 & 0 & 0 & -1 \end{pmatrix},$$

with Greek indices running over 0,1,2,3. Repeated indices are summed in all cases. Light italic roman type will be used for four-vectors, while boldface italic will be used for three-vectors. The scalar product of two four-vectors $x = (x^0, x^1, x^2, x^3)$ and $y = (y^0, y^1, y^2, y^3)$ reads

$$x \cdot y = g_{\mu\nu} x^\mu y^\nu,$$

where the Einstein summation convention is applied.

Light-cone vectors Light-cone vectors will be indicated as

$$a^\mu = \left[a^-,\ a^+,\ \boldsymbol{a}_T\right] = \left[\frac{a^0 - a^3}{\sqrt{2}},\ \frac{a^0 + a^3}{\sqrt{2}},\ a^1,\ a^2\right].$$

The dot-product in light-cone components is

$$\begin{aligned} a \cdot b &= a^+ b^- + b^- a^+ - \boldsymbol{a}_T \cdot \boldsymbol{b}_T \\ &= a^+ b^- + b^- a^+ - a^i b^i \\ &= a^+ b^- + b^- a^+ - a_x b_x - a_y b_y \end{aligned}$$

The two-dimensional transverse parts of the vectors will be written in boldface with an index T and Latin indices will be used to denote the two transverse components only.

Note that

$$\boldsymbol{a}_T = (a_x,\ a_y), \qquad a_T^\mu = [0,\ 0,\ \boldsymbol{a}_T], \qquad a_{T\mu} = [0,\ 0,\ -\boldsymbol{a}_T].$$

We introduce the projector on the transverse subspace

$$g_T^{\mu\nu} = \begin{pmatrix} 0 & 0 & 0 & 0 \\ 0 & -1 & 0 & 0 \\ 0 & 0 & -1 & 0 \\ 0 & 0 & 0 & 0 \end{pmatrix},$$

We define the antisymmetric tensor so that

$$\epsilon^{0123} = +1, \qquad \epsilon_{0123} = -1.$$

and we define the transverse part of the antisymmetric tensor as

$$\epsilon_T^{\mu\nu} = \epsilon^{-+\mu\nu} = \epsilon^{03\mu\nu}.$$

Dirac matrices Dirac matrices will be often expressed in the chiral or Weyl representation, *i.e.*,

$$\gamma^0 = \begin{pmatrix} 0 & \mathbf{1} \\ \mathbf{1} & 0 \end{pmatrix}, \qquad \gamma^i = \begin{pmatrix} 0 & -\boldsymbol{\sigma}^i \\ \boldsymbol{\sigma}^i & 0 \end{pmatrix}, \qquad \gamma_5 = \begin{pmatrix} \mathbf{1} & 0 \\ 0 & -\mathbf{1} \end{pmatrix},$$

and we will make use of the Dirac structure

$$\sigma^{\mu\nu} \equiv \frac{\mathrm{i}}{2}\left[\gamma^\mu, \gamma^\nu\right].$$

Appendix B

Dihadron Fragmentation with Transverse Momentum

If we consider the correlation functions with transverse momentum dependence Eq. (2.61a) and Eq. (2.76), their decompositions become richer than what was shown in Eq. (2.78)

$$
\begin{aligned}
&\mathcal{P}_-\,\Delta(z,\zeta,M_h^2,\phi_{R\perp},\boldsymbol{k}_T)\,\gamma^- \\
=&\frac{1}{8\pi}\Bigg(D_1\big(z,\zeta,M_h^2,\boldsymbol{k}_T^2,\boldsymbol{k}_T\cdot\boldsymbol{R}_T\big)\;+\mathrm{i}H_1^{\triangleleft\prime}\big(z,\zeta,M_h^2,\boldsymbol{k}_T^2,\boldsymbol{k}_T\cdot\boldsymbol{R}_T\big)\,\frac{\not{R}_T}{M_h} \\
&+\mathrm{i}H_1^{\perp}\big(z,\zeta,M_h^2,\boldsymbol{k}_T^2,\boldsymbol{k}_T\cdot\boldsymbol{R}_T\big)\,\frac{\not{k}_T}{M_h}\;+\;G_1^{\perp}\big(z,\zeta,M_h^2,\boldsymbol{k}_T^2,\boldsymbol{k}_T\cdot\boldsymbol{R}_T\big)\,\frac{\epsilon_T^{\mu\nu}\,R_{T\mu}k_{T\nu}}{M_h^2}\,\gamma_5\Bigg)\,\mathcal{P}_-,
\end{aligned}
\tag{B.1}
$$

where the transverse momentum dependent functions have the dependence on the variables z, ζ, M_h^2, $\boldsymbol{k}_T^2$, $\boldsymbol{k}_T\cdot\boldsymbol{R}_T$. By introducing the projection $\boldsymbol{a}_T\wedge\boldsymbol{b}_T=a_i\epsilon_T^{ij}b_j$, we have the cross section formulae with transverse momentum dependence

$$
\begin{aligned}
&\mathrm{d}^9\sigma_{UU} \\
=&\sum_q\frac{\alpha^2e_q^2}{2\pi sxy^2}\Bigg\{A(y)\,\mathcal{I}\left[f_1\,D_1\right]-B(y)\,\frac{|\boldsymbol{R_T}|}{M_h}\,\cos(\phi_h+\phi_{R\perp})\,\mathcal{I}\left[\frac{\boldsymbol{p_T}\cdot\hat{\boldsymbol{P}}_{h\perp}}{M}\,h_1^{\perp}\,H_1^{\triangleleft\prime}\right] \\
&-B(y)\,\frac{|\boldsymbol{R_T}|}{M_h}\,\sin(\phi_h+\phi_{R\perp})\,\mathcal{I}\left[\frac{\hat{\boldsymbol{P}}_{h\perp}\wedge\boldsymbol{p_T}}{M}\,h_1^{\perp}\,H_1^{\triangleleft\prime}\right] \\
&-B(y)\,\cos(2\phi_h)\,\mathcal{I}\left[\frac{2(\boldsymbol{p_T}\cdot\hat{\boldsymbol{P}}_{h\perp})(\boldsymbol{k_T}\cdot\hat{\boldsymbol{P}}_{h\perp})-\boldsymbol{p_T}\cdot\boldsymbol{k_T}}{MM_h}\,h_1^{\perp}\,H_1^{\perp}\right] \\
&-B(y)\,\sin(2\phi_h)\,\mathcal{I}\left[\frac{(\boldsymbol{p_T}\cdot\hat{\boldsymbol{P}}_{h\perp})(\hat{\boldsymbol{P}}_{h\perp}\wedge\boldsymbol{k_T})+(\boldsymbol{k_T}\cdot\hat{\boldsymbol{P}}_{h\perp})(\hat{\boldsymbol{P}}_{h\perp}\wedge\boldsymbol{p_T})}{MM_h}\,h_1^{\perp}\,H_1^{\perp}\right]\Bigg\},
\end{aligned}
\tag{B.2}
$$

$$
\begin{aligned}
&\mathrm{d}^9\sigma_{UT} \\
&= \sum_q \frac{\alpha^2 e_q^2}{2\pi s x y^2}\, |\boldsymbol{S}_T|\, A(y) \left\{ -\frac{|\boldsymbol{R_T}|}{M_h} \sin(\phi_{R\perp} - \phi_S)\, \mathcal{I}\left[\frac{\boldsymbol{p_T}\cdot\boldsymbol{k_T}}{2MM_h} \mathrm{g}_{1T}\, G_1^{\perp}\right] \right. \\
&\quad - \frac{|\boldsymbol{R_T}|}{M_h} \cos(\phi_{R\perp} - \phi_S)\, \mathcal{I}\left[\frac{(\boldsymbol{p_T}\cdot\hat{\boldsymbol{P}}_{h\perp})(\hat{\boldsymbol{P}}_{h\perp}\wedge\boldsymbol{k_T}) - (\boldsymbol{k_T}\cdot\hat{\boldsymbol{P}}_{h\perp})(\hat{\boldsymbol{P}}_{h\perp}\wedge\boldsymbol{p_T})}{2MM_h} \mathrm{g}_{1T}\, G_1^{\perp}\right] \\
&\quad + \frac{|\boldsymbol{R_T}|}{M_h} \sin(2\phi_h - \phi_{R\perp} - \phi_S)\, \mathcal{I}\left[\frac{2(\boldsymbol{p_T}\cdot\hat{\boldsymbol{P}}_{h\perp})(\boldsymbol{k_T}\cdot\hat{\boldsymbol{P}}_{h\perp}) - \boldsymbol{p_T}\cdot\boldsymbol{k_T}}{2MM_h}\, \mathrm{g}_{1T}\, G_1^{\perp}\right] - \frac{|\boldsymbol{R_T}|}{M_h} \\
&\quad \times \cos(2\phi_h - \phi_{R\perp} - \phi_S)\, \mathcal{I}\left[\frac{(\boldsymbol{p_T}\cdot\hat{\boldsymbol{P}}_{h\perp})(\hat{\boldsymbol{P}}_{h\perp}\wedge\boldsymbol{k_T}) + (\boldsymbol{k_T}\cdot\hat{\boldsymbol{P}}_{h\perp})(\hat{\boldsymbol{P}}_{h\perp}\wedge\boldsymbol{p_T})}{2MM_h}\, \mathrm{g}_{1T}\, G_1^{\perp}\right] \\
&\quad \left. - \sin(\phi_h - \phi_S)\, \mathcal{I}\left[\frac{\boldsymbol{p_T}\cdot\hat{\boldsymbol{P}}_{h\perp}}{M}\, f_{1T}^{\perp}\, D_1\right] + \cos(\phi_h - \phi_S)\, \mathcal{I}\left[\frac{\hat{\boldsymbol{P}}_{h\perp}\wedge\boldsymbol{p_T}}{M}\, f_{1T}^{\perp}\, D_1\right]\right\} \\
&\quad + \sum_q \frac{\alpha^2 e_q^2}{2\pi s x y^2}\, |\boldsymbol{S}_T|\, B(y) \left\{ -\sin(\phi_h + \phi_S)\, \mathcal{I}\left[\frac{\boldsymbol{k_T}\cdot\hat{\boldsymbol{P}}_{h\perp}}{M_h}\, h_1\, H_1^{\perp}\right] + \cos(\phi_h + \phi_S) \right. \\
&\quad \times \mathcal{I}\left[\frac{\hat{\boldsymbol{P}}_{h\perp}\wedge\boldsymbol{k_T}}{M_h}\, h_1\, H_1^{\perp}\right] - \frac{|\boldsymbol{R_T}|}{M_h} \sin(\phi_{R\perp} + \phi_S)\, \mathcal{I}\left[h_1\, H_1^{\sphericalangle\prime}\right] - \sin(3\phi_h - \phi_S) \\
&\quad \times \mathcal{I}\left[\frac{4(\boldsymbol{p_T}\cdot\hat{\boldsymbol{P}}_{h\perp})^2(\boldsymbol{k_T}\cdot\hat{\boldsymbol{P}}_{h\perp}) - 2(\boldsymbol{p_T}\cdot\hat{\boldsymbol{P}}_{h\perp})(\boldsymbol{p_T}\cdot\boldsymbol{k_T}) - \boldsymbol{p_T}^2(\boldsymbol{k_T}\cdot\hat{\boldsymbol{P}}_{h\perp})}{2M^2M_h}\, h_{1T}^{\perp}\, H_1^{\perp}\right] \\
&\quad + \cos(3\phi_h - \phi_S)\, \mathcal{I}\left[\left(\frac{2(\boldsymbol{p_T}\cdot\hat{\boldsymbol{P}}_{h\perp})^2(\hat{\boldsymbol{P}}_{h\perp}\wedge\boldsymbol{k_T}) + 2(\boldsymbol{k_T}\cdot\hat{\boldsymbol{P}}_{h\perp})(\boldsymbol{p_T}\cdot\hat{\boldsymbol{P}}_{h\perp})(\hat{\boldsymbol{P}}_{h\perp}\wedge\boldsymbol{p_T})}{2M^2M_h}\right.\right. \\
&\quad \left.\left. - \frac{\boldsymbol{p_T}^2(\hat{\boldsymbol{P}}_{h\perp}\wedge\boldsymbol{k_T})}{2M^2M_h}\right) h_{1T}^{\perp}\, H_1^{\perp}\right] - \frac{|\boldsymbol{R_T}|}{M_h} \sin(2\phi_h + \phi_{R\perp} - \phi_S) \\
&\quad \times \mathcal{I}\left[\frac{2(\boldsymbol{p_T}\cdot\hat{\boldsymbol{P}}_{h\perp})^2 - \boldsymbol{p_T}^2}{2M^2}\, h_{1T}^{\perp}\, H_1^{\sphericalangle\prime}\right] + \frac{|\boldsymbol{R_T}|}{M_h} \cos(2\phi_h + \phi_{R\perp} - \phi_S) \\
&\quad \left. \times \mathcal{I}\left[\frac{(\boldsymbol{p_T}\cdot\hat{\boldsymbol{P}}_{h\perp})(\hat{\boldsymbol{P}}_{h\perp}\wedge\boldsymbol{p_T})}{2M^2}\, h_{1T}^{\perp}\, H_1^{\sphericalangle\prime}\right]\right\}.
\end{aligned}
\tag{B.3}
$$

By an assumption of Gaussian Ansatz for the distribution and fragmentation functions with dependence on both $\boldsymbol{p_T}$ (initial quark's transverse momentum) and $\boldsymbol{k_T}$ (fragmenting quark's transverse momentum), *e.g.*,

$$\begin{aligned} \widetilde{F}(x, \boldsymbol{p_T^2}) &= \frac{1}{\pi \langle \boldsymbol{p_T^2} \rangle} e^{-\boldsymbol{p_T^2}/\langle \boldsymbol{p_T^2} \rangle} \widetilde{F}(x) \\ \widetilde{D}(z, \zeta, M_h^2, \boldsymbol{k_T^2}, \boldsymbol{k_T} \cdot \boldsymbol{R_T}) &= \frac{1}{z^2 \pi \langle \boldsymbol{k_T^2} \rangle} e^{-\boldsymbol{k_T^2}/\langle \boldsymbol{k_T^2} \rangle} \widetilde{D}(z, \zeta, M_h^2), \end{aligned} \tag{B.4}$$

where $\widetilde{F}(x, \boldsymbol{p_T^2})$ and $\widetilde{D}(z, \zeta, M_h^2, \boldsymbol{k_T^2}, \boldsymbol{k_T} \cdot \boldsymbol{R_T})$ are the general symbols for the distribution and fragmentation functions in Eq. (B.2) and Eq. (B.3), one can get the simpler equations [1]:

$$\begin{aligned} &\mathrm{d}^9 \sigma_{UU} \\ &= \sum_q \frac{\alpha^2 e_q^2}{2\pi^2 s x y^2} \Bigg\{ A(y) \, \frac{1}{\langle \boldsymbol{P_{h\perp}^2} \rangle} f_1 \, D_1 - B(y) \, \frac{|\boldsymbol{R}_T|}{M_h} \, \cos(\phi_h + \phi_{R\perp}) \, z \, \frac{\langle \boldsymbol{p_T^2} \rangle \, |\boldsymbol{P_{h\perp}}|}{M \langle \boldsymbol{P_{h\perp}^2} \rangle^2} h_1^\perp \, H_1^{\sphericalangle\prime} \\ &\quad + B(y) \, \cos(2\phi_h) \, z^4 \frac{\langle \boldsymbol{p_T^2} \rangle \, \langle \boldsymbol{k_T^2} \rangle \, |\boldsymbol{P_{h\perp}}|^2}{M M_h \langle \boldsymbol{P_{h\perp}^2} \rangle^3} \, h_1^\perp \, H_1^\perp \Bigg\} e^{-\boldsymbol{P_{h\perp}^2}/\langle \boldsymbol{P_{h\perp}^2} \rangle}, \end{aligned} \tag{B.5}$$

$$\begin{aligned} &\mathrm{d}^9 \sigma_{UT} \\ &= \sum_q \frac{\alpha^2 e_q^2}{2\pi^2 s x y^2} \, |\boldsymbol{S}_T| \, A(y) \Bigg\{ \frac{|\boldsymbol{R_T}|}{M_h} \, \sin(\phi_{R\perp} - \phi_S) \, z^4 \, \frac{\langle \boldsymbol{p_T^2} \rangle \, \langle \boldsymbol{k_T^2} \rangle \, [\langle \boldsymbol{P_{h\perp}^2} \rangle - |\boldsymbol{P_{h\perp}}|^2]}{2 M M_h \langle \boldsymbol{P_{h\perp}^2} \rangle^3} \, \mathrm{g}_{1T} \, G_1^\perp \\ &\quad - \frac{|\boldsymbol{R_T}|}{M_h} \, \sin(2\phi_h - \phi_{R\perp} - \phi_S) \, z^4 \, \frac{\langle \boldsymbol{p_T^2} \rangle \, \langle \boldsymbol{k_T^2} \rangle \, |\boldsymbol{P_{h\perp}}|^2}{2 M M_h \langle \boldsymbol{P_{h\perp}^2} \rangle^3} \, \mathrm{g}_{1T} \, G_1^\perp \\ &\quad - \sin(\phi_h - \phi_S) \, z \, \frac{\langle \boldsymbol{p_T^2} \rangle \, |\boldsymbol{P_{h\perp}}|}{M \langle \boldsymbol{P_{h\perp}^2} \rangle^2} \, f_{1T}^\perp \, D_1 \Bigg\} e^{-\boldsymbol{P_{h\perp}^2}/\langle \boldsymbol{P_{h\perp}^2} \rangle} \\ &\quad + \sum_q \frac{\alpha^2 e_q^2}{2\pi^2 s x y^2} \, |\boldsymbol{S}_T| \, B(y) \Bigg\{ \sin(\phi_h + \phi_S) \, z \, \frac{\langle \boldsymbol{k_T^2} \rangle \, |\boldsymbol{P_{h\perp}}|}{M_h \langle \boldsymbol{P_{h\perp}^2} \rangle^2} \, h_1 \, H_1^\perp \\ &\quad - \frac{|\boldsymbol{R_T}|}{M_h} \, \sin(\phi_{R\perp} + \phi_S) \, \frac{1}{\langle \boldsymbol{P_{h\perp}^2} \rangle} \, h_1 \, H_1^{\sphericalangle\prime} + \sin(3\phi_h - \phi_S) z^{11} \, \frac{\langle \boldsymbol{p_T^2} \rangle^2 \, \langle \boldsymbol{k_T^2} \rangle \, |\boldsymbol{P_{h\perp}}|^3}{2 M^2 M_h \langle \boldsymbol{P_{h\perp}^2} \rangle^4} \, h_{1T}^\perp \, H_1^\perp \\ &\quad - \frac{|\boldsymbol{R_T}|}{M_h} \, \sin(2\phi_h + \phi_{R\perp} - \phi_S) \, z^4 \, \frac{\langle \boldsymbol{p_T^2} \rangle^2 \, |\boldsymbol{P_{h\perp}}|^2}{2 M^2 \langle \boldsymbol{P_{h\perp}^2} \rangle^3} \, h_{1T}^\perp \, H_1^{\sphericalangle\prime} \Bigg\} e^{-\boldsymbol{P_{h\perp}^2}/\langle \boldsymbol{P_{h\perp}^2} \rangle}, \end{aligned} \tag{B.6}$$

where $\langle \boldsymbol{P_{h\perp}^2} \rangle / z^2 = \langle \boldsymbol{p_T^2} \rangle + \langle \boldsymbol{k_T^2} \rangle$.

---

[1] Due to the fact that no $\boldsymbol{k_T} \cdot \boldsymbol{R_T}$ dependence is taken into account for the fragmentation functions, about half of the ϕ_h-dependent terms drop out of the complete expression for the polarized cross section.

Appendix C

Asymmetry Formula

Adopting a simple correlation with detector acceptance, we can have the counting number of the inclusive events in experiment as:

$$N_{\mathrm{DIS}}^{\uparrow}(\boldsymbol{r}) = \alpha^{\uparrow}(\boldsymbol{r})\phi^{\uparrow}(\boldsymbol{r})t_{\mathrm{DIS}}^{\uparrow}(\boldsymbol{r})\mathrm{d}\sigma_{\mathrm{DIS}}^{\uparrow}(\boldsymbol{r}), \tag{C.1}$$

$$N_{\mathrm{DIS}}^{\downarrow}(\boldsymbol{r}) = \alpha^{\downarrow}(\boldsymbol{r})\phi^{\downarrow}(\boldsymbol{r})t_{\mathrm{DIS}}^{\downarrow}(\boldsymbol{r})\mathrm{d}\sigma_{\mathrm{DIS}}^{\downarrow}(\boldsymbol{r}), \tag{C.2}$$

where ↑ (↓) indicates the upward(downward) transversely polarized target state. $\boldsymbol{r}$ is the dependent kinematic variables. $\alpha(\boldsymbol{r})$ is the acceptance and detection efficiency of DIS outgoing lepton. $\phi(\boldsymbol{r})$ is the beam flux and target density. $t_{\mathrm{DIS}}(\boldsymbol{r})$ is the measuring time. $\mathrm{d}\sigma_{\mathrm{DIS}}(\boldsymbol{r})$ is the DIS cross section. At leading twist, no transverse target asymmetry contributes to the DIS cross section as described in Eq. (2.51). Hence

$$\mathrm{d}\sigma_{\mathrm{DIS}}^{\uparrow}(\boldsymbol{r}) = \mathrm{d}\sigma_{\mathrm{DIS}}^{\downarrow}(\boldsymbol{r}). \tag{C.3}$$

With the help of the frequent flips of target spin (cf. Sec. 3.2), the data taking periods for two target polarization states are same

$$t_{\mathrm{DIS}}^{\uparrow}(\boldsymbol{r}) = t_{\mathrm{DIS}}^{\downarrow}(\boldsymbol{r}). \tag{C.4}$$

Let $\beta(\boldsymbol{r})$ is the acceptance and detection efficiency of outgoing pion pair, with Eq. (2.63) and Eq. (2.67) the transverse single-spin asymmetry A_{UT} can be related with the semi-inclusive pion pair yields in experiment by the following equations:

$$N^{\uparrow}(\boldsymbol{r}) = \alpha^{\uparrow}(\boldsymbol{r})\beta^{\uparrow}(\boldsymbol{r})\phi^{\uparrow}(\boldsymbol{r})t^{\uparrow}(\boldsymbol{r})\mathrm{d}\sigma(\boldsymbol{r})\{1 + \langle|\boldsymbol{P_T^{\uparrow}}|\rangle A_{\mathrm{UT}}(\boldsymbol{r})\}, \tag{C.5}$$

$$N^{\downarrow}(\boldsymbol{r}) = \alpha^{\downarrow}(\boldsymbol{r})\beta^{\downarrow}(\boldsymbol{r})\phi^{\downarrow}(\boldsymbol{r})t^{\downarrow}(\boldsymbol{r})\mathrm{d}\sigma(\boldsymbol{r})\{1 - \langle|\boldsymbol{P_T^{\downarrow}}|\rangle A_{\mathrm{UT}}(\boldsymbol{r})\}. \tag{C.6}$$

The following equation is safely satisfied as Eq. (C.4):

$$t^{\uparrow}(\boldsymbol{r}) = t^{\downarrow}(\boldsymbol{r}). \tag{C.7}$$

Assuming the hadron detection efficiency $\beta(\boldsymbol{r})$ is identical for different the target polarization state

$$\beta^{\uparrow}(\boldsymbol{r}) = \beta^{\downarrow}(\boldsymbol{r}), \tag{C.8}$$

Neglecting the indications of the variables dependence, we can have the asymmetry formula in experiment:

$$A_{\mathrm{UT}} \;=\; \frac{N^{\uparrow}/N^{\uparrow}_{\mathrm{DIS}} - N^{\downarrow}/N^{\downarrow}_{\mathrm{DIS}}}{\langle|\boldsymbol{P}^{\downarrow}_{\boldsymbol{T}}|\rangle N^{\uparrow}/N^{\uparrow}_{\mathrm{DIS}} + \langle|\boldsymbol{P}^{\uparrow}_{\boldsymbol{T}}|\rangle N^{\downarrow}/N^{\downarrow}_{\mathrm{DIS}}}. \tag{C.9}$$

If we can achieve the balance target polarization $\langle|\boldsymbol{P}^{\uparrow}_{\boldsymbol{T}}|\rangle = \langle|\boldsymbol{P}^{\downarrow}_{\boldsymbol{T}}|\rangle = \langle|\boldsymbol{P}_{\boldsymbol{T}}|\rangle$, we can get the simpler asymmetry formula:

$$A_{\mathrm{UT}} = \frac{1}{\langle|\boldsymbol{P}_{\boldsymbol{T}}|\rangle}\frac{N^{\uparrow}/N^{\uparrow}_{\mathrm{DIS}} - N^{\downarrow}/N^{\downarrow}_{\mathrm{DIS}}}{N^{\uparrow}/N^{\uparrow}_{\mathrm{DIS}} + N^{\downarrow}/N^{\downarrow}_{\mathrm{DIS}}}. \tag{C.10}$$

Due to the spectrometer acceptance limit, the cross section cannot be directly measured at experiment. On the other hand, the acceptance effect can be cancelled out in the measurement of the asymmetry. Therefore, the asymmetry is a more general physics quantity, which connects the theoretical prediction to the experimental data.

Appendix D

Random Drop Beam Helicity Balance Method

To achieve the net beam helicity closer to 0, we can keep dropping those events with the same polarization direction as the spare polarizations, until the left events have the minimum average beam polarizations $\langle P_b \rangle$. That is to say that we aim to get the most balanced data samples which satisfy $\langle P_b \rangle \simeq 0$. In this analysis, net beam helicity is negative, so the negative beam polarization events are dropped until the minimum average absolute value of beam polarization is reached. Generally, there is a simple way to make it by cutting off the events with higher beam polarization to keep more statistics, or removing a bound of runs. But the balance cut thresholds are chosen casually by different analyzers. So the personal favor of the threshold selection will somehow affect the kept data samples, though the influence may be small. The method we need is what can get rid of the individual influence on the helicity balanced data and eliminate the fluctuation of the results. Random Drop (RD) Helicity Balance Method (HBM) is developed for that purpose [270]. It not only can accords with the above requirements, but also can estimate the systematic uncertainty from the nonzero beam polarization.

The main idea of this method is that by many times of extraction of the asymmetry amplitudes from the kept data samples, whose beam polarization P_b are balanced closet to zero after random drop the events, the Gaussian distribution of the extracted amplitudes can be used to estimate the center value and systematic uncertainties of the helicity balanced results. The balance spectator was chosen on the run or burst level in order to set up a relevant relationship between the DIS luminosity counting and the $\pi^+\pi^-$ pair data samples. From the main thought of Random Drop method, the detailed approaches are listed below:

1. Calculate S_{P_b}. S_{P_b} is the sum of the polarizations of the bursts in the $\pi^+\pi^-$ pair samples.

2. Start randomly dropping the $\pi^+\pi^-$ pair data sample with the same beam polariza-

tion direction as the extra beam polarization:

   (a) RD–Run: run by run until reach the minimum absolute value of S_{P_b}. Record the dropped run list (denoted as RL).
   (b) RD–Burst: burst by burst until reach the minimum absolute value of S_{P_b}. Record the dropped run list (denoted as BL).

3. Apply the list RL or BL to the DIS samples and the $\pi^+\pi^-$ pair samples: drop those runs or bursts in the corresponding list.
4. Extract the amplitudes from the kept balanced data samples a lot of times and estimate the mean values and standard deviation of the distribution of these amplitudes.

In this analysis, RD–Run and RD–Burst are both performed to check the beam polarization effect. From Fig. D.1 by RD–Run HBM or Fig. D.2 by RD–Burst HBM, the net beam polarization can be nicely balanced to the order of 0.5% or 0.00005%. The balanced data were used to extract the asymmetry amplitude $A_{\rm UT}^{\sin(\phi_{R\perp}+\phi_S)\sin\theta}$. As an example, we show the Gaussian behaviors of the extracted amplitudes from these operations in four x kinematic bins and the estimated results can be given by the fit by Gaussian curve. As indicated in the above two plots, we see the stable mean values of the amplitudes and the zero systematic uncertainties. The statistical uncertainties were taken as the average values of all the fitted statistical uncertainties from each RD operation. The same plots with same conclusions in $M_{\pi\pi}$ and z bins were also checked and the final amplitudes were plotted in Fig. 4.10. The results from the two RD HBMs are highly consistent with difference less than an absolute value of 0.001. From RD study, we could conclude the negligible effect from beam polarization to the final asymmetry amplitude.

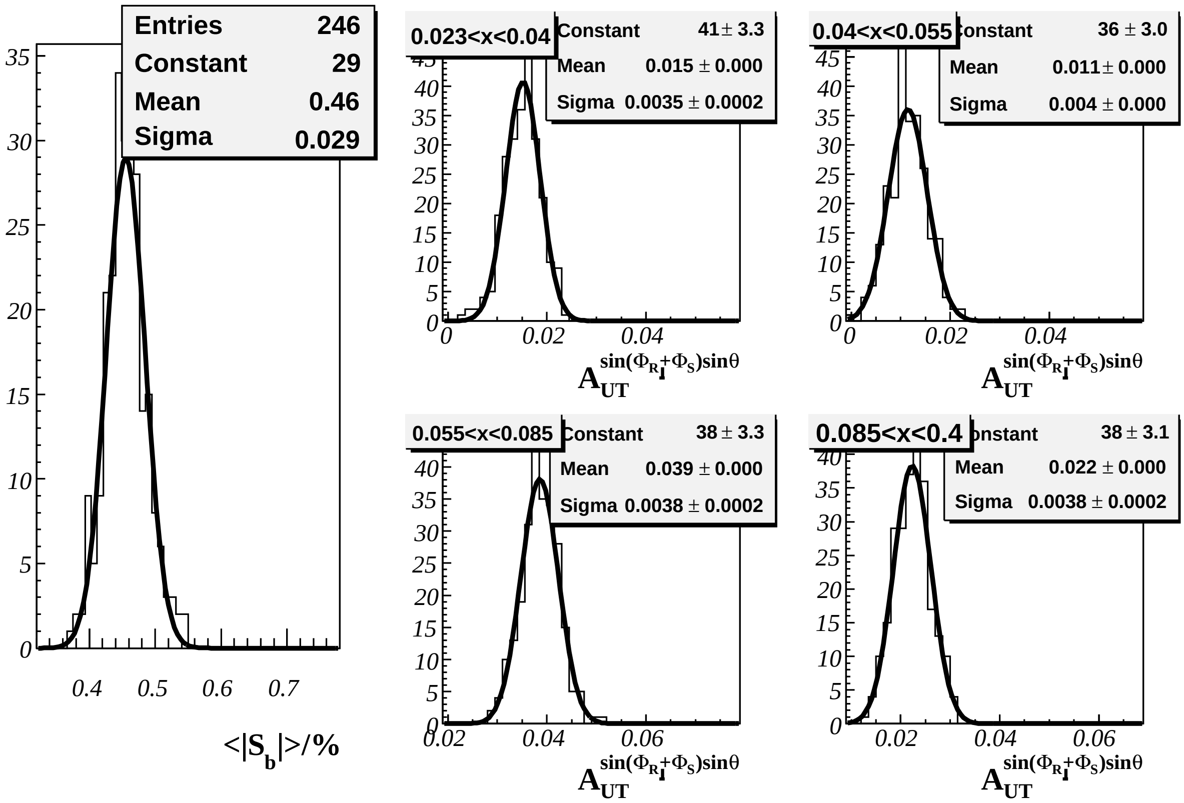

Figure D.1: As an example, the histogram of the average absolute values of the beam polarizations in many different beam helicity balanced data using RD–Run HBM is shown in the left plot, and the extracted amplitudes from those different balanced data within 4 x kinematic bins are plotted in the right 4 panels, respectively. The real data are from years 2002 to 2005. Every distributions were fitted with Gaussian curves, which can be used to estimate the mean value and the systematic uncertainty of the amplitudes extracted from the balanced data.

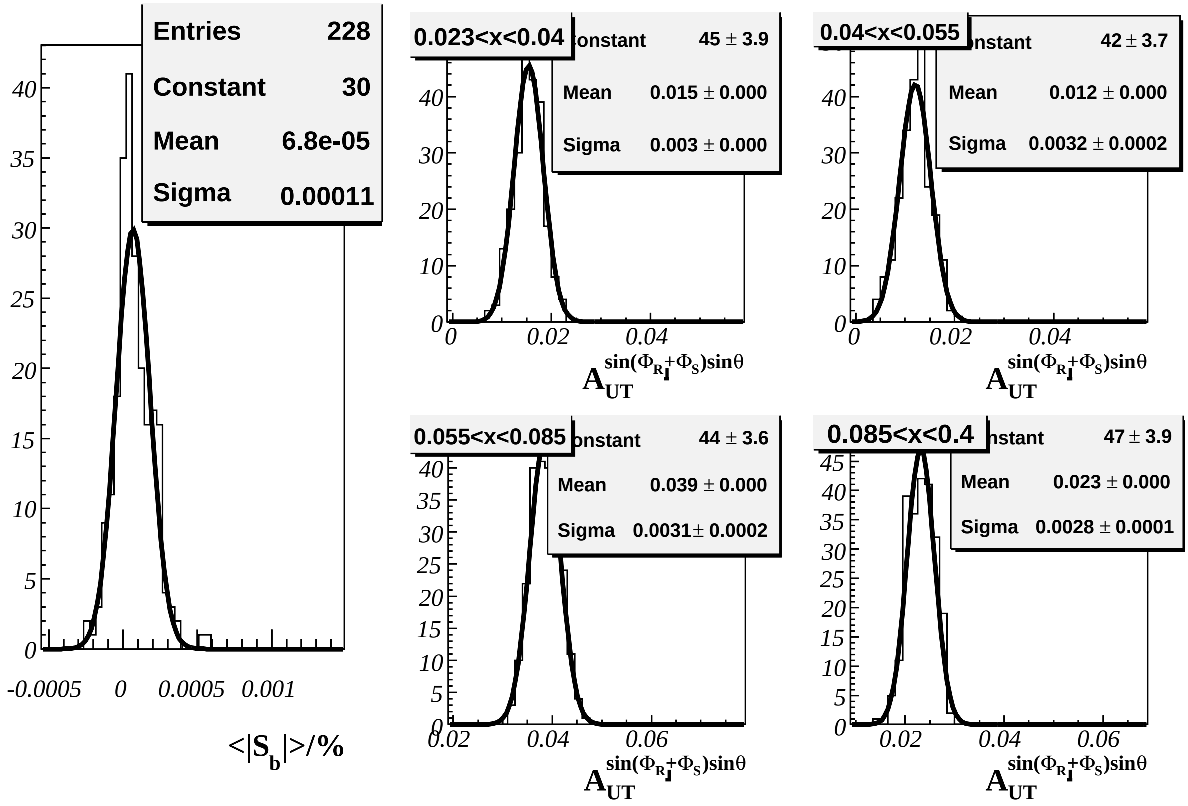

Figure D.2: As an example, same as Fig. D.1, but with many times of RD–Burst HBM operations.

List of Tables

List of Figures

Bibliography

[1] B. Povh, K. Rith, C. Scholz, and F. Zetsche. *Particles and nuclei : an introduction to the physical concepts*. Springer, New York, USA, 2006.

[2] H. Geiger and E. Marsden. On a diffuse reflection of the α-particles. *Proc. Roy. Soc.*, A82:495–500, 1909.

[3] E. Rutherford. The scattering of α and β particles by matter and the structure of the atom. *Phil. Mag.*, 21:669–688, 1911.

[4] E. D. Bloom et al. High-energy inelastic $e-p$ scattering at 6° and 10°. *Phys. Rev. Lett.*, 23:930–934, 1969.

[5] Guthrie Miller et al. Inelastic electron-proton scattering at large momentum transfers. *Phys. Rev.*, D5:528, 1972.

[6] F. Halzen and Alan D. Martin. Quarks and leptons: An introductory course in modern particle physics. New York, Usa: Wiley (1984) 396p.

[7] R. P. Feynman. The behavior of hadron collisions at extreme energies. Invited paper at the Third Conference on High-Energy Collisions, Stony Brook, New York, 5-6 Sep 1969.

[8] J. Ashman et al. A measurement of the spin asymmetry and determination of the structure function g(1) in deep inelastic muon proton scattering. *Phys. Lett.*, B206:364, 1988.

[9] J. Ashman et al. An investigation of the spin structure of the proton in deep inelastic scattering of polarized muons on polarized protons. *Nucl. Phys.*, B328:1, 1989.

[10] P. L. Anthony et al. Deep inelastic scattering of polarized electrons by polarized ^{3}he and the study of the neutron spin structure. *Phys. Rev.*, D54:6620–6650, 1996.

[11] K. Abe et al. Precision determination of the neutron spin structure function g_1^n. *Phys. Rev. Lett.*, 79:26–30, 1997.

[12] B. Adeva et al. A next-to-leading order QCD analysis of the spin structure function g1. *Phys. Rev.*, D58:112002, 1998.

[13] B. Adeva et al. Spin asymmetries a_1 of the proton and the deuteron in the low x and low q^2 region from polarized high energy muon scattering. *Phys. Rev.*, D60:072004, 1999.

[14] B. Adeva et al. Spin asymmetries a_1 of the proton and the deuteron in the low x and low q^2 region from polarized high energy muon scattering. *Phys. Rev.*, D62:079902, 2000.

[15] K. Abe et al. Measurements of the proton and deuteron spin structure functions g_1 and g_2. *Phys. Rev.*, D58:112003, 1998.

[16] P. L. Anthony et al. Measurements of the Q**2 dependence of the proton and neutron spin structure functions g1(p) and g1(n). *Phys. Lett.*, B493:19–28, 2000.

[17] E. S. Ageev et al. Measurement of the spin structure of the deuteron in the dis region. *Phys. Lett.*, B612:154–164, 2005.

[18] A. Airapetian et al. Precise determination of the spin structure function g_1 of the proton, deuteron, and neutron. *Phys. Rev.*, D75:012007, 2007.

[19] Hepdata - the durham hep databases. `http://www.slac.stanford.edu/spires/hepdata`, `http://durpdg.dur.ac.uk/HEPDATA/PDF`.

[20] B. Adeva et al. Polarised quark distributions in the nucleon from semi- inclusive spin asymmetries. *Phys. Lett.*, B420:180–190, 1998.

[21] A. Airapetian et al. Quark helicity distributions in the nucleon for up, down, and strange quarks from semi-inclusive deep-inelastic scattering. *Phys. Rev.*, D71:012003, 2005.

[22] Jr Jackson, Harold E. Measurement of delta(s) in the nucleon from semi-inclusive dis on deuterium. *AIP Conf. Proc.*, 915:379–382, 2007.

[23] John R. Ellis and Marek Karliner. The strange spin of the nucleon. 1995.

[24] Guido Altarelli, Richard D. Ball, Stefano Forte, and Giovanni Ridolfi. Theoretical analysis of polarized structure functions. *Acta Phys. Polon.*, B29:1145–1173, 1998.

[25] John R. Ellis and Marek Karliner. Direct estimate of the gluon polarization in the nucleon. *Mod. Phys. Lett.*, A21:721–728, 2006.

[26] M. Karliner. Goodbye to large δg? direct estimate of gluon polarization in the nucleon. *Nucl. Phys. Proc. Suppl.*, 161:116–122, 2006.

[27] Xiang-Dong Ji. Gauge invariant decomposition of nucleon spin. *Phys. Rev. Lett.*, 78:610–613, 1997.

[28] C. Adloff et al. Measurement of deeply virtual compton scattering at hera. *Phys. Lett.*, B517:47–58, 2001.

[29] S. Chekanov et al. Measurement of deeply virtual compton scattering at hera. *Phys. Lett.*, B573:46–62, 2003.

[30] A. Aktas et al. Measurement of deeply virtual compton scattering at hera. *Eur. Phys. J.*, C44:1–11, 2005.

[31] S. Stepanyan et al. First observation of exclusive deeply virtual Compton scattering in polarized electron beam asymmetry measurements. *Phys. Rev. Lett.*, 87:182002, 2001.

[32] S. Chen et al. Measurement of deeply virtual compton scattering with a polarized proton target. *Phys. Rev. Lett.*, 97:072002, 2006.

[33] M. Garcon. Deeply virtual compton scattering and nucleon structure. *AIP Conf. Proc.*, 870:93–101, 2006.

[34] A. Airapetian et al. Measurement of the beam spin azimuthal asymmetry associated with deeply-virtual Compton scattering. *Phys. Rev. Lett.*, 87:182001, 2001.

[35] A. Airapetian et al. The beam-charge azimuthal asymmetry and deeply virtual compton scattering. *Phys. Rev.*, D75:011103, 2007.

[36] A. Airapetian et al. Measurement of Azimuthal Asymmetries With Respect To Both Beam Charge and Transverse Target Polarization in Exclusive Electroproduction of Real Photons. 2008.

[37] B. L. G. Bakker, E. Leader, and T. L. Trueman. A critique of the angular momentum sum rules and a new angular momentum sum rule. *Phys. Rev.*, D70:114001, 2004.

[38] Robert L. Jaffe. Spin, twist and hadron structure in deep inelastic processes. 1996. Proceedings of the Ettore Majorana International School on the Spin Structure of the Nucleon, Erice, Italy, 3-10 Aug 1995.

[39] John P. Ralston and Davison E. Soper. Production of dimuons from high-energy polarized proton- proton collisions. *Nucl. Phys.*, B152:109, 1979.

[40] A. Airapetian et al. Single-spin asymmetries in semi-inclusive deep-inelastic scattering on a transversely polarized hydrogen target. *Phys. Rev. Lett.*, 94:012002, 2005.

[41] Markus Diefenthaler. Hermes measurements of collins and sivers asymmetries from a transversely polarised hydrogen target. 2007.

[42] V. Yu. Alexakhin et al. First measurement of the transverse spin asymmetries of the deuteron in semi-inclusive deep-inelastic scattering. *Phys. Rev. Lett.*, 94:202002, 2005.

[43] E. S. Ageev et al. A new measurement of the collins and sivers asymmetries on a transversely polarised deuteron target. 2006.

[44] M. Alekseev et al. Collins and Sivers Transverse Spin Asymmetries for Pions and Kaons on Deuterons. 2008.

[45] John C. Collins. Fragmentation of transversely polarized quarks probed in transverse momentum distributions. *Nucl. Phys.*, B396:161–182, 1993.

[46] Dennis W. Sivers. Single-spin production asymmetries from the hard scattering of pointlike constituents. *Phys. Rev.*, D41:83, 1990.

[47] Xiang-dong Ji, Jian-Ping Ma, and Feng Yuan. Qcd factorization for spin-dependent cross sections in dis and drell-yan processes at low transverse momentum. *Phys. Lett.*, B597:299–308, 2004.

[48] John C. Collins and Andreas Metz. Universality of soft and collinear factors in hard- scattering factorization. *Phys. Rev. Lett.*, 93:252001, 2004.

[49] M. Anselmino et al. Transversity and collins functions from sidis and e+ e- data. *Phys. Rev.*, D75:054032, 2007.

[50] A. V. Efremov, L. Mankiewicz, and N. A. Tornqvist. Jet handedness as a measure of quark and gluon polarization. *Phys. Lett.*, B284:394–400, 1992.

[51] John C. Collins, Steve F. Heppelmann, and Glenn A. Ladinsky. Measuring transversity densities in singly polarized hadron-hadron and lepton-hadron collisions. *Nucl. Phys.*, B420:565–582, 1994.

[52] K. Ackerstaff et al. Hermes spectrometer. *Nucl. Instrum. Meth.*, A417:230–265, 1998.

[53] Alessandro Bacchetta, Umberto D'Alesio, Markus Diehl, and C. Andy Miller. Single-spin asymmetries: The trento conventions. *Phys. Rev.*, D70:117504, 2004.

[54] Vincenzo Barone, Alessandro Drago, and Philip G. Ratcliffe. Transverse polarisation of quarks in hadrons. *Phys. Rept.*, 359:1–168, 2002.

[55] S. Chekanov et al. A ZEUS next-to-leading-order QCD analysis of data on deep inelastic scattering. *Phys. Rev.*, D67:012007, 2003.

[56] B. Adeva et al. Spin asymmetries A(1) and structure functions g1 of the proton and the deuteron from polarized high energy muon scattering. *Phys. Rev.*, D58:112001, 1998.

[57] E. S. Ageev et al. Spin asymmetry A(1)(d) and the spin-dependent structure function g1(d) of the deuteron at low values of x and Q**2. *Phys. Lett.*, B647:330–340, 2007.

[58] K. Ackerstaff et al. Measurement of the neutron spin structure function g1(n) with a polarized He-3 internal target. *Phys. Lett.*, B404:383–389, 1997.

[59] P. L. Anthony et al. Measurement of the deuteron spin structure function g1(d)(x) for 1 $(\mathrm{GeV/c})^2 < Q^2 < 40$ $(\mathrm{GeV/c})^2$. *Phys. Lett.*, B463:339–345, 1999.

[60] U. Stosslein. Status and perspectives of spin physics. *Acta Phys. Polon.*, B33:2813–2834, 2002.

[61] F. E. Close and R. G. Roberts. Consistent analysis of the spin content of the nucleon. *Phys. Lett.*, B316:165–171, 1993.

[62] Guido Altarelli, Richard D. Ball, Stefano Forte, and Giovanni Ridolfi. Determination of the Bjorken sum and strong coupling from polarized structure functions. *Nucl. Phys.*, B496:337–357, 1997.

[63] William A. Bardeen, A. J. Buras, D. W. Duke, and T. Muta. Deep Inelastic Scattering Beyond the Leading Order in Asymptotically Free Gauge Theories. *Phys. Rev.*, D18:3998, 1978.

[64] S. A. Larin, T. van Ritbergen, and J. A. M. Vermaseren. The alpha(s)**3 approximation of quantum chromodynamics to the Ellis-Jaffe sum rule. *Phys. Lett.*, B404:153–160, 1997.

[65] J. D. Bjorken. Applications of the Chiral U(6) x (6) Algebra of Current Densities. *Phys. Rev.*, 148:1467–1478, 1966.

[66] J. D. Bjorken. Inelastic Scattering of Polarized Leptons from Polarized Nucleons. *Phys. Rev.*, D1:1376–1379, 1970.

[67] John R. Ellis and Robert L. Jaffe. A Sum Rule for Deep Inelastic Electroproduction from Polarized Protons. *Phys. Rev.*, D9:1444, 1974.

[68] Steven D. Bass. The Spin structure of the proton. World Scientific, 2007. (ISBN 978-981-270-946-2 and ISBN 978-981-270-947-9). 212 p.

[69] Guido Altarelli and Graham G. Ross. The Anomalous Gluon Contribution to Polarized Leptoproduction. *Phys. Lett.*, B212:391, 1988.

[70] Geoffrey T. Bodwin and Jian-Wei Qiu. The Gluonic Contribution to G(1) and Its Relationship to the Spin Dependent Parton Distributions. *Phys. Rev.*, D41:2755, 1990.

[71] Xiang-Dong Ji. Deeply-virtual Compton scattering. *Phys. Rev.*, D55:7114–7125, 1997.

[72] Pervez Hoodbhoy, Xiang-Dong Ji, and Wei Lu. Quark orbital-angular-momentum distribution in the nucleon. *Phys. Rev.*, D59:014013, 1999.

[73] S. Chekanov et al. An NLO QCD analysis of inclusive cross-section and jet- production data from the ZEUS experiment. *Eur. Phys. J.*, C42:1–16, 2005.

[74] A. Bacchetta, Mariaelena Boglione, A. Henneman, and P. J. Mulders. Bounds on transverse momentum dependent distribution and fragmentation functions. *Phys. Rev. Lett.*, 85:712–715, 2000.

[75] A. Airapetian et al. Measurement of Parton Distributions of Strange Quarks in the Nucleon fromCharged-Kaon Production in Deep-Inelastic Scattering on the Deuteron. 2008.

[76] R. L. Jaffe and N. Saito. Qcd selection rules in polarized hadron collisions. *Phys. Lett.*, B382:165–172, 1996.

[77] Philip G. Ratcliffe. Qcd evolution of transversity in leading and next-to- leading order. *Czech. J. Phys.*, 53:B27–B46, 2003.

[78] A. Bacchetta. *Probing the transverse spin of quarks in deep inelastic scattering.* PhD thesis, Vrije Universiteit Amsterdam, 2002.

[79] Jacques Soffer. Positivity constraints for spin-dependent parton distributions. *Phys. Rev. Lett.*, 74:1292–1294, 1995.

[80] Sergio Scopetta and Vicente Vento. A quark model analysis of the transversity distribution. *Phys. Lett.*, B424:25–32, 1998.

[81] V. Barone, T. Calarco, and A. Drago. A confinement model calculation of h1(x). *Phys. Lett.*, B390:287–292, 1997.

[82] Hyun-Chul Kim, Maxim V. Polyakov, and Klaus Goeke. Nucleon “Tensor Charges” in the Chiral Quark–Soliton Model. *Phys. Rev.*, D53:4715–4718, 1996.

[83] P. V. Pobylitsa and Maxim V. Polyakov. Transverse spin distribution function of nucleon in chiral theory. *Phys. Lett.*, B389:350–357, 1996.

[84] L. P. Gamberg, H. Reinhardt, and H. Weigel. Odd structure functions from a chiral soliton. *Phys. Rev.*, D58:054014, 1998.

[85] M. Wakamatsu and T. Kubota. Chiral symmetry and the nucleon spin structure functions. *Phys. Rev.*, D60:034020, 1999.

[86] P. Schweitzer et al. Transversity distributions in the nucleon in the large-n_c limit. *Phys. Rev.*, D64:034013, 2001.

[87] K. Suzuki and W. Weise. Chiral constituent quarks and their role in quark distribution functions of nucleon and pion. *Nucl. Phys.*, A634:141–165, 1998.

[88] Bo-Qiang Ma and Ivan Schmidt. New sum rules for nucleon tensor charges. *J. Phys.*, G24:L71–L77, 1998.

[89] F. Cano, P. Faccioli, and M. Traini. Probing relativistic spin effects in the nucleon by means of drell-yan processes. *Phys. Rev.*, D62:094018, 2000.

[90] R. Jakob, P. J. Mulders, and J. Rodrigues. Modelling quark distribution and fragmentation functions. *Nucl. Phys.*, A626:937–965, 1997.

[91] Katsuhiko Suzuki and Takayuki Shigetani. Chiral-odd transversity spin structure function h1(x) of the nucleon in a constituent quark model. *Nucl. Phys.*, A626:886–910, 1997.

[92] B. L. Ioffe and A. Khodjamirian. Calculation of chirality violating proton structure function h-1 (x) in qcd. *Phys. Rev.*, D51:3373–3380, 1995.

[93] S. Aoki, M. Doui, T. Hatsuda, and Y. Kuramashi. Tensor charge of the nucleon in lattice qcd. *Phys. Rev.*, D56:433–436, 1997.

[94] R. C. Brower, S. Huang, J. W. Negele, A. Pochinsky, and B. Schreiber. Calculation of moments of nucleon structure functions. *Nucl. Phys. Proc. Suppl.*, 53:318–320, 1997.

[95] M. Gockeler et al. The drell-yan process and deep inelastic scattering from the lattice. *Nucl. Phys. Proc. Suppl.*, 53:315–317, 1997.

[96] S. Capitani et al. Towards a lattice calculation of delta(q) and delta(q). *Nucl. Phys. Proc. Suppl.*, 79:548–550, 1999.

[97] D. Dolgov et al. Moments of structure functions in full qcd. *Nucl. Phys. Proc. Suppl.*, 94:303–306, 2001.

[98] Jacques Soffer, Marco Stratmann, and Werner Vogelsang. Accessing transversity in double-spin asymmetries at the bnl-rhic. *Phys. Rev.*, D65:114024, 2002.

[99] V. A. Korotkov, W. D. Nowak, and K. A. Oganessyan. Transversity distribution and polarized fragmentation function from semi-inclusive pion electroproduction. *Eur. Phys. J.*, C18:639–644, 2001.

[100] M. Wakamatsu. Chiral-odd distribution functions in the chiral quark soliton model. *Phys. Lett.*, B509:59–68, 2001.

[101] D. Boer and P. J. Mulders. Time-reversal odd distribution functions in leptoproduction. *Phys. Rev.*, D57:5780–5786, 1998.

[102] P. J. Mulders and R. D. Tangerman. The complete tree-level result up to order $1/q$ for polarized deep-inelastic leptoproduction. *Nucl. Phys.*, B461:197–237, 1996. Erratum-ibid. **B484** (199s6) 538.

[103] Xavier Artru and Mustapha Mekhfi. Transversely polarized parton densities, their evolution and their measurement. *Z. Phys.*, C45:669–676, 1990.

[104] X. Artru and M. Mekhfi. What can we learn from unpolarized and polarized electroproduction of fast baryons? *Nucl. Phys.*, A532:351–358, 1991.

[105] R. L. Jaffe. Polarized λ's in the current fragmentation region. *Phys. Rev.*, D54:6581–6585, 1996.

[106] Markus Diefenthaler. Transversity measurements at hermes. *AIP Conf. Proc.*, 792:933–936, 2005.

[107] L. Trentadue and G. Veneziano. Fracture functions: An improved description of inclusive hard processes in qcd. *Phys. Lett.*, B323:201–211, 1994.

[108] John C. Collins and Davison E. Soper. Parton distribution and decay functions. *Nucl. Phys.*, B194:445, 1982.

[109] Daniel Boer, R. Jakob, and P. J. Mulders. Angular dependences in electroweak semi-inclusive leptoproduction. *Nucl. Phys.*, B564:471–485, 2000.

[110] Daniela Amrath, Alessandro Bacchetta, and Andreas Metz. Reviewing model calculations of the Collins fragmentation function. *Phys. Rev.*, D71:114018, 2005.

[111] R. L. Jaffe, Xuemin Jin, and Jian Tang. Interference fragmentation functions and the nucleon's transversity. *Phys. Rev. Lett.*, 80:1166–1169, 1998.

[112] R. L. Jaffe, Xuemin Jin, and Jian Tang. Interference fragmentation functions and valence quark spin distributions in the nucleon. *Phys. Rev.*, D57:5920–5922, 1998.

[113] A. Bianconi, S. Boffi, R. Jakob, and M. Radici. Two-hadron interference fragmentation functions. i: General framework. *Phys. Rev.*, D62:034008, 2000.

[114] A. Bianconi, S. Boffi, R. Jakob, and M. Radici. Two-hadron interference fragmentation functions. ii: A model calculation. *Phys. Rev.*, D62:034009, 2000.

[115] John C. Collins and Glenn A. Ladinsky. On $\pi - \pi$ correlations in polarized quark fragmentation using the linear sigma model. 1994.

[116] Marco Radici, Rainer Jakob, and Andrea Bianconi. Accessing transversity with interference fragmentation functions. *Phys. Rev.*, D65:074031, 2002.

[117] Alessandro Bacchetta and Marco Radici. Modeling dihadron fragmentation functions. *Phys. Rev.*, D74:114007, 2006.

[118] Xavier Artru and John C. Collins. Measuring transverse spin correlations by 4 particle correlations in $e^+e^- \to 2$ jets. *Z. Phys.*, C69:277–286, 1996.

[119] Daniel Boer, Rainer Jakob, and Marco Radici. Interference fragmentation functions in electron positron annihilation. *Phys. Rev.*, D67:094003, 2003.

[120] Alessandro Bacchetta and Marco Radici. Dihadron interference fragmentation functions in proton proton collisions. *Phys. Rev.*, D70:094032, 2004.

[121] P. B. van der Nat. *Transveristy in Two-Hadron Fragmentation.* PhD thesis, Vrije Universiteit Amsterdam, 2007.

[122] Alessandro Bacchetta and Marco Radici. Two-hadron semi-inclusive production including subleading twist. *Phys. Rev.*, D69:074026, 2004.

[123] D. de Florian and L. Vanni. Two hadron production in e^+e^- annihilation to next-to-leading order accuracy. *Phys. Lett.*, B578:139–149, 2004.

[124] Federico A. Ceccopieri, Marco Radici, and Alessandro Bacchetta. Evolution equations for extended dihadron fragmentation functions. *Phys. Lett.*, B650:81–89, 2007.

[125] Marco Radici. Extended dihadron fragmentation functions and extraction of transversity, 2008. Talk at DIS 2008: `http://indico.cern.ch/contributionDisplay.py?contribId=273&sessionId=22&confId=24657.`

[126] Alessandro Bacchetta and Marco Radici. Partial-wave analysis of two-hadron fragmentation functions. *Phys. Rev.*, D67:094002, 2003.

[127] J. J. Aubert et al. ρ^0 production in deep inelastic μp interactions. *Phys. Lett.*, B133:370, 1983.

[128] K. Konishi, A. Ukawa, and G. Veneziano. A simple algorithm for qcd jets. *Phys. Lett.*, B78:243, 1978.

[129] I. Vendramin. Two - hadron fragmentation functions: A study of their q**2 evolution. *Nuovo Cim.*, A66:339, 1981.

[130] U. P. Sukhatme and K. E. Lassila. q^2 evolution of multi-hadron fragmentation functions. *Phys. Rev.*, D22:1184, 1980.

[131] A. Majumder and Xin-Nian Wang. The dihadron fragmentation function and its evolution. *Phys. Rev.*, D70:014007, 2004.

[132] A. Majumder and Xin-Nian Wang. Evolution of the parton dihadron fragmentation functions. *Phys. Rev.*, D72:034007, 2005.

[133] P. Estabrooks and Alan D. Martin. pi pi phase shift analysis below the k anti-k threshold. *Nucl. Phys.*, B79:301, 1974.

[134] H. Meyer and P. J. Mulders. Polarized and unpolarized structure functions in a diquark model for the nucleon. *Nucl. Phys.*, A528:589–607, 1991.

[135] Wally Melnitchouk, Andreas W. Schreiber, and Anthony William Thomas. Deep inelastic scattering from off-shell nucleons. *Phys. Rev.*, D49:1183–1198, 1994.

[136] M. Gluck, E. Reya, and A. Vogt. Dynamical parton distributions revisited. *Eur. Phys. J.*, C5:461–470, 1998.

[137] M. Gluck, E. Reya, M. Stratmann, and W. Vogelsang. Next-to-leading order radiative parton model analysis of polarized deep inelastic lepton - nucleon scattering. *Phys. Rev.*, D53:4775–4786, 1996.

[138] Jun She, Yang Huang, Vincenzo Barone, and Bo-Qiang Ma. Transversity from two pion interference fragmentation. *Phys. Rev.*, D77:014035, 2008.

[139] Bo-Qiang Ma. The x-dependent helicity distributions for valence quarks in nucleons. *Phys. Lett.*, B375:320–326, 1996.

[140] M. Hirai, S. Kumano, and N. Saito. Determination of polarized parton distribution functions and their uncertainties. *Phys. Rev.*, D69:054021, 2004.

[141] John David Jackson. On Understanding Spin-Flip Synchrotron Radiation and the Transverse Polarization of Electrons in Storage Rings. *Rev. Mod. Phys.*, 48:417–433, 1976.

[142] A. A. Sokolov and I. M. Ternov. On polarization and spin effects in the theory of synchrotron radiation. *Phys. Dokl.*, 8:1203–1205, 1964.

[143] Jean Buon and Klaus Steffen. Hera variable energy 'mini' spin rotator and headon e p collision scheme with choice of electron helicity. *Nucl. Instr. Meth.*, A245:248, 1986.

[144] M. Beckmann et al. The longitudinal polarimeter at hera. *Nucl. Instrum. Meth.*, A479:334–348, 2002.

[145] D. P. Barber et al. The hera polarimeter and the first observation of electron spin polarization at hera. *Nucl. Instrum. Meth.*, A329:79–111, 1993.

[146] A. Airapetian et al. The hermes polarized hydrogen and deuterium gas target in the hera electron storage ring. *Nucl. Instrum. Meth.*, A540:68–101, 2005.

[147] M. Dueren. The hermes experiment: From the design to the first results. *DESY Grey Report: DESY-HERMES*, 95-02, 1995.

[148] A. Nass. The hermes polarized atomic beam source. *AIP Conf. Proc.*, 675:929–933, 2003.

[149] C. Baumgarten et al. The storage cell of the polarized h/d internal gas target of the hermes experiment at hera. *Nucl. Instrum. Meth.*, A496:277–285, 2003.

[150] C. Baumgarten et al. An atomic beam polarimeter to measure the nuclear polarization in the hermes gaseous polarized hydrogen and deuterium target. *Nucl. Instrum. Meth.*, A482:606–618, 2002.

[151] C. Baumgarten et al. A gas analyzer for the internal polarized target of the hermes experiment. *Nucl. Instrum. Meth.*, A508:268–275, 2003.

[152] M. Beckmann. Target polarisation values and their uncertainties used by the deltaq analysis group for the 1996 to 2000 running periods. *DESY-HERMES*, 03-005, 2003.

[153] HERMES Target Group. Hermes polarized targets. Webpage: `http://www-hermes.desy.de/groups/tgtgrp/www_target/ana_all.html`.

[154] M. G. van Beuzekom et al. A silicon micro-strip telescope for the hermes experiment: A design study. *Nucl. Instrum. Meth.*, A409:255–257, 1998.

[155] A. J. Reischl. *Quasi-real photo-production of hyperons and their impact on the Lambda polarization measurements*. PhD thesis, University of Amsterdam, 2007.

[156] J. T. Brack et al. The hermes forward tracking chambers: Construction, operation, and aging effects. *Nucl. Instrum. Meth.*, A469:47–54, 2001.

[157] S. Bernreuther et al. The hermes back drift chambers. *Nucl. Instrum. Meth.*, A416:45–58, 1998.

[158] A. Andreev et al. Multiwire proportional chambers in the hermes experiment. *Nucl. Instrum. Meth.*, A465:482–497, 2001.

[159] S. Wang. *Improvements of the HERMES Transverse Polarized Hydrogen Target and Calculations of the Sextupole Magnet.* PhD thesis, China Institute of Atomic Energy, 2004.

[160] T. Weiland et al. Mafia version 4. *AIP Conf. Proc.*, 391:65–70, 1997. Prepared for CAP 96: The 1996 Computational Accelerator Physics Conference, Williamsburg, Virginia, USA 24-27 Sep 1996.

[161] W Augustyniak, A Miller, G Schnell, S Yen, and P Zupranski. TMC- vertex reconstruction in the presence of the hermes transverse target magnet. HERMES Internal Report, 2007. DESY-HERMES-07-008.

[162] S. B. Kowalski and H. A. Enge. The ion-optical program raytrace. *Nucl. Instrum. Meth.*, A258:407, 1987.

[163] Ulrike Elschenbroich. *Transverse Spin Structure of the Proton Studied in Semi-inclusive DIS.* PhD thesis, Universiteit Gent, Belgium, 2006.

[164] Zhenyu Ye. *Transverse Target-Spin Asymmetry Associated with Deeply Virtual Compton Scattering on the Proton and A Resulting Model-Dependent Constraint on the Total Angular Momentum of Quarks in the Nucleon.* PhD thesis, University of Hamburg, 2007.

[165] D. De Schepper et al. The hermes cerenkov detector. *DESY-HERMES*, 00-021, 2000.

[166] N. Akopov et al. The hermes dual-radiator ring imaging cerenkov detector. *Nucl. Instrum. Meth.*, A479:511–530, 2002.

[167] P.A. Cerenkov. Visible radiation produced by electron moving in a medium with velocities exceeding that of light. *Phys. Rev.*, 52:378, 1937.

[168] Lin-Feng Zhang. Ring imaging Cerenkov counter with aerogel radiator for HERMES. DESY-HERMES-99-64.

[169] E. Aschenauer et al. Optical characterization of n = 1.03 silica aerogel used as radiator in the RICH of HERMES. *Nucl. Instrum. Meth.*, A440:338–347, 2000.

[170] D. De Schepper, R. Kaiser, and E. Cisbani. Particle identification with the hermes rich detector: Description of the different approaches. *DESY-HERMES*, 98-008, 1998.

[171] R. Lamb. Event level rich algorithm: An explanation and user guide. *DESY-HERMES*, 07-017, 2007.

[172] HERMES RICH Group. Using the rich detector for physics analysis. Webpage: `http://www-hermes.desy.de/groups/richgrp/rich/richanalysis/index.html`.

[173] H. Avakian et al. Performance of the electromagnetic calorimeter of the hermes experiment. *Nucl. Instrum. Meth.*, A417:69–78, 1998.

[174] H. Avakian et al. Performance of f101 radiation resistant lead glass shower counters. *Nucl. Instrum. Meth.*, A378:155–161, 1996.

[175] H. Tanaka et al. A gain monitoring system with a nd:yag laser for the photomultipliers of the hermes experiment. *Nucl. Instrum. Meth.*, A515:725–732, 2003.

[176] X. Artru, G. B. Yodh, and G. Mennessier. Practical theory of the multilayered transition radiation detector. *Phys. Rev.*, D12:1289, 1975.

[177] J. Ely. Hermes calorimeter position reconstruction study. *DESY-HERMES*, 01-056, 2001.

[178] T. Benisch et al. The luminosity monitor of the hermes experiment at desy. *Nucl. Instrum. Meth.*, A471:314–324, 2001.

[179] J. Wendland. *Polarized Parton Distributions Measured at the HERMES Experiment.* PhD thesis, Simon Fraser University, 2003.

[180] HERMES Data Quality Group. Offline data quality - μdst productions. Webpage: `http://www-hermes.desy.de/groups/daqlgrp/OFFLINE_DQ/uDST/index.html`.

[181] Marc Beckmann. *Extraction of polarised quark distributions of the nucleon from deep inelastic scattering at the HERMES experiment.* PhD thesis, Albert-Ludwigs-Universität Freiburg, 2000. DESY-THESIS-2000-029.

[182] W. M. Yao et al. Review of particle physics. *J. Phys.*, G33:1–1232, 2006.

[183] P. B. van der Nat and H. P. Blok. (another) correction in binned fitting of asymmetries. HERMES Internal Report, 2005. DESY-HERMES-05-026.

[184] Xianguo Lu and Zhenyu Ye. Simultaneous extraction of the bsas and the bca associated with dvcs with the extended maximum likelihood method. HERMES Internal Report, 2007. DESY-HERMES-07-001.

[185] F. James and M. Roos. 'minuit' a system for function minimization and analysis of the parameter errors and correlations. *Comput. Phys. Commun.*, 10:343–367, 1975.

[186] Markus Diefenthaler and Luciano Pappalardo. Collins and sivers amplitudes for charged and neutral pion production and charged kaon production from sidis, using the full run 2 transverse-target data set. HERMES release report, `http://www-hermes.desy.de/reports`, 2007. Release meeting, April 10-11.

[187] Maurice George Kendall and Alan Stuart. *The Advanced Theory of Statistics*. Macmillan, New York, USA, 1983.

[188] G.S. Fishman. *Monte Carlo: Concepts, Algorithms, and Applications*. Springer, New York, USA, 1996.

[189] Torbjorn Sjostrand, Leif Lonnblad, Stephen Mrenna, and Peter Skands. Pythia 6.3: Physics and manual. 2003.

[190] Patricia Liebing. *Can the gluon polarization in the nucleon be extracted from HERMES data on single high-p_T hadrons?* PhD thesis, Universität Hamburg, 2004. DESY-THESIS-2004-036.

[191] B. Hommz. *A Study of Fragmentation Processes in the HERMES experiment using a Ring Imaging Cerenkov Detector*. PhD thesis, University of Gent, 2003.

[192] Bino Maiheu, Achim Hillenbrand, and Elke Aschenauer. Monte-carlo study of the influence of possible moments on the hermes acceptance function for hadrons. HERMES Internal Report, 2005. DESY-HERMES-05-004.

[193] Antje Bruell and Alexander Kisselev. Top/bottom misalignment for 1996-2003 data. Mailing list: offline-list@hermes.le.desy.de, June 9 June 9, 2003.

[194] Z. Ye and E.C. Aschenauer. Misalignment effects on the beam-spin and beam-charge asymmetries in dvcs. HERMES Internal Report, 2005. DESY-HERMES-05-038.

[195] P. B. van der Nat and K. Griffioen. Two-hadron single target-spin asymmetries: First measurements by hermes. 2005. Proceedings of 16th International Spin Physics Symposium (SPIN 2004), Trieste, Italy, 10-16 Oct 2004.

[196] M. Diehl and S. Sapeta. On the analysis of lepton scattering on longitudinally or transversely polarized protons. *Eur. Phys. J.*, C41:515–533, 2005.

[197] Alessandro Bacchetta and Marco Radici. Single-spin asymmetries with two-hadron fragmentation functions. 2004.

[198] R. D. Tangerman and P. J. Mulders. Polarized twist-three distributions g_t and h_l and the role of intrinsic transverse momentum. 1994.

[199] P. J. Mulders and R. D. Tangerman. The complete tree-level result up to order $1/q$ for polarized deep-inelastic leptoproduction. *Nucl. Phys.*, B461:197–237, 1996. Erratum-ibid. **B484** (1997) 538.

[200] Paul Bastiaan van der Nat and T. Kobayashi. Interference fragmentation on a transversely polarised hydrogen target. HERMES release report, `http://www-hermes.desy.de/reports`, 2005. Release meeting, April 21.

[201] P. B. van der Nat. First measurement of interference fragmentation on a transversely polarized hydrogen target. 2005. Proceedings of International Workshop on Transverse Polarization Phenomena in Hard Processes (Transversity 2005), Villa Olmo, Como, Italy, 7-10 Sep 2005.

[202] P. B. van der Nat. First measurement of interference fragmentation on a transversely polarized hydrogen target. *AIP Conf. Proc.*, 792:953–956, 2005. Proceedings of the 13th International Workshop on Deep- Inelastic Scattering (DIS 2005), Madison, Wisconsin, U.S.A. 27 Apr - 1 May 2005.

[203] Marco Contalbrigo. Measurement of transverse asymmetries from interference fragmentation at hermes. *AIP Conf. Proc.*, 915:650–653, 2007.

[204] P. Abbon et al. The COMPASS Experiment at CERN. *Nucl. Instrum. Meth.*, A577:455–518, 2007.

[205] R. Joosten. Transversity signals in two-hadron correlation at compass. Prepared for 16th International Spin Physics Symposium (SPIN 2004), Trieste, Italy, 10-16 Oct 2004.

[206] R. Joosten. Transversity signals in two hadron correlation at compass. *AIP Conf. Proc.*, 792:957–960, 2005.

[207] Rainer Joosten. Transversity signals in two hadron correlation at compass. *AIP Conf. Proc.*, 915:646–649, 2007.

[208] Christian Schill. Transversity Signals in Two-Hadron Production at COMPASS. 2007.

[209] R. Joosten. Transversity signals in two hadron correlation at compass. 2006. Proceedings of 17th International Spin Physics Symposium (SPIN 2006), Kyoto, Japan, 2-7 Oct 2006; to be published.

[210] Marco Radici. Transversity and inclusive two-pion production. *AIP Conf. Proc.*, 915:654–657, 2007.

[211] A. Bravar. Hadron azimuthal distributions and transverse spin asymmetries in dis of leptons off transversely polarized targets from smc. *Nucl. Phys. Proc. Suppl.*, 79:520–522, 1999.

[212] Vincenzo Barone. Understanding transversity: Present and future. 2005.

[213] X. Artru, J. Czyzewski, and H. Yabuki. Single-spin asymmetry in inclusive pion production, collins effect and the string model. *Z. Phys.*, C73:527–534, 1997.

[214] A. Schafer and O. V. Teryaev. Sum rules for the t-odd fragmentation functions. *Phys. Rev.*, D61:077903, 2000.

[215] N. Makins. Summary talk. 2004. Talk delivered at the transversity workshop, Trento, Italy, 13-18 June 2004:
`http://www.lnf.infn.it/conference/transversity04/Talks/summary.pdf`.

[216] K. Abe et al. Measurement of azimuthal asymmetries in inclusive production of hadron pairs in e^+e^- annihilation at belle. *Phys. Rev. Lett.*, 96:232002, 2006.

[217] A. Ogawa, Matthias Grosse Perdekamp, Ralf-Christian Seidl, and Kazumi Hasuko. Spin dependent fragmentation functions analysis at Belle. *AIP Conf. Proc.*, 915:575–578, 2007.

[218] Akio Ogawa. Results from belle on the collins fragmentation function, 2008. Talk at DIS 2008:
`http://indico.cern.ch/contributionDisplay.py?contribId=278&sessionId=22&confId=24657`.

[219] Alexei Prokudin. Effects of intrinsic parton motion in sidis, 2008. Talk at DIS 2008:
`http://indico.cern.ch/contributionDisplay.py?contribId=279&sessionId=22&confId=24657`.

[220] M. Wakamatsu. Comparative analysis of the transversities and the longitudinally polarized distribution functions of the nucleon. *Phys. Lett.*, B653:398–403, 2007.

[221] B. Pasquini, M. Pincetti, and S. Boffi. Chiral-odd generalized parton distributions in constituent quark models. *Phys. Rev.*, D72:094029, 2005.

[222] I. C. Cloet, Wolfgang Bentz, and Anthony William Thomas. Transversity quark distributions in a covariant quark- diquark model. *Phys. Lett.*, B659:214–220, 2008.

[223] The Jefferson Lab Hall A collaboration. Measurement of single-target-spin asymmetry in semi-inclusive pion electroproduction on a transversely polarized ^{3}he target. `http://hallaweb.jlab.org/experiment/transversity`, 2006. The E06-010 and E06-011 experiments (approved).

[224] H. Avakian, P. Bosted, V. Burkert, and L. Elouadrhiri. Studies of transverse spin effects at jlab. prepared for international workshop on transverse polarization phenomena in hard processes (Transversity 2005), Villa Olmo, Como, Italy, 7-10 Sep 2005.

[225] A. V. Efremov, K. Goeke, and P. Schweitzer. Collins effect in semi-inclusive deeply inelastic scattering and in e^+e^- annihilation. 2006.

[226] A. V. Efremov and O. V. Teryaev. On spin effects in quantum chromodynamics. *Sov. J. Nucl. Phys.*, 36:140, 1982.

[227] Xiangdong Ji. Chiral-odd and spin-dependent quark fragmentation functions and their applications. *Phys. Rev.*, D49:114–124, 1994.

[228] M. Anselmino, Mariaelena Boglione, J. Hansson, and F. Murgia. Polarized inclusive leptoproduction, $\ell n \to hx$, and the hadron helicity density matrix $\rho(h)$: Possible measurements and predictions. *Phys. Rev.*, D54:828–837, 1996.

[229] A. Bacchetta and P. J. Mulders. Deep-inelastic leptoproduction of spin-one hadrons. *Phys. Rev.*, D62:114004, 2000.

[230] Xavier Artru. Proposals for measuring transversity distributions in deep- inelastic electron scattering and a model for e-704 asymmetries. 1993.

[231] Mauro Anselmino. Transversity and Lambda polarization. 2003.

[232] F. Bradamante. Transversity physics at compass. 2006.

[233] A. Ferrero. Lambda asymmetries. prepared for international workshop on transverse polarization phenomena in hard processes (Transversity 2005), Villa Olmo, Como, Italy, 7-10 Sep 2005.

[234] C. Schill. Transversity Measurements at COMPASS. 2007.

[235] Michiel Demey. *The polarization of* Λ^0 *hyperons in quasi-real photoproduction.* PhD thesis, Universiteit van Amsterdam (UvA), 2007. DESY-HERMES-07-05.

[236] Bernard Pire and John P. Ralston. SINGLE SPIN ASYMMETRIES IN THE DRELL-YAN PROCESS. *Phys. Rev.*, D28:260, 1983.

[237] Gerry Bunce, Naohito Saito, Jacques Soffer, and Werner Vogelsang. Prospects for spin physics at rhic. *Ann. Rev. Nucl. Part. Sci.*, 50:525–575, 2000.

[238] Xiangdong Ji. Probing the nucleon's transversity distribution in polarized p p, p anti-p, and pi p collisions. *Phys. Lett.*, B284:137–143, 1992.

[239] V. Barone, T. Calarco, and A. Drago. Double-spin transverse asymmetries in drell-yan processes. *Phys. Rev.*, D56:527–530, 1997.

[240] O. Martin, A. Schafer, M. Stratmann, and W. Vogelsang. Tranverse double-spin asymmetries for muon pair production in pp collisions. *Phys. Rev.*, D60:117502, 1999.

[241] Vincenzo Barone et al. Antiproton-proton scattering experiments with polarization. 2005.

[242] M. Anselmino, V. Barone, A. Drago, and N. N. Nikolaev. Accessing transversity via j/ψ production in polarized $p^{\uparrow}\bar{p}^{\uparrow}$ interactions. 2004.

[243] A. V. Efremov, K. Goeke, and P. Schweitzer. Transversity distribution function in hard scattering of polarized protons and antiprotons in the pax experiment. *Eur. Phys. J.*, C35:207–210, 2004.

[244] Frank Rathmann. Towards polarized antiprotons at FAIR. *AIP Conf. Proc.*, 915:924–931, 2007.

[245] Alexander Nass. Spin-filtering studies at COSY and AD. *AIP Conf. Proc.*, 980:153–160, 2008.

[246] Daniel Boer. Investigating the origins of transverse spin asymmetries at rhic. *Phys. Rev.*, D60:014012, 1999.

[247] L. Dick et al. Spin effects in the inclusive reactions $\pi^{\pm} + p^{\uparrow} \rightarrow \pi^{\pm} + x$ at 8 gev/c. *Phys. Lett.*, B57:93, 1975.

[248] R. D. Klem et al. Measurement of asymmetries of inclusive pion production in proton-proton interactions at 6 gev/c and 11.8 gev/c. *Phys. Rev. Lett.*, 36:929–931, 1976.

[249] W. H. Dragoset et al. Asymmetries in inclusive proton-nucleon scattering at 11.75 gev/c. *Phys. Rev.*, D18:3939–3954, 1978.

[250] D. Aschman et al. Spin dependence of inclusive reactions from proton-proton collisions at 7.9 gev/c. *Nucl. Phys.*, B142:220–228, 1978.

[251] S. Saroff et al. Single-spin asymmetry in inclusive reactions $p^{\uparrow} + p \rightarrow \pi^{+} + x, \pi^{-} + x$, and $p + x$ at 13.3 gev/c and 18.5 gev/c. *Phys. Rev. Lett.*, 64:995, 1990.

[252] D. L. Adams et al. Analyzing power in inclusive π^{+} and π^{-} production at high x_f with a 200 gev polarized proton beam. *Phys. Lett.*, B264:462–466, 1991.

[253] D. L. Adams et al. Large-x_f spin asymmetry in π^0 production by 200 gev polarized protons. *Z. Phys.*, C56:181–184, 1992.

[254] J. Adams et al. Cross sections and transverse single-spin asymmetries in forward neutral-pion production from proton collisions at $\sqrt{s} = 200$ gev. *Phys. Rev. Lett.*, 92:171801, 2004.

[255] B. I. Abelev et al. Forward Neutral Pion Transverse Single Spin Asymmetries in p+p Collisions at $\sqrt{s}$=200 GeV. 2008.

[256] F. Videbaek. Single-spin asymmetries in the brahms experiment. *AIP Conf. Proc.*, 842:401–403, 2006.

[257] I. Arsene et al. Single Transverse Spin Asymmetries of Identified Charged Hadrons in Polarized p+p Collisions at $\sqrt{s} = 62.4$ GeV. 2008.

[258] Doug Fields. Recent phenix results in transverse polarized *pp* collisions at $\sqrt{s} =$ 200 gev, 2008. Talk at DIS 2008: `http://indico.cern.ch/contributionDisplay.py?contribId=284&sessionId=22&confId=24657`.

[259] S. S. Adler et al. Measurement of transverse single-spin asymmetries for mid- rapidity production of neutral pions and charged hadrons in polarized p+p collisions at $\sqrt{s} = 200$ gev. *Phys. Rev. Lett.*, 95:202001, 2005.

[260] Gordon L. Kane, J. Pumplin, and W. Repko. Transverse Quark Polarization in Large p(T) Reactions, e+ e- Jets, and Leptoproduction: A Test of QCD. *Phys. Rev. Lett.*, 41:1689, 1978.

[261] Dennis W. Sivers. Hard scattering scaling laws for single-spin production asymmetries. *Phys. Rev.*, D43:261–263, 1991.

[262] Umberto D'Alesio and Francesco Murgia. Parton intrinsic motion in inclusive particle production: Unpolarized cross sections, single spin asymmetries and the Sivers effect. *Phys. Rev.*, D70:074009, 2004.

[263] Jian-wei Qiu and George Sterman. Single transverse-spin asymmetries in hadronic pion production. *Phys. Rev.*, D59:014004, 1999.

[264] Jiro Kodaira and Kazuhiro Tanaka. Polarized structure functions in QCD. *Prog. Theor. Phys.*, 101:191–242, 1999.

[265] Chris Kouvaris, Jian-Wei Qiu, Werner Vogelsang, and Feng Yuan. Single transverse-spin asymmetry in high transverse momentum pion production in p p collisions. *Phys. Rev.*, D74:114013, 2006.

[266] M. Anselmino, M. Boglione, U. D'Alesio, E. Leader, and F. Murgia. Parton intrinsic motion: Suppression of the collins mechanism for transverse single-spin asymmetries in $p^{\uparrow}p \to \pi x$. *Phys. Rev.*, D71:014002, 2005.

[267] K. Oleg Eyser. Summary of PHENIX transverse spin physics results. Prepared for 15th International Workshop on Deep-Inelastic Scattering and Related Subjects (DIS2007), Munich, Germany, 16-20 Apr 2007.

[268] B. Aubert et al. The BaBar detector. *Nucl. Instrum. Meth.*, A479:1–116, 2002.

[269] M. Ablikim et al. BESII detector simulation. *Nucl. Instrum. Meth.*, A552:344–356, 2005.

[270] Xiaorui Lu, Xun Chen, Yajun Mao, and Bo-Qiang Ma. New analysis on helicity balance method in longitudinal spin transfer to lambda hyperon. HERMES Internal Report, 2005. DESY-HERMES-05-003.

Acknowledgement

First of all, I would thank my doctoral advisor, Prof. Toshi-Aki Shibata who provides me the opportunities of studying, working and living in Japan. He has an extraordinary perspective and thorough knowledge in physics. Without his support for my research activities in the HERMES experiment, this thesis would not have been completed.

Prof. Yoshiyuki Miyachi helped me a lot in Shibata laboratory and DESY Tokyo office. I carried out the HERMES GMS works with his persistent help. Thanks to his efforts for the laboratory facility, I enjoy the comfort working environment in the laboratory. I obtained the invaluable suggestions from the discussions with him.

Special gratitude goes to my master thesis advisors Prof. Bo-Qiang Ma and Prof. Yajun Mao, who first lead me to the HERMES collaboration and taught me how to work in high energy experiment. They always keep motivating my studies, which is very important for my career.

I am happy to be a member of the HERMES collaboration. This is a wonderful community, where you can express your ideas freely and get much inspiration from experts in different fields. Many appreciations to the HERMES colleagues, who helped me a lot in taking shifts, GMS on–call service and data analysis. Also I would like to express my thanks to all the members of the drafting committee DC64. Many thanks go to Gunar Schnell, who coordinated the analysis and worked a lot on the paper draft. Impressively cooperative work with Riccardo Fabbri really gave me much enjoyment. The discussion with Alessandro helped me very much and his work is quite important for the work in this thesis. Paul van der Nat shared with me a lot of information in analysis. Thanks Andy Miller for those fresh ideas and suggestions. Thanks to the HERMES secretaries: Sabine Krohn and Evelyn Olabisi, who helped me a lot in DESY.

I enjoyed working very much with all the members in Shibata Laboratory, and received many helps from them. I am grateful to them for their kindness. Also thanks to the secretaries: Akiko Okawa and Ami Saito, for the help in administration works.